ORIGIN AND STRATIGRAPHIC SETTING OF THE SACKVILLE SPUR BOTTOM SIMULATING REFLECTOR, OFFSHORE NEWFOUNDLAND

by

Jane Elizabeth Hawken

Submitted in partial fulfilment of the requirements
for the degree of Master of Science

at

Dalhousie University
Halifax, Nova Scotia
March 2017

To my father, my foundational mentor, for imparting an appreciation for and curiosity of the natural world.

“Love many, trust few and always paddle your own canoe.”

TABLE OF CONTENTS

LIST OF TABLES

LIST OF FIGURES

ABSTRACT

Bottom Simulating Reflectors (BSRs) may represent free gas trapped below gas hydrates or a diagenetic transition such as that of opal-A to opal-CT in biosiliceous sediments. Determination of the origin of BSRs is important because they potentially result from vastly different geological processes. Gas hydrates represent a potential future hydrocarbon source and their dissociation, whether anthropogenic or natural, can result in sediment destabilization. Potential subsequent methane release may contribute to past and future climate change. This study investigates the origin of a segmented BSR imaged on industry-acquired 3D seismic reflection data offshore Newfoundland. The BSR cross-cuts Pliocene and younger contourite drift deposits of the Sackville Spur. The results show that depths to the prominent primary BSR and two deeper, poorly defined BSRs correlate to the theoretical base of hydrate stability depths for hydrates of variable thermogenic gas composition. Gas below the BSR is inferred based on a correlative low velocity zone on the F-09 well log. Effective medium models of these velocities predict minimal free gas concentrations of 0.5% and overlying gas hydrates concentrations of 2 to 10%. Free gas between and underlying the BSRs create amplitude, frequency and phase anomalies along the stratigraphic beds that intersect the BSRs. Based on these observations, the Sackville Spur BSRs are caused by hydrate accumulations. The top of an opal-A to opal-CT diagenetic front is interpreted to occur 365-660 m below the BSR. This diagenetic front is recognized as a high amplitude, faulted, late Miocene reflection that is generated by a dramatic increase in bulk density observed on well logs. Seismic stratigraphic analysis of the 3D volume shows post Miocene deposition was dominated by drift development on the flanks of Flemish Pass. The onset of sediment failures in the Pleistocene correlates to less drift development and increased deposition in the base of Flemish Pass. There is no direct spatial association between the BSRs and MTDs although the onset of pockmarks and failure scarps are stratigraphically equivalent, suggesting hydrate dissociation and sediment failure may have a common triggering mechanism. The Sackville Spur gas hydrate deposit represents a potential geohazard and must be considered during future development of the Mizzen hydrocarbon field.

LIST OF ABBREVIATIONS USED

2w	vertical analysis window height (coherency)
3D	three dimensional
a	point *c* projected onto the real axis
A_r	amplitude of reflected energy
A(t)	Instantaneous amplitude
b	point *c* projected onto the imaginary axis
BGHS	Base of Hydrate Stability
BHSZ	Base of Hydrate Stability Zone
bsf	below seafloor
C	coherency
c	complex point
cm	centimetres
D	depth in metres below seafloor
DMR	Drilling Mud Record
f(t)	time series of values
F(t)	complex trace of *f(t)*
FP	Flowing Pressure
FSI	Final Shut-In
$f(x_n)$	hydrate stability function
$f'(x_n)$	derivative of the hydrate stability function
g(t)	imaginary trace of *f(t)*
g	gravitational constant
G	shear modulus
GPa	gigapascals
g/cm^3	grams per centimetres cubed
H	Hilbert transform (coherency)
HP	Hydrostatic Pressure
J	number of traces (coherency)
j	$\sqrt{-1}$
K	bulk modulus
K	half height vertical analysis window height (coherency)
kPa/m	kiloPascals per metre

LAT	latitude
M	phasor length
MDT	Modular Formations Dynamic Tester
MLR	Mudlogger's Report
mm	millimetres
n	empirically derived constant (Archie's method)
OBS	Ocean Bottom Seismomenter
P	pressure
p	apparent dip in the x direction (coherency)
q	apparent dip in the y direction (coherency)
qXRD	Qualitative x-ray diffraction
R	reflection coefficient
RFT	Repeat Formation Tester
R0	resistivity of water saturated sediments (Archie's method)
Rt	resistivity log values (Archie's method)
SIP	Shut-In Pressure
SF	seafloor
S_w	water saturation (Archie's method)
Δt	temporal sample increment (coherency)
u	real seismic trace (coherency)
x_n	initial input approximation (hydrate stability)
V	velocity
VR	vertical resolution
z	depth (modelled porosity)
δg	thermal gradient
$\Theta(t)$	instantaneous phase
λ	exponential decay factor (modelled porosity)
ρ	density
τ	time
$\boldsymbol{\phi}$	phasor angle from the real axis
ϕ	surface porosity (modelled porosity)

ACKOWLEDGMENTS

Thank you to Statoil, Husky Energy and Suncor who made this project possible through the donation of the shallow portion of the Baynord 3D seismic volume and the F-09 well logs. I would also like to thank the Geological Survey of Canada – Atlantic for providing facilities and access to these data. Thank you NSERC for partial funding of this project.

My gratitude extends to my committee including my co-supervisor Dr. David Mosher for facilitating and overseeing this project. Thank you to my other co-supervisor Dr. John Gosse for your consistent support, guidance and comments throughout my MSc experience. Thank you Dr. Calvin Campbell for sharing your knowledge, for your reviews and for your understanding of the graduate student experience. Most importantly, thank you for planting many small seeds that led me down the paths of exploration that made this thesis what it is. Thank you Dr. Keith Louden for your valuable contributions at committee meetings and specifically for your help on the effective medium modelling.

I would like to thank my employer McGregor GeoScience Limited for providing financial, hardware and software support throughout my master's project. Also many thanks for the printing of everything and for working around my academic time requirements.

Although a solitary journey, there are many along my path who provided moral support. Most notable are fellow grad students Irena (don't ever finish!), Yanni, Colin, Janice, Bryan, Glenn and Janette who shared in my thesis pain and helped put things in perspective. To Norma and Darlene of the Dalhousie Earth Sciences office who were always there to listen and sign add/drop forms; you guys really should get therapist pay for listening to and consoling everyone! To Brian MacLean of NRCan for his moral support and unwavering belief in my abilities. I will always cherish our many lunches and early morning teas. You prove that friendship knows no age restrictions. Most importantly I would like to thank my husband Garth and my best friend Roxy for their unwavering support and belief in all that is me.

CHAPTER ONE: INTRODUCTION

1.1 STATEMENT OF PROBLEM

Seismic reflections that cross-cut stratigraphic reflections, mimic the seafloor, and do not represent acquisition artifacts are known as bottom simulating reflectors (BSRs). BSRs represent acoustic impedance contrasts that primarily result from two post depositional processes: 1) trapping of free gas below solid gas hydrates, and 2) changes in the physical properties of siliceous sediments at the diagenetic transition of silica from opal-A to opal-CT through to microcrystalline quartz. Gas hydrates represent a geological hazard, a potential future energy source, and may contribute to past and future climate changes. In contrast, diagenetic boundaries provide information on the lithology and physical properties of the sediments. The high risk associated with exploratory drilling further underscores the need to distinguish hydrocarbon-related BSRs from those created by silica diagenesis. Despite the importance of distinguishing the origin of BSRs, determining the cause is often challenging and requires additional information beyond seismic datasets.

A BSR offshore Newfoundland, first identified in 1985 on industry 2D seismic lines (Campbell et al. 2002), is fully imaged on modern 3D seismic data. The origin of this BSR, which transects late Cenozoic sediment drift deposits of the Sackville Spur, has been debated. Mosher (2011) related it to the presence of gas hydrates based on its phase reversal, the geometric nature of the cross-cutting relationship, and its correlation with the base of hydrate stability depths. However, consultants hired by the operators of the lease block attributed the BSR to the diagenetic transition of silica (E. Stacey personal communication, 2011) and compared it to a high amplitude, cross cutting reflector (CCR) imaged on various seismic profiles from Davis Strait off western Greenland (Pegrum et al. 2001). The Davis Strait CCR was originally interpreted as a water on gas contact and as such was targeted in the Qulleq-1 exploration well (Christiansen et al. 2001). Examination of the well's side cores indicated that the flat spot was not related to hydrocarbon accumulations but instead was produced by the diagenetic transition of opal-CT to microcrystalline quartz (Pegrum et al. 2001; Christiansen et al. 2001). The high risk and expense associated with exploratory drilling thus further underscores the need to distinguish hydrocarbon related BSRs from those created by silica diagenesis.

This study investigates the origin of the Sackville Spur BSR through assessment of seismic attributes along key horizons and through comparison of BSR depths and modelled hydrate stability depths. Seismic to well correlations provide valuable lithologic information and ages for the sediments transected by and underlying the BSR and ultimately allow for a detailed stratigraphic evolution of the Sackville Spur. The combination of these various observations, and improved calculation of the hydrate depth fields, provide key factors for distinguishing between hydrate and diagenetic silica BSRs within the North Atlantic. The results of this study reveal that the Sackville Spur BSR is caused by gas hydrates. This has direct implications for hazards and exploration risks in the immediate region, but also has implications for the interpretation of BSRs throughout the Atlantic margin.

1.2 OBJECTIVES

The central hypothesis of this thesis is that the Sackville Spur BSR is caused by gas hydrates. This study will use geophysical and geologic observations to test the hypothesis, and improve our understanding of the local seismic stratigraphy. If the hypothesis is not falsified, the study will estimate the concentration and composition of the gas hydrate and free gas in the sediments.

The main objectives of this thesis are:

(1) To describe the seismic stratigraphic setting of the Sackville Spur BSR
(2) To determine the origin of the Sackville Spur BSR
(3) If present, estimate the concentration of gas hydrate and underlying free gas
(4) Provide key indicators for distinguishing between gas hydrate versus silica diagenetic BSRs

1.3 THESIS ORGANIZATION

This thesis follows a traditional monograph style and is divided into seven chapters. Chapter 2 provides background information on the formation, detection, and significance of gas hydrates versus those for silica diagenesis. A brief review of the regional geology and local stratigraphy around the Sackville Spur is provided in Chapter 3. Chapter 4 details the methodological approaches with emphasis on seismic data interpretation and base of hydrate stability calculations. Chapter 5 provides the results of the seismic

interpretation and hydrate stability calculations. Combining the new and previously published results, Chapter 6 provides a detailed interpretation for the stratigraphy of the Sackville Spur, along with evidence to the genesis of the Sackville Spur BSR. The conclusions and implications for future work on the BSRs in the North Atlantic are summarized in Chapter 7.

CHAPTER TWO: GAS HYDRATES AND SILICA DIAGENISIS

2.1 THE BASICS

Gas hydrates are naturally occurring ice-like solids composed of a lattice of hydrogen bonded water molecules that encase a guest gas molecule. A subgroup of clathrates, which are compounds formed by the inclusion of molecules of one kind into the crystal structure of another compound, gas hydrates were first noted in 1811 by English chemist Sir Humphrey Davy (Davy 1811). Hydrates remained a scientific curiosity until the 1930's when hydrate blockages began to impede flow in oil and gas pipelines (Hammerschmidt 1934). The need to prevent such blockages led to significant research into understanding and predicting the conditions under which hydrates form. In 1967, Russian scientists were the first to discover a large naturally occurring gas hydrate deposit in the Siberian permafrost. This discovery was followed in the 1970's with the direct observation of gas hydrates in the Black Sea as reported by Russian scientists Yefremova and Zhizhchenko (1974).

Today the thermodynamic conditions required for hydrate formation are generally well defined and include regimes dominated by low temperature, typically less than 25°C and high pressure, normally greater than 0.6 MPa (Sloan 1998). These conditions occur naturally in the first few hundred metres of sediments of the world's outer continental margins. At such locations the zone of hydrate stability extends from the seafloor to the depth at which temperatures become too high for hydrate formation. Below this zone, water and free gas occupy the pore spaces.

Silica diagenesis is another post depositional process that modifies sediments on the world’s continental margins. When siliceous sediments go through diagenesis, opal-A transitions to opal-CT and can subsequently transition to quartz. Opal-A represents the siliceous oozes composed of the tests of silica-secreting organisms such as diatoms and radiolarians. As an amorphous mineral phase, opal-A is unstable during diagenesis (Hein et al. 1978). It dissolves at increased burial depths and opal-CT as porcellanite and chert is subsequently precipitated (Williams and Crerar 1985). This diagenetic transition reduces porosity and in turn increases the density and seismic velocities of sediments leading to a BSR on seismic profiles.

Silica diagenesis and the formation of gas hydrates are the result of two very different post-depositional processes. The following overview highlights the importance of distinguishing between them.

2.2 GAS HYDRATE PROPERTIES

Like all clathrates, there is a lack of bonding between the guest and host molecules that comprise gas hydrates. Instead, the hydrate structure is thermodynamically stabilized through non-bonded interactions between the guest and water lattice (Sloan 1998). Gas hydrates most commonly form with one of three repeating unit hydrate crystal structures, sI, sII and sH. The crystal structures differ in the number and sizes of the cages and their unit cells. Sloan (1998) proposed that the size of the gas molecules in the pore spaces dictates the hydrate crystal structure that will form in a particular deposit. Without the proper sized guest molecule the hydrate structure is not stable and hydrates will not form. Figure 2.1 relates the type of hydrate that forms when different guest molecules are present.

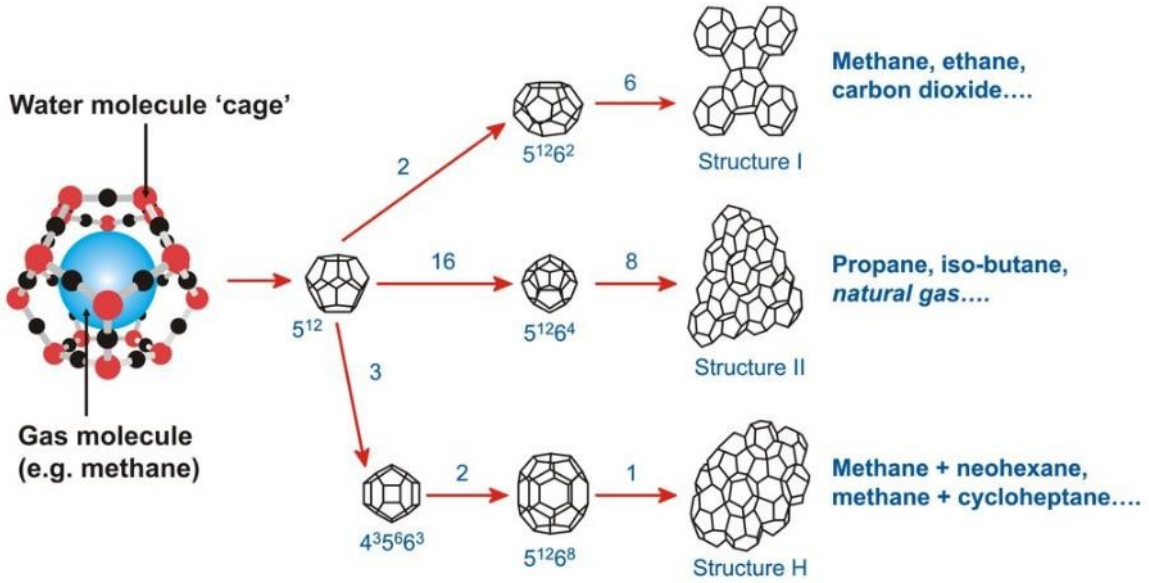

Figure 2.1 Gas hydrate formers and crystal structures. Modified after Sloan (2003).

The sI hydrate unit cell is a cubic lattice composed of 46 water molecules that form six large, and two small cages. The sI hydrates contain smaller guest molecules such as methane (CH_4), ethane (C_2H_6), carbon dioxide (CO_2) and hydrogen sulfide (H_2S). Methane occupies around 95% of the large and 85% of the small cages (Sloan, 1998). The sI hydrates predominate in Earth's natural environments with biogenic methane the most common guest molecule. The sII hydrates have a diamond lattice with cubic framework composed of 136 water molecules that contain eight large cages and 16 smaller cages (Sloan 1998). The sII small cage is the same as that of the sI hydrates.

Common sII formers include larger guest molecules such as propane (C_3H_8). Where larger gas molecules are thermogenic in origin, sII hydrates commonly form during hydrocarbon production (Sloan 1998). The third and least commonly observed hydrate crystal structure are sH hydrates, which have a hexagonal framework and require a mixture of very large and small gas molecules; of which the small must be present for sH hydrates to form. sH hydrates can occur in nature but are more commonly encountered in hydrocarbon production environments (Sloan 2003). The geometric parameters of the three crystal structures are summarized in Figure 2.1.

2.2.1 Physical Properties

Gas hydrates contain ~80% (mol) water in solid form and ~15% (mol) gas, which suggests gas hydrates have physical properties similar to those of ice. Indeed the presence of gas hydrates in the shallow sediments is akin to that of ice and just as ice would, gas hydrates act to cement and strengthen the host sediment (Stoll and Bryan 1979). Studies on hydrate bearing sediments from the Eastern Nankai Trough showed that sediments with 63% hydrate saturation experienced brittle failure when exposed to compressional triaxial stress while hydrate free sediments deformed ductilely (Yoneda at al. 2015). Yoneda et al. (2015) concluded that with increasing hydrate saturation the stiffness of the sediment increases.

The hydrate-ice analogy is generally true except for thermal conductivity (Stoll and Bryan 1979) and thermal expansivity (Sloan 1998). Unlike ice, the thermal conductivity of bulk hydrates is anomalously low; about one fourth that of ice (Waite et al. 2007). The thermal conductivities of hydrates are more like that of glass given that the hydrate guest molecules disrupt and slow the transfer of heat through the hydrate (Giavarini and Hester 2011). A comparison of the physical properties of hydrates versus ice are included in Table 2.1. Of note is the similarity of properties between the sI and sII hydrates.

Table 2.1 Comparison of the properties of ice, sI and sII hydrate crystal structures (Gabitto and Tsouris, 2010).

Property	Ice (I_h)	Structure I	Structure II
Water molecules number	4	46	136
Lattice parameters at 273 K, nm	$a = 0.452,\ c = 0.736$	1.20	1.73
Dielectric constant at 273 K	94	~58	58
Water diffusion correlation time, μs	220	240	25
Water diffusion activation energy, kJ/m	58.1	50	50
Isothermal Young's modulus at 268 K, 10^9 Pa	9.5	8.4 (est.)	8.2 (est.)
Poisson's ratio	0.33	~0.33	~0.33
Bulk modulus (272 K)	8.8	5.6	*NA*
Shear modulus (272 K)	3.9	2.4	*NA*
Compressional velocity (V_p), m/s	3870.1	3778.0	3821.8
Shear velocity (V_s), m/s	1949	1963.6	2001.1
Velocity ratio (comp./shear)	1.99	1.92	1.91
Linear thermal expn., at 200 K, K^{-1}	$56\ 10^{-6}$	$77\ 10^{-6}$	$52\ 10^{-6}$
Adiab. bulk compress. (273 K), 10^{-11} Pa	12	14 (est.)	14 (est.)
Heat Capacity, J kg^{-1} $K-1$	3800	3300	3600
Thermal conductivity (263 K), W m^{-1} K^{-1}	2.23	0.49 ± 0.02	0.51 ± 0.02
Refractive index, 638 nm, −3°C	1.3082	1.3460	1.350
Density, kg m^{-3}	916	912	940

A comparison with ice is useful but in the marine environment gas hydrates replace water in the pores and it is this contrast that helps detect them. A comparison of hydrate and water bearing sediments shows the thermal diffusivity of water is half that of gas hydrates (Sloan 1998). As a result hydrate bearing sediments change temperature more rapidly than hydrate free sediments (Stern et al. 2000). Hydrate bearing sediments store less heat than water bearing sediments as the specific heat of hydrates is half that of water (Sloan 1998; Stern et al. 2000). Another important characteristic of hydrates is that their dissociation is an endothermic process. When hydrates dissociate, heat is absorbed from the surrounding sediments and in turn the sediments cool. Conversely, the formation of hydrates is an exothermic process, leading to positive system enthalpy (Stern et al. 2000; Waite et al. 2007).

2.3 GAS HYDRATE PHASE BOUNDARIES

Gas hydrate equilibrium calculations are used to determine the temperature and pressure at which gas hydrates form from a water/gas mixture. The water can occur in solid or liquid phases and gas in the vapour phase. Based on laboratory experiments, researchers determined gas hydrate phase boundaries for various mixtures of water, including salts and other impurities, as well as for various gas compositions (Sloan

1998). These various phase boundary lines define the temperatures and pressures at which hydrocarbon gas co-occur with various water phases. Above the gas hydrate phase boundary, water, with gas in solution, is present in the liquid phase while below the phase boundary, the water and gas mixture forms solid hydrate Figure 2.2.

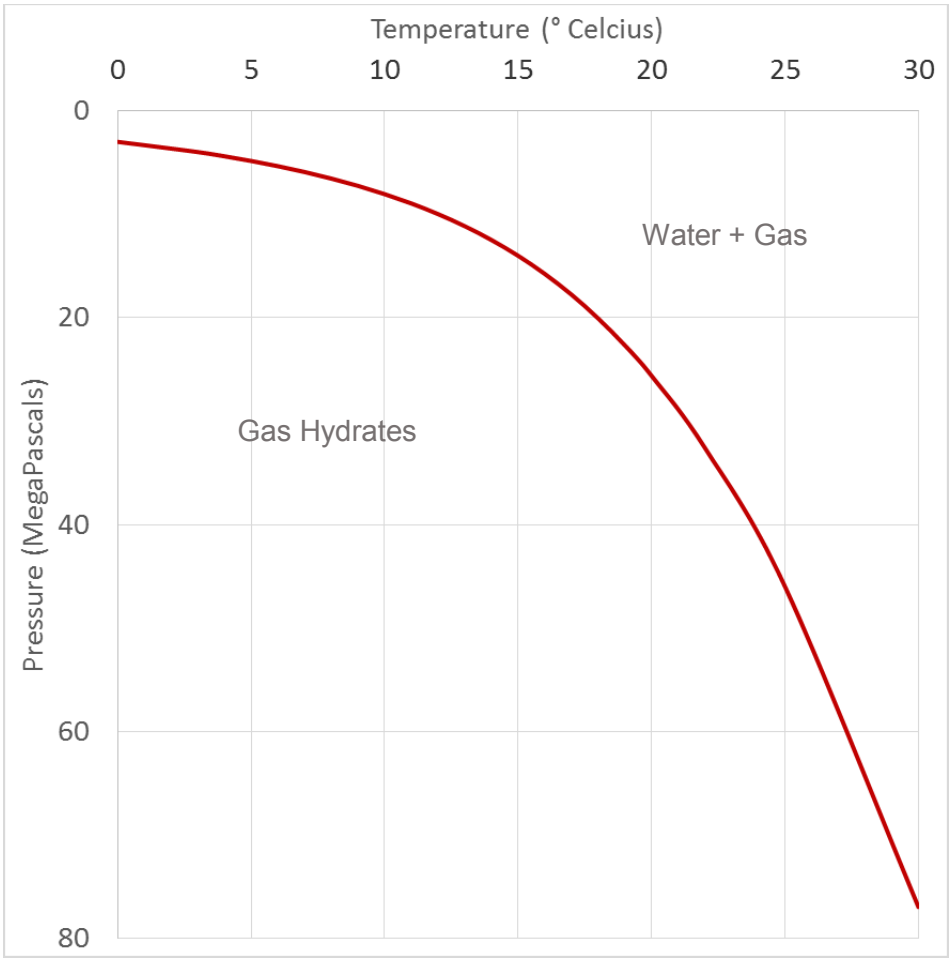

Figure 2.2 Gas hydrate phase diagram. Red line represent the phase boundary for a methane and salt water mixture (Sloan 1998).

Predictions of phase boundaries and in turn gas hydrate stability regimes were originally developed, and are most commonly used, to predict and prevent hydrate formation in gas pipelines (Carroll 2003). As the study of subsea gas hydrates has developed, researchers have used hydrate equilibrium calculations to model the predicted base of the gas hydrate stability zone in its natural setting (Dickens and Quinby-Hunt 1994; Majorowicz and Osadetz 2003; and León et al. 2009).

2.3.1 Gas Hydrate Formation

At its most basic level and much like a classic petroleum system, formation of natural gas hydrates requires a number of fundamental components. First, there must be sufficient gas in the system. Natural gases may be dissolved in the pore water or present as free gas in the pores. Secondly, there must be sufficient porosity for the hydrates to form and finally, the pressure and temperature regime must be favourable for their formation. The temperature and pressure regime can be thought of as a thermodynamic trap (Max and Johnson 2014).

Currently, three models of gas hydrate formation are proposed in the literature. The first is in-situ formation by biogenic methane (Kvenvolden and Barnard 1983). This mode creates uniform and extensive deposits with maximum hydrate concentrations of 3% (Klauda and Sandler 2005). The second model is formation by upwardly migrating free gas (Paull et al. 1994). The free gas may travel along faults or fissures or may represent dissociated hydrates. With continued deposition and subsequent subsidence temperatures at the base of the hydrate stability zone increase and eventually become too high for the hydrates to be stable. The hydrates dissociate and the free gas migrates upward until temperatures once again become favourable for hydrate formation (Figure 2.3). The third and final formation mode is a process by which upward rising methane-under-saturated water becomes methane saturated at lower pressures. As the saturated waters pass through the hydrate stability zone, hydrate formation occurs without an underlying free gas zone (Hyndman and Davis 1992).

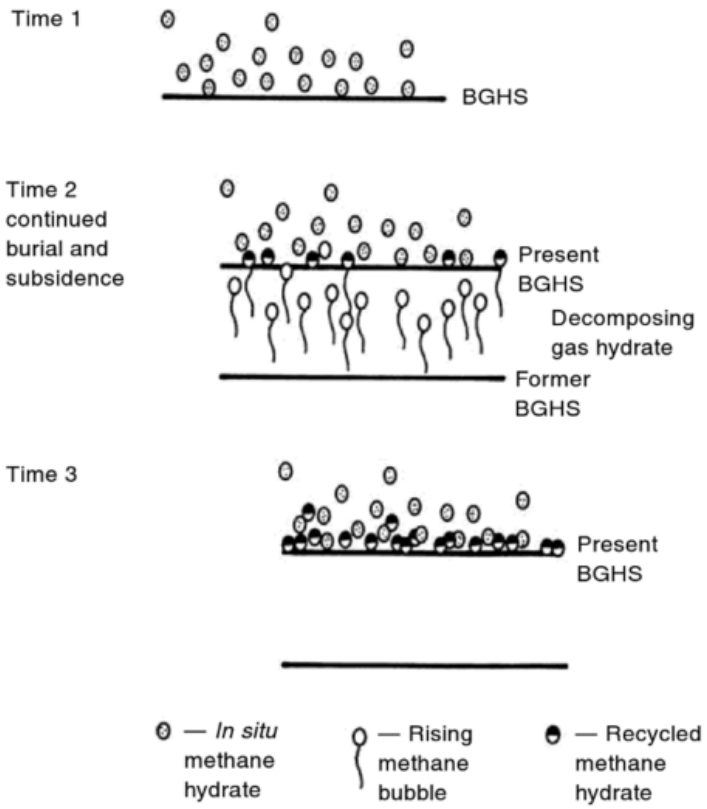

Figure 2.3 Proposed model for hydrate formation by upward migrating gas and hydrate recycling (Paull et al. 1994). BGHS represents the base of gas hydrate stability.

The presence of gas and migrating fluids are important for hydrate formation. But available porosity is also critical. Sandy sediments allow for increased hydrate formation relative to muds while faults can create secondary porosity and form focused areas of high hydrate concentrations. Faults may also provide conduits to more permeable sediment layers (Milkov and Sassen 2002).

In an overview of gas hydrate research Malone (1985) identified four types of naturally occurring hydrate deposits. The first are disseminated deposits that have low hydrate concentrations. These hydrates rapidly dissociate in core samples brought to the surface. Their presence is indicated in cores by reduced sediment temperatures as a result of hydrate's endothermic heat of dissociation. Disseminated deposits represent the majority of the ocean's hydrate deposits (Sloan 1998). Hydrate nodules represent the second type of hydrate deposit. The nodules can measure up to 5 cm in diameter and the methane or other guest gases (such as ethane and propane) may be thermogenic in origin. Layered hydrates separated by thin layers of sediment form the

third type of natural hydrate deposit. These layers represent porous versus non porous units. The final type of deposit is massive hydrates, which in marine environment are found at the seabed in areas with high methane flux such as at mud volcanoes. Massive hydrates can be 3-4 m thick with more than 95% hydrate (Malone 1985).

2.4 GEOPHYSICAL INDICATORS OF GAS HYDRATES

Gas hydrates easily dissociate at standard atmospheric pressures and temperatures. Difficulty in recovering samples has led scientists to rely heavily on geophysical indicators to identify, characterize and assess gas hydrate deposits (Riedel et al. 2010). Gas hydrates can act to cement grains and increase the rigidity of the sediment. Given the proper saturation and distribution, the presence of gas hydrates increases the sonic velocity through the affected sediments. On downhole resistivity logs gas-hydrate bearing sediments present as resistivity highs owing to hydrate's high resistance to electrical current. These geophysical indicators are useful but are limited to deposits through which well logs were acquired. A more universal indicator of gas hydrates in marine sediments is the observation of a bottom simulating reflector on seismic reflection profiles.

2.4.1 Bottom Simulating Reflectors

Seismic reflections that cross-cut stratigraphy and parallel the seafloor are known as bottom simulating reflectors (BSRs) and are observed on continental margins throughout the world (Kim et al. 2013; Mosher 2011; Riedel et al. 2010; Berndt et al. 2004; Lee et al. 1994).

A gas hydrate BSR forms when sub-seafloor temperatures become too high for hydrates to form and gas and water fill the pore spaces. If present in significant quantities, gas hydrates will act as a seal trapping the underlying free gas. A strongly negative acoustic impedance contrast results from elevated velocities in the hydrate bearing zone and reduced velocities in the underlying free gas bearing sediments. This negative acoustic impedance contrast results in a high amplitude, phase reversed reflection on seismic profiles (Haacke et al. 2007).

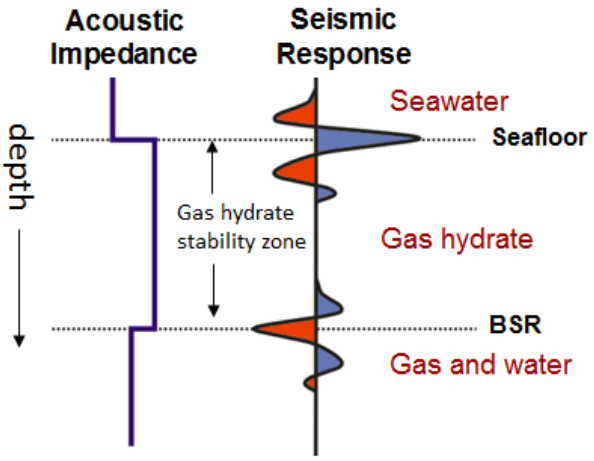

Figure 2.4 Phase reversed gas hydrate BSR.

The diagenetic transition of minerals, most notably the transition of opal-A to opal-CT in siliceous sediments, may also form a BSR. At increased burial depths, biogenic opal-A dissolves and opal-CT or porcellanite is subsequently precipitated (Williams and Crerar 1985). This diagenetic transition increases the density and velocity of the sediments, creating a positive acoustic impedance contrast that is imaged on seismic profiles as a high amplitude, positive phase BSR (Figure 2.5). In rare conditions, gas trapping below diagenetic boundaries has produced a phase-reversed diagenetic BSR (Cant 1986).

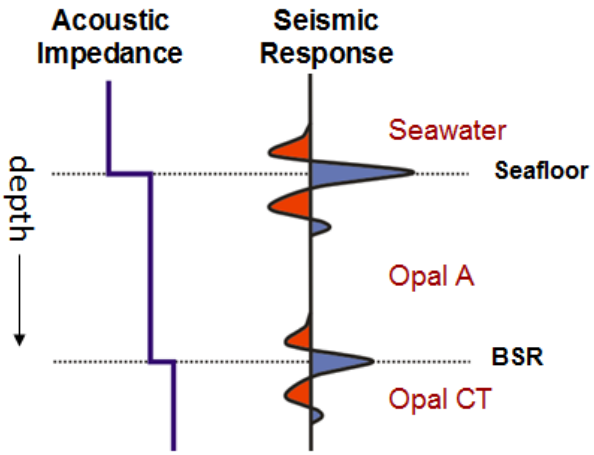

Figure 2.5 Positive phase diagenetic BSR.

2.5 SILICA DIAGENESIS

Unlike gas hydrates, which are primarily temperature and pressure dependant, silica diagenesis is complex and is controlled by composition, temperature, burial depth, time, pore water chemistry and sediment permeability (Hein et al. 1978; Williams and Crerar 1985). That said, sediments rich in biogenic silica are the key ingredient to the development of diagenetic fronts. Sediment composition can also influence the diagenetic reaction rate with the formation of opal-CT inhibited in the presence of clay minerals and accelerated in the presence of carbonates (Williams and Crerar 1985). The dissolution of carbonate provides the proper alkalinity to promote silica diagenesis and seawater provides the magnesium required for the diagenesis. In clay rich sediments the clay minerals compete with the seawater alkalinity (Kastner et al. 1977). The silica transformation typically occurs in sediments older than Miocene age (Riech and von Rad 1979) and at temperatures ranging from 35°C to 56°C although temperatures as low as 2°C have been reported (Meadows and Davies, 2010).

In a global assessment of biogenic silica diagenesis, Neagu (2011) noted a correlation between the presence of silica diagenetic fronts and the development of polygonal fault systems. Polygonal faults are defined as a network of layer-bound extensional faults with throws generally from 10-100 m and arranged in a polygonal structure like that observed in mudcracks (Cartwright and Dewhurst 1998). These faults develop in sediments that experienced subsidence and burial in a passive margin setting (Neagu 2011). Various hypothesis for the genesis of polygonal faults have been proposed with the latest by Cartwright (2011) who proposed that polygonal faults are formed through diagenetically induced shear failure.

2.6 HYDRATE AND DIAGENTIC SILICA CASE STUDIES AND OCCURANCES

The United States Geologic Survey (USGS) compiled a map of all documented gas hydrate deposits both inferred and recovered. Along the Atlantic margin of North America, the only recovered gas hydrates are offshore the southern US at Blake Ridge.

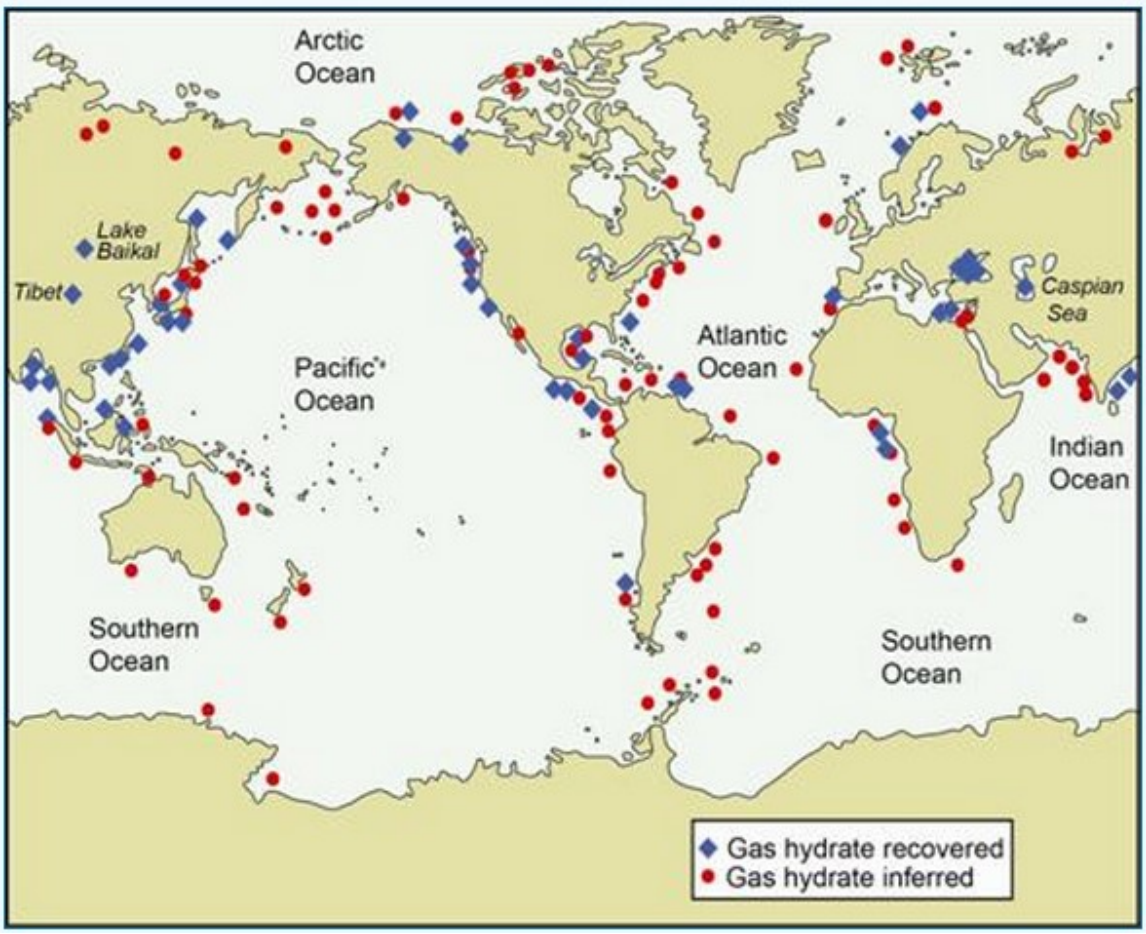

Figure 2.6 Global gas hydrate occurrences as compiled by the USGS in 2014 (USGS 2014)

2.6.1 Blake Ridge Gas Hydrates

Gas hydrate BSRs were first identified by Markl et al. (1970) in sediments of the Blake Ridge on the southeastern passive continental margin of North America (Figure 2.7). The Blake Ridge BSR covers 55,000 km^2 and is observed in water depths of ~800-4000 m and occurs ~190 and 450 m sub-seafloor in Miocene and younger drift sediments (Borowski 2004). The seismic character of the Blake Ridge BSR is variable, ranging from a high amplitude continuous reflection to one inferred from underlying high amplitude events (Figure 2.7) (Lee et al. 1994). Collett and Ladd (2000) showed that Blake Ridge BSR depths are coincident with theoretical base of hydrate stability depths.

Abundant gas hydrates deposits at Blake Ridge were confirmed from direct sampling in DSDP/ODP wells as well as from geochemical proxies (Borowski 2004) and downhole wireline logs. In particular, resistivity log values (Figure 2.7c) are distinctly elevated in the sediments overlying the BSR (Collett and Ladd 2000).

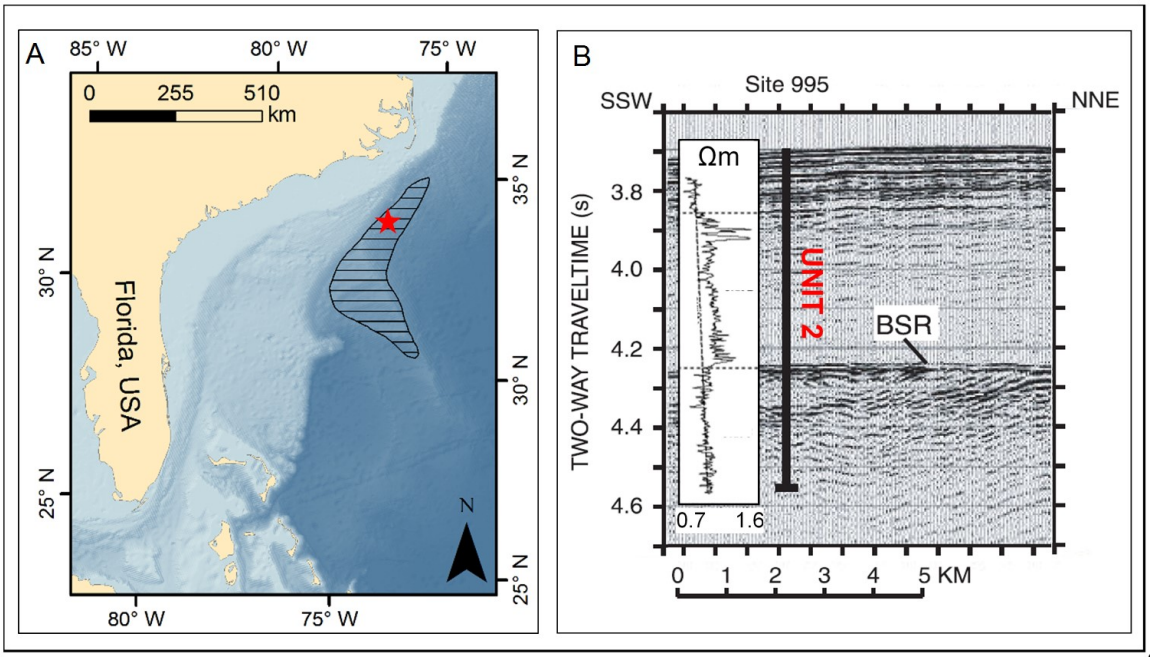

Figure 2.7 The location and areal extent of the Blake Ridge BSR within the western Atlantic (A). A red star identifies the location of a seismic profile through the gas hydrates (B) showing the character of the BSR. The resistivity log from Site 995 (B) shows elevated values through the gas hydrate bearing sediments (UNIT 2). Modified after Collett and Ladd (2000).

2.6.2 BSRs along Canadian East Coast Margin

Mosher (2011) identified seven BSR locations along the passive margin of eastern Canada in a margin wide study of available seismic profiles, (Figure 2.8). The BSRs occur between 250 and 445m sub-seafloor in water depths of 620-2850m. The BSRs are associated with Cenozoic contouritic drift deposits, which are typically primarily composed of muddy and silty sediments with fewer sandy horizons (Faugères and Stow 2008). Mosher (2011) attributed these BSRs to the presence of gas hydrates.

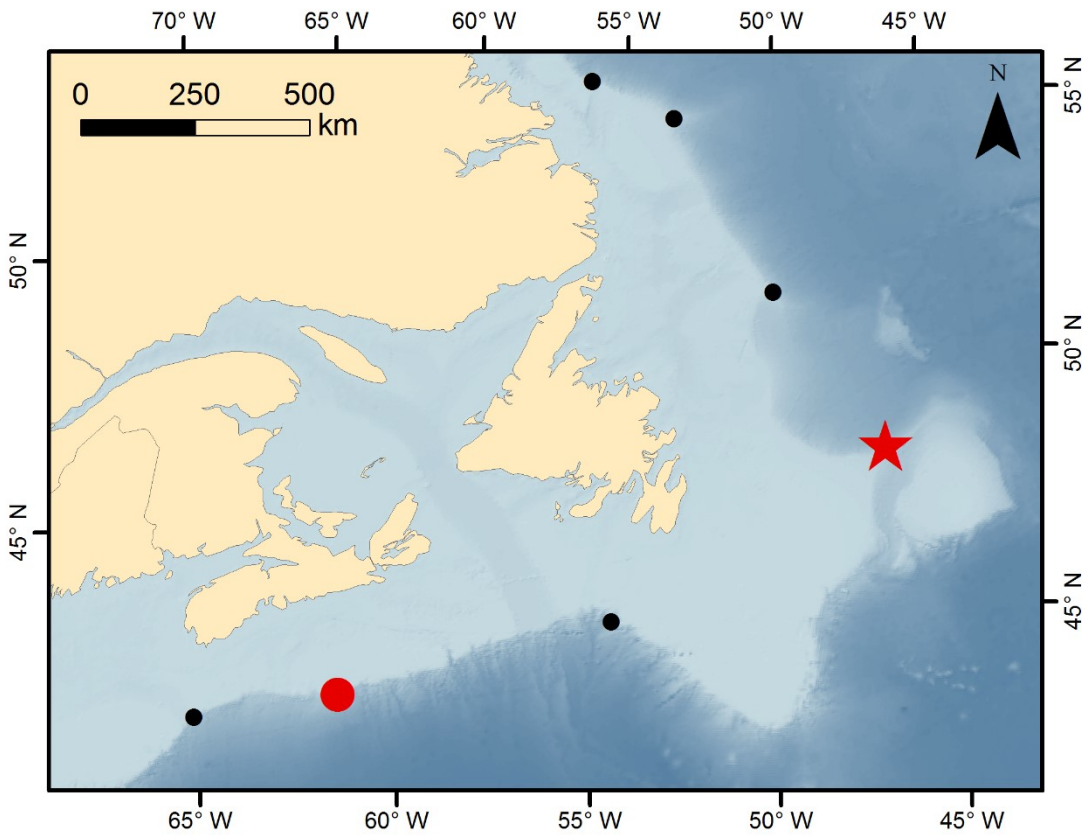

Figure 2.8 Locations of BSRs (circles) along the eastern margin of Canada as identified by Mosher (2011). The large red circle shows the location of the Mohican BSR while the red star shows the Sackville Spur BSR location. Modified after Mosher (2011).

Of the seven locations identified by Mosher (2011), the Mohican Channel BSR is the only location at which the BSR and associated gas hydrate deposits were studied in detail. The BSR transects Pliocene and younger drift deposits. Using velocity information from wide-angle seismic profilesLeBlanc et al. (2007) showed that the Mohican Channel BSR, which occurs in water depths of ~2000 m and is present ~290 m below the seabed, is associated with an overlying high velocity zone ~100-150 m thick and an underlying low velocity zone. In later work, Schlesinger et al. (2012) used wide angle and reflection seismic data to model a 90-110 m thick high velocity zone above the BSR (~220-330 m below the seafloor) with velocity increases on the order of 200-300 m/s. While below the BSR, a 30-150 m thick low velocity zone with velocities decreases on the order of 130 m/s was modelled (Schlesinger et al. 2012). The increased velocities are interpreted to reflect the presence of solid gas hydrates which act to cement the

sediment grains while the reduced velocities below are assumed to represent the presence of free gas within the sediment pore spaces at the base of the hydrate stability zone (LeBlanc et al. 2007; Mosher 2011; Schlesinger et al. 2012). Hydrates were successfully sampled in 2016 on the Scotian margin marking the first reported hydrate recovery on the Canadian Atlantic margin (Campbell and Mac Donald 2017).

2.6.3 Silica Diagenesis in the North Atlantic

The opal-A to opal-CT transition along the eastern North Atlantic was investigated in cores from the Deep Sea Drilling Project (DSDP) collected along the New Jersey margin (Thein and von Rad 1987) and in the Labrador Sea (Bohrmann and Stien 1989).

On the New Jersey margin, Site 605 from Leg 93 and Sites 612 and 613 from Leg 95 were drilled in 2194 m, 1404 m and 2323 m of water respectively. The silica diagenetic front was encountered at sub-seafloor depths of 350 m, 325 m, and 443 m respectively. These sub-seafloor depths correspond to Eocene sediments aged 49 to 52 Ma (Thein and von Rad 1987). The silica transition along the New Jersey margin, as determined from DSDP cores, occurs as a relatively sharp boundary marked by a change from unsilicified or weakly silicified radiolarian, diatomaceous, clay bearing nannofossil chalks without opal-CT to underlying porcellanitic nannofossil chalks and limestones with opal-CT (Thein and von Rad 1987). The appearance of opal-CT corresponds not only to a prominent lithological boundary where major compositional characteristics change but also to a change in the physical properties of the sediments. The appearance of opal-CT is typically associated with increases in downhole sonic velocities as well as increases in grain and bulk densities and reductions in the porosity and water content (Thein and von Rad 1987; Meadows and Davies 2010). These changes in physical properties result in the Eocene aged A^c seismic reflector identified by Tucholke and Mountain (1979) that occurs throughout the western North Atlantic.

When sampling Eocene to Holocene aged sediments in the southern Labrador Sea for Ocean Drilling Program Site 647 (Leg105), siliceous sediments were first noted in abundance in Miocene through Oligocene sediments (Bohrmann and Stien 1989). The opal-A to opal-CT diagenetic front is found in earliest Oligocene to late Eocene strata while opal-CT was transformed into authigenic iron-rich smectites in early to middle Eocene aged sediments (Bohrmann and Stien 1989). Riech and Von Rad (1979) noted

that in the Atlantic, porcellanites (opal-CT) are rare in Pliocene and Miocene aged sediments with increasing occurrence in pre-Miocene sediments with a marked maximum at ~50 Ma in the early to early middle Eocene. Globally, Pliocene and younger porcellanites are rarely observed and where they occur they are associated with an abundance of diatoms, reactive volcanogenic material, elevated heat flow, or hydrothermal solutions (Riech and von Rad 1979).

Biogenic silica production and/or preservation in the Atlantic was strongest in the early to middle Eocene (Riech and von Rad 1979). Similar Eocene cherts were sampled in drillholes from the eastern North Atlantic, Caribbean and equatorial Pacific (Thein and von Rad 1987). This abundance of silica is attributed to multiple factors that remain under debate (Miller et al. 2009). The early and middle Eocene was a period of unimpeded equatorial circulation between the Tethys, Atlantic, Caribbean and Pacific oceans. This circulation caused coastal upwelling which provided additional sources of silica (Riech and von Rad 1979). The higher sedimentation rates favoured the preservation of skeletal opal at the seafloor. A rapid depression of the CCD allowed carbonate-rich sediments to accumulate in deep waters (Penman et al. 2016). Increased volcanic activity in the late Paleocene to early Eocene increased nutrient-phosphorous and silica supply to the surface waters. In addition, the tropical to sub-tropical climate of the circum-Atlantic, especially during the Paleocene and Eocene (Frakes 1979), caused extensive chemical weathering at lower latitudes that mobilized silica and may have triggered explosive silicoplankton productivity (Thein and von Rad 1986).

On the other hand, Miller et al. (2009) attributed the development of a large Antarctic ice sheet at the Eocene-Oligocene transition to increased ocean circulation that in turn resulted in increased latitudinal and vertical thermal gradients. These increased thermal gradients led to increased wind driven upwelling and eddy turbulence, which triggered increased nutrient recycling that in turn resulted in a rapid diversification of diatoms in the Oligocene (Falkowski et al. 2004). Conditions with high turbulent mixing are favoured by diatoms over other eukaryotic phytoplankton (Katz et al. 2005). The lowered CCD allowed for preservation of the diatom tests which allowed significant Eocene-Oligocene biogenic silica deposits to develop in the Atlantic.

2.7 SIGNIFICANCE

Distinguishing between gas hydrates and silica diagenetic fronts is primarily important because gas hydrates represent a significant hydrocarbon resource, a

potential geohazard and may play a key role in past and future climate change. While silica diagenesis changes the properties of the sediment and in some cases may represent a drilling constraint; drilling through hard cherts can require specialized bits (Nierenberg and Peterson, 1971).

2.7.1 Potential Geohazard

A geohazard is a geological state or condition that can lead to widespread damage or human fatalities. Where gas hydrates act to cement and stiffen the host sediments, hydrate dissociation acts to weaken the sediment. In the marine environment, this weakening can result in sediment instability and potentially lead to sediment failure and sub-marine landslides. Although it is difficult to directly link hydrate instability and slope failure, various authors have proposed hydrate dissociation as a potential cause for massive seabed failures (Vanneste et al. 2014; Owen et al. 2007; Lee 2009). Sediment instability and failure, even on a local scale, can have catastrophic consequences for seabed infrastructure. Hovland and Gudmestad (2001) noted that warm pipelines at or just below the seabed as well as heavy structures on the seabed have the potential to modify the thermodynamic regime in the shallow sediments leading to hydrate dissociation and in turn sediment and infrastructure destabilization.

One significant risk associated with natural gas hydrates occurs when drilling offshore through hydrate saturated sediments. Given that the well's casing and blow out preventers are not set until such a depth that consolidated sediments are encountered, the well is particularly vulnerable through the hydrate bearing zone. Drilling induced hydrate dissociation resulting from sediment depressurization as well as formation heating by drilling and friction present significant potential hazards (McConnell et al. 2012). In a worst case scenario, drilling induced hydrate dissociation can lead to the loss of well control due to the introduction of shallow gas as well as failure of the shallow portion of the borehole through the loss of sediment competence. There is also potential for the loss of well control due to over-pressurized free gas below the hydrate bearing zone (Hovland and Gudmestad 2001). In 2001 a Joint Industry Project in the Gulf of Mexico was established to assess hazards of drilling through hydrate bearing sediments. In Leg 1, clay dominated sediments with low hydrate saturations (saturations were estimated to vary between 1-20%) were drilled (Ruppel et al. 2008). Experience from that drilling revealed that cool drilling fluids circulated at a constant and relatively low rate allowed heat to dissipate to the ocean reducing viscous heating of the drill pipe

enough to maintain formation temperatures below that of hydrate dissociation (Birchwood et al. 2008).

In the second leg of the Joint Industry Project, hydrate bearing sands with high hydrate concentrations were targeted (Frye et al. 2009). It was found that the higher hydrate concentrations (20-40%) did not pose a risk to drilling and instead acted to cement the well allowing for better control in the shallow section (Collet et al. 2012). In these more highly saturated sediments, the hazard is the pressurized free gas underlying the hydrates. On seismic profiles, the typical bright spots and elevated amplitudes associated with gas can be masked by the overlying hydrate deposits (McConnell et al. 2012). To mitigate drilling risks, sediments with high hydrate saturations, which typically do not have significant regional extent, are identified in the predrilling hazard assessment phase and subsequently avoided during drilling.

2.7.2 Role of hydrates in climate change

The stability of natural gas hydrates is sensitive to temperature and to a lesser degree pressure. Increases in oceanic temperature and changes in sea-level modify the thermodynamic conditions in the shallow sediments and may cause hydrates to dissociate. Dickens et al. (1995) and Dickens (2011) argued that this process was responsible for the Paleocene-Eocene thermal maximum. They propose that increased bottom water temperatures destabilized the sediment hosted hydrates causing a release of methane into the ocean. This methane was rapidly oxidized to carbon dioxide which provided a positive feedback that further increased global temperatures (Dickens 2011). It is currently unclear what would cause the initial rise in seabed temperatures but one possible process may be a change in ocean circulation. Phrampus and Hornbach (2012) observed shallow BSRs on seismic profiles on the southern US Atlantic margin that, along with thermal models from the continental shelf, suggest hydrate dissociation is actively occurring at the seabed. They proposed that the shoaling BSR is induced by increased seabed temperatures resulting from changes in the flow of the Gulf Stream. They associated these changes with increased temperatures along the western North Atlantic margin over the last 5000 years. Similarly, Westbrook et al. (2009) proposed that hydrate dissociation related to warming of the West Spitsbergen current by 1°C over the last 30 years is responsible for the more than 250 active plumes of methane emanating from the seabed on the West Spitsbergen continental margin.

2.7.3 Resource Potential

Gas hydrates represent a significant storehouse of methane both in permafrost regions and on continental shelves. Hydrates act to concentrate hydrocarbons with one cubic metre of hydrates containing as much as 180 standard cubic metres of methane gas (Sloan 1998). Global values of methane gas volumes housed in gas hydrates range from 5×10^{15} m^3 (Buffett and Archer 2004) through 4×10^{16} m^3 (Wood and Jung 2008) to 1.2×10^{17} m^3 (Klauda and Sandler 2005). In terms of global resource potential, Boswell and Collett (2011) estimated 2.4×10^{12} m^3 of total recoverable gas in hydrate deposits.

Research wells to test the viability of gas hydrate production were drilled in the Nankai Trough offshore Japan and in the permafrost hydrate deposits of the Mackenzie Delta of the Northwest Territories. Gas hydrate production tests, first undertaken in 2002 at the Mallik well, used a hot water circulation method to increase the sediment temperature and dissociate the gas. Water was heated to 80 °C then circulated through the sediments surrounding the well. A total of 470 m^3 of methane gas was produced over a five day period (Moridis 2005). This hot water method was not ideal as significant energy was required to heat the water to the proper temperature. A second less energy intensive depressurization method was tested in 2007. This method pumped water out of the well reducing the pressures at depth and dissociating the gas hydrates through pressure-drawdown. After overcoming issues with sand obstructing flow through the pumps, 13 000 m^3 of methane was produced in 2008 over 5.5 days (Uddin et al. 2012).

In 2013, Japan successfully extracted methane gas from marine gas hydrate layers in the Eastern Nankai Trough through depressurization of the hydrate reservoir (JOGMeC 2013). In this 2013 test, methane gas flowed unimpeded for six days with an average production of 20 000 m^3 a day. Once pressures dropped to 4.5 MPa the sand obstructed flow through the pumps and the test was terminated (Cyranoski 2013). With the onset of shale gas in recent years, Canada and the United States have significantly reduced their efforts in extracting methane from gas hydrates. In contrast, research continues in Asian countries where the energy requirements from the growing middle class are creating increased demands for domestic fuel sources.

Gas hydrate reservoirs have been proposed as a potential method for sequestering and storing carbon dioxide. Given the current global concerns on the rising amount of anthropogenic CO_2 and CH_3 in the atmosphere, various authors have proposed that CO_2 be stored as gas hydrates (Ersland et al. 2009; Castellani et al. 2013; Jadhawar et al. 2006). Husebø et al. (2009) suggest that methane produced from

hydrate reservoirs be replaced by CO_2. In theory, this is an appealing proposition given that CO_2 and methane both produce sI hydrates, thus minimizing the amount of sediment volume change. The lack of volume change maintains the competence of the formation hence reducing the risk of sediment failures. Also, unlike conventional natural gas production, no water is produced when removing methane and replacing it with carbon dioxide (Husebø et al. 2009).

CHAPTER THREE: BACKGROUND GEOLOGY

3.1 STUDY LOCATION

The Sackville Spur is an elongated contourite drift that extends off the northeastern tip of the Grand Banks offshore Newfoundland Canada (Figure 3.1). North of the Spur, water depths increase relatively rapidly into Orphan Basin, while to the south the regional gradient is significantly lower as water depth increase into the relatively shallow Flemish Pass (Figure 3.1). The Spur is deposited and shaped by the cold Labrador Current that flows south along the Labrador coast and then splits in Orphan Basin (Kennard et al. 1990). The current's primary branch continues east around Flemish Cap while the secondary branch flows over the Spur and south through Flemish Pass (Figure 3.1). Throughout the Cenozoic, the Labrador Current transported sediment, winnowed the fines and created the sand and silt dominated Sackville Spur sediment drift (Kennard et al. 1990). Campbell (2014) noted that drift deposits generally correlate to significant changes in a margin's trend that in some cases are formed by ancient fault and fracture zones. The Sackville Spur marks a significant change in the margin or shelf break trend, from an E-W orientation in Orphan Basin north of the Spur to N-S in Flemish Pass south of the Spur (Figure 3.1). This change in margin trend owes itself to the underlying crustal Cumberland Belt Transfer Fault Zone formed during Mesozoic rifting (Grant and McAlpine 1990).

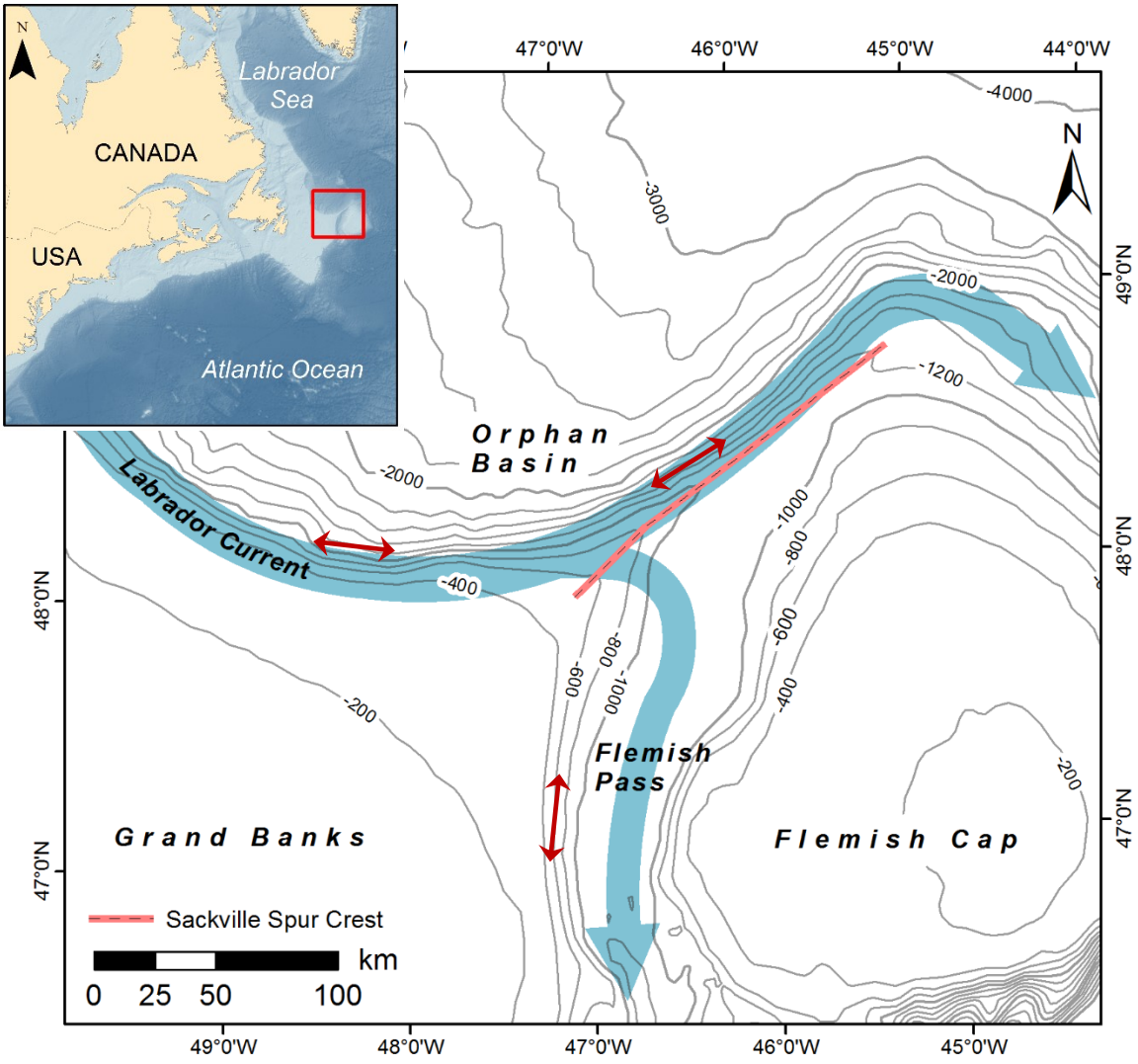

Figure 3.1 A map of the study location offshore Newfoundland Canada. Bathymetry is indicated by 200-m contours. The generalized flow pattern for the modern Labrador Current is shown in blue while the red arrows represent the margin trend north and south of the Spur.

3.2 BACKGROUND GEOLOGY

The basement on the Newfoundland margin consists of rocks accreted onto North America during the closing of the Paleozoic Iapetus and Rheic oceans (Grant and McAlpine 1990). Representing the most northern reaches of the Appalachian Orogen, these Precambrian to Paleozoic rocks are ordered into four zones along the Newfoundland margin; the Dunnage, Gander, Avalon, and Meguma zones. The Avalon zone, which underlies the study area as well as much of the Grand Banks, contains a

thick unit of Upper Precambrian sedimentary and volcanic sequences overlain by Cambrian shales (Williams and Hatcher 1982, 1983).

3.2.1 Rift History

The modern continental margin offshore Eastern Canada evolved through Mesozoic extension associated with the opening of the Atlantic Ocean. This extension was concentrated into three rift phases. The first rift phase, occurring from Late Triassic to lowest Jurassic, is coincident with the opening of the Central Atlantic (Tucholke and Witmarsh 2012) and resulted in the formation of large, deep rift basins on the Grand Banks. Following this initial rift phase, the Newfoundland margin experienced a period of subsidence from Lower through Middle Jurassic. Rifting was reactivated in the Upper Jurassic and continued through the Lower Cretaceous. This second rift phase was followed by separation of the Grand Banks from Iberia towards the end of the Lower Cretaceous (Tankard and Balkwill 1989). The Cumberland Belt Transform Zone formed during this rift phase as the Flemish Cap rotated south (Gacal-İşler 2009). The final rift phase in the Aptian-Albian was followed in the beginning of the Upper Cretaceous by separation of Greenland from Canada and the opening of the Labrador Sea (Grant and McAlpine 1990). The cessation of rifting and the onset of normal seafloor spreading in the Upper Cretaceous marked a transition to passive margin subsidence and sedimentation in rift basins.

3.2.2 Basin Geology

The Mesozoic rift basins along the Newfoundland margin generally formed in half grabens bounded by normal faults resulting from reactivation of existing structural fabrics in the Avalon and Meguma terranes (Welsink et al. 1989). The Flemish Pass basin, which underlies the Sackville Spur, shares a common evolution and comparable stratigraphy to the Jeanne d'Arc Basin (Foster and Robinson, 1993; Enachescu et al. 2010) as deposition was continuous between the two basins until the Upper Cretaceous when uplift formed a ridge separating the basins (Enachescu et al. 2010) (Figure 3.2). The Jeanne d'Arc Basin is the largest and most extensively studied basin offshore Newfoundland and the only North American East Coast basin containing giant (≥ 500 million barrels) hydrocarbon producing fields.

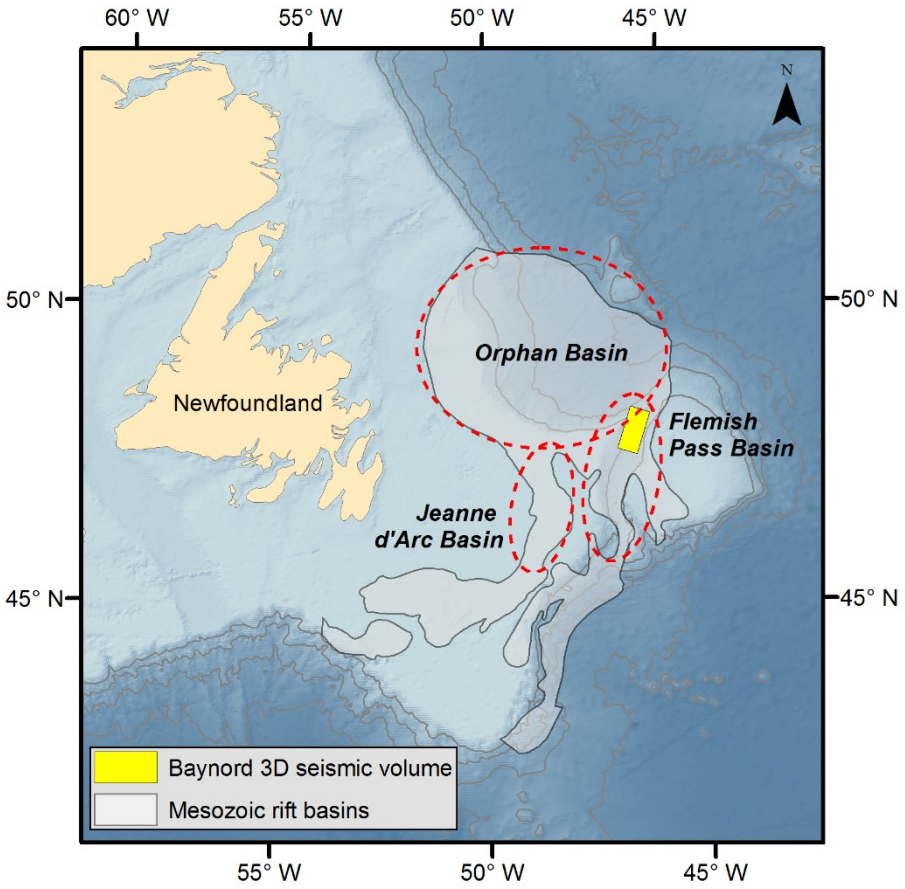

Figure 3.2 A map of Mesozoic rift basins offshore Newfoundland**.**

3.2.2.1 Exploration History

The discovery of hydrocarbons was first made on the Newfoundland margin in 1979 with the discovery of the Hibernia field in the Jeanne d'Arc Basin. It was not until 1997 that the first barrel of oil was produced. Two additional fields in the Jeanne d'Arc Basin have since been developed on the margin: White Rose and Terra Nova while the Hebron field is undergoing development. Given the genetic relationship between the Jeanne d'Arc and Flemish Pass Basins, the Flemish Pass Basin was promoted as having a high potential for hydrocarbon production although, given the abundance of icebergs in the Flemish Pass and water depth reaching 1000 m, exploration proved too expensive (DeSilva 1997). Oil shows in the Gabriel and Bacceleau wells further suggested the presence of an active hydrocarbon system. In 2009 this system was proven with the discovery of oil at the Mizzen O-16 exploration well. The F-09 and

Harpoon O-85 wells have were subsequently drilled with an aim to further delineate the prospect and to better understand the shallow sediments in the northern Flemish Pass.

Gas hydrate deposits can occur in the shallow sediments overlying conventional hydrocarbon fields. In the Beaufort Sea and Mackenzie Delta, Majorowicz and Osadetz (2001) note gas hydrate deposits overlying conventional hydrocarbon reservoirs. On the Scotian margin, Campbell and MacDonald (2017) recovered hydrates in the Shelburne and Sable sub-basins. These basins are areas of hydrocarbon exploration. Mosher (2011) noted that of the seven BSR's identified along the Canadian Atlantic margin, six occur in areas of conventional hydrocarbon exploration.

3.2.2.2 Flemish Pass Basin

In a regional seismic-stratigraphic study, Foster and Robinson (1993) identified four megasequences in the Flemish Pass basin, MS1, MS2, MS3 and PR. The oldest megasequence, MS1, is not well defined in the basin owing to a lack of well control and inconsistent seismic penetration. Through comparison with other basins along the North American Atlantic margin, the base of MS1 is interpreted as Upper Triassic (Jansa et al. 1980). MS1 is thought to contain both synrift and postrift sediments (Foster and Robinson 1993) as observed in other basins on the North American Atlantic margin (Manspeizer 1988). The MS1 megasequence, has Kimmeridgian marine mudstones that include important source rocks deposited in a shallow sea or lagoon (Foster and Robinson 1993). These source rocks are equivalent to the Egret member source rocks in the Jeanne d'Arc Basin (von der Dick 1989).

The top of MS1 is marked by a regional onlap surface that represents a regional phase of deepening associated with northwest-southeast extension resulting from rifting between Newfoundland and Iberia (Enachescu et al. 2010). In a second period of basin filling, a series of wedges of clastic shelf sediments were deposited (Foster and Robinson 1993). These clastic wedges are the principal focus of exploration in the Jeanne d'Arc Basin (Tucholke et al. 1989). The top of MS2 is marked by an unconformable surface interpreted as Aptian age given the recognition of a regional Aptian unconformity over much of the Grand Banks (Jansa and Wade 1975). Marking the separation of Newfoundland from Iberia, this break-up unconformity is the result of uplift associated with extensional unloading, as well as thermal and isostatic uplift along the margin (Tucholke et al. 1989).

Rifting related to the separation of Labrador and Greenland led to further subsidence and the deposition of MS3. Based on seismic facies analysis, Foster and Robinson (1993) interpreted MS3 to consist of muddy sediments containing interbedded turbidite sands, presumably deposited in deep water. A major unconformity that marks the top of MS3 is shown to be older than Santanion with a likely Albian age (Early Cretaceous) based on analogous megasequence boundary in the Jeanne d'Arc Basin (Foster and Robinson 1993, Tucholke et al. 1989). MS3 is overlain by post-rift sediments (PR), the base of which is marked by the Labrador-Greenland break-up unconformity that in places has significantly eroded the underlying megasequences (Enachescu et al. 2010).

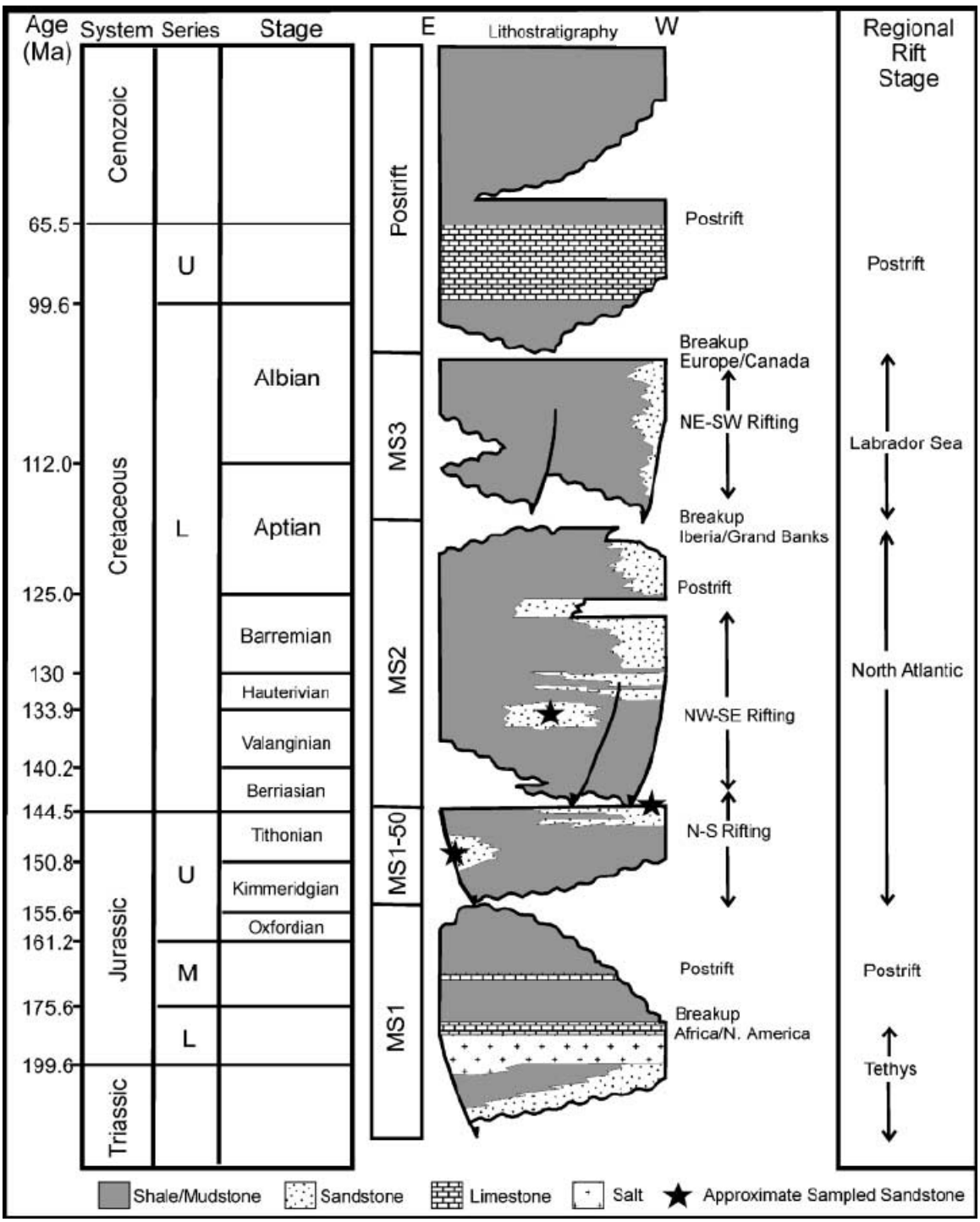

Figure 3.3 General regional stratigraphy of the Flemish Pass Basin. Modified by Lowe et al. (2011) after Foster and Robinson (1993).

3.2.3 Post Rift Sediments

Deptuck (2003) divided the post rift stratigraphic succession of the Grand Banks and Flemish Pass into four depositional stages. In stages 1 and 2, which extend from the Turonian into the middle Eocene, sediments were deposited in confined rift basins separated by basement highs. During stages 3 and 4, which extend from late Middle Eocene to the present, the margin continued to subside and the depositional environment shifted to an unconfined passive-margin shelf and slope system (Deptuck 2003).

As the Atlantic Ocean grew with seafloor spreading, the effects of deep currents increased (Arthur et al. 1989). In the Miocene, the currents began to sculpt and plaster sediments on the western continental rise forming sediment drift deposits (Myers and Piper 1988; Arthur et al. 1989; Kennard et al. 1990; Muller-Michaelis et al. 2013; Campbell 2014; Campbell and Mosher 2016). In the Early Miocene, the Greenland-Scotland Ridge was breached enough to allow cold Norwegian overflow water into the north Atlantic (Stoker et al. 2005). This change was accompanied by more extensive drift development (Arthur et al. 1989; Campbell 2014). The onset of the cold, low salinity Labrador Current, which controlled Sackville Spur sediment drift growth, can be traced back to the late Miocene (Arthur et al. 1989).

A massive interval of early to mid Miocene intraclastic chalks are capped by the Merlin reflection in the Blake Bahama Basin off the eastern U.S. continental margin. Merlin represents an erosional unconformity that can be traced into deposits of migrating sediment waves (Mountain and Tucholke 1985; Tucholke and Mountain 1986). The Merlin unconformity was formed by a pulse of strengthened abyssal currents in late middle Miocene (Tucholke and Mountain 1986). Mountain and Tucholke (1985) note that north of 45° virtually every borehole drilled on the margin of the western North Atlantic Basin records a well-developed, late Miocene hiatus that is presumably the result of bottom current erosion. At the Sackville Spur, the Labrador Current was fully established after the middle Pliocene as determined by a dramatic change in benthic foraminiferal assemblages along the Atlantic margin (Kennard et al. 1990). An erosional unconformity dated near the Pliocene-Miocene boundary, was noted by Kennard et al. (1990) and mapped in detail by Deptuck (2003) (T80 marker) below the Sackville Spur while within the Flemish Pass, Piper and Pereira (1992) and Piper and Nomark (1989) noted a distinct late Miocene unconformity that they correlated with sea-level lowering.

Along the western North Atlantic margin, post-Merlin seismic sequences are generally well layed with little reflection truncation (Mountain and Tucholke 1985; Arthur et al. 1989). The lack of truncation is indicative of coherent deposition presumably resulting from moderate currents and the development of a stable North Atlantic circulation pattern (Arthur et al. 1989). Siliceous fossils are distinctly absent in the sediments overlying the Merlin reflector (Mountain and Tucholke 1985). In the Late Pliocene, currents intensified and formed a margin wide Blue unconformity along the US Atlantic margin (Mountain and Tucholke 1985; Arthur et al. 1989).

Current controlled deposition continued into the late Pliocene and through the Quaternary. Through the Pleistocene, slumping, nonchannelized debris flows and turbidity currents became increasingly prominent processes delivering sediments to the continental rise (Mountain and Tucholke 1985; Myers and Piper 1987; Deptuck 2003; Brackenridge et al. 2011). On the Flemish Pass seafloor, sediments were deposited by turbidites during periods of shelf-crossing ice sheets, but most sediments were derived from icebergs and proglacial sediment plumes transported in the Labrador Current (Piper and Pereira 1992; Huppertz and Piper 2009). Throughout the Canadian continental margin, Piper and Normark (1989) note a marked change in sedimentation style in the Middle Pleistocene resulting from shelf crossing ice sheets that delivered coarse sediments directly to the continental slope. In a study of Flemish Pass turbidites, Huppertz (2007) determined that Quaternary turbidites were emplaced during stades while contourites were deposited during interstadial periods. In a study of recent failures in northern Flemish Pass, Cameron et al. (2014) noted a series of failures that occurred during last glacial maximum and retreat.

During glacial periods, ice sheets terminated along the Grand Banks margin during OIS 6 (210 to 160 ka) and OIS 4 (75 to 54 ka) which correspond to the highest observed sedimentation rates on the slope (Shaw et al. 2006; Huppertz 2007). The Newfoundland Ice Sheet did not reach the shelf break on the outer most bank during the last glacial maximum (LGM) (King and Sonnichsen 1999; Huppertz 2007). Cameron et al. (2014) suggest that following ice retreat, glaciostatic effects resulted in increased earthquake frequency providing a trigger for the observed sediment failures. E. King (personal communication, 2017) suggests an absence of a bulge effect during the LGM based on a lack of observed isostatic warping on the middle to outer shelf of the Grand Banks. Currently, the role that glacio-isostatic depression or uplift played in sedimentation on

the margin is not clear (King and Sonnichsen 1999, E. King personal communication, 2017)

CHAPTER FOUR: METHODS

The primary method of investigation used in this study was the interpretation of reflection events and seismic attributes from the Baynord 3D seismic volume (Figure 4.1). Interpretation was aided by the integration of key near-by exploration wells. This study also investigated the calculated depth to the base of gas hydrate stability of different gas compositions for comparison to the reflection events mapped on the 3D seismic volume. Quantifiable estimates of gas hydrate and free gas concentrations were made at the F-09 exploration well using measured velocities and electrical resistivity. The following provides detailed theoretical and practical information on these methods.

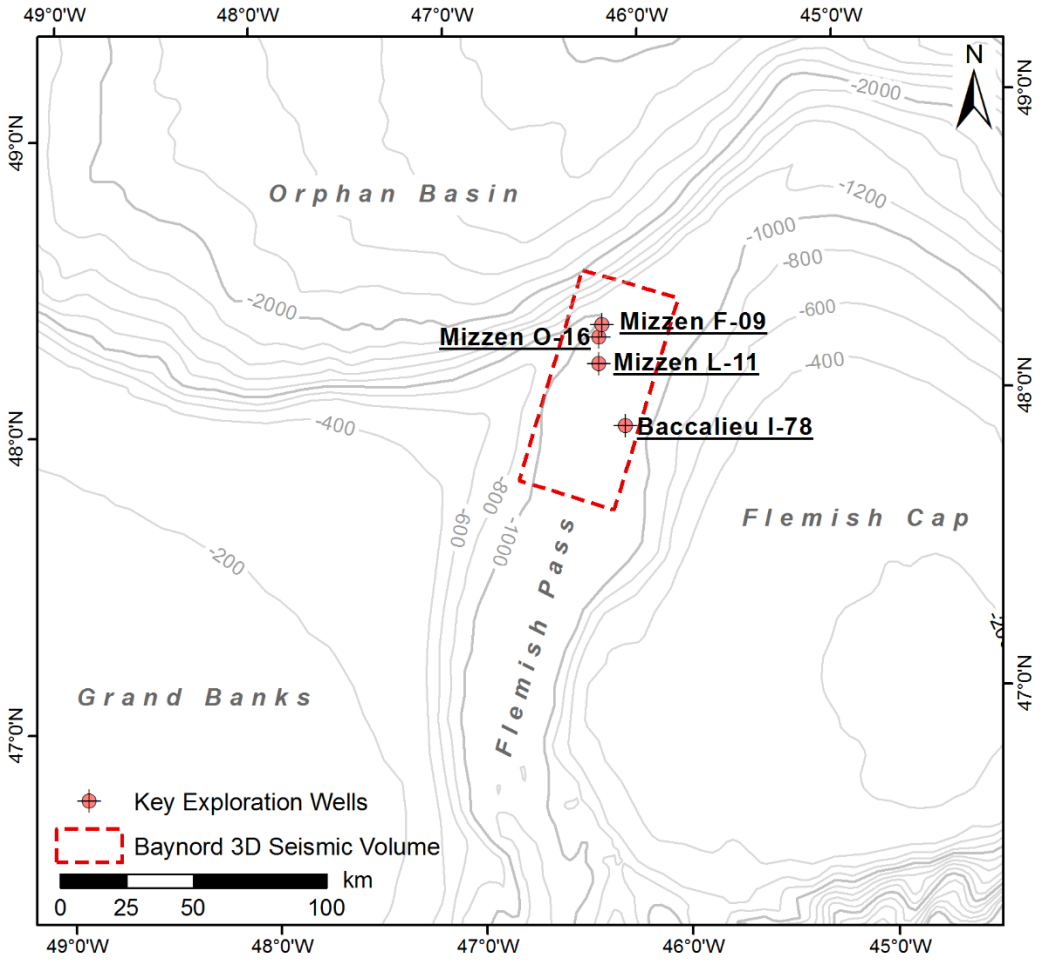

Figure 4.1 A map showing the location of the Baynord 3D seismic volume.

4.1 SEISMIC REFLECTION

Seismic reflection data result from the transmission and reflection of acoustic energy to image the subsurface structure. For this study, the Baynord 3D multichannel seismic volume was interpreted. The Baynord 3D seismic dataset covers ~3115 km^2 on the Sackville Spur and Northern Flemish Pass (Figure 4.1). This digital, time migrated 3D seismic dataset was donated in SEG-Y format to Natural Resources Canada by Statoil. The data are in American polarity (positive phase wavelet represented by a peak positive amplitude) with a 4ms sample rate. These data extend from the sea surface to the Miocene, approximately 2500 m below sea level. The data were clipped to the Miocene by Statoil to remove the reflections imaging their exploration targets.

4.1.1 Seismic Amplitudes

Reflection seismology is a common geophysical method used for mapping the subsurface structure and stratigraphy of an area. In basic seismic reflection theory an acoustic source creates a wave front that spreads spherically from the source by means of particle motion. As the wave front propagates into the subsurface it encounters various geologic interfaces, across which the acoustic impedance changes. At these interfaces a fraction of the acoustic energy is reflected while another portion is refracted and transmitted through the underlying medium. The transmitted portion of the acoustic energy continues into the substrate where it encounters additional interfaces and the energy is further partitioned. The various reflected wave fronts return to the surface where sensitive receivers detect the particle motion and convert it to a voltage. The amplitude of this voltage is recorded at discrete time intervals forming the reflected signal. The amplitude of the transmitted and reflected energy are defined as:

$$A_r = \rho_2 V_2 - \rho_1 V_1 \qquad \text{Equation 4.1}$$

$$A_t = \rho_2 V_2 + \rho_1 V_1 \qquad \text{Equation 4.2}$$

where A_r is the amplitude of the reflected energy, A_t is the amplitude of the transmitted energy, and ρ_1, ρ_2 and $V_1 V_2$ are the densities and velocities of the material overlying and underlying a subsurface interface, respectively. Zoeppritz (1919) developed a set of equations that describe the partitioning of energy at an interface in terms of the product of velocity and density termed acoustic impedance. Assuming normal or close to normal incidence, which assumes no refraction of energy at an interface, the Zoeppritz equations can be simplified to describe the amount of reflected energy R as:

$$R = A_r/A_i$$ Equation 4.3

where R is the reflection coefficient, A_r is the amplitude of the reflected energy and A_i is the amplitude of the incipient energy. These equations show the amount of reflected energy is reduced when the acoustic impedance contrasts are low but the fraction of reflected energy increases when impedance contrasts between the over and underlying units are high. Most importantly, units with anomalously high densities and or velocities are represented on seismic profiles by anomalously high amplitudes.

When seismic data are processed, the amplitudes are modified. The source signal and in turn the reflected energy weakens with depth. Gains are applied to the seismic data to increase the amplitudes at depth. Once processed, the seismic amplitudes no longer have true absolute values but the relative values remain useful for characterizing the subsurface reflectors. For this study the processing steps applied to the 3D seismic data are unknown and hence the amplitudes are useful for relative or qualitative comparison but cannot be used to extract geophysical properties of the sediment such as density and velocity.

4.1.2 Seismic Phase and Frequency

An important consideration in reflection seismology is the characteristics of the seismic source, or source signature. The seismic source signal is a wavelet, a signal with a finite duration and like a sine wave, is characterized by its duration, frequency, peak amplitude, and phase. Unlike a simple oscillatory function, a seismic wavelet is the product of a series of sine waves each with distinct frequency, peak amplitude (power) and phase. As such, the seismic wavelet has a finite frequency spectrum or bandwidth and is most often of mixed phase, where phase describes the symmetry of the wavelet's peak amplitude around time zero. During seismic acquisition, the mixed phase source wavelet is convolved with the Earth's reflection coefficient series to generate the final recorded seismic trace. Where energy partitioning at the interfaces modifies the amplitude of the reflected energy, the convolution modifies the phase and frequency of the original source signal.

Modification of the source wavelet's frequency spectrum occurs as a result of attenuation, geometric spreading, signal absorption and signal scattering (Yilmaz and Doherty 1987). Scattering is only applicable when wavelengths are of similar size to the heterogeneities in the sediment (Priest et al. 2006). Absorption is a function of the characteristics of the medium as well as the frequency of the source wavelet. As elastic

waves travel through a medium, the wave's mechanical energy is progressively converted to heat. Signals with more oscillations, or higher frequencies, will lose energy more readily than lower frequencies, which have fewer oscillations. As the higher frequencies are attenuated, the signal broadens, which decreases the frequency spectra of the data. The transmitting medium also influences attenuation; the more elastic the medium the less the seismic signal is attenuated. Gas, which is compressible, results in more attenuation (absorption) than a cemented sediment. The effect of gas hydrates on attenuation are debatable. Pecher and Holbrook (2003) and Sain et al.(2009) argue that gas hydrates act to cement sediments and hence decrease attenuation, while work by Priest et al. (2006) and Best et al. (2013) shows that attenuation increases non-linearly with increasing hydrate concentration. Chand and Minshull (2004) suggest these observed increases in attenuation result from energy loss associated with fluid flows in the pores of the hydrate matrix.

During data acquisition the seismic source signature is recorded or extracted from the data then used to deconvolve the reflection data and create zero phase data. A zero phase wavelet has peak amplitude symmetry around time zero. Seismic data are typically processed to zero phase although the process is not often truly successful (Henry 1997). Processing to zero phase aids in the interpretative process as the peak amplitudes, which are where much of the seismic information is contained, correlate to the time position of the subsurface interface.

The 3D seismic data used for this study were processed to zero phase although a slight trace asymmetry persists above and below the peak that defines the seafloor (Figure 4.2).

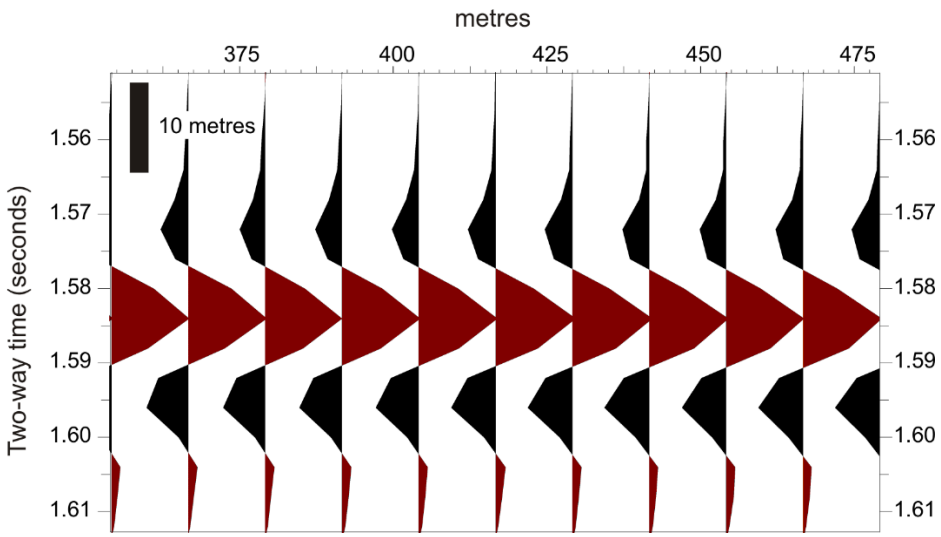

Figure 4.2 Seismic wiggle display of a portion of the seafloor reflection event. The red peaks represent the high amplitude seafloor while the black are the troughs above and below the seafloor peak. Note the upper trough is broader with lower amplitudes than the lower trough. Hence the data are not truly zero phase.

4.1.3 Seismic Interpretation

Seismic interpretation is a broad term that encompasses a series of quantitative and qualitative methods used to determine the geologic significance of seismic data (Brown 2011). Commonly, the end goal of seismic interpretation is to determine the geologic evolution of the study area through identification of changes in depositional environment and post depositional modifications to the sediment. For this study seismic stratigraphic analysis was completed on the 3D seismic volume. Initially the 3D seismic volume was divided into seismic facies; units with similar reflection characteristics such as configuration, continuity and amplitude. Reflection events marking the boundaries to these facies were mapped and described. Figure 3.2 presents the main reflection configurations observed in this 3D volume. Reflection events through the BSR were interpreted to aid in identifying the effects, if any, of potential gas hydrates and free gas in the sediment. To follow are details on the parameters used for mapping the reflection events also referred to as horizons.

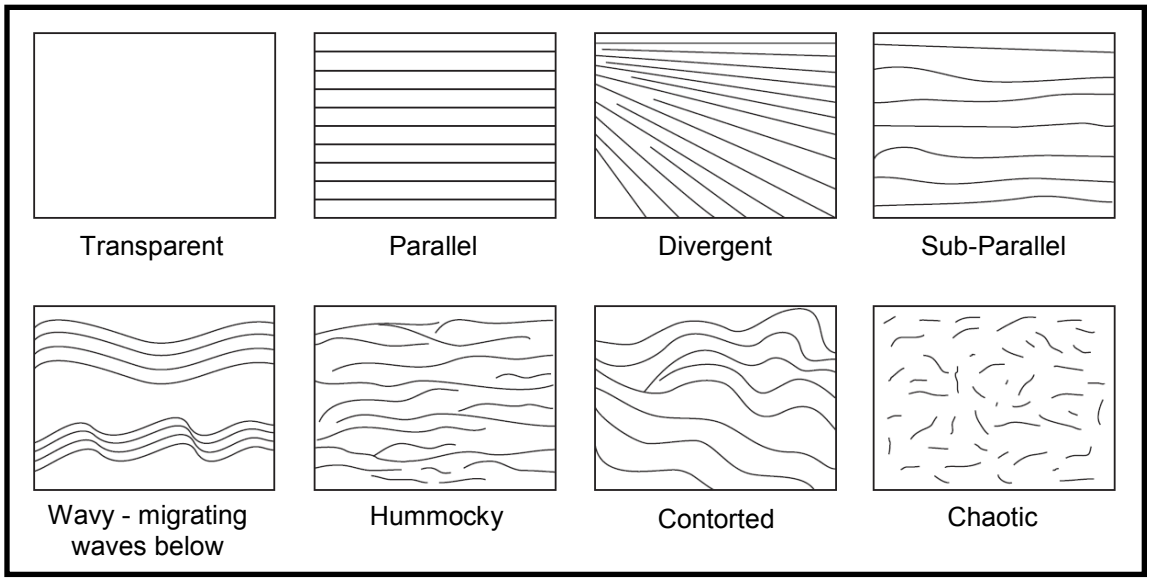

Figure 4.3 Reflection Configurations that aid in interpretation of depositional environments (modified after Mitchum et al. 1977).

The 3D seismic SEG-Y files were imported into SMT's Kingdom® seismic interpretation software. The BSR was digitized in Kingdom® using two modes: manual and snapped picking (Figure 4.4). Manual picking, which represents the most qualitative picking method, is completely user controlled. Conversely, in snapped picking the user guides the interpretation and the software automatically snaps the picked horizon to the highest amplitude within a predefined window. The manual and snapped picks were made on every 10th line with increased density in areas of greater slope. An automated interpolation was then applied to infill the seed picks and create a continuous surface.

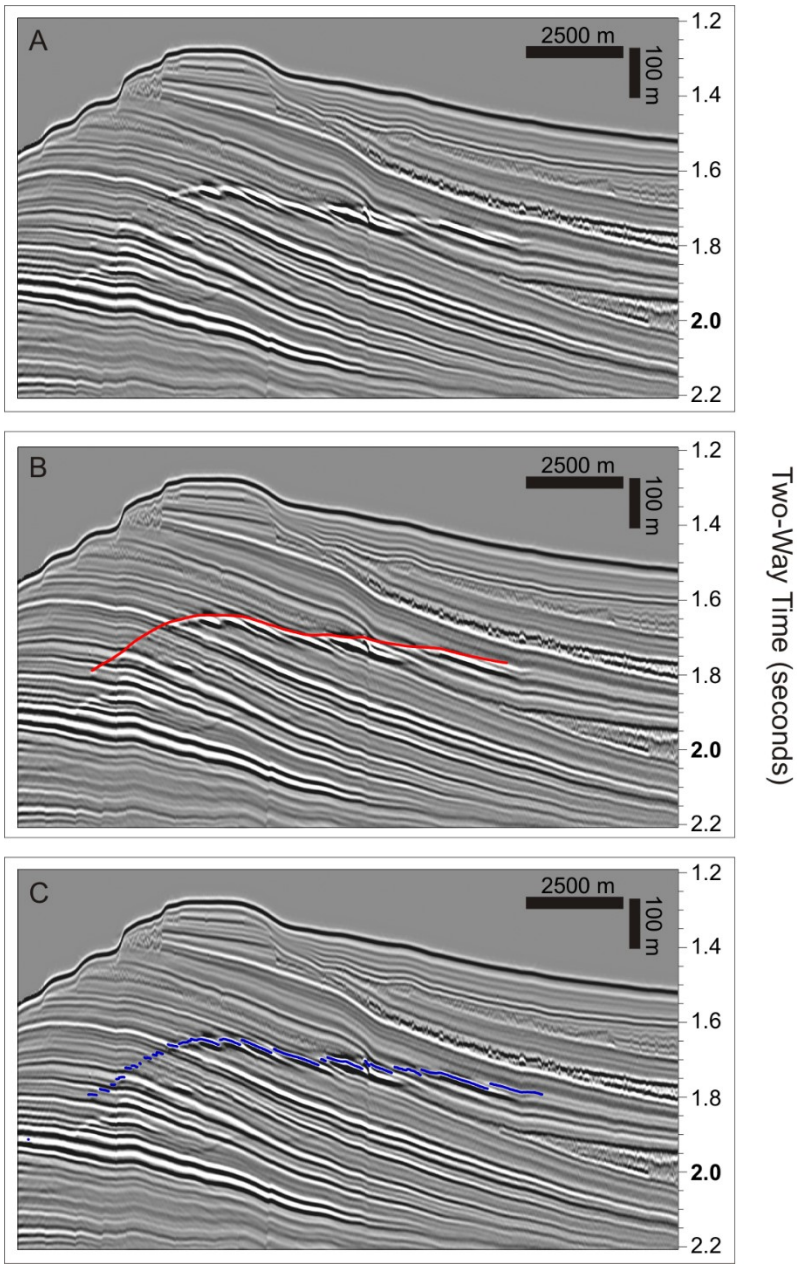

Figure 4.4 Arbitrary seismic profile through the Baynord 3D seismic volume showing the high amplitude, phase reversed, tiered reflections that constitute the BSR (A). The manual pick (B) connects the high amplitude peaks to create a continuous surface while the snapped pick (C) follows the high amplitude, tiered reflections that define the BSR.

Given the continuity of the various horizons that underlie and intersect the BSR, all other picks were made using the auto-hunt function on a relatively coarse grid of lines. As for the BSR, an automated interpolation was then applied to infill the grid of seed picks and create a continuous surface. The surfaces were then all exported and

brought into Surfer, a gridding and mapping software, for final surface generations. Surfer's Kriging gridding method was used to create the final surface grids. Kriging is a geostatistical gridding method that predicts the value of a function at a given point by computing a weighted average of the known values of the function around each point (Cressie 1990). One of the Kriging method inputs is search radius, which defines the distance from each point that the weighted average must be taken. Each gridded surface was created with a 50 m search radius and a 20 m grid cell spacing. Once the grids were generated, shaded relief map surfaces (light position of 135° from horizontal and 45° from the vertical) and contours were generated in and exported from Surfer. Geotiffs were then exported from Surfer and imported into ArcGIS for final figure generation.

4.1.4 Seismic Attribute Analysis

Instantaneous attributes as well coherency and dip of maximum coherency were calculated in Kingdom® Rock Solid Attributes for the entire 3D seismic volume. The attribute values were extracted along the various interpreted horizons. Sequential time slices through the various 3D attribute volumes were inspected in Kingdom's® 3D imaging software making note of any depositional, structural or anomalous features. To follow is theoretical background on these seismic attributes.

Seismic attributes are defined as a quantitative measure of a seismic characteristic of interest. Liner (2004) defines seismic attributes as specific quantities of geometric, kinematic, dynamic, or statistical features derived from seismic data. In practice, seismic attributes are used like filters to reveal subtle trends or patterns that are not readily apparent in the classic time-amplitude displays (Barnes 2001). There are no rules governing how attributes are computed or even what they can be, with any quantity calculated from seismic data considered an attribute. The most basic attributes are the fundamental elements of the seismic trace - time and amplitude.

Seismic attributes were calculated from the 3D seismic data in the Kingdom® Rock Solid Attributes software. In particular, instantaneous amplitude, frequency, and phase, as well as similarity and dip of maximum similarity were calculated. The instantaneous volumes were used to identify anomalous values (e.g. values that do not reflect primary lithological variations) indicative of the presence of gas hydrates and underlying free gas. Similarity, which is the measurement of the likeness of adjacent traces, was used to identify and map structural features such as faults, which provide potential conduits for the migration of gas from depth. To best understand the application

of the seismic attribute products it is important to understand how the attributes are calculated.

4.1.4.1 Instantaneous Attributes

Instantaneous attributes, representing some of the first seismic attributes, were first calculated by the petroleum industry in the early 1970's (Barnes 2001) with the first published work by Taner and Sherriff (1977). In this context instantaneous means that the various attributes are calculated for each time sample along the seismic trace. These attributes are calculated by modeling the seismic signal as a complex trace constructed from the seismic trace and an imaginary trace (Taner et al. 1979). A Hilbert transformation of the seismic or real trace yields the imaginary trace, which is simply the seismic trace rotated by 90°. Another way to think of the Hilbert transform of a signal *f*(*t*) is the convolution of the signal with 1/πr or as a filter which shifts the phases of the frequency components of the inputs by 1/πt (Barnes 1998).

To understand how the complex trace is constructed from the real and imaginary traces, imagine a point in complex space as represented in Figure 4.5. The seismic trace represents a point on the real axis while the imaginary trace defines a point on the imaginary axis; note the 90° offset between these axes. The complex point *c* is the sum of the imaginary and real components:

$$c = a + jb \qquad \text{Equation 4.4}$$

where *j* is equal to $\sqrt{-1}$.

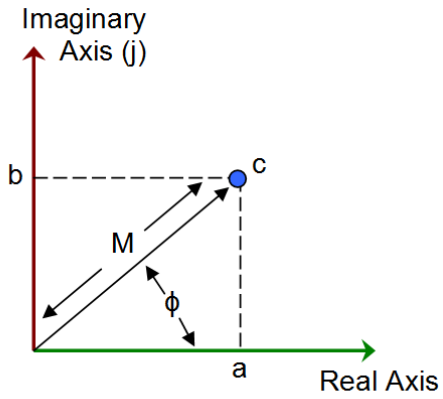

Figure 4.5 A point in complex space used to understand instantaneous attributes. The point c, presented in complex space, when projected onto the real axis is equal to a, and when projected onto the imaginary axis equals b. The point c can also be described by a phasor of length M with an angle of ϕ from the real axis.

Instead of a point in complex space consider a time series of values *f*(*t*), such as a seismic trace. The complex trace *F*(*t*) is then defined as:

$$F(t) = f(t) + jg(t) \qquad \text{Equation 4.5}$$

where *g(t)* is the imaginary trace. Equation 4.6 is represented graphically for a sine function in Figure 4.6. The figure shows how the projection of the helical complex trace on the real and imaginary planes are the seismic (real) trace and the Hilbert transform of the seismic trace (imaginary trace) respectively (Barnes 1998).

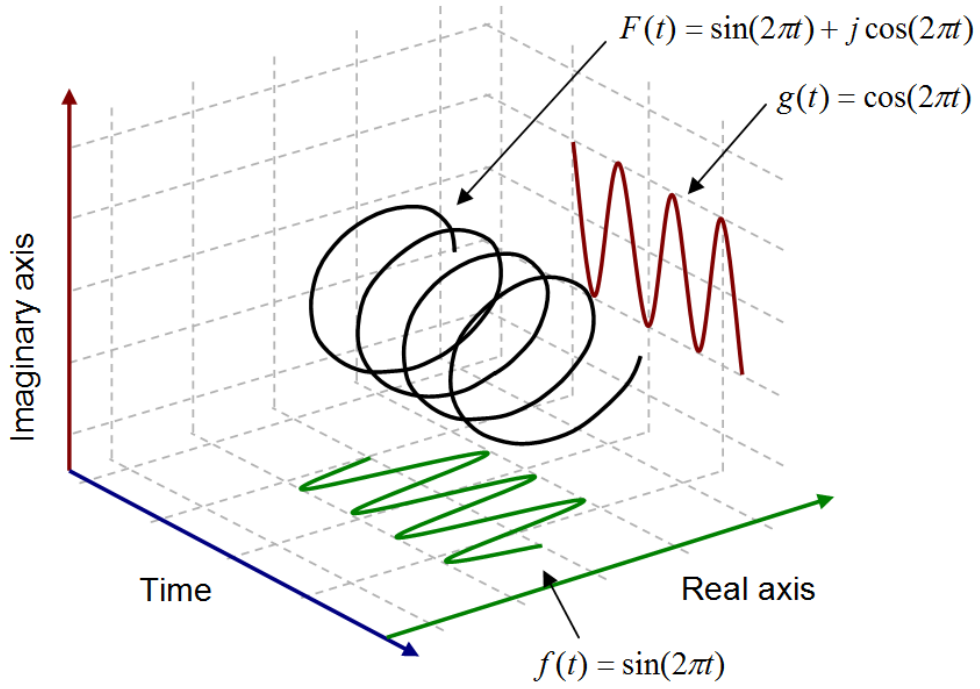

Figure 4.6 Example of the Cartesian projection of a complex trace, helical black line, onto the real and imaginary planes. The real or seismic trace is presented in green with the imaginary trace in red. Modified after Taner et al. (1979).

To represent the complex trace in Cartesian form as in Figure 4.6, aids in understanding but it is the trace's polar form that allows for computation of the instantaneous attributes (Barnes 1998). In polar form, the complex point c of Figure 4.5 is the tip of a phasor on the complex plane with magnitude M in the direction of ϕ relative to the positive real axis. In Polar form the complex trace is defined as:

$$F(t) = A(t)e^{j\phi(t)} \qquad \text{Equation 4.7}$$

For a time series of points in complex space, the line connecting the ends of the phasors as shown in Figure 4.7 forms the complex trace as represented for the sine function in Figure 4.6. For each time sample along the complex trace, the phasor angle, ϕ, represents the instantaneous phase, $\Theta(t)$ while the phasor length M is the instantaneous amplitude $A(t)$ or envelope (Barnes 1998).

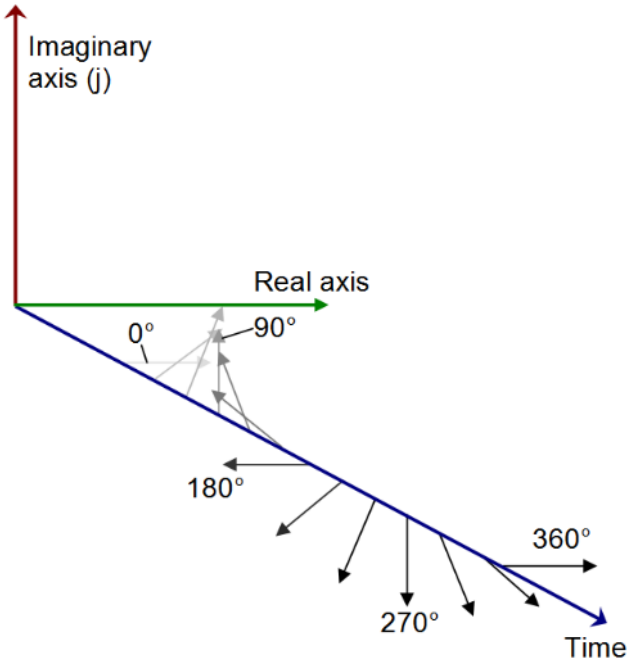

Figure 4.7 The complex trace of **Figure 4.6** presented in Polar form. The Polar form defines each point along the complex trace as a phasor with length M and at an angle ϕ from the real axis.

When the imaginary and real trace values are known the instantaneous amplitude and instantaneous phase can be calculated with simple trigonometry:

$$\theta(t) = \arctan\left(\frac{g(t)}{f(t)}\right) \qquad \text{Equation 4.8}$$

$$A(t) = \sqrt{f^2(t) + jg^2(t)} \qquad \text{Equation 4.9}$$

Instantaneous frequency, *w(t)*, is defined as the rate of change or derivative of the time dependant or instantaneous phase *Θ(t)*

$$w(t) = \frac{\partial\theta}{\partial d} \qquad \text{Equation 4.10}$$

Figure 4.8 is an example seismic trace showing the real and imaginary traces with the amplitude envelop overlain (a and b) as well as the instantaneous phase (c) and instantaneous frequency (d). The instantaneous phase forms a saw tooth pattern as the phase jumps between +180° and -180°. The instantaneous frequency shows a relatively consistent regional trend overlain by spikes in values, some of which result in negative frequencies (Taner et al. 1979).

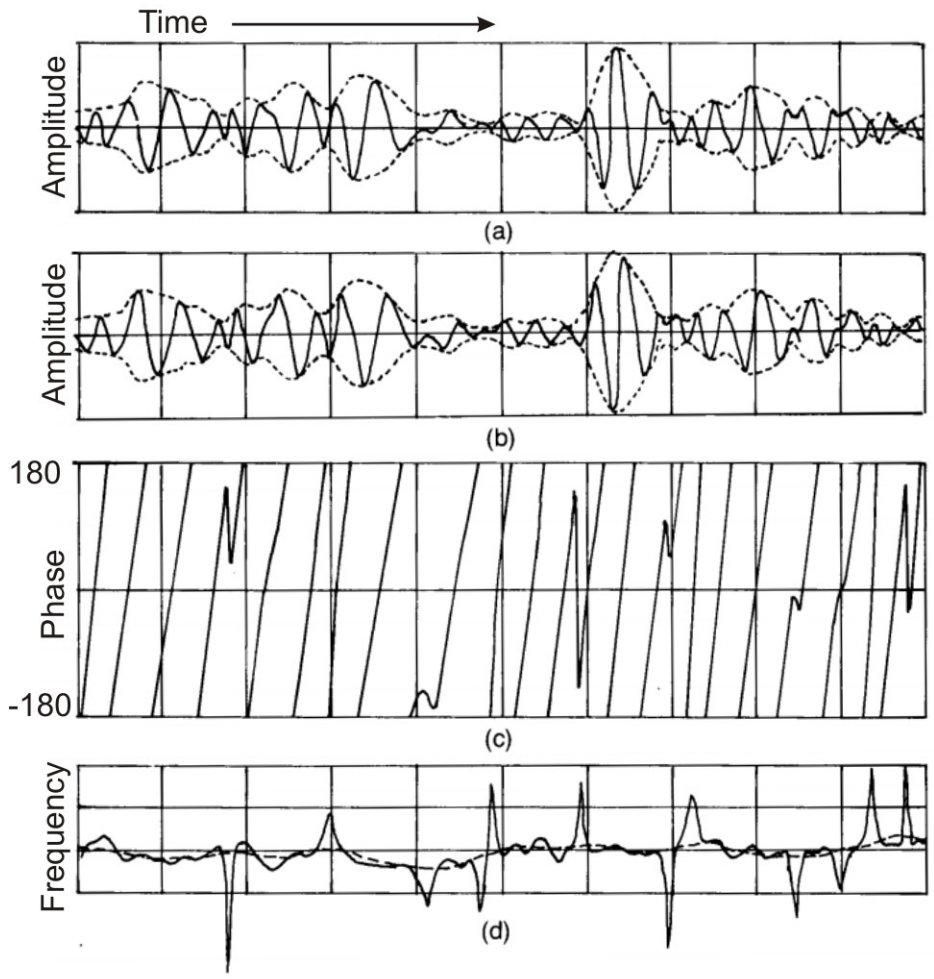

Figure 4.8 Sample seismic trace and its associated instantaneous attributes. The sample trace with the envelope overlain (dotted line) is presented in (a). The absolute value of the envelope is the trace's instantaneous amplitude (a). The associated imaginary trace with the envelope overlain is presented in (b), with the corresponding instantaneous phase (c) and frequency (d). Modified after Taner et al. (1979).

4.1.4.2 Similarity/Coherence

Seismic data are traditionally processed to image continuous reflections rather than to image discontinuities resulting from faults and abrupt variations in stratigraphy. Traditionally, time slices, representing the amplitude values at a constant time in a 3D seismic dataset, are used to view such features by allowing the user to inspect the seismic amplitude data in map view. Although discontinuities are visible on the time slices, the interpretation is complicated by the fact that, unless the beds are horizontal,

time slices cut through stratigraphic horizons of varying ages. This effect can be avoided by using horizon slices, which represent the amplitudes associated with interpreted surfaces. The pitfall of the horizon slice is that it requires the interpreter to pick the stratigraphic horizon, which is time consuming and imposes an interpretive bias on the dataset.

Coherence, referred to as Similarity in the Kingdom® Rock Solid Attributes software, is a mathematical measure of trace to trace similarity (Bahorich and Farmer 1995; Chopra 2002). When applied to seismic data, coherency values indicate the degree of continuity between two or more windowed traces (Marfurt et al. 1998). Ideally the amount of seismic continuity is a direct indication of geologic continuity (Barnes, 2001). Coherence is measured on a scale of zero to one with zero representing low trace to trace similarity and one representing exact trace to trace similarity (Bahorich and Farmer 1995; Marfurt et al. 1998). Displayed in map form either in a time slice or along a picked horizon, coherency calculations allow the seismic continuity to be quantified and translated into a visual image that reveals subtle geologic variations such as faults and channels. Various coherency algorithms have been developed and used in structural and stratigraphic mapping (Chopra 2002). SMT's Kingdom® seismic interpretation software uses a semblance based algorithm (Kingdom® 2013).

A multi-trace semblance based coherency algorithm was first presented by Bahorich and Farmer (1995). Similar semblance calculations are used extensively in velocity analyses and f-x deconvolution algorithms (Yilmaz and Doherty 1987). For the semblance based coherency calculations an elliptical or rectangular analysis window is defined containing *J* traces and centered about the analysis point. The number of traces used, *J,* depends on the signal to noise ratio with more traces required when the data are noisy. The value of *J* also depends on bed curvature, with less traces required when curvature is high, and on lateral discontinuity resolution with less traces required when the resolution is increased (Kingdom® 2013). Marfurt et al. (1999) define the average semblance over a vertical analysis window of height 2ω ms or of half-height $K = \omega / \Delta\tau$ samples as the coherency estimate, *c*:

$$c(\tau,p,q)=\frac{\sum_{k=-K}^{+K}\left\{\left[\sum_{j=1}^{J}u\left(\tau+k\Delta t-px_j-qy_j,x_{j,y_j}\right)\right]^2+\left[\sum_{j=1}^{J}u^H\left(\tau+k\Delta t-px_j-qy_j,x_{j,y_j}\right)\right]^2\right\}}{J\sum_{k=-K}^{+K}\sum_{j=1}^{J}\left\{\left[u(\tau+k\Delta t-px_j-qy_j,x_{j,y_j})\right]^2+\left[u^H(\tau+k\Delta t-px_j-qy_j,x_{j,y_j})\right]^2\right\}}$$

Equation 4.11

Where the triple (τ,p,q) defines a local planar event at time τ, *p* and *q* are the apparent dips in the x and y directions measured in milliseconds per metre. The superscript *H* represents the Hilbert transform of the real seismic trace, *u*, while Δt is the temporal sample increment (Marfurt et al. 1998).

Semblance can be interpreted as the ratio of the energy in the average trace within the analysis window to the average energy of the independent traces (Chopra 2002). The apparent dips *p* and *q*, which are user defined are calculated using horizon-based estimates or through a search over a user-defined range of discrete apparent dips, with dips that have the highest semblance values corresponding to the local reflector dip (Marfurt et al. 1998, 1999). In Kingdom® when similarity is calculated so is the dip value that corresponds to the maximum observed similarity. The dip of maximum similarity enhances subtle semblance variations, emphasizing trace to trace differences.

4.2 EXPLORATION WELLS

The study area is one of active hydrocarbon exploration with a total of five wells drilled within the 3D seismic area. Wireline logs and cuttings were acquired from different depth intervals within four of the wells (Harpoon O-85 was not used). These data allowed for correlation of the well geology with the 3D seismic volume. The locations of the wells used in this study are presented below in Figure 4.9.

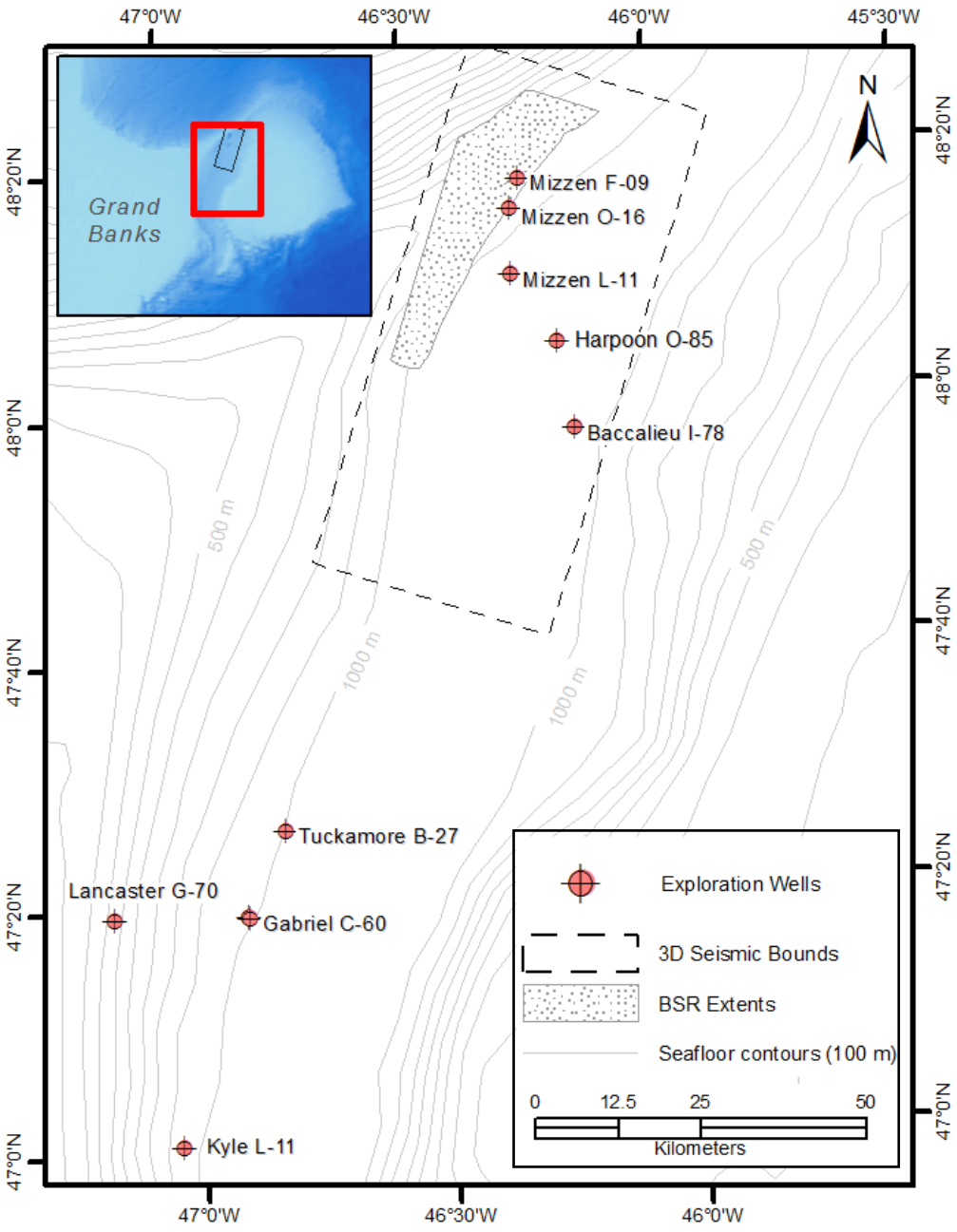

Figure 4.9 Exploration Wells used in this study.

This study analyzed resistivity, gamma ray, density, and sonic logs. Resistivity is the measure of the resistance of the flow of an electrical signal through the sediment and reflects the porosity, minerology and pore fluid chemistry of the sediment (Serra 1984). Increased fluid content typically results in decreased resistivity values as water conducts electricity better than sediment. Lithologic information is provided by the gamma ray log, which measures the naturally occurring gamma radiation of the sediments. Where clays

generally emit more radiation than sands, increases on the gamma ray logs are typically associated with clay dominated sediments while reductions are typically associated with sands or carbonates (Serra 1984). The sonic log, which measures compressional slowness, is used to correlate the well data to the 3D seismic as well as to convert the seismic interpretation from the time to depth domain (described in Section 4.2.1). Density logs provide information on the bulk density of a given formation, which is the combined density of the rocks/sediment and its fluid-filled pore spaces. If there is gas in the pore spaces the bulk density will be reduced. Muddy sediments typically have a higher bulk density as there is less porosity than coarser grained sediments.

Previous biostratigraphic work used cuttings to determine chronostratiographic ages in three exploration wells within the study area: the O-16, L-11, and Baccalieu well. Extending from the Miocene into the Pleistocene, the O-16 well provided the most complete age record of the three wells. The L-11 provides Miocene ages while the youngest age at the Baccalieu well is from the Base Paleogene. Biostartigraphic data combined with well ties provide age calibration for seismic markers mapped in this study.

4.2.1 Time to Depth Conversion

Seismic data are typically presented in two-way travel time; the time it takes for sound to travel down and then back from a reflecting interface. To correlate the well data to the seismic, the well data must be converted to the time domain, which requires some knowledge of sediment velocities. Velocities recorded in the F-09 pilot hole were used for this study. Compressional slowness, the inverse of velocity, was logged in the F-09 well from the seabed to approximately 2200 m sub-sealevel. Downhole compressional slowness was recorded every 0.2 m, which provided a resolution far above that of the 3D seismic data (see 4.5.1.1Seismic Resolution). Redundant velocity values were removed while velocity variations, potentially indicative of gas and hydrate in the sediments, were preserved. The velocity values were then used to convert the recorded depths to times through generation of a synthetic seismogram.

A synthetic seismogram is a simulated seismic response obtained by convolving a source wavelet with a reflection coefficient series (White and Simm 2003) and allows for calibration of the correlation between the seismic and well log data. To generate a synthetic seismogram, acoustic impedances are calculated using well log velocities and densities. For this study, velocity was taken from the F-09 compressional slowness log and densities from the F-09 downhole density log. The F-09 well was chosen because it

provides a continuous record through the sediments imaged on the 3D seismic volume. The resultant synthetic seismogram is presented below in Figure 4.10.

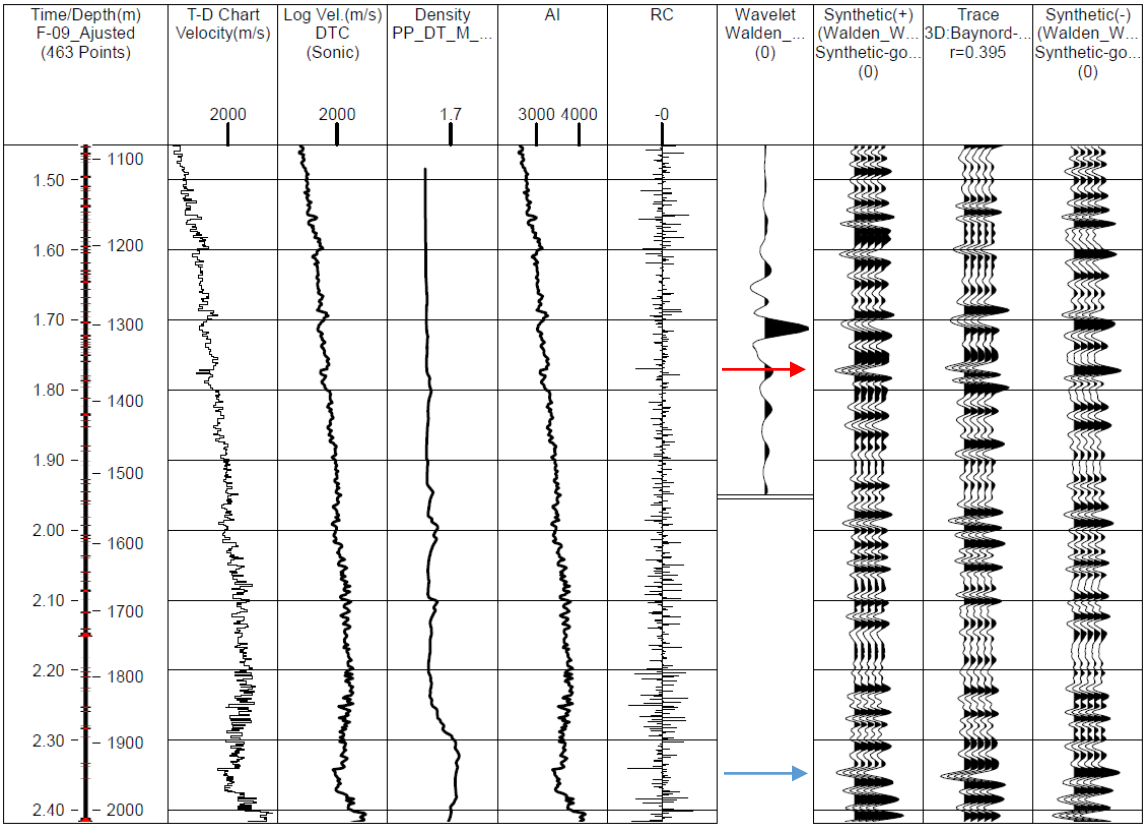

Figure 4.10 Synthetic seismogram from the F-09 well. AI is the acoustic impedances calculated from the velocity and densities log. RC is the resulting reflection coefficients calculated from the acoustic impedances. The resultant traces are presented as normal (+) and reverse (-) phase and are compared to traces extracted at the well from the 3D seismic volume. The lower (blue) arrow marks the H9 horizon and the red arrow marks the Primary BSR.

The velocity function was also used to convert the interpreted horizons from the time to the depth domain. To remove the water column all horizons were exported as time thickness maps, isochrons, between the seafloor and the specific horizons. In the time-to-depth function the seafloor depth and times were subtracted from all values creating a time to depth thickness relationship. Thickness in metres was plotted on the x-axis and time in milliseconds was plotted on the y-axis (Figure 4.11). A third order polynomial curve was then fitted to the points to define an isochron to isopach relationship. The equation was then applied to a gridded isochron map. Once converted the seafloor depth was added to the isopach map. The seafloor depth was determined

by taking the seafloor two-way time from the 3D seismic and depth converting it using a constant velocity of 1480 m/s as determined from recorded values contained within the Fisheries and Oceans online database (http://www.meds-sdmm.dfo-mpo.gc.ca/isdm-gdsi/ocean/index-eng.htm) and as noted in the F-09 well log.

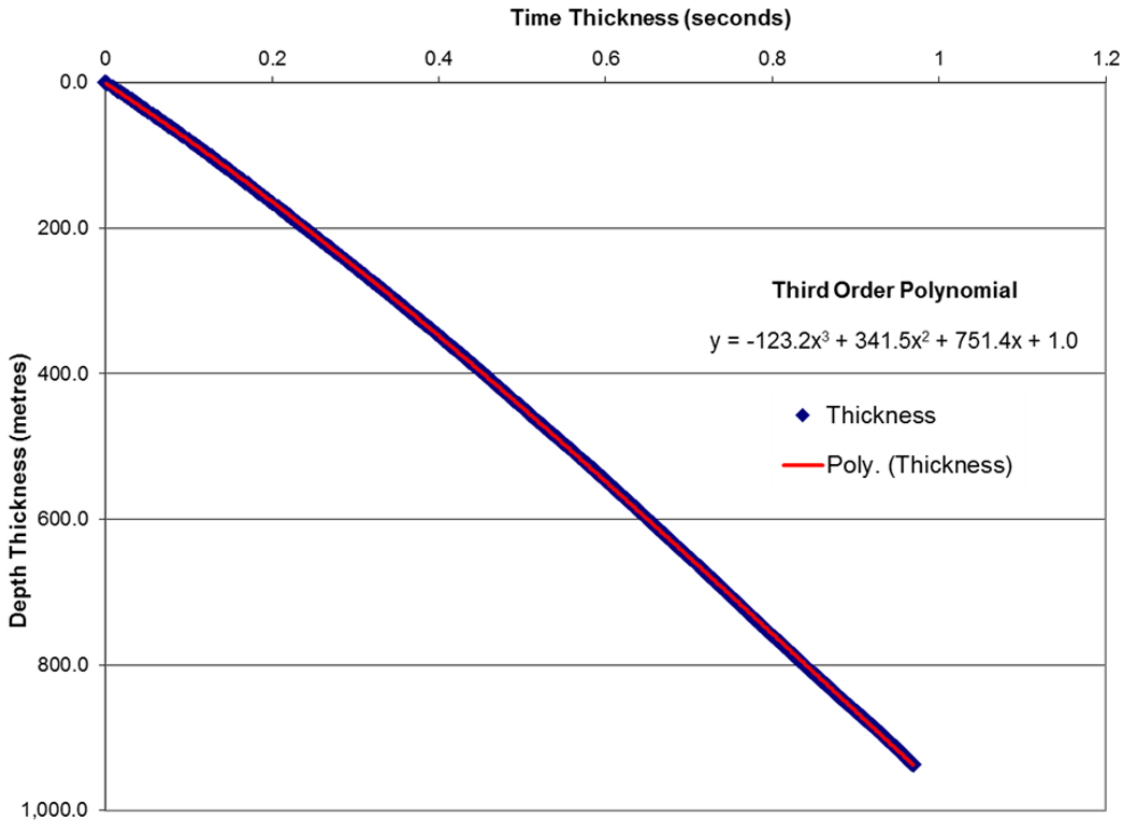

Figure 4.11 Time to depth function using sediment thickness.

4.3 GAS HYDRATE PHASE EQUILIBRIUM

In a system of water and hydrocarbon gas, as exists in the pore waters of unconsolidated sediments, gas hydrates will begin to form at specific temperatures and pressures, as shown by the hydrate stability curve. This curve represents the temperature and pressure at which liquid water, methane vapour and gas hydrates co-occur. Sloan's (1998) CMDHyd software uses a statistical thermodynamic approach to calculate the pressure of hydrate formation given a specific temperature (Figure 4.12). When temperatures are too high or pressure too low, the hydrogen bonded water molecules that form the lattice of the hydrate are no longer stable and the water transitions from the solid to the liquid phase.

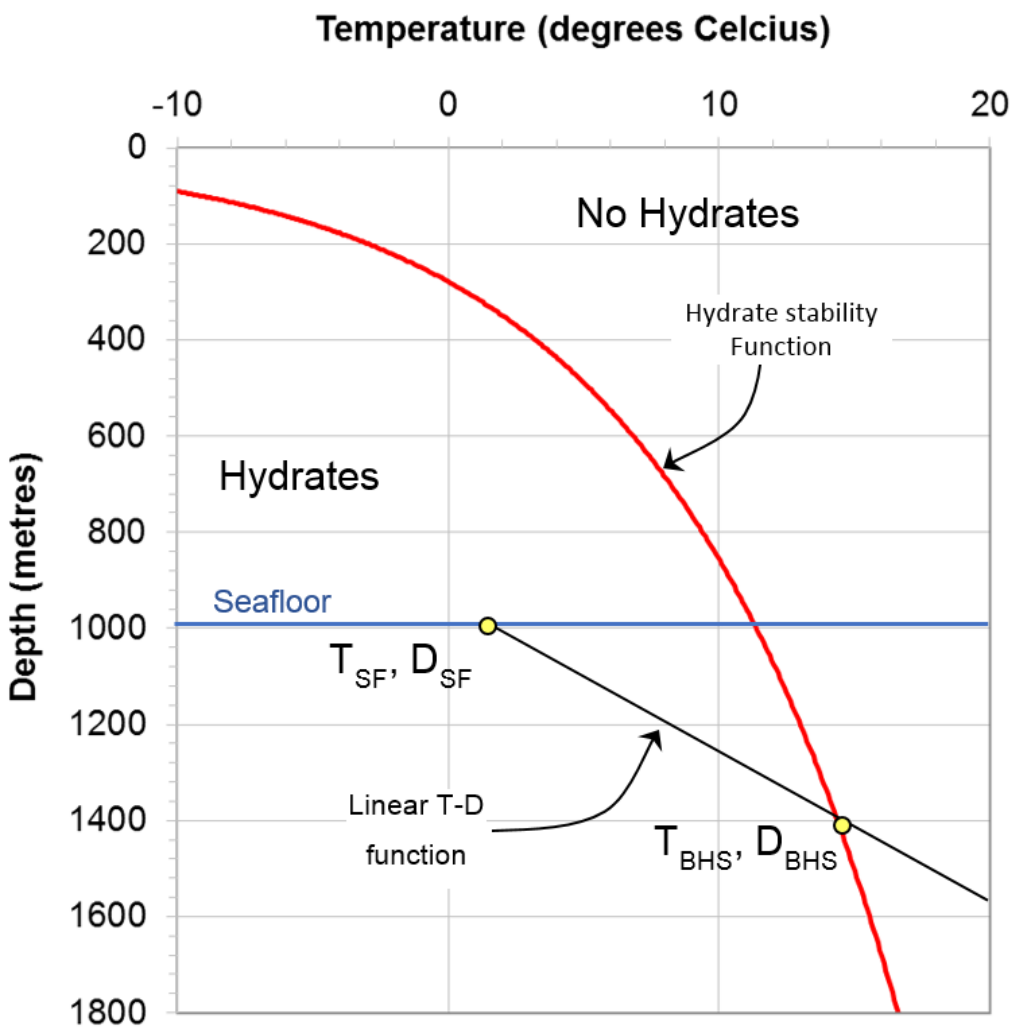

Figure 4.12 Methane gas hydrate stability function and depth temperature function of (seafloor depth of 1080m). The intersection of the two functions defines the temperature and depth at the base of the hydrate stability zone (BHSZ). Method modified after León et al. (2009).

4.3.1 Depth to the Base of Hydrate Stability

Assuming the pore gas is methane and the pore waters have a weight per cent of 3.5% NaCl, Sloan's (1998) CSMHYD software can determine the associated pressure required for hydrate formation. For this study, the calculated pressures were converted to depth, which requires an understanding of the pore pressure regime within the study area. In a study of downhole overpressures in wells on the Grand Banks, Wielens and Jauer (2001) noted no overpressure zones in the shallow sediments. Their data also

showed that pore pressures in the shallow sections are typically at hydrostatic pressure for seawater.

Downhole pressures from the four exploration wells drilled within the study area were taken from the online BASIN database of wells (Natural Resources Canada, 2014). These pressures are plotted versus depth with a hydrostatic gradient of seawater of 10.7 kPa/m and a lithostatic gradient of 22.6 kPa/m (Wielens and Jauer 2001) for comparison (Figure 4.13). The hydrostatic gradient of 10.7 kPa/m is based on the maximum salinity values observed offshore Newfoundland, which occur at Hibernia. The multiple datasets for the wells in Figure 4.13 reflect the different methods used to record downhole pressures. Wielens and Jauer (2001) noted the most reliable pressure data are Shut-In (SIP) and Final-Shut-In (FSI) Repeat Formation Tester (RFT) measurements. Mudweight data, though more prevalent, are artificial and based on expected pressures. Hence overpressures as indicated by mudweights are considered suspect. For their large dataset on the Grand Banks, Wielens and Jauer (2001) did not use hydrostatic measurements although given the limited data in the study area these values were included in the pressure plot of Figure 4.13. Wielens and Jauer (2001) note the onset of overpressures requires a minimum depth of 1200 m but are not related to specific depths or formations. They hypothesize that the extensive faults are responsible for the seemingly arbitrary overpressure distribution. Wielens and Jauer (2001) suspect leakage from the faults is episodic and related to the migration of hydrocarbons.

Based on these well results, a simple linear regression produces the following equation for depth as a function of pressure:

$$D = 111.6 + 0.0835 * P \qquad \text{Equation 4.12}$$

where D is depth in metres below the seafloor and P is pressure (kPa) as output from CMDHYD.

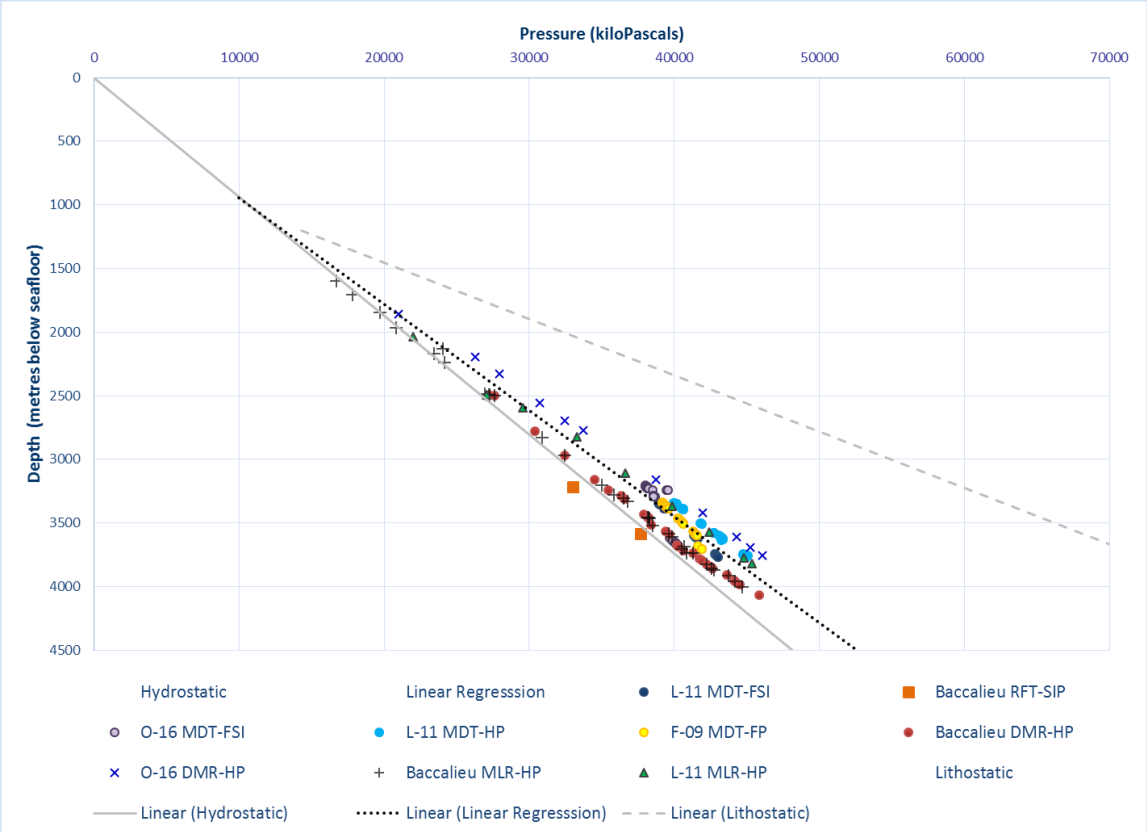

Figure 4.13 Downhole pressures from the four exploration wells within the study area. Acronyms are as follows: MDT – Modular Formations Dynamic Tester, FSI – Final Shut-In, RFT – Repeat Formation Tester, SIP – Shut-In Pressure, HP – Hydrostatic Pressure, FP – Flowing Pressure, DMR – Drilling Mud Record, MLR – Mudlogger's Report. The linear hydrostatic gradient is 10.7 kPa/m while the lithostatic is 22.6 kPa/m. Refer to Figure 4.9 for well locations.

The conversion of pressure to depth can also be calculated using the equation

$$D = \frac{1000P}{\rho} * g \qquad \text{Equation 4.13}$$

where D is depth, P is pressure, ρ is the density of seawater and g is the gravitational constant. The gravitational constant is not truly constant and varies with latitude given the Earth's slight equatorial bulge. Fofonoff and Millard (1983) developed a standardized approach for latitude dependant pressure to depth conversions by applying an updated equation of state to Saunders and Fofonoff's (1976) method. This approach uses the following equation:

$$D = \frac{(((1.82E{-}15{*}P{+}2.279E{-}10){*}P{-}2.2512E{-}5){*}P{+}9.72659){*}P}{Sin\left(\frac{LAT}{57.29578}\right)} \qquad \text{Equation 4.14}$$

where D is depth, P is pressure and LAT is the latitude of the area of interest. For this study a latitude of 48 was used.

Seawater is slightly compressible therefore its density changes with pressure. Fofonoff and Millard (1983) describe a standardized method for determining density variations with pressure. Given the complexity of the density calculations and the availability of simple online conversion tools, density values based on the temperature and pressures that define the stability curve, along with an assumed salinity of 35 PPT, were calculated. The corrected density and gravitational constants along with the pressures were input into Equation 4.14 to determine the depths and hence define the hydrate stability in terms of depth and temperature.

Once the pressure values were converted to depth the temperatures were plotted versus the natural log of the depth values. Plotting the natural log of depth produced a linear relationship between depth and temperature. A simple linear regression of temperature and ln (D) yielded a gas hydrate phase equilibrium described by the equation:

$$T_{BHSZ} = 9.01 * ln(D_{BHSZ}) - 50.4 \quad \text{Equation 4.15}$$

where T_{BHSZ} is temperature at the base of hydrate stability. Assuming a linear relationship between depth and sediment temperature, T_{BHSZ} can also be described by the equation:

$$T_{BHSZ} = \delta g * D_{BHSZ} + b \quad \text{Equation 4.16}$$

where δg is thermal gradient in degrees Celsius per metre (°C/m) and b is the y-intercept (Figure 4.12). The y-intercept is defined by the equation:

$$b = T_{SF} - \delta g * D_{SF} \quad \text{Equation 4.17}$$

where T_{SF} and D_{SF} are seafloor temperature (°C) and depth (m) respectively. Substitution of Equation 4.17 into 4.16 yields:

$$T_{BHSZ} = T_{SF} + \delta g\,(D_{BHSZ} - D_{SF}) \quad \text{Equation 4.18}$$

Further substitution of Equation 4.18 into Equation 4.15 produces the function:

$$ln(D_{BHSZ}) = [T_{SF} + \delta g(D_{BHSZ} - D_{SF}) + 50.4] / 9.01 \quad \text{Equation 4.19}$$

where T_{SF}, δg and D_{SF} are known and D_{BHSZ} is unknown. Equation 4.19 has no real solution therefore an accurate approximation was determined by applying the iterative process of Newton's Method described by the equation:

$$x_n + 1 = x_n - (f(x_n) / f'(x_n)$$ Equation 4.20

where x is D_{BHSZ} the variable we are solving for, n represents the number of iterations and $f(x_n)$ is Equation 4.19 and $f'(x_n)$ its derivative. The initial input approximation, x_n, was determined by taking the seafloor depth and adding 300m, which is the approximate thickness of the hydrate stability zone as determined by the BSR depth on the 3D seismic volume. Each iteration refined the previous estimate and after three iterations an answer accurate to the second decimal place was determined.

In the final equation for hydrate stability depth, Equation 4.19, the seafloor depth is derived from the 3D seismic by depth converting the seafloor pick. A constant velocity of 1480 m/s, as taken from the F-09 well log, was applied to convert the seafloor from the time to depth domain.

Seafloor temperature, another known variable in Equation 4.19, is taken from a study of shallow sediments by Froján et al. (2012) where sediment temperatures in box core samples were recorded. These seabed temperatures taken in the vicinity of the 3D seismic survey (Figure 4.14) correlate well with bottom water temperatures reported by Colbourne and Foote (1994). Based on an average of Froján et al.'s (2012) sediment temperatures closest to the BSR, a seabed temperature of 3.9°C was used for the stability calculations.

A similar calculation was undertaken using the hydrate stability curve defined by Majorowicz and Osadetz (2003), who also used the CMDHyd software. These results were compared to the hydrate formation temperatures and pressures observed in the laboratory as reported by Dickens and Quinby-Hunt (1994).

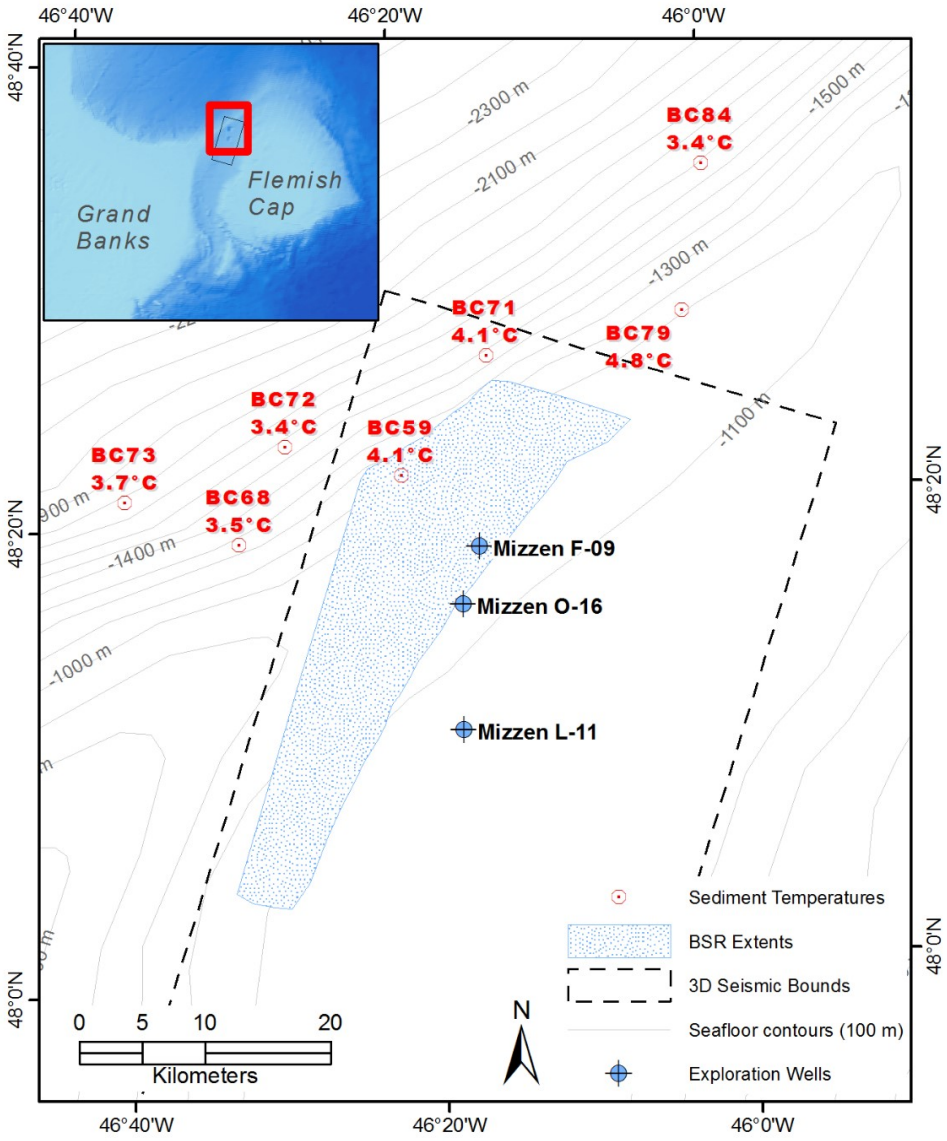

Figure 4.14 Seabed sediment temperatures taken from box core samples. These sediment samples were acquired to assess the benthic macrofaunal community structure north of the Sackville Spur (Froján et al. 2012).The sediment temperature labels include the sample name followed by the recorded sediment temperatures.

4.3.2 Downhole temperatures

To determine the geothermal gradient for use in the final hydrate stability calculation of Equation 4.19, downhole temperatures from the eight exploration wells in the vicinity of the study area were assessed (Figure 4.15). As reported by Wielens and Jauer (2001), the temperature dataset is limited on the Newfoundland margin. Despite

the limited data Wielens and Jauer (2001) note that the geothermal gradient is highly variable probably even within fields. The downhole temperatures, corrected with a Horner Plot, were plotted versus sub-seafloor depth. Assuming the gradient in linear, a least squares line was determined for the data with the slope of the least squares line representing the geothermal gradient. When all Flemish Pass wells are used the geothermal gradient is ~26.7 °C/km. If the three deepest downhole temperatures are removed the geothermal gradient rises to ~37.8 °C/km. If only the temperatures from the nearest well, Baccalieu I-78, are used the geothermal gradient is 35.8 °C/km. The temperature depth plots, along with the linear equations, whose slopes define the geothermal gradients, are presented in Figure 4.15. In a margin wide study of the hydrate stability field Majorowicz and Osadetz (2003) used an average regional geothermal gradient of 32°C/km. Their calculation used those wells included in Figure 4.15 in addition to others along Canada's east coast margin. This study's stability calculations used a geothermal gradient of 35.8 °C/km, derived from the well nearest to the BSR in the study area.

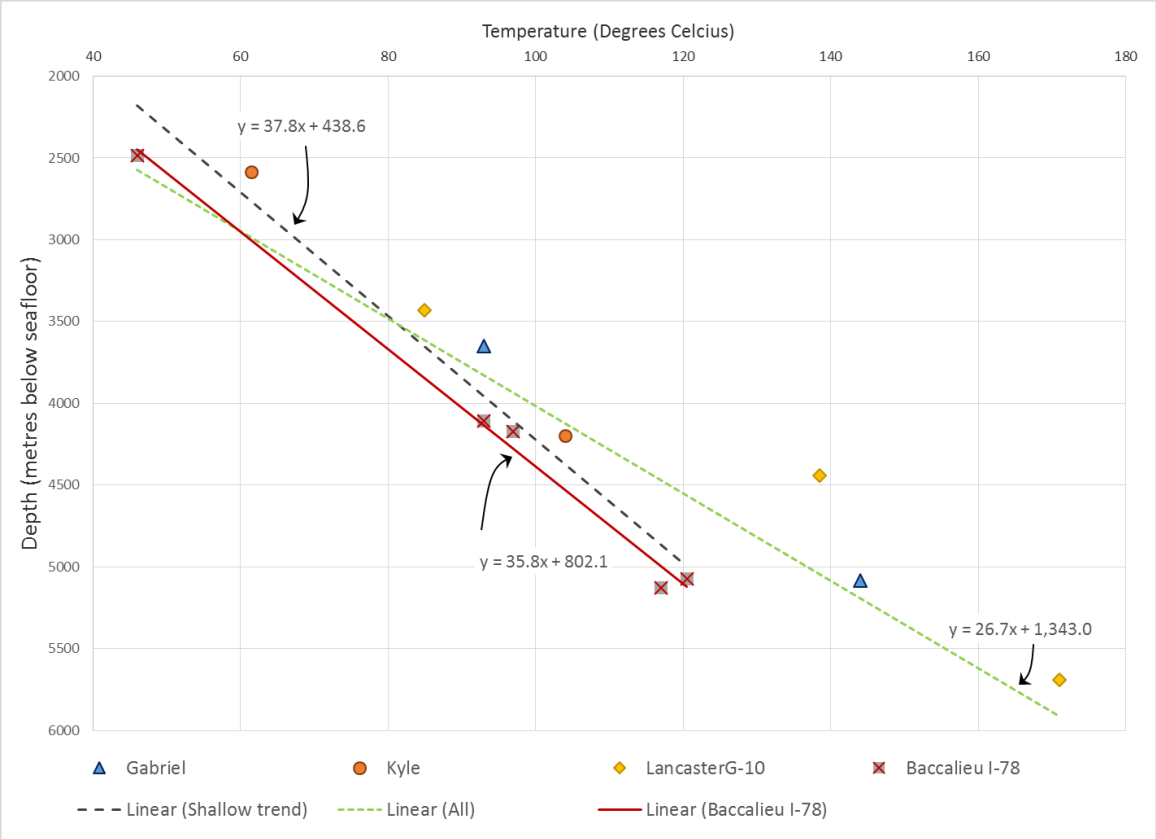

Figure 4.15 Downhole Temperatures from Flemish Pass exploration wells.

4.3.3 Gas Composition

The size of the gas molecules that constitute a gas hydrates deposit determines the geometry of the hydrate crystal structure. Methane, a relatively small hydrocarbon molecule, forms sI hydrates, while the larger thermogenic gas molecules such as butane, ethane, and propane form the more stable sII hydrates (Sloan 1998). A reduction in the methane content reduces the ratio of sI to sII hydrates. Where sII hydrates are stable at higher temperatures and pressures than sI hydrates, a reduction in methane concentration increases the depth to the BHSZ as shown by the stability curves of Figure 4.16.

The gas composition within the shallow sediments of the Sackville Spur was not determined but based on the results from other deposits both along the Atlantic margin and globally, a gas composition of 100% methane was assumed for the hydrate stability calculations. Head Space gas analysis, which uses gas chromatography to separate and measure the concentrations of individual vapour contents to determine the C1 through

C5 hydrocarbon composition, was undertaken on sediment samples taken from the shallow sediments overlying the Mohican Channel BSR offshore Nova Scotia. Theses analyses showed the gas consisted of 100% methane gas (Cullen et al. 2008).

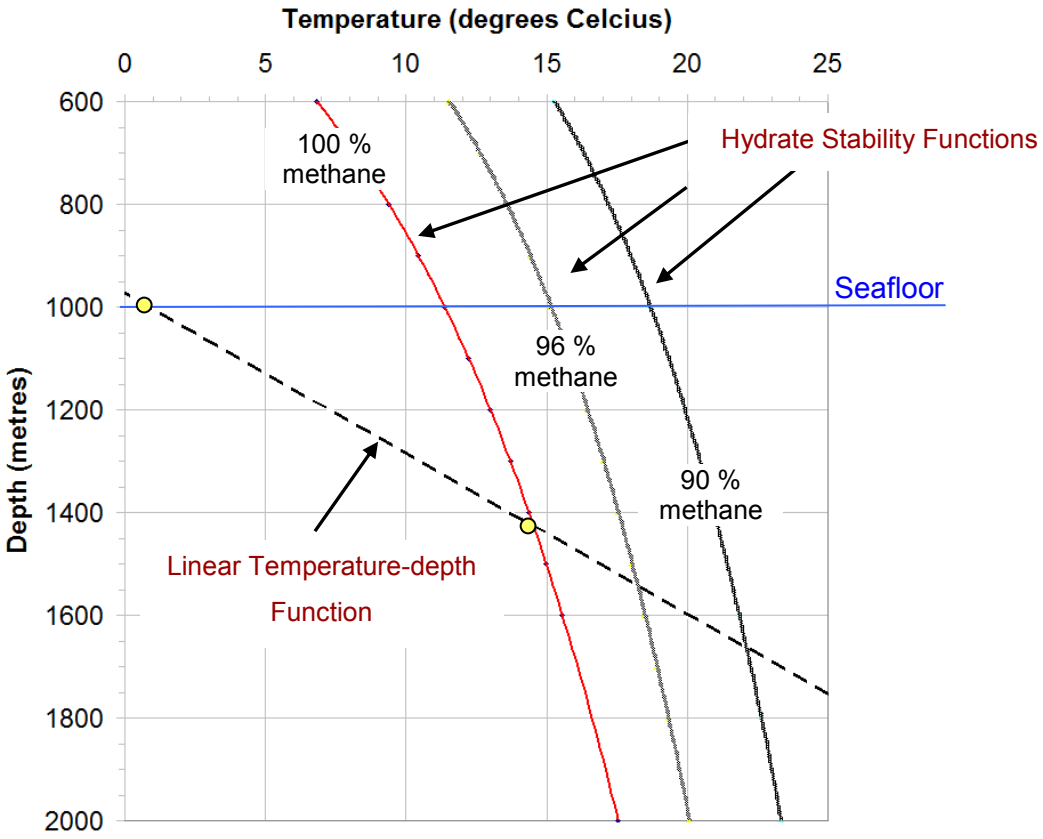

Figure 4.16 Hydrate stability curves for various methane concentrations. As the methane composition decreases the intersection of a hypothetical temperature-depth function and the hydrate stability function, which defines the base of the hydrate stability zone, occurs at higher temperatures and pressures. The hydrate stability curves are taken from Majorowicz and Osadetz (2003).

4.3.4 Gas Hydrate Inhibitors

Ions that are present in the pore water/gas mixture act to inhibit gas hydrate formation (Sloan 1998). CMDHyd uses pure water in its stability calculations and allows the user to input various inhibitors to see how these modify the gas hydrate stability curve. Salts and other impurities within the pore water act to inhibit the formation of gas hydrates. When present in the pore waters, the salts and other impurities decrease the

temperature and pressure at which gas hydrates form. Where gas hydrate formation can occur in pipelines, salts and other gas hydrates inhibitors are routinely added to prevent hydrate formation (Carroll 2009). In the marine environment the pore waters are saline with a typical weight percent of 3.5% in the North Atlantic. Dickens and Quinby-Hunt (1994) presented experimental results of the temperature and pressures at which gas hydrates form in salt (with a weight percent of 3.35 %) versus fresh water. Although the pressures (depths) encountered in the study area are greater than those sampled by Dickens and Quinby-Hunt (1994), their experimental values clearly show that the presence of salt inhibits gas hydrate formation (Figure 4.17).

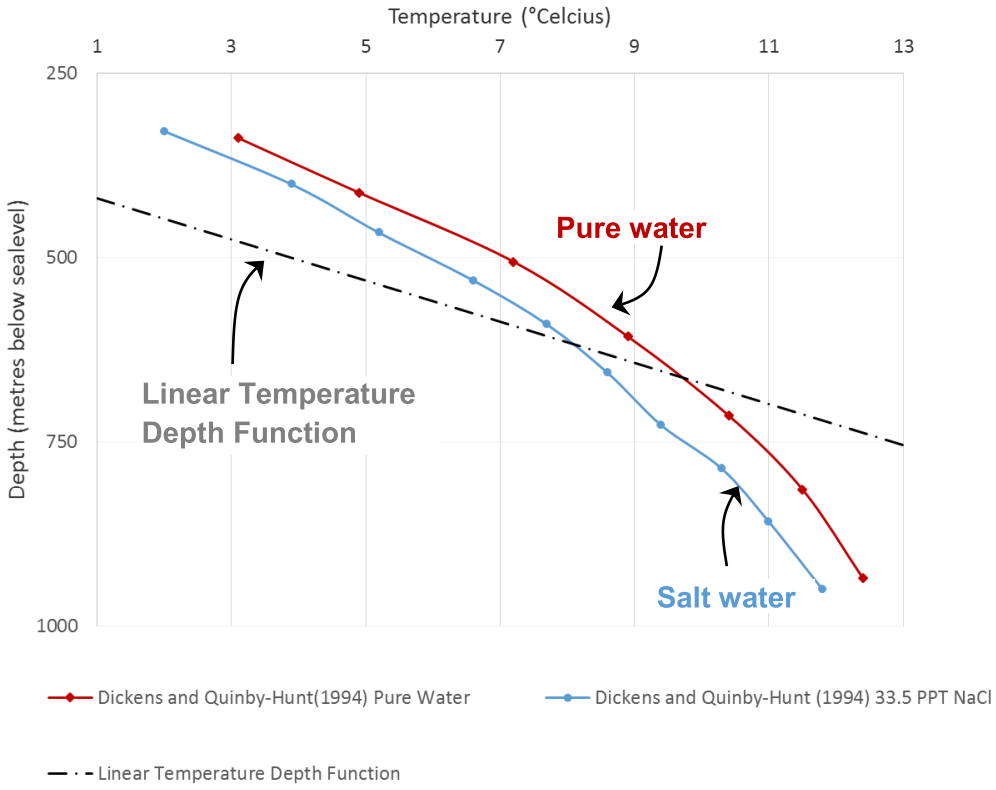

Figure 4.17 Laboratory values for the temperature and depth of gas hydrate formation as reported by Dickens and Quinby-Hunt (1994). When salt is added to water the intersection of a hypothetical linear temperature-depth function and the hydrate stability function, which defines the base of the hydrate stability zone, occurs at lower temperatures and pressures. The salt water in the experiments had a weight percent of 3.35% NaCl. Pressures were converted to depths using a simple hydrostatic gradient of 10 MPa/km.

4.4 GAS AND HYDRATE SATURATIONS

Two methods were used to estimate the gas hydrate concentration at the F-09 pilot hole: 1) the effective medium model and 2) Archie's Quick Look method.

4.4.1 Effective Medium Modelling

Estimates of the fraction of free gas and gas hydrate in the sediment at the Mizzen F-09 well were determined through modelling velocities for different gas and gas hydrate concentrations using the model of Helgerud et al. (1999). The MatLab script for determining the saturations is included in Appendix A.

Helgerud et al. (1999) developed an effective medium model to relate both gas and gas hydrate fraction with elastic wave velocity in unconsolidated, highly porous seabed sediments. This model is based on the rock physics model of Dvorkin et al. (1999) which defines the shear and bulk moduli of saturated marine sediments as functions of porosity and pressure (depth). In the model of Helgerud et al. (1999) gas hydrate is accounted for by assuming that the hydrate is either (a) part of the pore fluid and does not affect the stiffness of the dry frame or (b) that it is a load bearing component of the frame. Case (a) assumes that gas hydrate and water are homogeneously distributed in the pores and the bulk modulus of the fluid phase becomes the average of the water and gas hydrate bulk moduli. In case (b) the gas hydrate reduces the porosity and alters the solid phase elastic properties. Gas in the pores is modelled as either homogeneously distributed or patchily distributed.

Porosity, a key component when calculating the elastic constants, was modelled using a simple depth dependant logarithm function. Where Mizzen F-09 downhole porosity values were not logged, they were modelled as a function of depth using the equation:

$$\phi = \phi_0 \exp^{(-\frac{z}{\lambda})} \qquad \text{Equation 4.21}$$

where ϕ is surface porosity, z is depth, and λ the exponential decay factor. An estimate of surface porosities came from the near-by piston core 2001-043 core 14, while the decay function was varied to fit the F-09 velocity data. For this study a surface porosity of 0.65 and a decay factor of 800 provided a best fit for the recorded velocities. These values are comparable to those used by LeBlanc et al. (2007) on the Scotian and Vancouver margins.

To calculate the elastic constants and hence the velocity variations for different gas and gas hydrate concentrations, the bulk and shear moduli of the solid phase were

calculated from the elastic constant and density values of the sediment's mineral constituents using Hill's (1952) average formula. Mineral constituents were taken from Piston Core 059; a 10.65m core collected in 2011 by NRCan in the northern Flemish Pass. Seismic profiles through the core show drift sediments similar to those observed on the 3D seismic at the Mizzen F-09 well (Cameron et al. 2014).

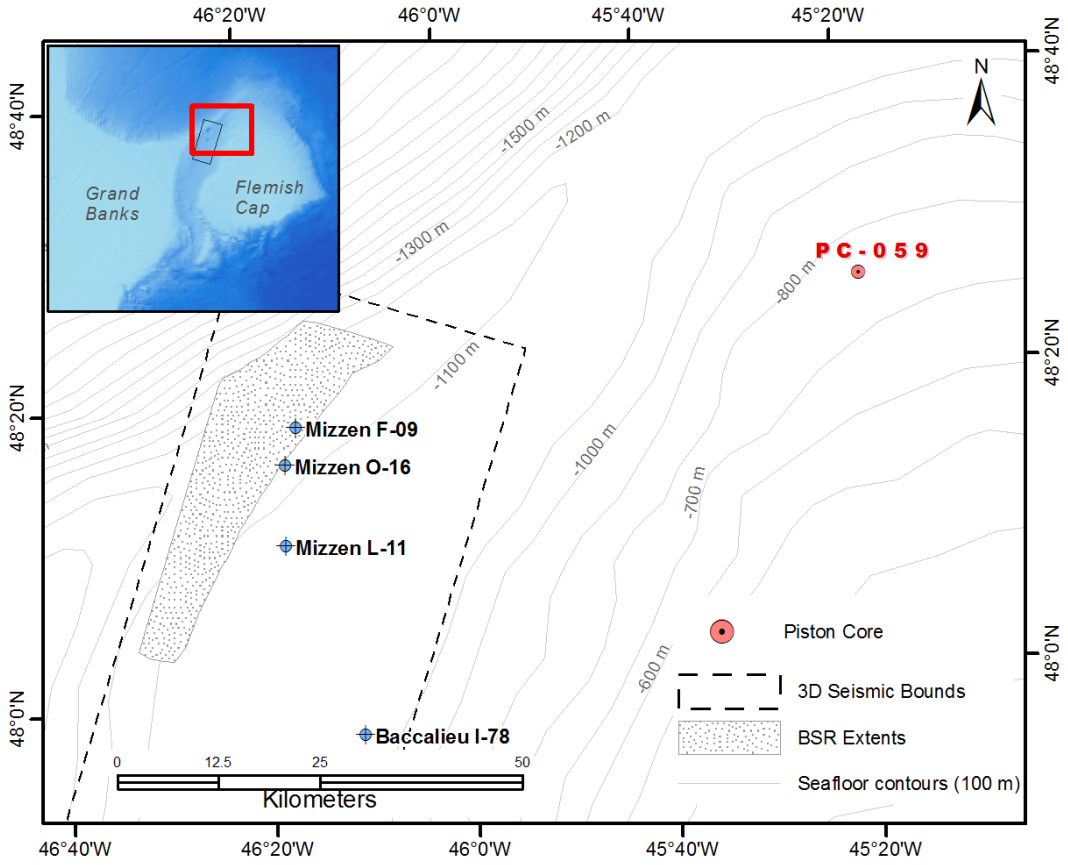

Figure 4.18 Location of piston core 059.

Individual mineral constituents were determined by Qualitative x-ray diffraction (qXRD), which expands the quantitative method from estimates of quartz to a wide range of clay and non-clay (Eberl 2003). The analyses were completed by John Andrews at the Institute of Arctic and Alpine Research and the Department of Geological Sciences, University of Colorado. The qXRD methodology is described by Eberl (2003) and McCarty (2002). The qXRD was run on the <2 mm fraction of subsamples every 10 cm along the core. The raw results were run through RockJock6.0 to determine a best fit between the observed and predicted qXRD patterns. For core 059 duplicate errors were

typically within the range of ±1 weight per cent. Andrews et al. (2010) provide an assessment of the reliability of the data. For this study, average mineral concentrations along the entire core along with the individual mineral elastic constants and densities from Mavko et al. (2009) were used. The various constituents and their properties are summarized below in Table 4.1.

Table 4.1 Average volume, bulk modulus (K), Shear modulus (G) and densities (ρ) of sediment constituents. Mineralogical values taken from Mavko et al. (2009) while gas, gas hydrate and water values are from Helgerud et al. (1999). Quartz* includes chert and diatoms while Other** includes a weighted average of siderite, halite, amphibole, pyroxene, pyrite, hematite and maghemite.

Constituent	Volume %	K (GPa)	G (GPa)	ρ (g/cm^3)
Quartz*	28	36.6	45	2.65
Feldspar	30	37.5	15	2.62
Clay	19	20.9	6.9	2.58
Calcite	12	76.8	32	2.71
Dolomite	8	80.2	49	2.87
Other**	3	106	65	3.58
Gas Hydrate	Variable	7.9	3.3	0.9
Methane Gas	Variable	0.11	0	0.23
Water	Variable	2.5	0	1.032

Once calculated, the solid phase elastic constants were used to calculate Poison's ratio. The effective and dry frame elastic constants were determined assuming a reasonable value for critical porosity, 0.38 (Nur et al. 1998) and for the number of contacts per grain in a sphere pack at the critical porosity, 8.75 (Murphy 1982). The final bulk modulus of the saturated sediments was calculated using these values, while the shear modulus of the saturated sediment was made equal to that of the solid frame. Once known, the elastic moduli for the saturated sediments were used to determine the elastic wave velocities at various gas hydrate and gas concentrations. These velocities are then compared to those recorded at the well to estimate the hydrate and gas concentrations. Gas and hydrate concentration as determined from the F-09 compressional velocity log were compared to those determined from lower resolution

ocean bottom seismometer (OBS) velocities acquired by NRCan over the Sackville Spur BSR (Chian 2008).

4.4.2 Archie's Quick Look Method

An estimation of the gas hydrate saturation in the shallow sediments at the F-09 well was determined using the "Quick Look" Archie log analyses technique of Collett and Ladd (2000), which compares the resistivity of water saturated and hydrocarbon bearing sediments. The equations for the Quick Look method are as follows:

$$S_w = \left(\frac{R_0}{R_t}\right)^{\frac{1}{n}} \qquad \text{Equation 4.22}$$

where S_w is water saturation, R_0 is the resistivity of the sediment if the pores only contained water, R_t is the resistivity of the hydrate bearing units (log values) and n is an empirically derived constant of 1.9386 (Pearson et al. 1983). The hydrate saturation, S_h is then determined based on the following relationship:

$$S_h = 1.0 - S_w \qquad \text{Equation 4.23}$$

The key to this method is determining the R_0 value which represents the background or baseline value of the resistivity log. A linear function defining resistivity as a function of depth is fit to the background values. This linear function is then substituted into Equation 3.22 (Figure 4.19).

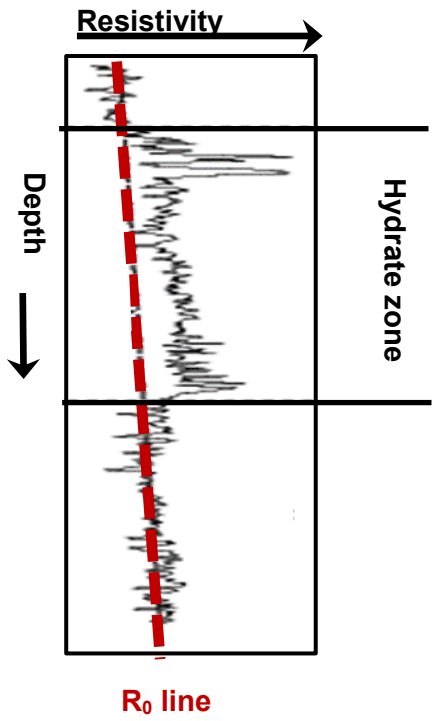

Figure 4.19 A sample resistivity log from the Blake Ridge off the southeastern US. Modified after Collett and Ladd (2000)

4.5 ERROR AND UNCERTAINTY

The primary sources of error and uncertainty are attributable to the resolution of the seismic data, the accuracy of the time to depth conversion and the precision in the values used for the hydrate stability calculation. Errors are also associated with the resolution of the well logging tool and the accuracy in its downhole position.

4.5.1 Seismic

Error and uncertainty in the interpretation of the BSR and other mapped reflection events, have three potential sources:

1. Limitations in data acquisition and processing which includes data resolution,
2. Errors or misties in the mapping of the reflector,
3. Velocity error in time to depth conversion.

Of these, seismic resolution is the easiest to quantify. Limited information is available on the 3D seismic data acquisition and on the data processing flows making it impossible to quantify the uncertainty and errors associated with the processing of the 3D seismic data. Errors associated with the seismic processing are best determined using sensitivity

analysis to observe the effects of minor changes to the data processing flows (Yilmaz and Doherty 1987). Such analyses require access to the raw seismic data which was not possible for this study. Errors and misties in the mapping of reflections of the 3D seismic volume are reduced by interpreting intersecting lines to tie the picked reflections across the study area. To minimize the errors in time to depth conversion, observed velocities were used for the conversion.

4.5.1.1 Seismic Resolution

The accuracy of any mapped reflections, including the BSR, is primarily limited by the vertical resolution of the seismic data. The vertical resolution is dependent on the frequency content of the data; higher source frequencies create higher seismic resolution. According to the Rayleigh criterion (Sheriff 1985) the minimum resolvable geologic layer is equal to 1/4 of the dominant wavelength of the data. Vertical Resolution (VR) is calculated using the equation:

$$VR = \frac{v}{f} \times \frac{1}{4} \qquad \text{Equation 4.24}$$

where v is the average velocity at the depth of interest and f is the frequency at the depth of interest. To determine the vertical resolution from the seafloor through to the base of the records frequency spectra were generated within Kingdom® for the 3D seismic data. The spectrum for the 3D seismic data, presented in Figure 4.20, shows the dominant frequency is approximately 37 Hz and the peak usable frequency is 70 Hz. Assuming a relatively constant dominant frequency vertically through the datasets and using the velocities from the F-09 well, the VR at the at the shallowest and deepest portions of the datasets along with the depths and velocities used are presented in Table 4.2. These calculations show beds or features less than 5 m would not be resolved on the 3D seismic data.

Table 4.2 Seismic Vertical Resolution. Depths are in metres below the seasurface.

Dataset	Dominant / Peak Frequency (Hz)	Depth (m)	Velocity (m/s)	Vertical Resolution (m)
3D Seismic	70	915	1540	5.5
	70	1960	2040	7.3

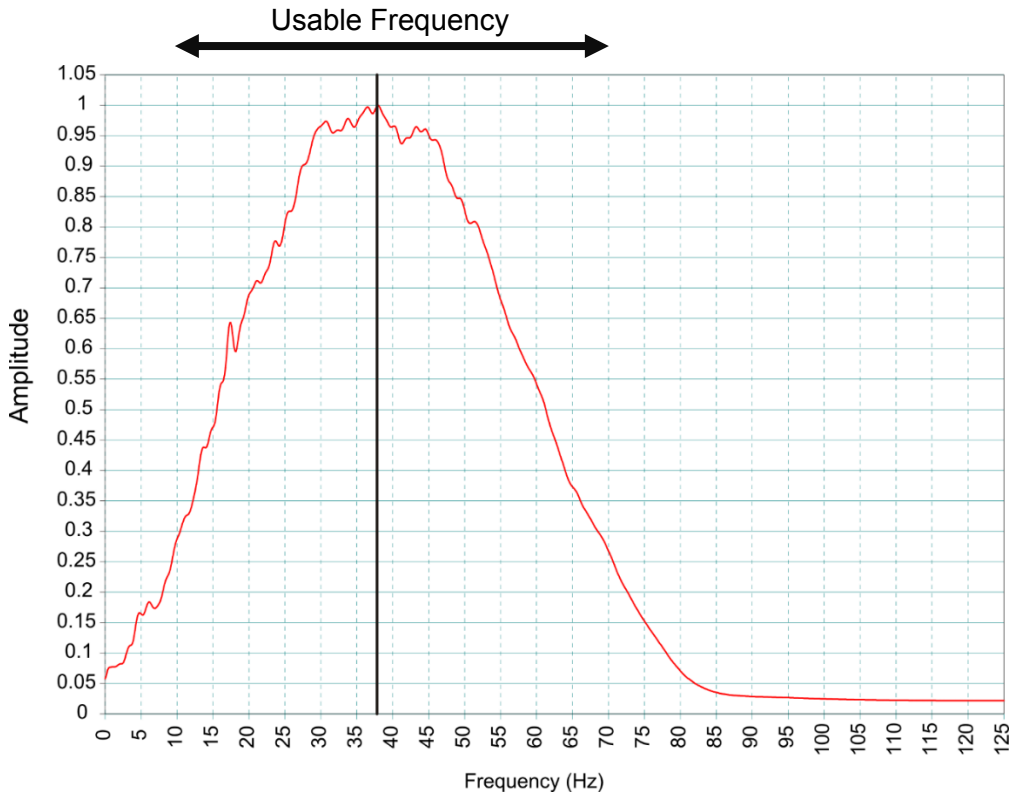

Figure 4.20 Frequency spectrum of the 3D seismic data.

The horizontal resolution of the data is dependent on the frequency of the data as well as the hydrophone array length (Mosher et al. 2006). For the 3D seismic data the spatial sampling rate or bin dimensions are greater than the minimum spatial resolution derived from the characteristics of the migrated seismic data. The 3D seismic volume was binned at 12.5 m intervals in both the x and y domains defining the minimum horizontal resolution of the data.

4.5.2 Hydrate stability error

Primary sources of error and uncertainty in the base of hydrate stability calculations include errors in the gas composition used to determine the hydrate phase equilibrium, errors in seafloor temperature and geothermal gradient as well as invalidity of the assumption that the geothermal gradient is constant in the shallow sediments. These internal, systematic errors affect the accuracy of the calculations. Sensitivity analyses are typically used to assess the uncertainty of hydrate stability calculations (Wood and Jung 2008, and León et al. 2009). Results of the sensitivity analysis show

errors in the geothermal gradient have a greater effect on the stability depths than errors in seafloor temperature do. Pore water salinity variations, which reflect those observed in seawater globally, have limited effect on the final base of hydrate stability depths. Details of the sensitivity analysis are presented in the results chapter.

4.5.3 Well Logs

The resolution of the well logs are on the order of 20cm. Errors in downhole positioning become insignificant given the much lower resolution of the seismic data. For this study it is not possible to quantify the error associated with the downhole positions. Although difficult to quantify, borehole conditions such as caving may produce false spikes in the sonic log that impact seismic to well correlations.

4.5.4 Gas and Hydrate Saturations

Errors in hydrate saturation calculations are primarily associated with inaccuracy of the porosity function. Sensitivity analyses were undertaken to assess the uncertainty associated with the porosity function. The results of the sensitivity analysis are included in the results chapter.

CHAPTER FIVE: RESULTS

Three bottom simulating reflectors (BSRs) and nine stratigraphic horizons were interpreted on the 3D seismic volume (Figure 5.1). Seismic attributes extracted along the nine regionally correlative stratigraphic horizons aided in characterizing the BSR and its surrounding sediments. Through correlation to available exploration wells, four depositional units that characterize important changes in the stratigraphic evolution of Sackville Spur and northern Flemish Pass were identified on the seismic volume. The BSRs were compared to calculated base of hydrate stability depths. Estimates of free gas and hydrate concentrations were made using velocity data from the F-09 exploration well.

5.1 SEISMIC INTERPRETATION

The stratigraphic succession in the study area is dominated by drift deposits and mass transport deposits (MTDs) (Campbell, et al. 2002). The drift deposits that make up the Sackville Spur and the eastern flank of Flemish Pass are generally characterized on the 3D seismic profiles by a series of well defined, continuous yet divergent reflections (Figure 5.1). Below the base of Flemish Pass are stacked packages of chaotic reflections that represent MTDs (Figure 5.1). Three BSRs crosscut the drift deposits below Sackville Spur (Figure 5.1). Reflection and correlation confidence diminish towards the floor of Flemish Pass making it difficult to trace all horizons from Sackville Spur through the Pass and into the deposits on the eastern flank of the Pass.

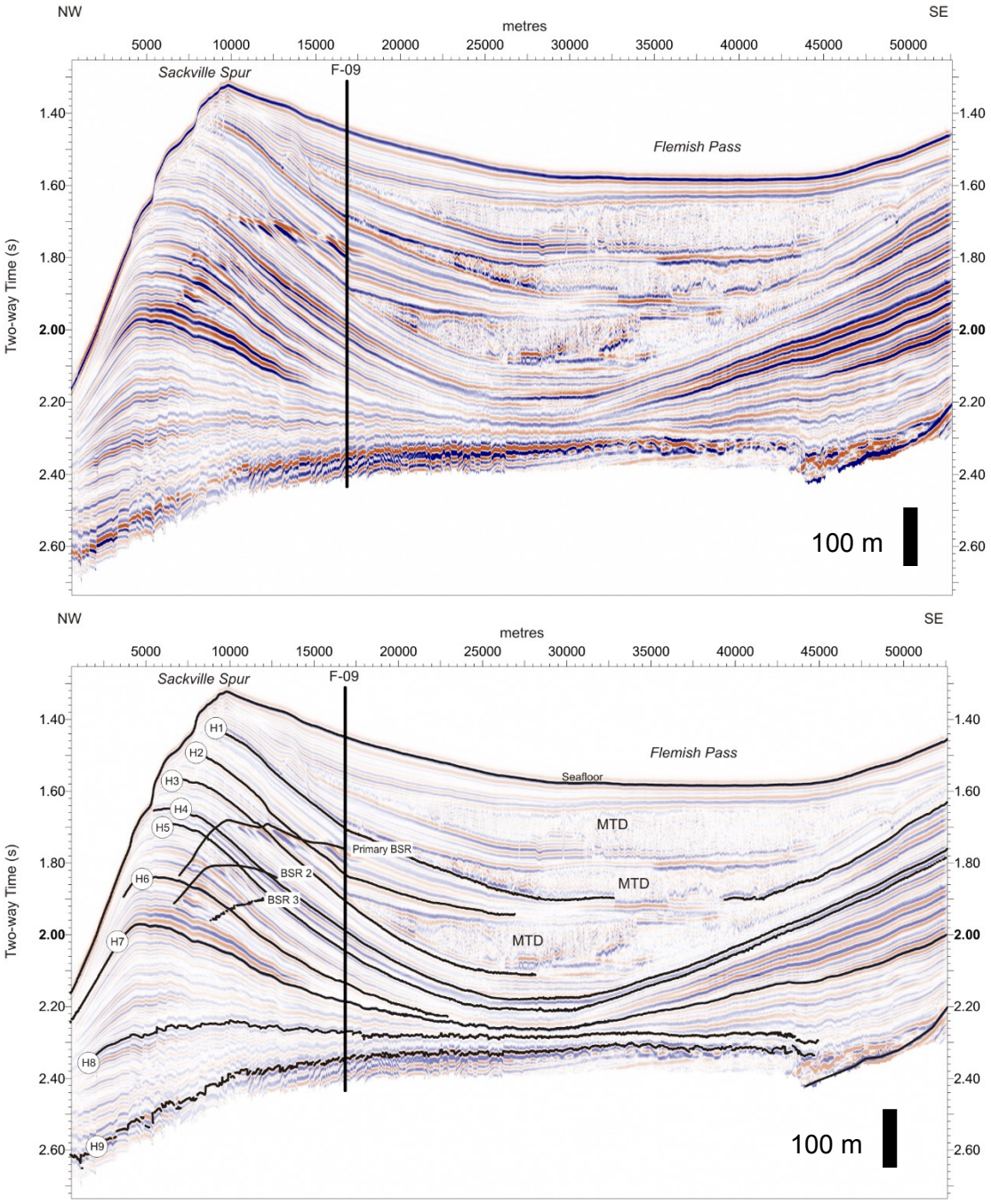

Figure 5.1 A typical dip seismic profile through the F-09 well extracted from the Baynord 3D seismic volume showing the various horizons discussed in the text. The uninterpreted profile is presented above and the interpreted profile below. MTD indicates a unit interpreted to be a mass transport deposit.

5.1.1 Bottom Simulating Reflectors

A total of three BSRs were interpreted from the 3D seismic volume (Figure 5.2). The most prominent BSR, herein referred to as the primary BSR, is the shallowest, most

extensive BSR and is well imaged on the 3D seismic data. The second and third BSRs are progressively deeper, significantly less extensive than the Primary BSR, and poorly imaged on the 3D seismic volume (Figure 5.2).

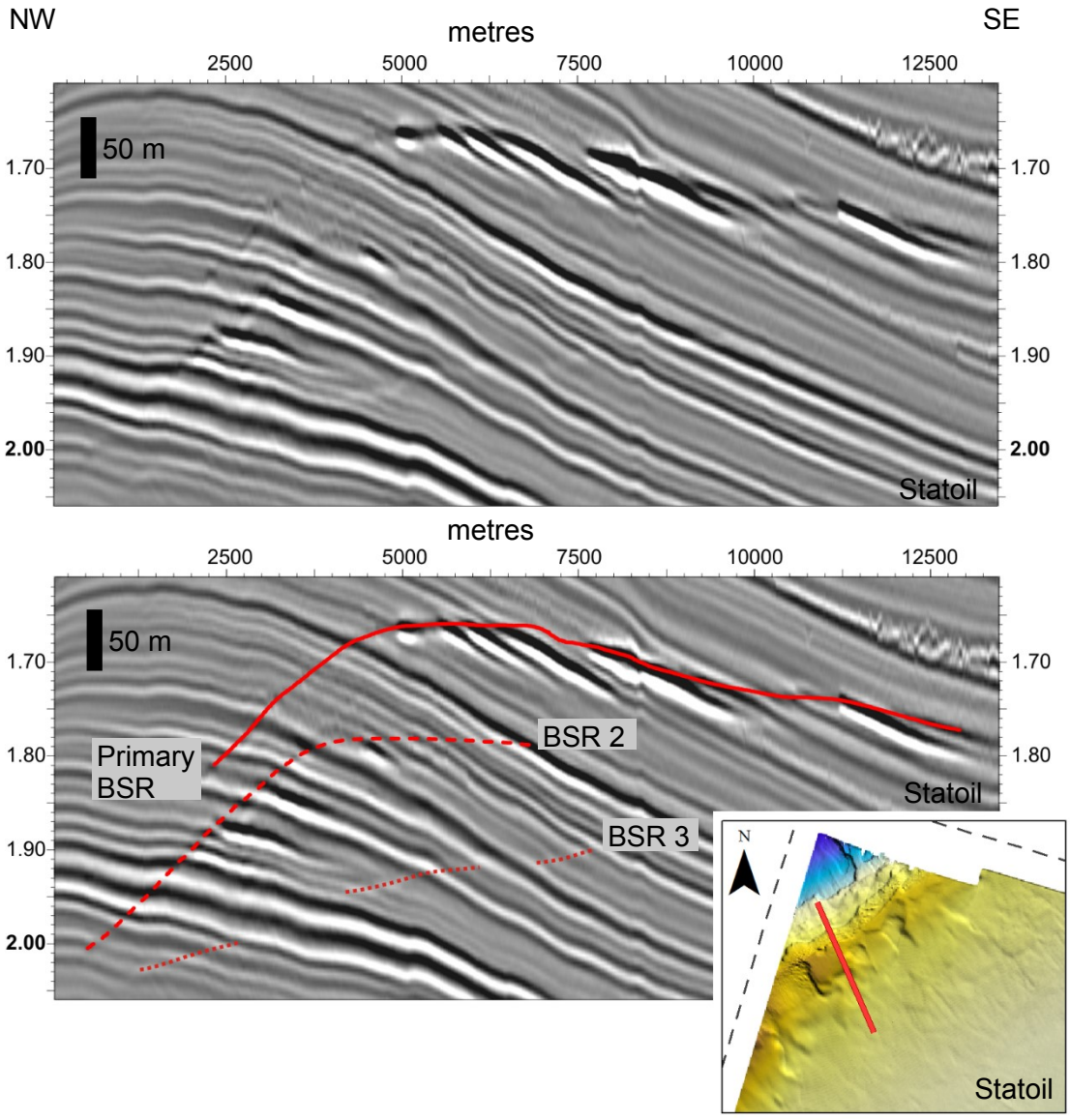

Figure 5.2 Uninterpreted and interpreted arbitrary seismic line through the three BSRs.Inset map shows the profile location in the northwest corner of the 3D seismic volume overlain on the seafloor depths. Vertical units are two-way time in seconds.

5.1.1.1 Primary BSR

The primary BSR, where best developed, is characteristic by a series of abruptly terminated, dipping, high amplitude (Figure 5.2), phase reversed (Figure 5.3) reflections. Elsewhere, particularly north of the spur's crest, the primary BSR is a more continuous

event defined by low amplitudes with no obvious phase change (Figure 5.2). Following the classification scheme of Shedd et al. (2009), the primary BSR is segmented with a shingled appearance like the BSR on Walker Ridge in the Gulf of Mexico (McConnell and Kendall, 2002). The primary BSR covers an area of ~350 km^2 in the northwest quadrant of the 3D seismic volume beneath the Sackville Spur. As outlined in the methods section, two horizons were interpreted for the primary BSR:

1. A horizon that snaps to the high amplitude reflections defining the BSR, referred to in the text as the “snapped BSR”.
2. A manually interpreted horizon that connects the tops of the high amplitude reflections that define the BSR to make a smooth continuous surface, referred to in the text as the “manual BSR”.

The segmented structure of the snapped BSR is readily apparent on the depth structure map of Figure 5.4 and the relative amplitude map of Figure 5.5. Gaps in the snapped BSR surface represent areas where the primary BSR is not apparent. The primary BSR is most continuous below the crest of the Sackville Spur where amplitudes along the BSR are highest (Figure 5.5). North of the Spur’s crest the BSR is apparent but is not well defined (Figure 5.6). The elevated amplitudes, which are concentrated along specific stratigraphic beds or segments, occur down-dip of the Spur’s crest and occur in three NE-SW trending bands. The middle band of high amplitudes corresponds to a package of chaotic reflections that result from an MTD (Figure 5.6). The primary BSR also intersects an overlying MTD through its south-central portion (Figure 5.5).The three NE-SW trending bands of high amplitude reflections are associated with reduced instantaneous frequencies (Figure 5.7) and more subtly, with negative instantaneous phases (Figure 5.8). These subtle changes are more apparent on the seismic profiles where the BSR reflection broadens and narrows as it moves into the areas of highest amplitude (Figure 5.6). Pockmarks downdip of the Spur’s crest are visible on the dip of maximum similarity surface (Figure 5.9).

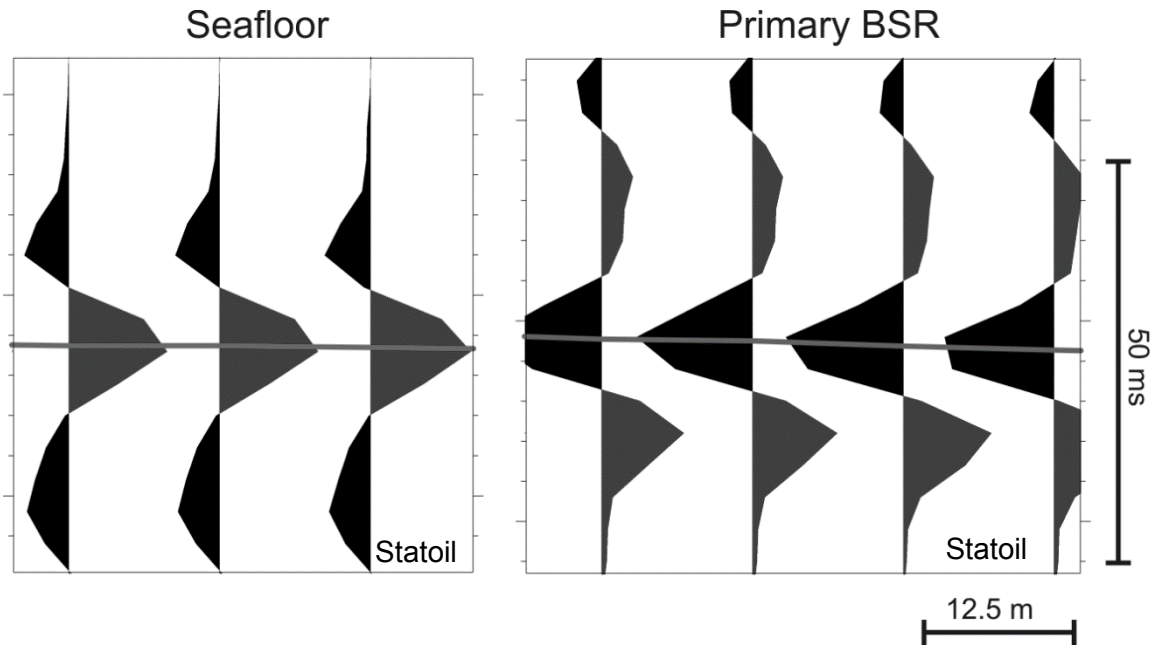

Figure 5.3 A comparison of seismic traces extracted from the Baynord seismic volume along the seafloor and the Primary BSR showing the distinct phase reversal of the Primary BSR.

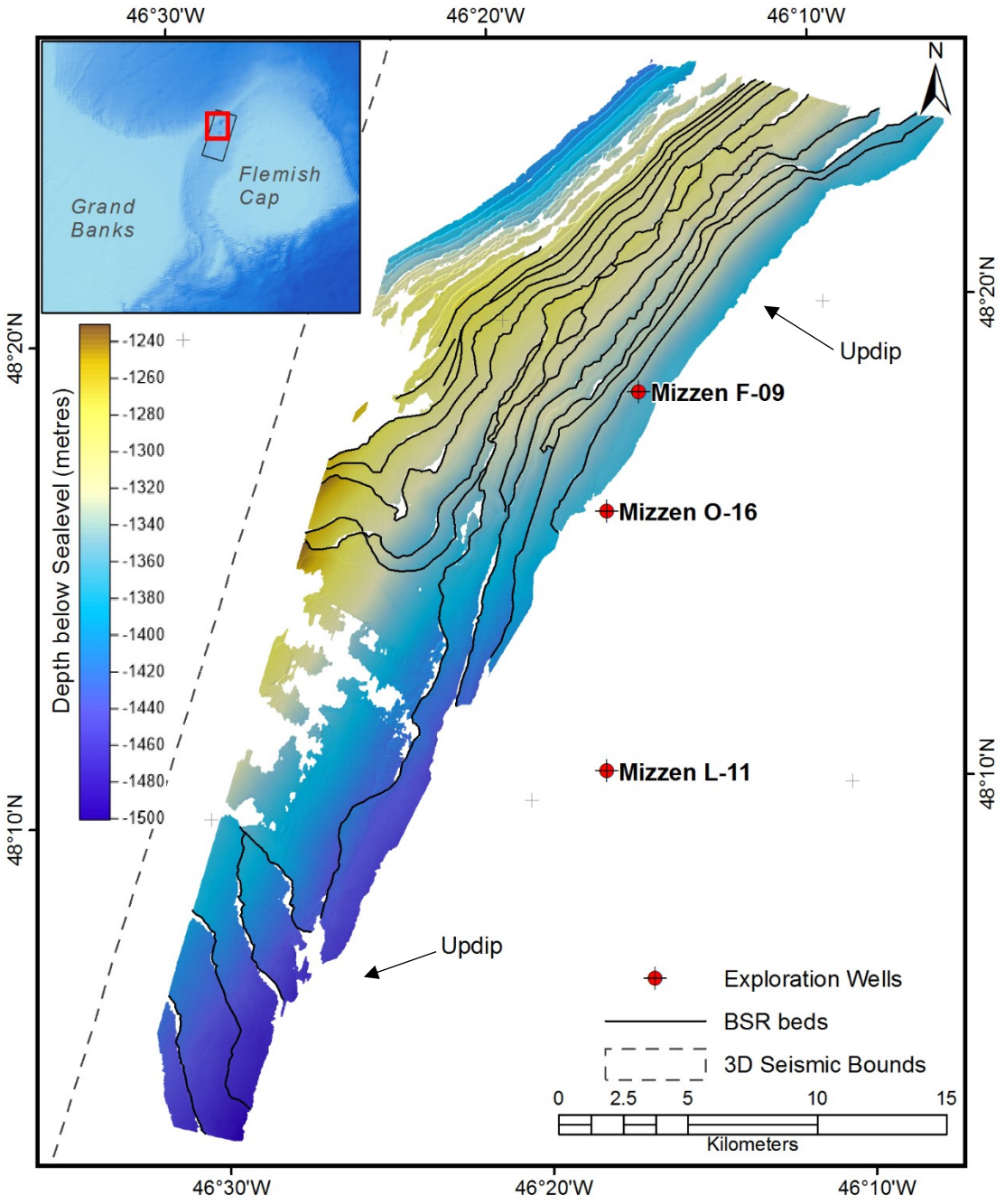

Figure 5.4 Depth structure along the snapped Primary BSR showing the BSR's segmented structure.

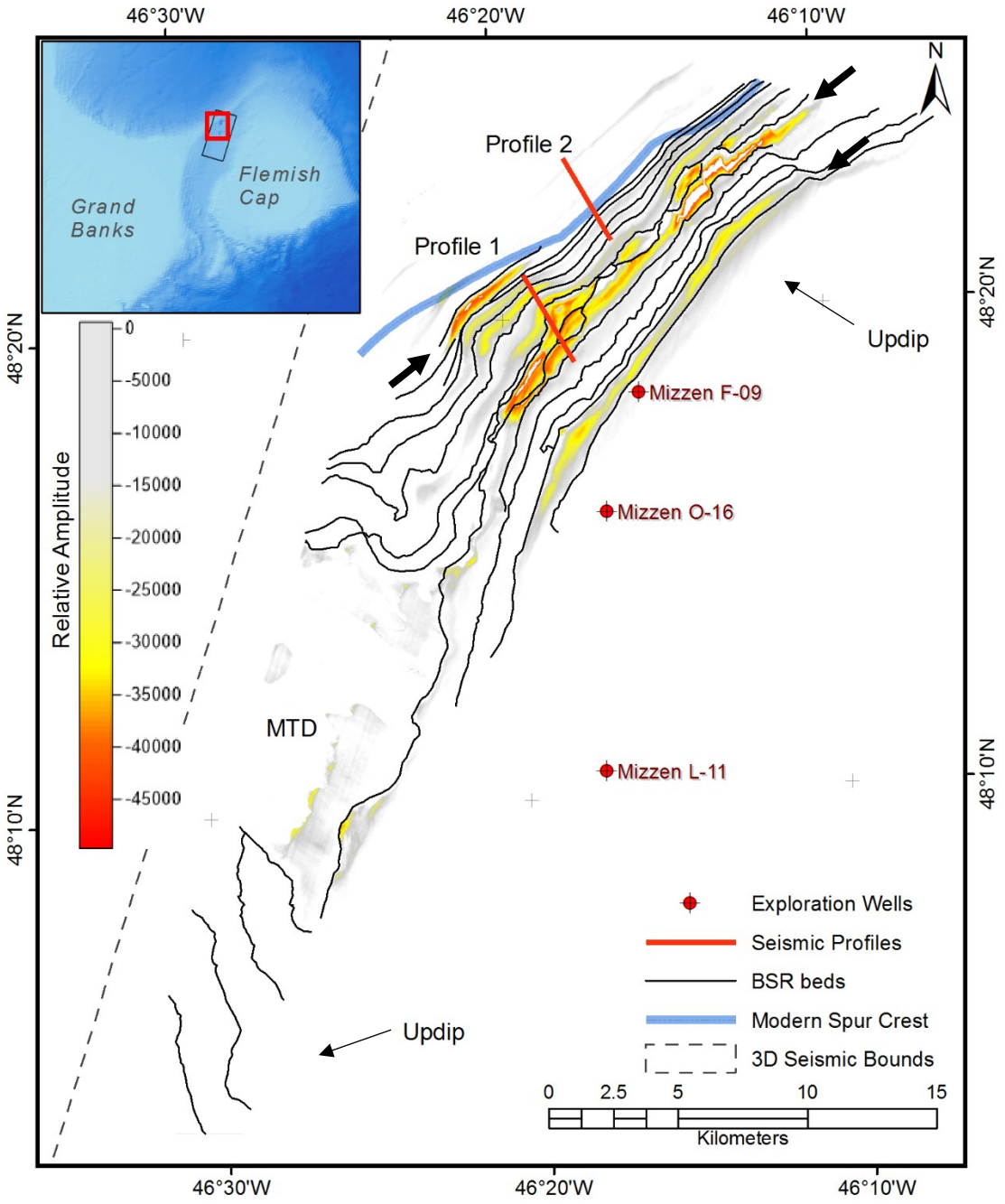

Figure 5.5 Relative amplitudes along the snapped Primary BSR surface with profile locations for Figure 5.6. The black arrows identify the three bands of high amplitudes referred to in the text.

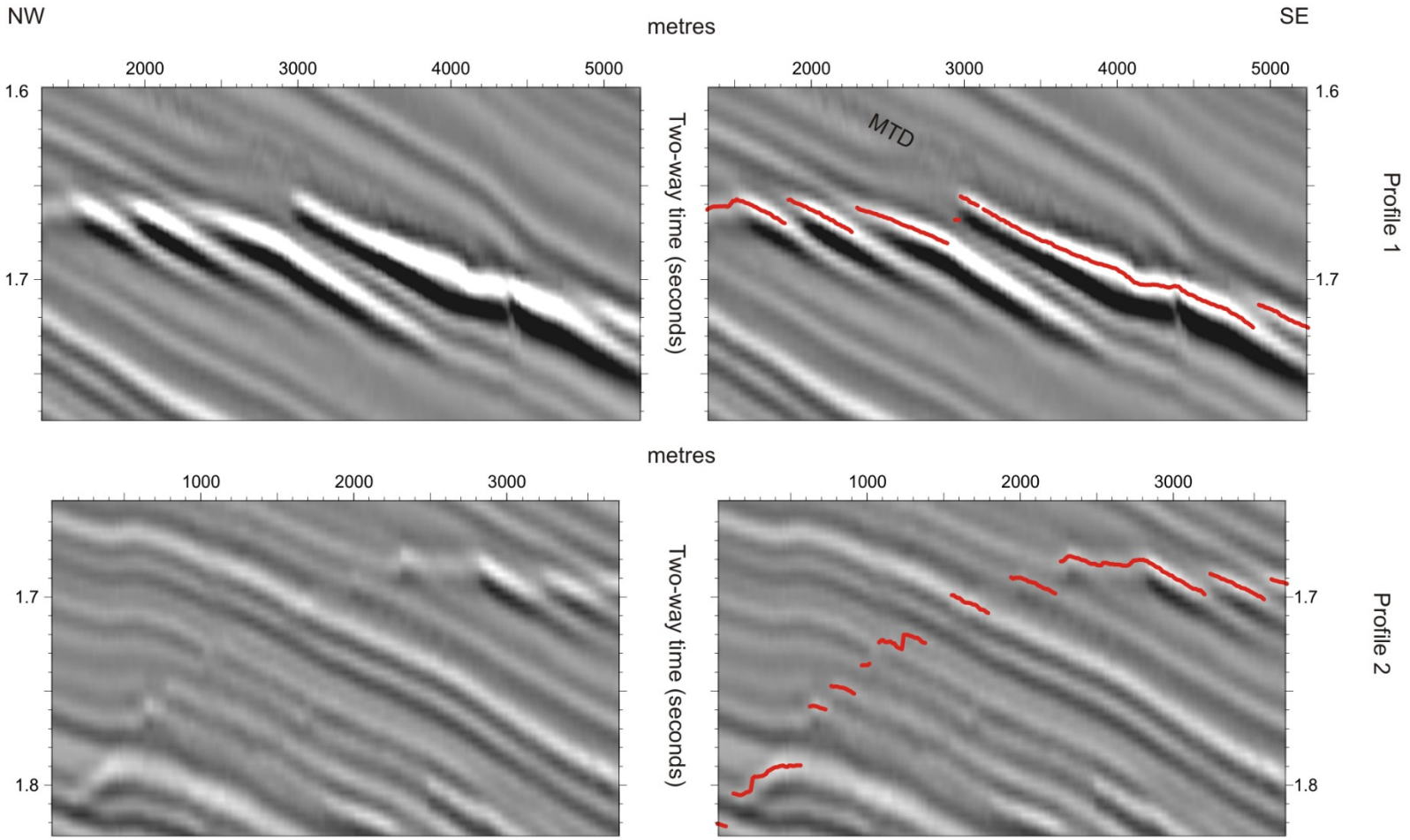

Figure 5.6 Uninterpreted (left) and interpreted (right) seismic profiles through the Primary BSR. The change in the shape of the high amplitude reflections that define the BSR and the BSR's intersection with an MTD are shown in Profile 1. Profile 2 shows how north of the Sackville Spur's crest the BSR is poorly developed. Refer to Figure 5.5 for profile locations.

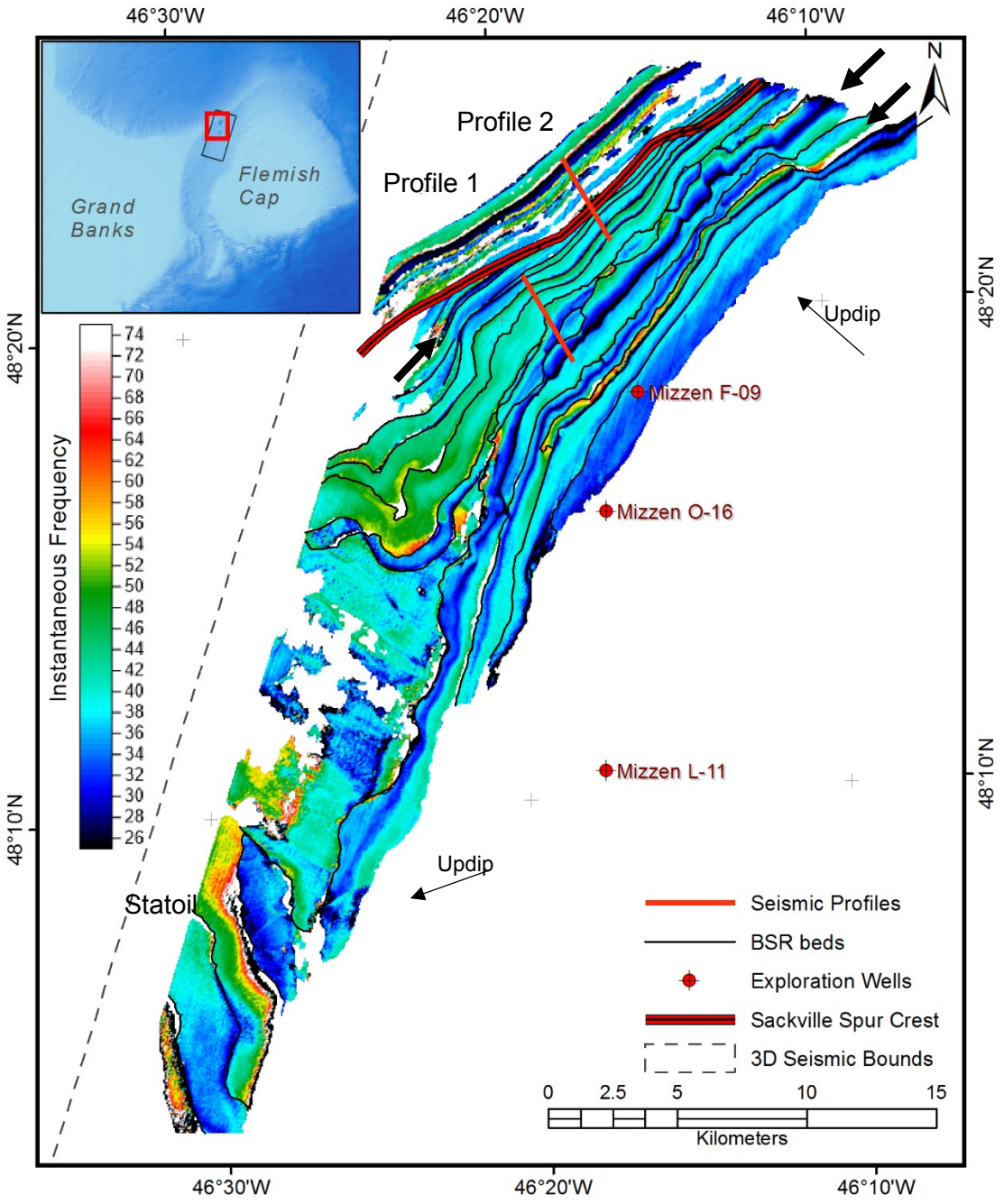

Figure 5.7 Instantaneous frequency along the snapped Primary BSR with profile locations for **Figure 5.6**. The black arrows identify the three bands of high amplitudes referred to in the text.

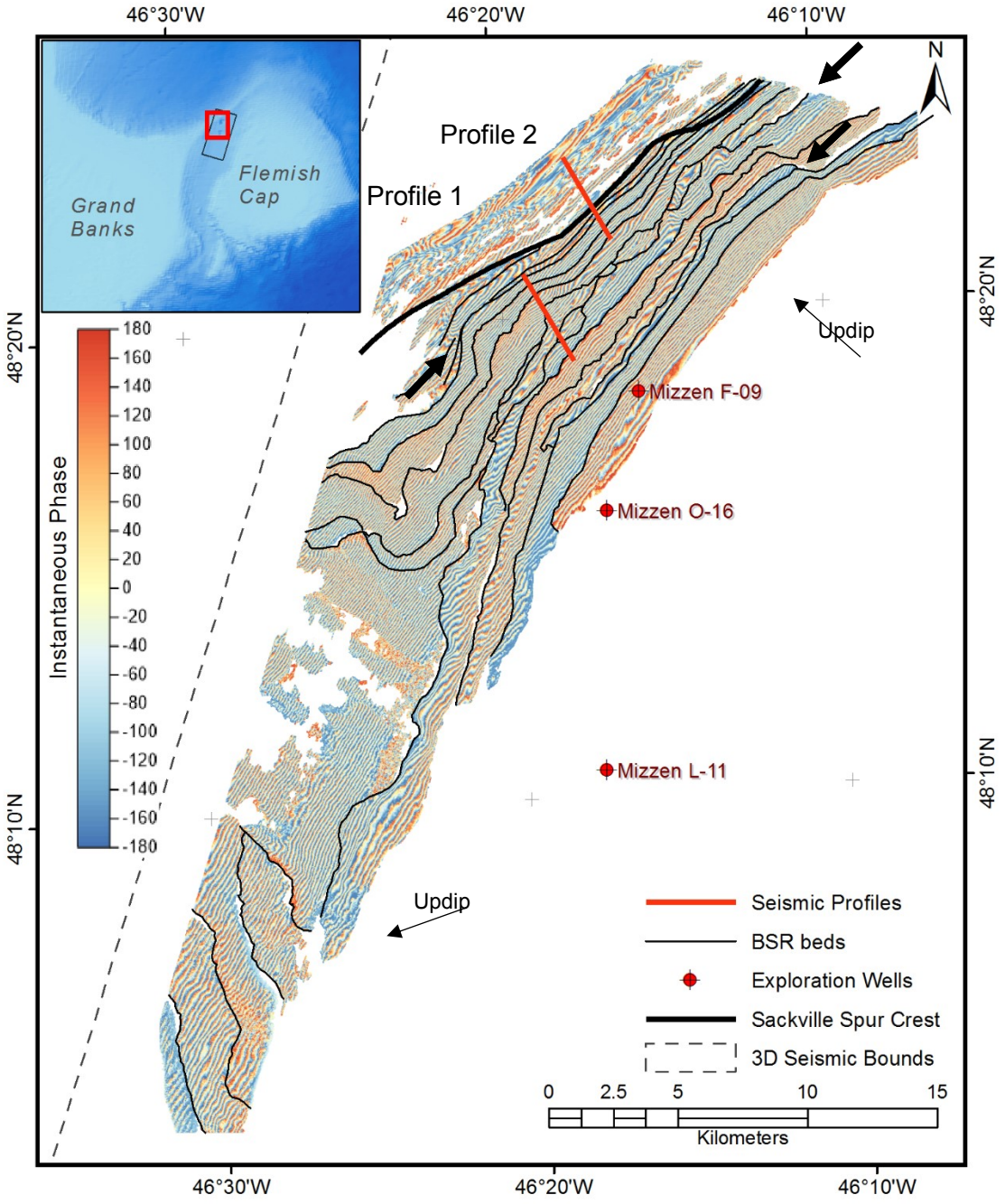

Figure 5.8 Instantaneous phase along the snapped Primary BSR with profile locations for Figure 5.6. The black arrows identify the three bands of high amplitudes referred to in the text.

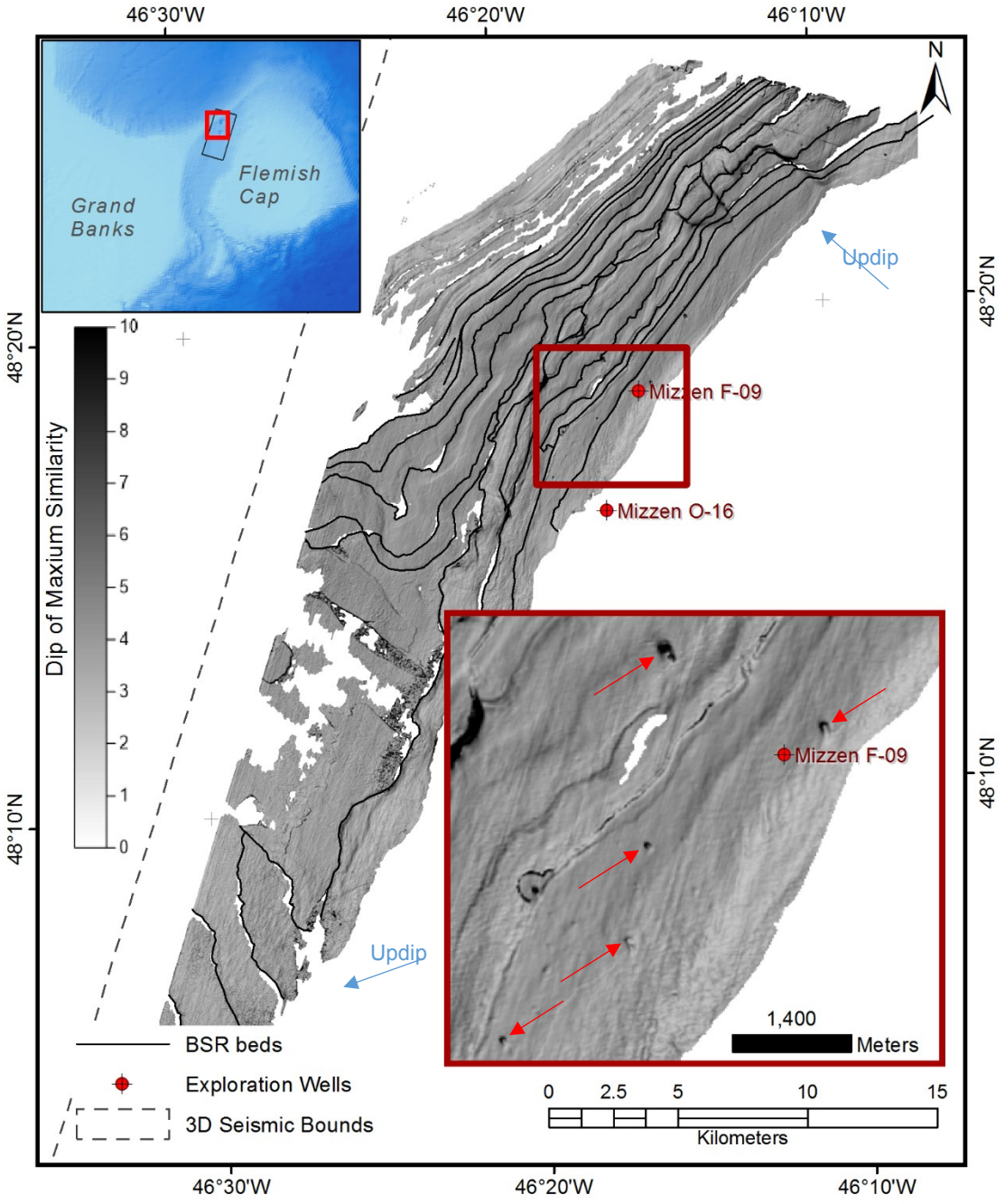

Figure 5.9 Dip of maximum similarity along the snapped primary BSR. Red arrows identify pockmarks in the zoomed inset.

The manual BSR surface was generated to allow comparison with other surfaces as well as to allow for the generation of an isopach map that is free from the segmented

structure present on the snapped BSR surface (Figure 5.10). A continuous surface is better for comparison with the theoretical base of the hydrate stability zone. Seafloor isobaths, which are overlain on the manual BSR depth structure map of Figure 5.10, have the same regional morphological trend as that of the primary BSR. The seafloor to primary BSR isopach highlights the areas of discordance between the seafloor and the primary BSR (Figure 5.11). If the primary BSR followed the seafloor exactly the isopach would have a consistent thickness, which is not the case. Instead, north of the modern Sackville Spur crest the primary BSR is 260 m (307 ms) below the seafloor in 1065 m of water while on the northwest flank of the Spur the primary BSR is 348 m (400 ms) below the seafloor in a water depth of 991 m.

Arbitrary 3D seismic profiles that intersect the BSR show the BSR structure represents a smoothed version of the seafloor shape (Figure 5.12). In the vicinity of the F-09 well, the seafloor gradients are greater than those along the BSR, resulting in the thinning of the isopach (Profile 2 of Figure 5.12). Conversely, seafloor gradients in the BSR's southwestern reaches are less than those along the underlying BSR. This change leads to divergence between the seafloor and BSR horizons resulting in thickening of the isopach (Profile 1 of Figure 5.12).

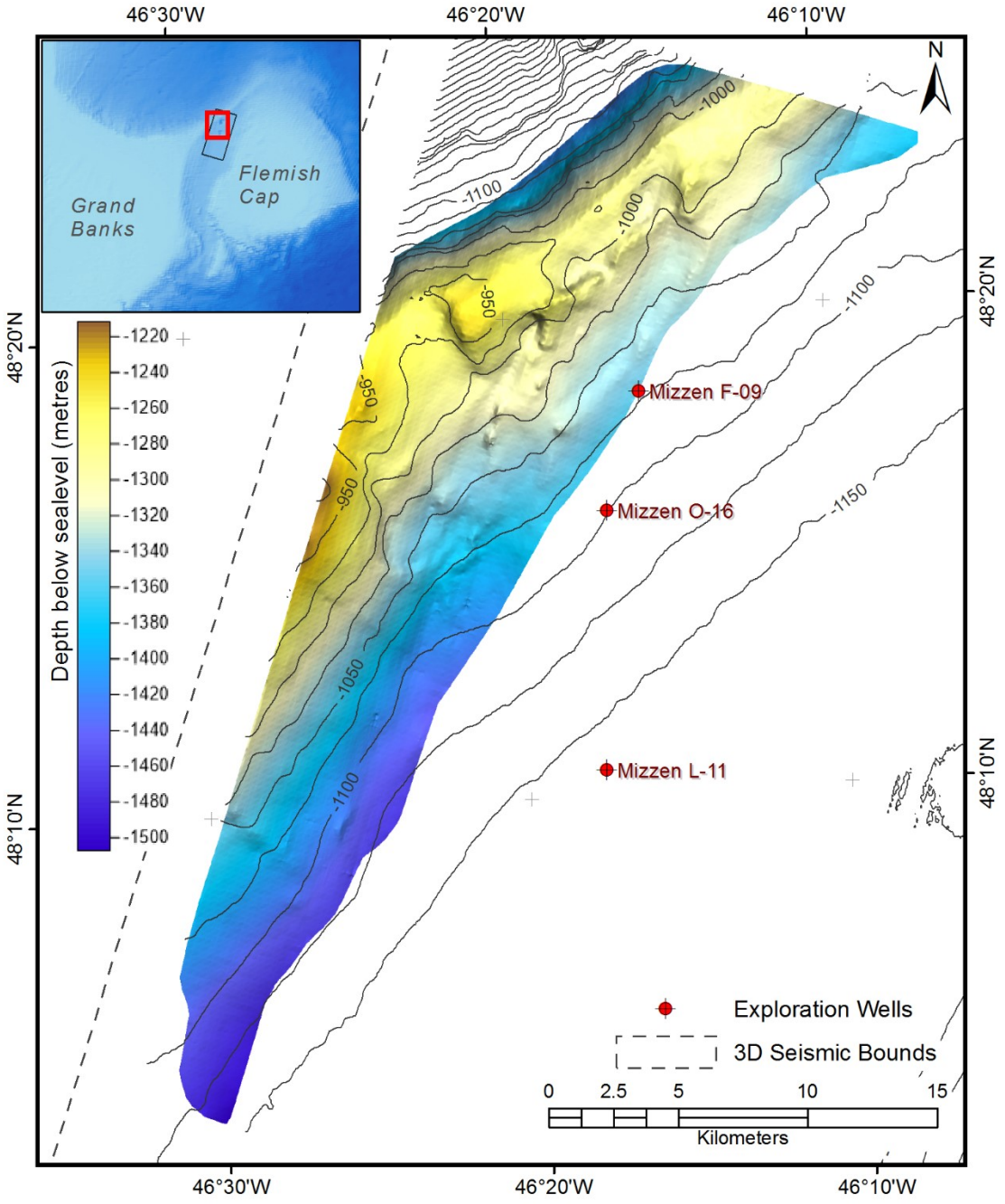

Figure 5.10 Depth structure along the manually interpreted Primary BSR with seafloor depth isobaths overlain.

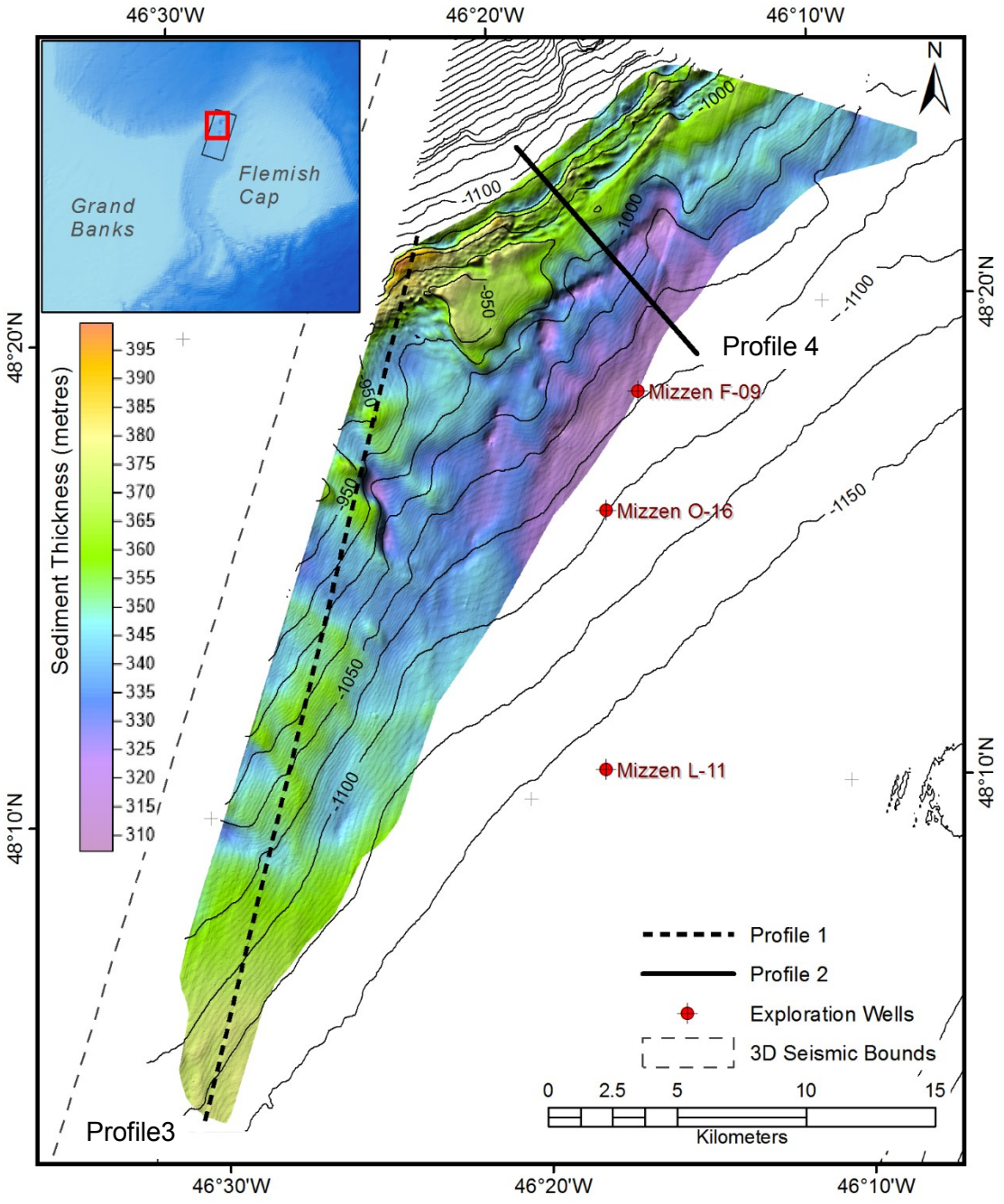

Figure 5.11 Isopach (sediment thickness) between the seafloor and the primary BSR with seafloor with isobaths overlain. Arbitrary seismic profiles 3 and 4 are presented below in Figure 5.12.

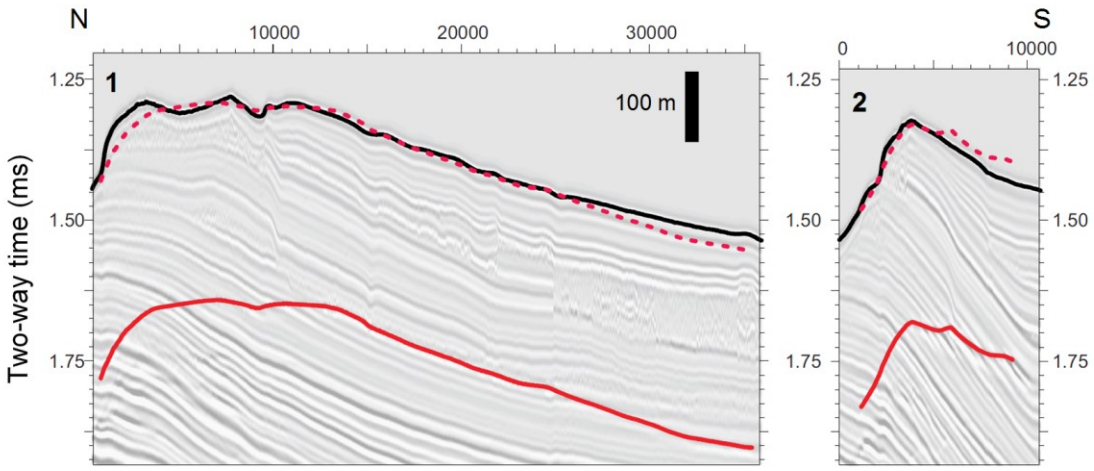

Figure 5.12 Arbitrary seismic profiles 3 (left) and 4 (right) (see Figure 5.11) comparing the manual BSR shape to that of the seafloor. The deeper solid lower red line and the upper solid black line trace the primary BSR and the seafloor, respectively. The primary BSR minus 350ms (dashed red line) allows detailed comparison between the seafloor and BSR structures. Horizontal scale in metres along line.

5.1.1.2 Deeper BSRs

The two BSRs that underlie the primary BSR are herein referred to as BSR 2 and BSR 3 (Figure 5.1). BSR 2 is present below the NW flank of Sackville Spur covering an area of ~95 km^2. It is deepest below the northern flank of the Spur measuring 464 m (513 ms) beneath the seabed in 1223 m of water. This BSR is shallowest on its eastern edge below the southern flank of the Spur where it occurs 348 m (398 ms) below the 1080 m deep seafloor.

BSR 2 was manually interpreted on seismic profiles where it is characterized by the termination of phase reversed, high amplitude reflections (Figure 5.2). The second BSR generally follows the shape of the seafloor in the west but becomes increasingly discordant in the east (Figure 5.13). In this area of discordance, the BSR becomes increasingly difficult to recognise. Amplitudes along this BSR are significantly lower than those observed along the primary BSR. Areas where the secondary BSR is best developed (i.e. has consistently elevated amplitudes), correspond well with reduced amplitudes and hence reduced continuity along the overlying primary BSR.

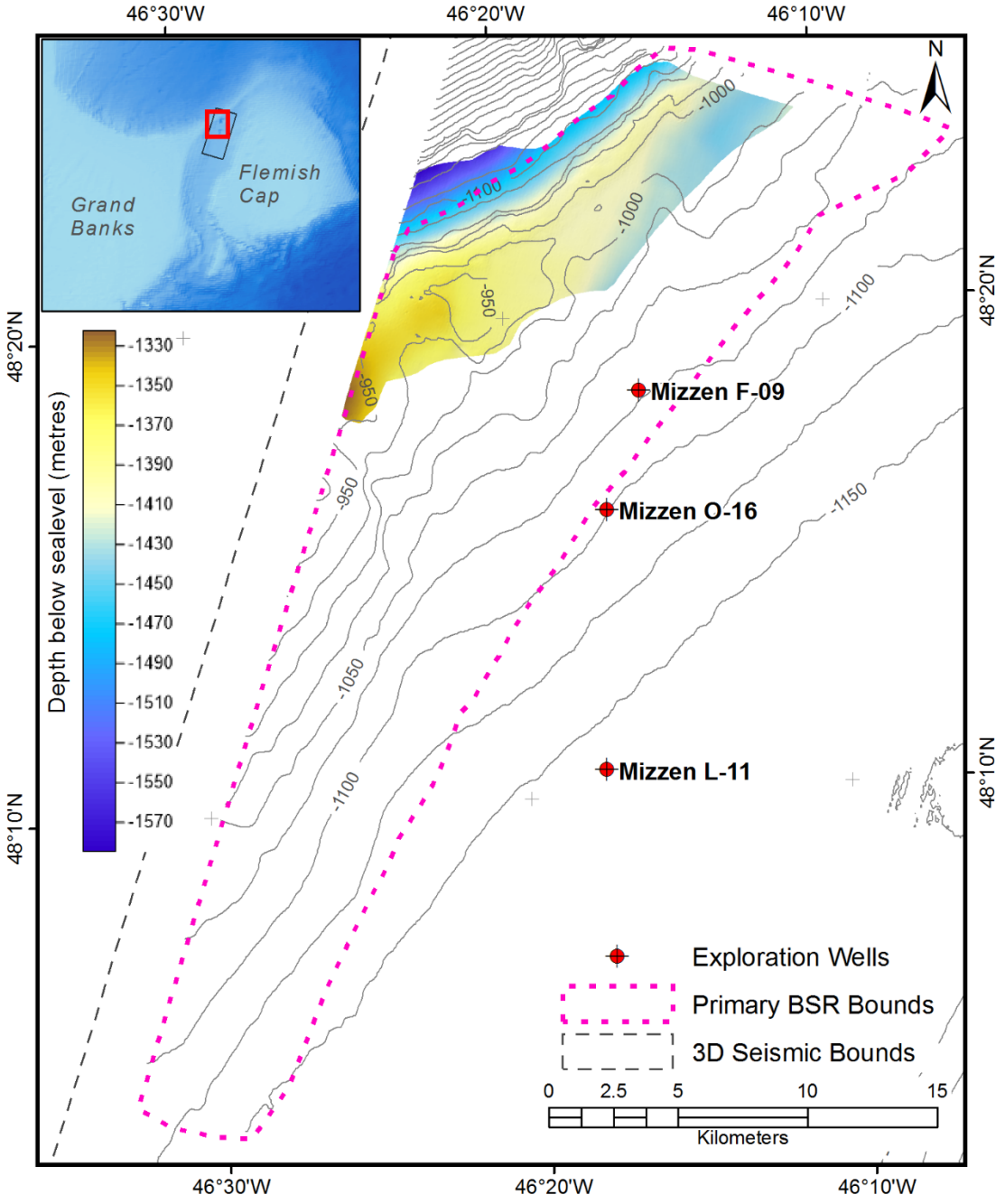

Figure 5.13 Depth structure along BSR 2 with water depth contours overlain.

BSR 3, which is the deepest BSR, is the least continuous of the three BSRs. This poorly imaged BSR covers an area of ~80 km^2. BSR3 is between 424 m (478 ms) and 640 m (688 ms) below the seafloor in 1059 m and 938 m of water, respectively. Unlike

the other two BSRs, BSR 3 is defined by a subtle positive amplitude event that crosscuts stratigraphy (Figure 5.2). BSR 3 is absent or obscured along a NE-SW trending band, in an area of high amplitude reflections. The third BSR forms a gently sloping surface that does not parallel the modern seafloor.

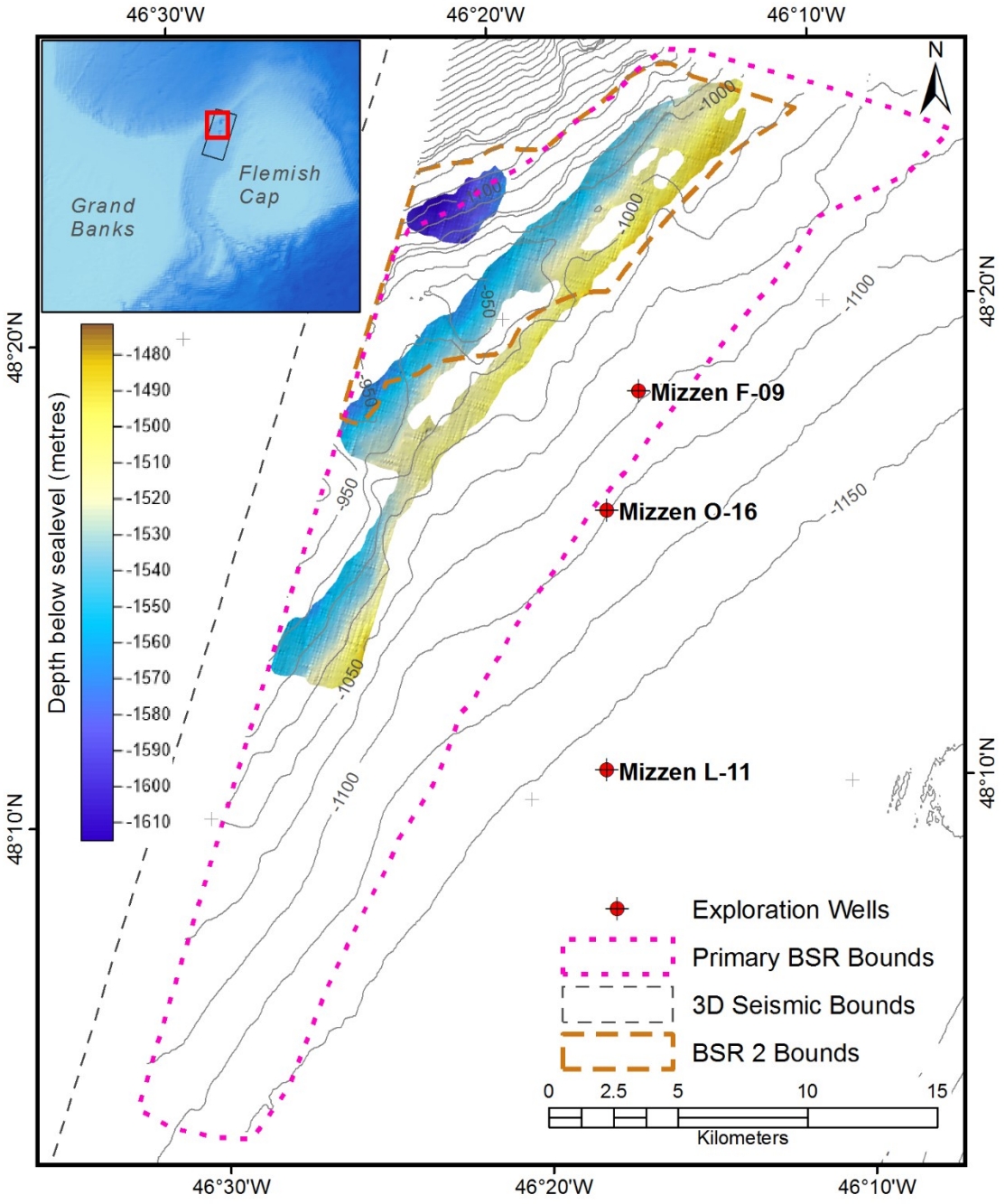

Figure 5.14 Depth structure along BSR 3 with seafloor isobaths overlain. The areal extents of the Primary BSR and BSR 2 are included for comparison.

5.1.2 Stratigraphic Horizons

A total of nine regionally correlative stratigraphic horizons were interpreted on the Baynord 3D seismic volume to both characterize the sediments over and underlying the BSR and to understand the stratigraphic setting of the BSR. The depth structure and seismic attributes for each horizon are described below, beginning with the deepest H9 Horizon.

5.1.2.1 Horizon H9

The basal H9 reflection is interpreted along a high amplitude trough and represents the deepest continuous reflection interpreted from the 3D seismic volume. Upon comparison with seafloor traces, H9's phase is opposite to that of the seafloor (Figure 5.15). This phase difference is also modelled on the synthetic seismogram (see arrow on Figure 4.10). In most places H9 appears conformable with underlying strata but the limited seismic data below H9 make this relationship difficult to assess, except in the south where H9 clearly truncates underlying horizons (Figure 5.16). The horizon is present throughout the dataset except along the southeastern edge of the study area where it onlaps a basement high (Figure 5.1).

The H9 depth structure map shows a broad ridge (~20 km wide) underlying the present day Flemish Pass (Figure 5.17). Subtle, ripple-like ridges occur over the northeastern portion of the survey (Figure 5.17, and Figure 5.18). The ridges trend NW-SE in the north and become curvilinear in the southwest with the crests having an increasingly E-W strike. The ridges have wavelengths on the order of 550 m to 950 m, increasing from north to south and although variable, the relief along the ridges is typically 15-20 m (Figure 5.18B). The H9 horizon is moated adjacent to the onlapped basement high in the SE (Figure 5.16B).

The depth structure, amplitude and dip of maximum similarity maps, (Figure 5.17, Figure 5.19, and Figure 5.20 respectively) show a robust fault pattern over much of the H9 surface. The faults are best represented on the H9 dip of maximum similarity surface where they are closely spaced and orthogonal over much of the NW portion of the survey. In this area, the fault pattern is described as long bands of NNE-SSW trending faults connected by much shorter orthogonal faults (Figure 5.20). The trend of these faults does not match the orientation of the Sackville Spur crest. In the northeast, the faults become less regular, more broadly spaced, and are eventually replaced by the ridges discussed

above (Figure 5.18C). Over the central and southern portions of the 3D seismic area, the faults become polygonal. In the SW the polygons become large, ~3 km across, while in the SE in the moated area the polygons are much smaller, ~400 m (Figure 5.20). The seismic sections show the vertical offsets along the faults are small throughout the study area ranging from 5-20 m (Figure 5.18A).

The H9 instantaneous frequency map is relatively uniform with elevated values in the SE corner of the study area and in the area of ridge development (Figure 5.21). Frequencies are slightly reduced below the northern flank of the Sackville Spur roughly corresponding to the area of reduced amplitudes along the horizon (Figure 5.16B). This area also corresponds to a subtle instantaneous phase change to more positive phases along the H9 horizon (Figure 5.22). Interestingly, the trend of this zone of reduced amplitudes, instantaneous phase and phase changes parallels the crest of the Sackville Spur. A package of high amplitude reflections, the base of which is defined by the H7 Horizon (see Section 5.1.2.3), overlies this area and may create a frequency and amplitude shadow along the H9 horizon Figure 5.16A). Instantaneous frequencies are also reduced in the south (Figure 5.21) where the traces have more positive instantaneous phase values (Figure 5.22). This area corresponds on seismic profiles to where H9 merges with an underlying high amplitude reflection (Figure 5.16B).

Amplitudes along the H9 horizon are greatest through the central portion of the 3D seismic volume area (Figure 5.19). Isolated areas of high amplitudes occur along the horizon's eastern edge where it onlaps an underlying high amplitude reflection (Figure 5.19). In this area, elevated amplitudes likely result from constructive interference as multiple horizons pinch out against the basement high. Amplitudes are lowest in the southern portion of the study area, in the NE where the ridges are observed, and below the Sackville Spur along a band oriented parallel to the crest of the Spur (Figure 5.19).

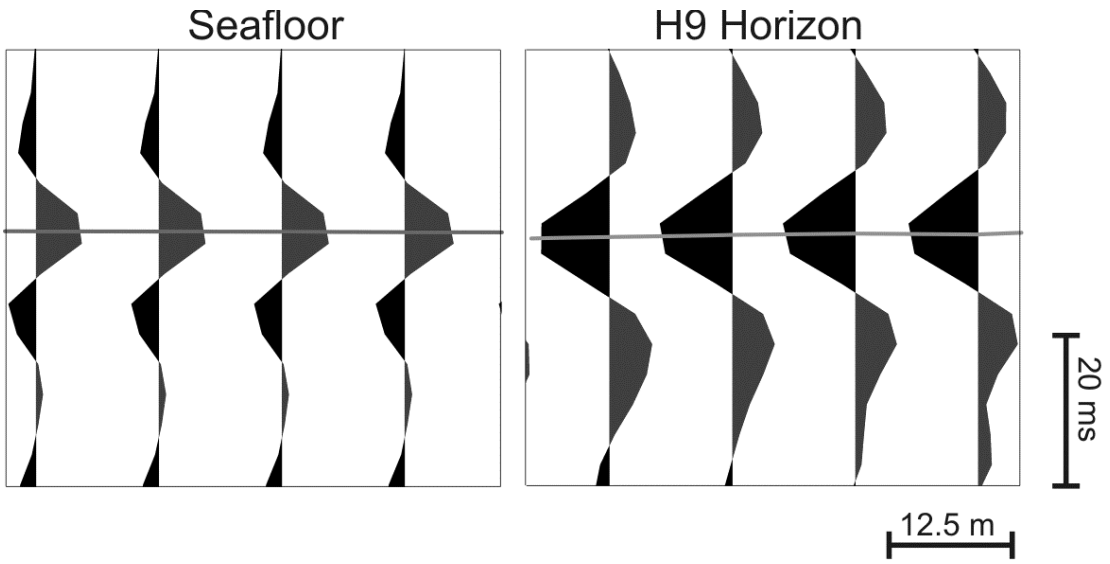

Figure 5.15 A comparison of seismic traces from along the seafloor and H9 Horizon.

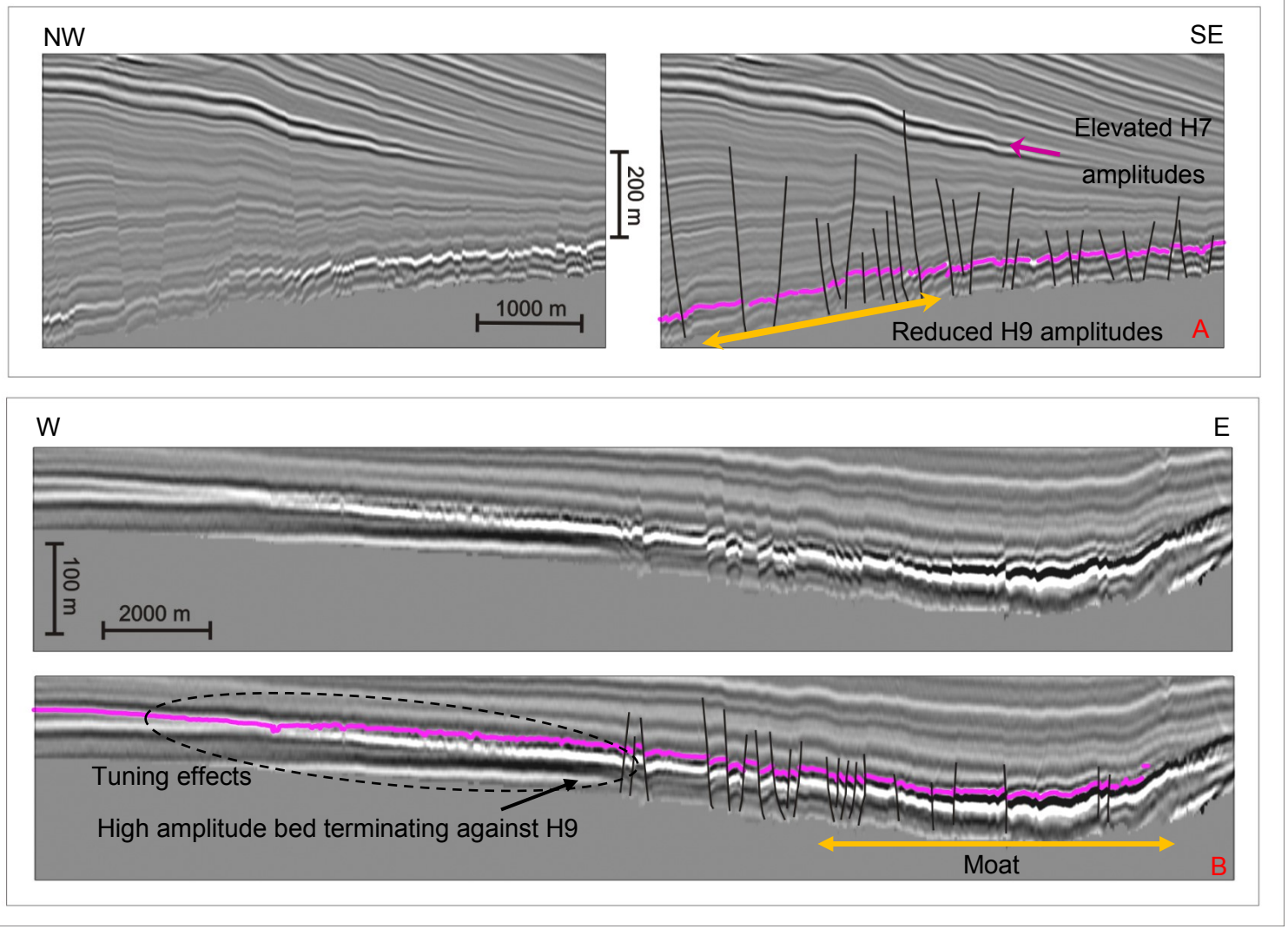

Figure 5.16 Uninterpreted and interpreted arbitrary seismic profiles from the 3D volume. Refer to the text for a discussion on these profiles

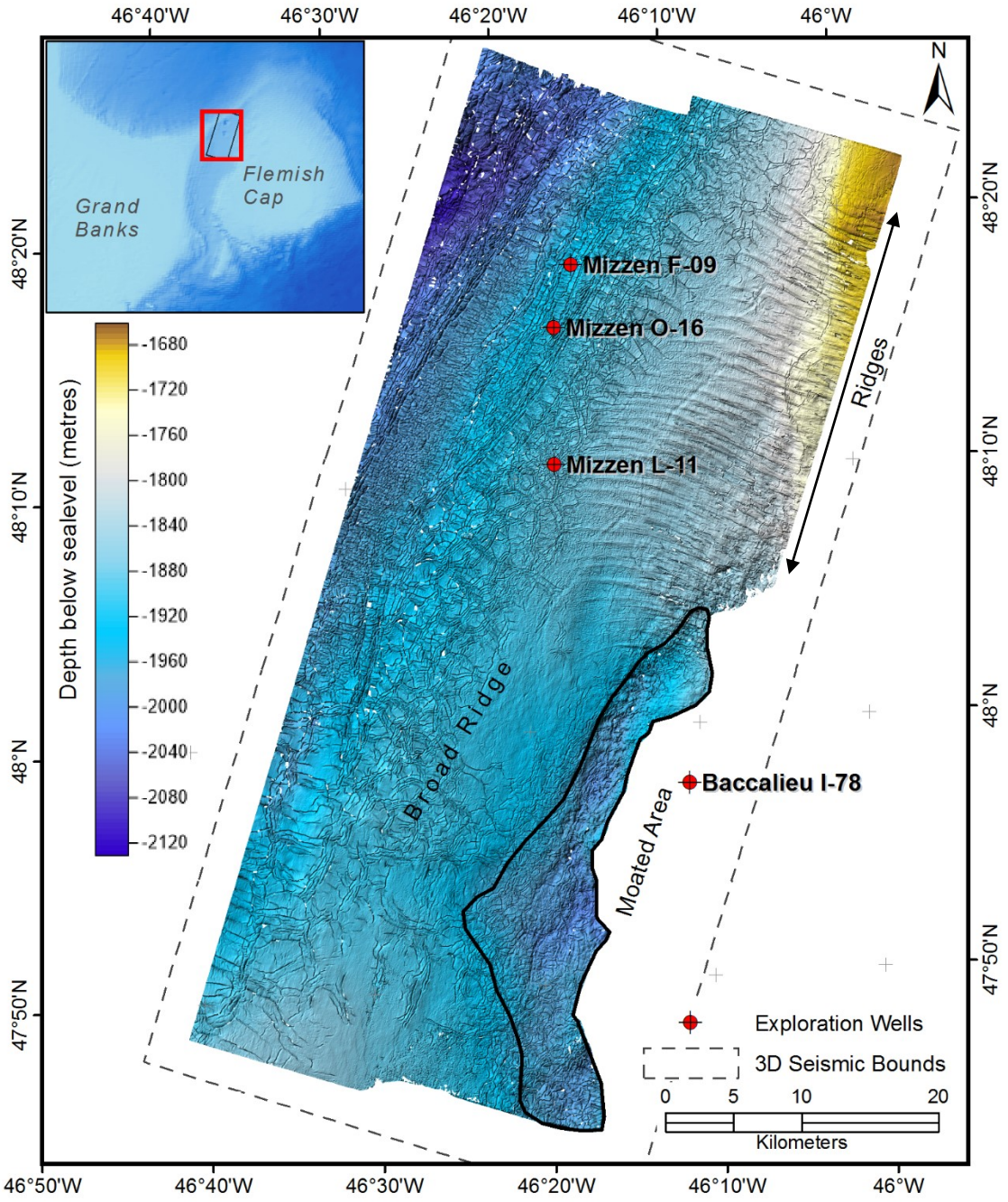

Figure 5.17 Depth structure along the H9 horizon.

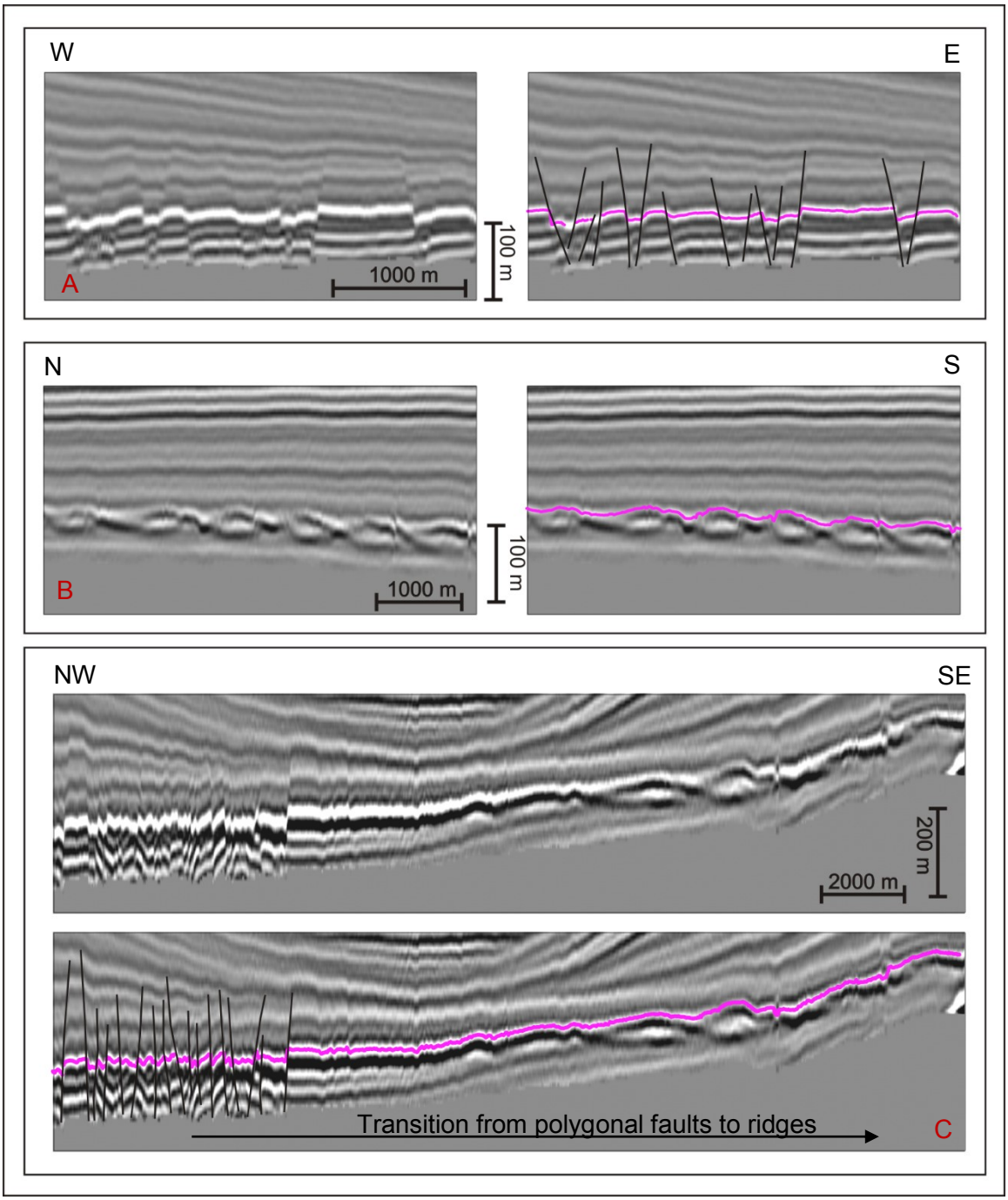

Figure 5.18 Uninterpreted and interpreted arbitrary seismic profiles from the 3D seismic detailing the faulting and ripple like ridges along the H9 Horizon. Refer to the text for a discussion on these profiles.

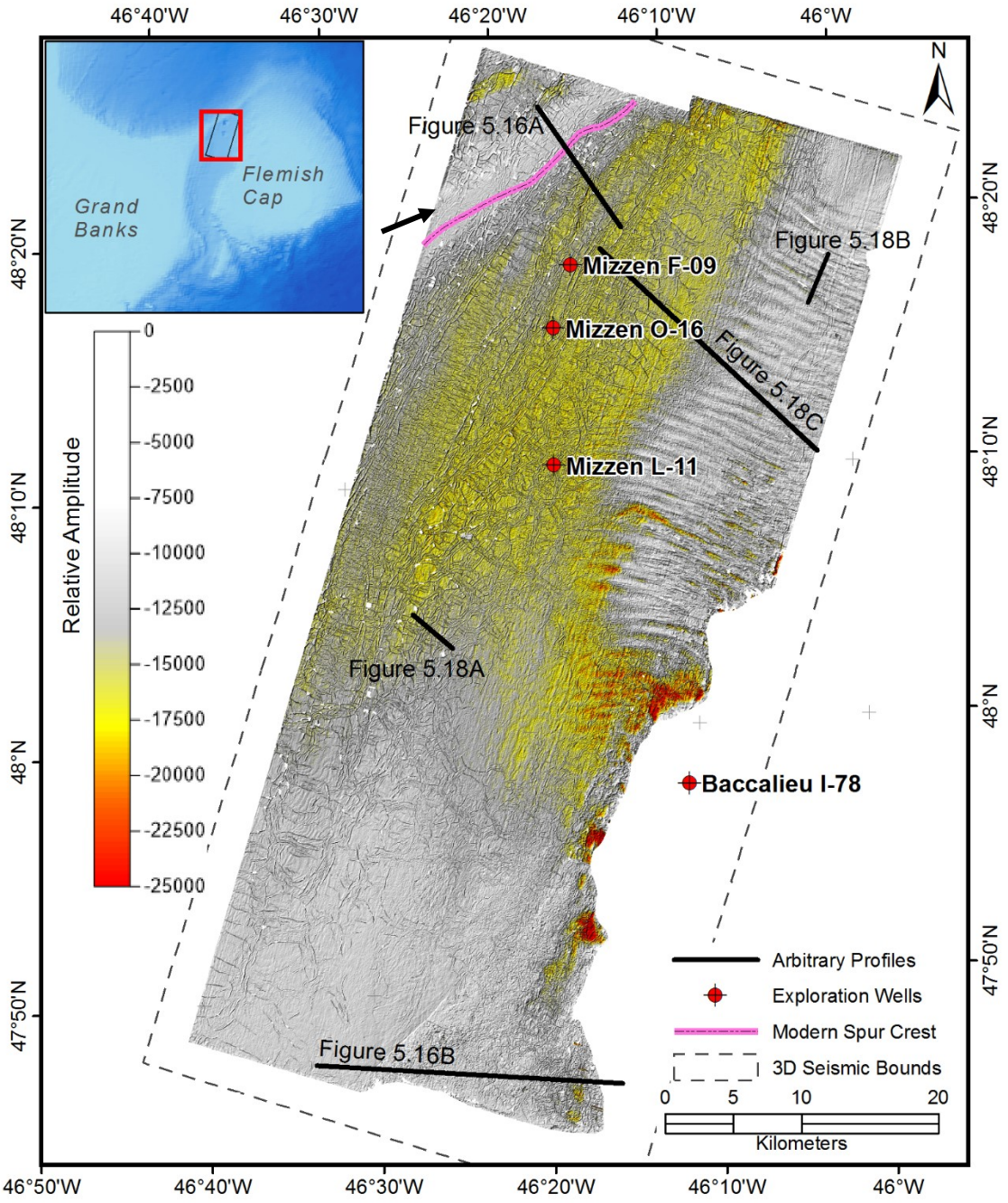

Figure 5.19 Relative amplitude along the H9 horizon.

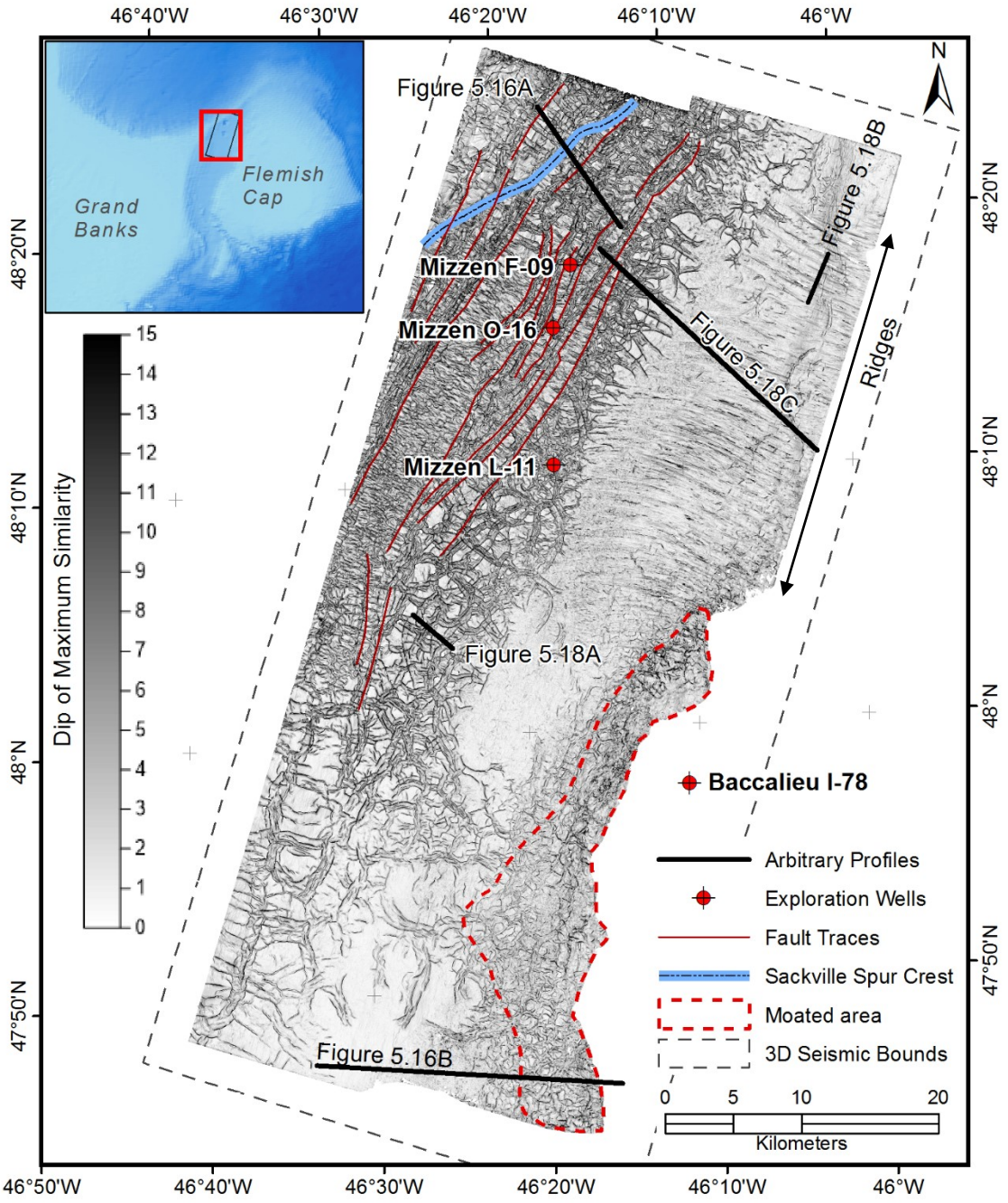

Figure 5.20 Dip of maximum similarity along the H9 horizon.

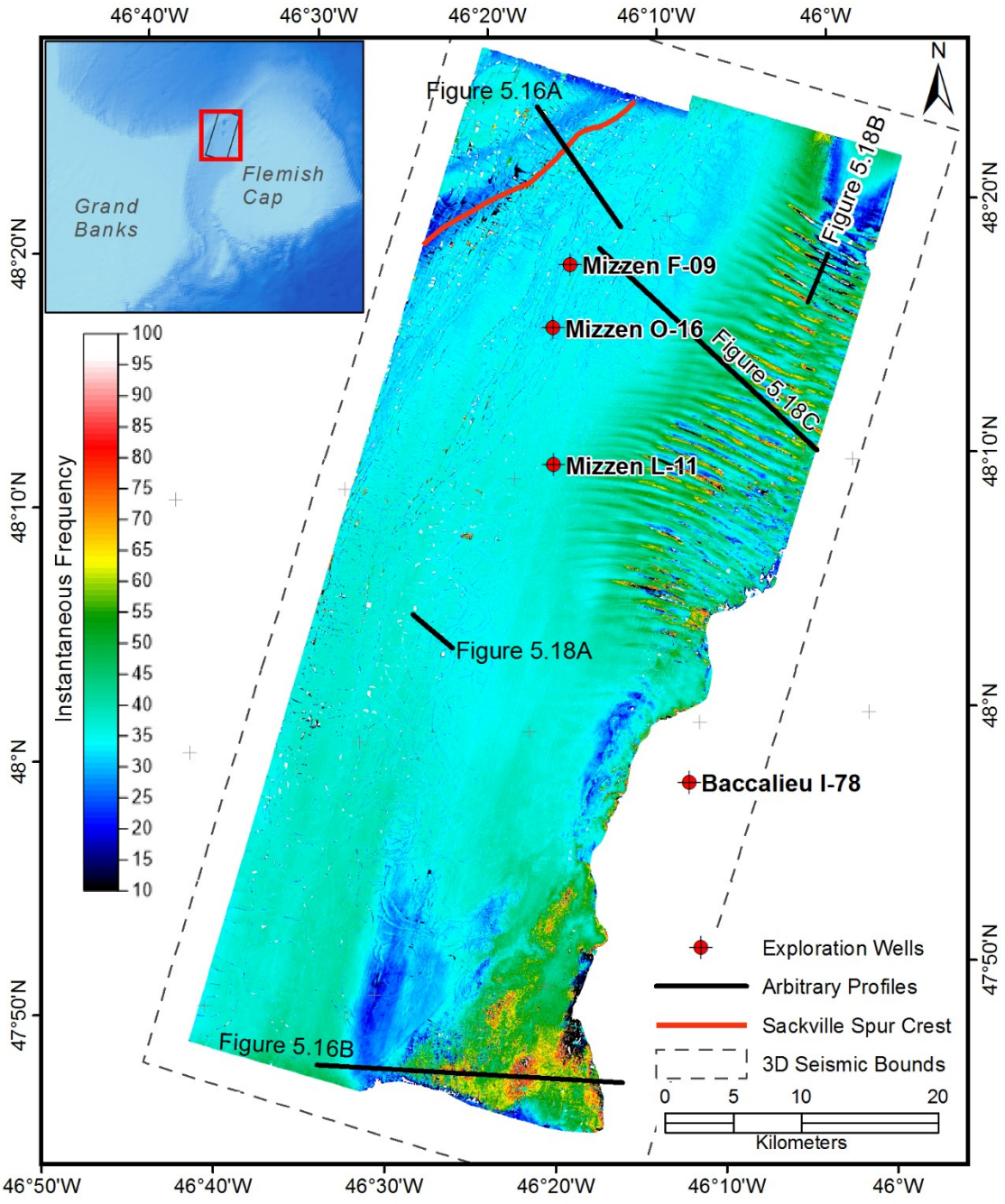

Figure 5.21 Instantaneous frequency along the H9 horizon.

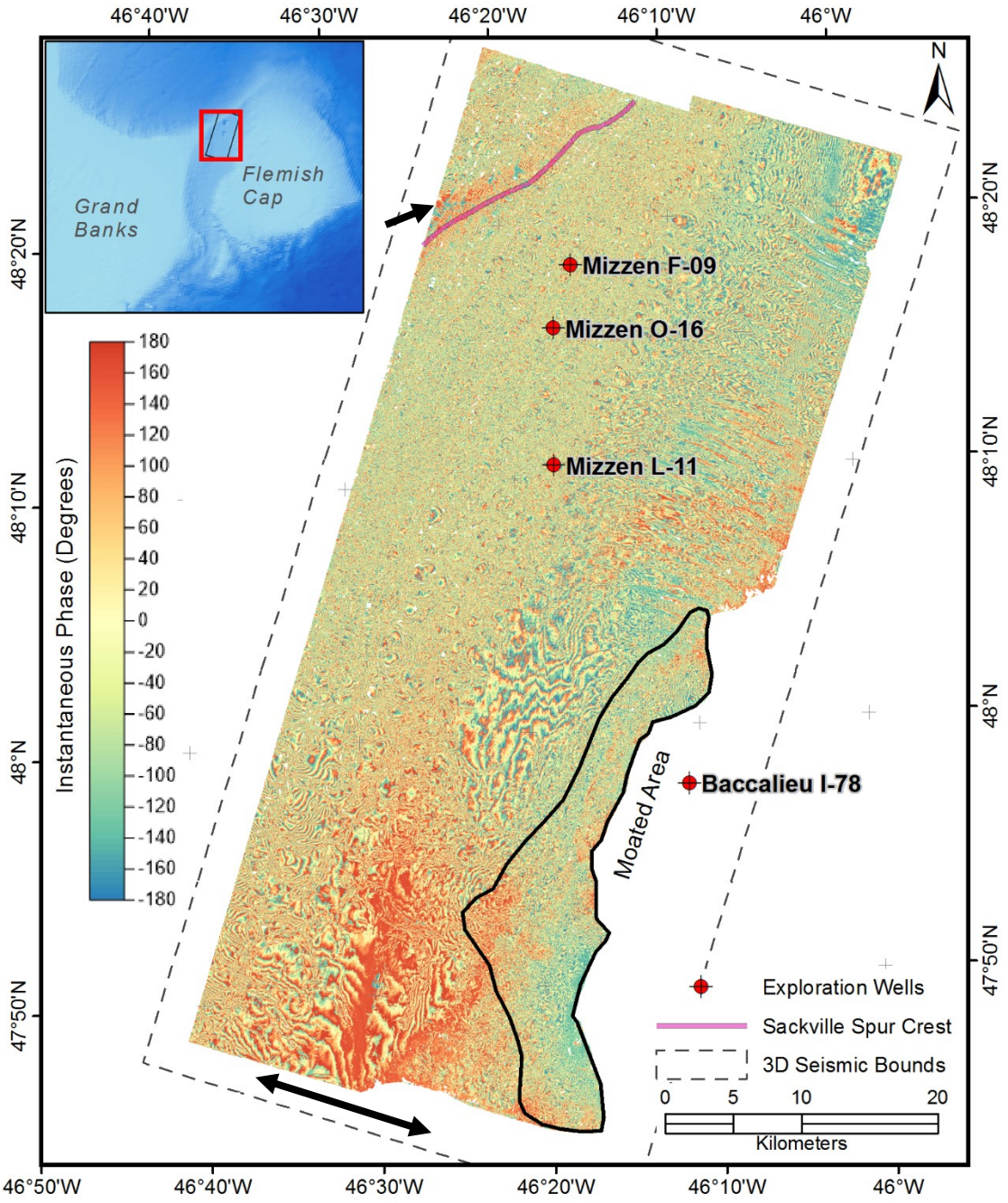

Figure 5.22 Instantaneous phase along the H9 horizon. The two black arrows highlight areas with positive phase that are discussed in the text.

5.1.2.2 Horizon H8

Horizon H8 was interpreted along a low to moderate amplitude trough at the base of an interval of more strongly convergent seismic reflections. H8 is present throughout most of the 3D seismic volume except in the SE and the NE (Figure 5.23) where the horizon onlaps the basement high and the H9 horizon, respectively. The H8 depth structure map mimics that of the underlying H9 horizon with one important exception; a subtle ridge measuring ~35 m high and ~6.5 km wide in the NW corner of the H8 depth structure map (Figure 5.23). The structural differences between the H9 and H8 surfaces are best represented by the H9 to H8 isopach of Figure 5.24. The interval between H8 and H9 is thickest below the Sackville Spur and thinnest in the NE above the H9 ridges where H8 approaches and eventually merges with H9. The interval below the modern Flemish Pass has a relatively consistent thickness (Figure 5.24).

The faults affecting the underlying H9 horizon are apparent on the H8 depth structure map and are best imaged on the dip of maximum similarity surface (Figure 5.25). The faults are less prominent on the H8 horizon than on H9. Similarly, the ridges in the NE are only apparent where the interval between the two horizons is thinnest. The depth structure map shows the ridges are replaced by subtle elongate lineations running sub-perpendicular to the H9 ridge crests (Figure 5.23).

Amplitudes along H8 do not mimic those of the underlying H9 horizon (Figure 5.26). Elevated amplitudes corresponds with the ridge or paleo spur in the study's NW corner (Figure 5.23). In the NE where the H9 to H8 interval thins, a prominent lobe of high amplitudes do not appear to be a tuning effect (Figure 5.26 and Figure 5.27). Tuning effects result in higher amplitudes on the flanks of the H8 horizon's central ridge and on the flanks of the basement high that represents the flank of the Flemish Cap (see pink arrows of Figure 5.26) both of which are onlapped by H8. The instantaneous frequency surface shows the same trends as those observed on the horizon's amplitude map (Figure 5.26).

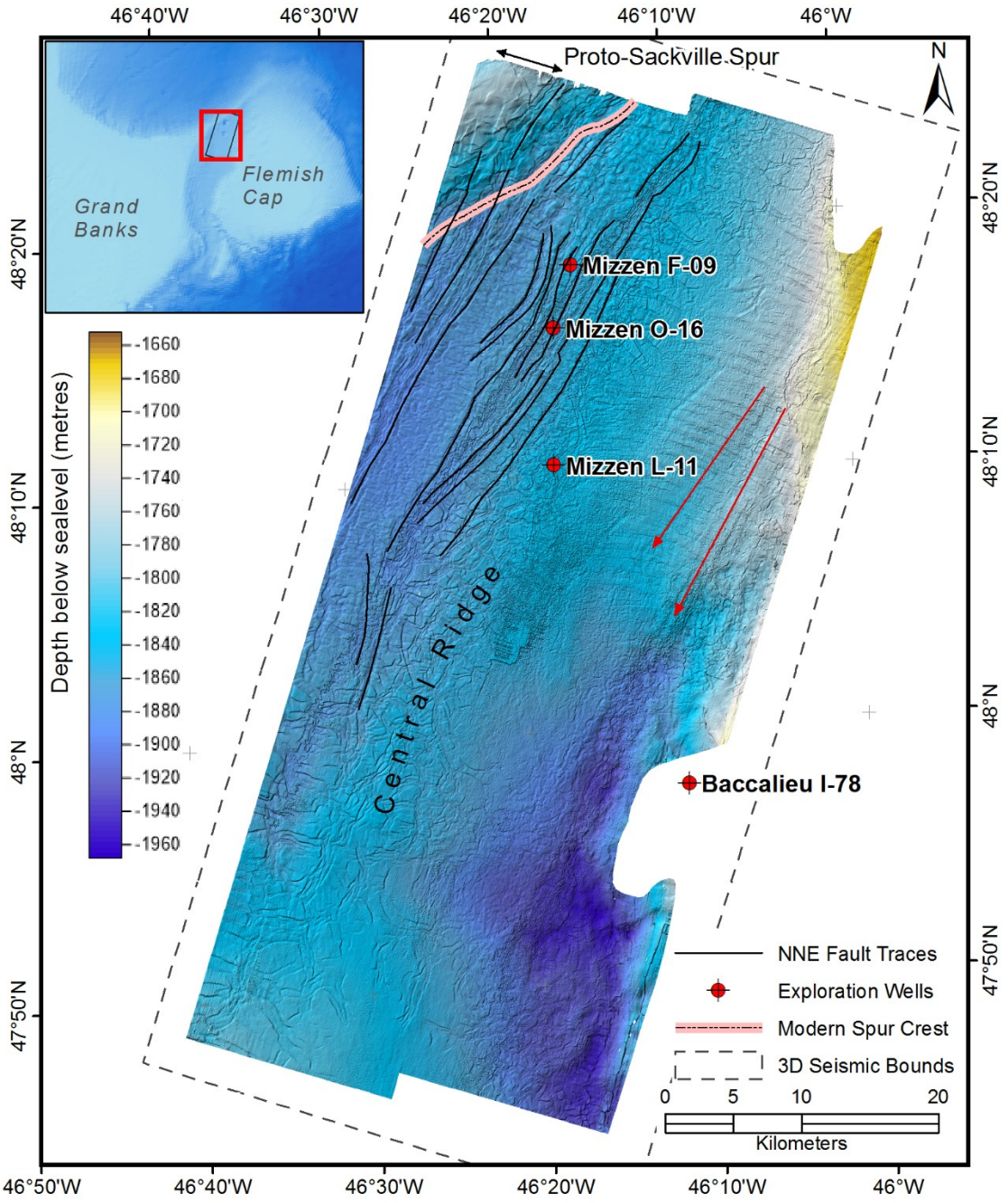

Figure 5.23 Depth structure along the H8 horizon with fault traces overlain. The red arrows highlight subtle lineations discussed in the text.

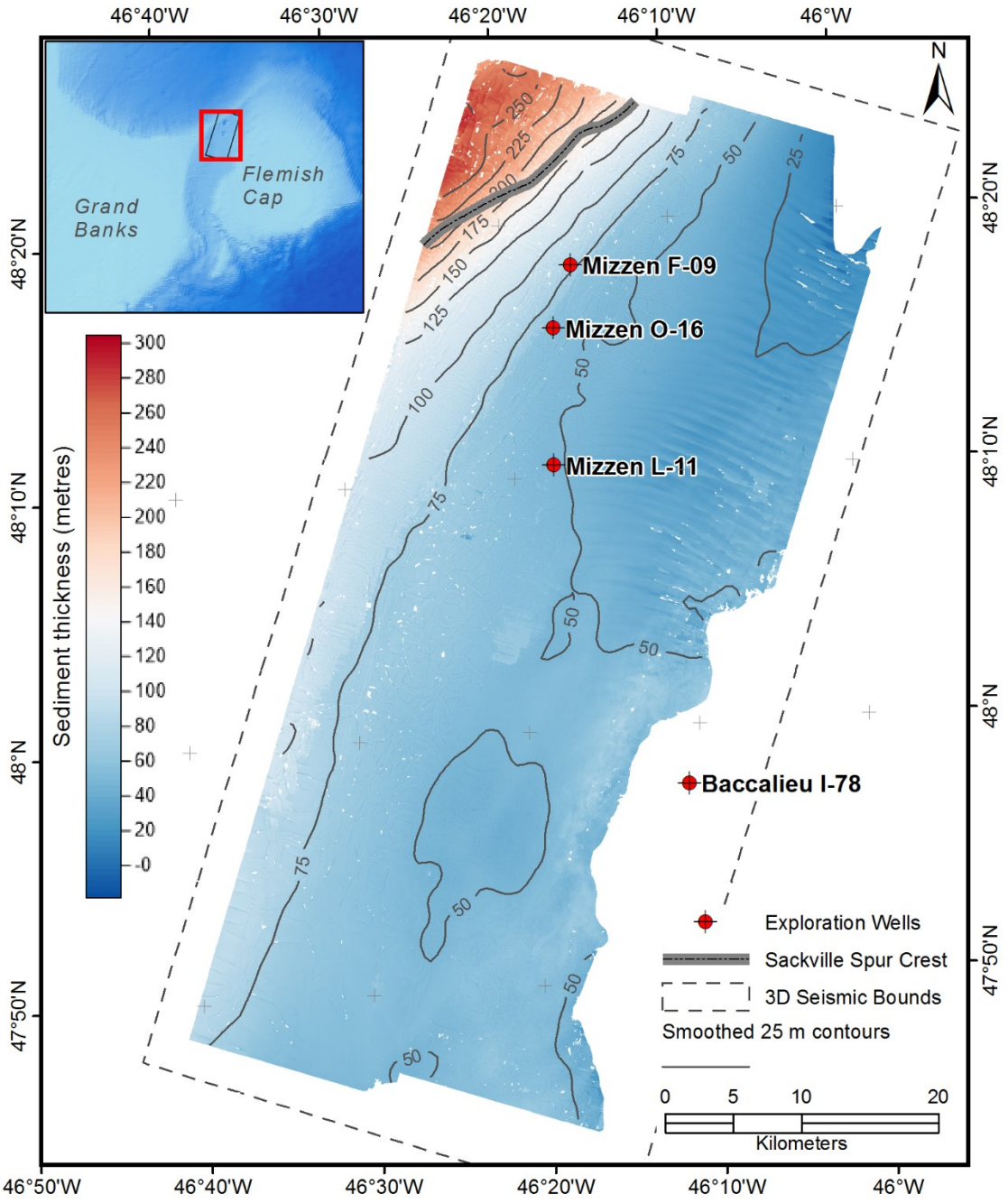

Figure 5.24 Isopach (thickness) map between the H9 and H8 horizons.

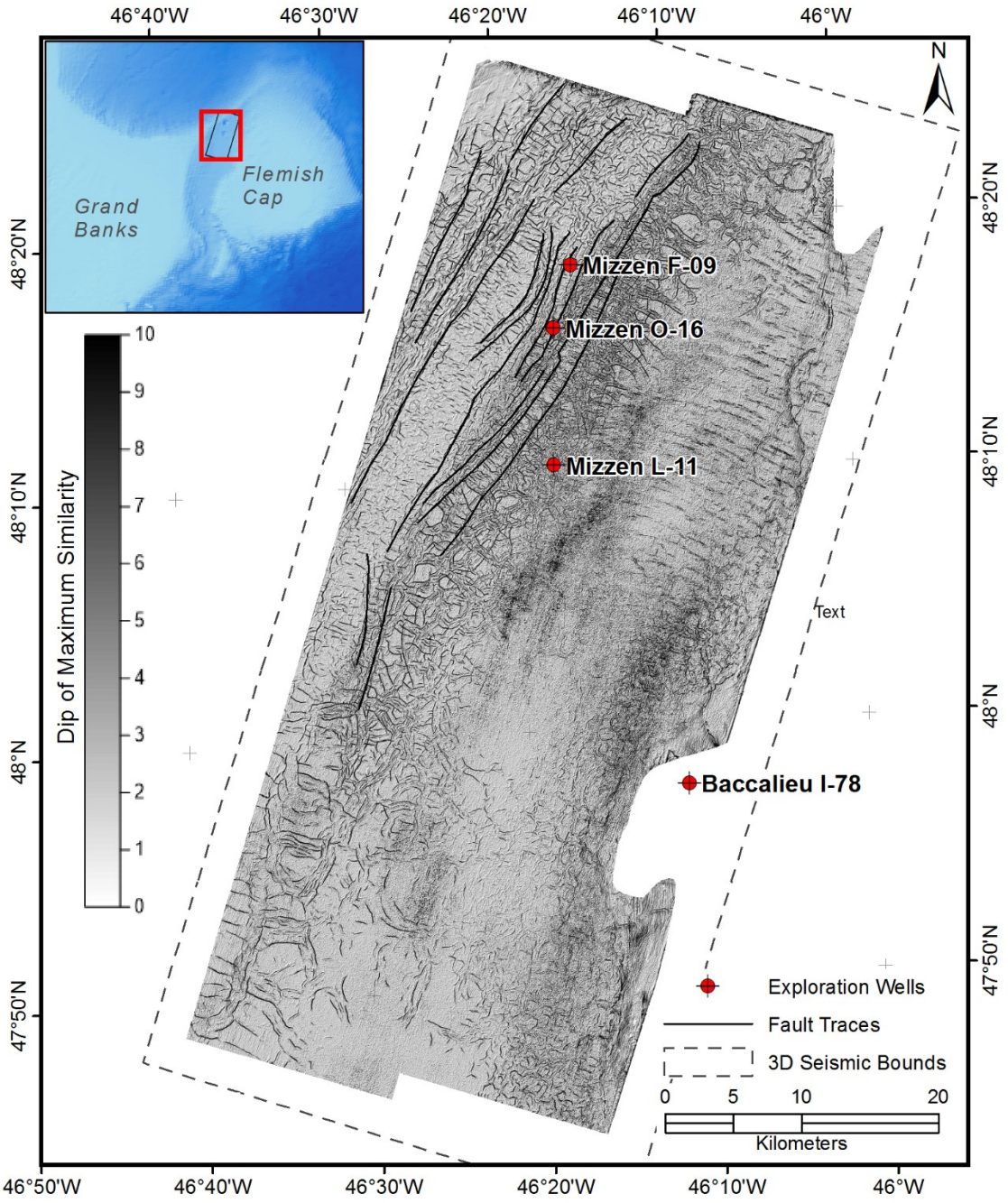

Figure 5.25 Dip of maximum similarity along the H8 horizon.

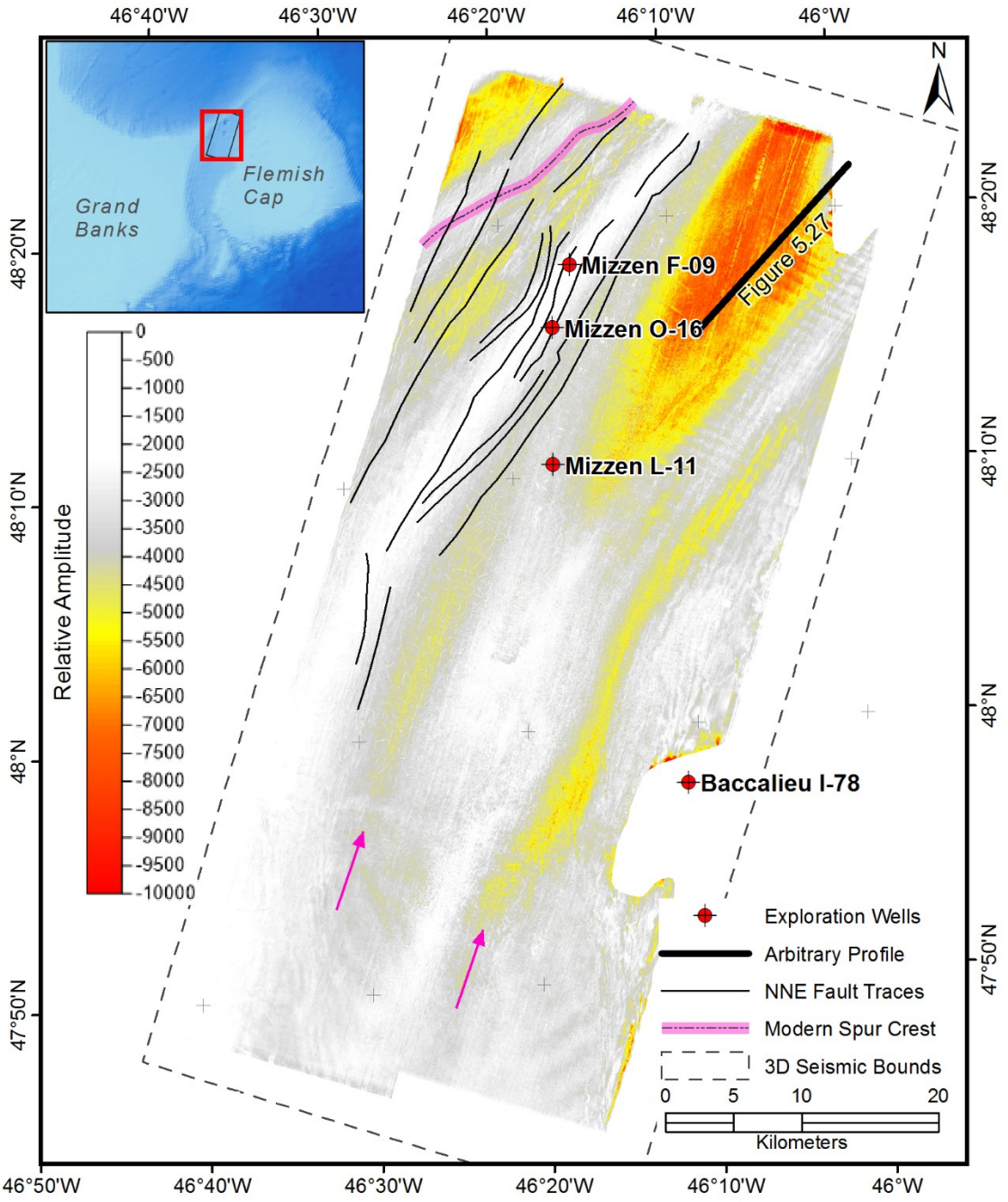

Figure 5.26 Relative amplitude along the H8 horizon with fault traces overlain. The pink arrows highlight amplitude anomalies discussed in the text.

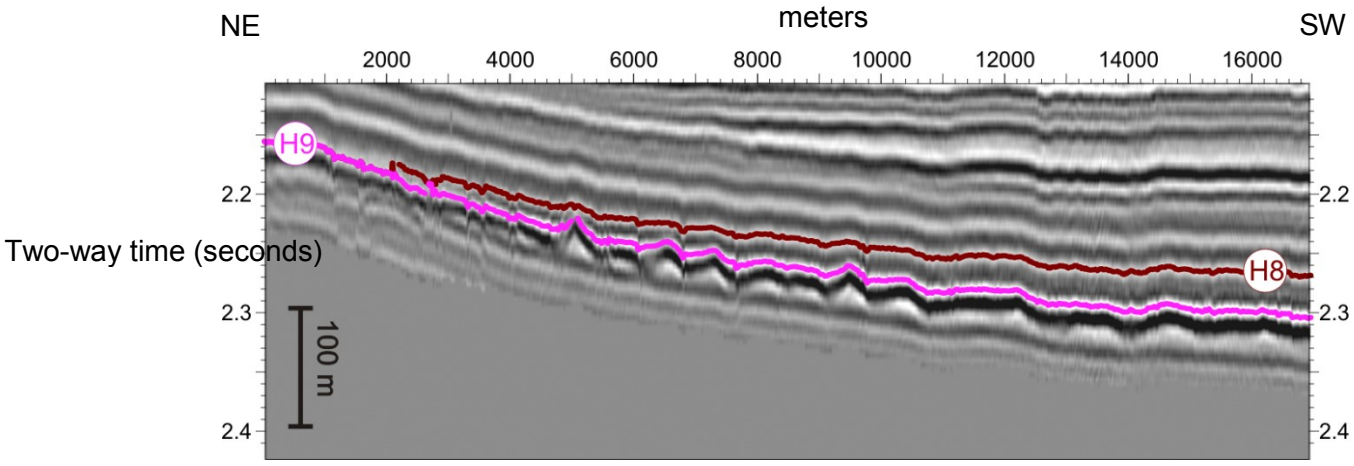

Figure 5.27 Seismic profiles showing the thinning of the H8 to H9 interval and eventual onlap of H8 onto H9. Refer to Figure 5.26 for the profile location.

5.1.2.3 Horizon H7

The H7 horizon was picked along a continuous amplitude peak that marks the base of a package of high amplitude, divergent events referred to in Section 5.1.2.1. The H7 horizon is continuous across the 3D area (Figure 5.28).

The depth structure map of the H7 horizon roughly parallels the shape of the modern seafloor, including a topographic low beneath Flemish Pass in the south and a ridge beneath the apex of Sackville Spur in the north. (Figure 5.28). The crest of this paleo-Spur is ~5 km farther north than the modern crest. The paleo-Pass is narrow with steep flanks relative to the modern pass (Figure 5.28). This deep structure owes itself to significant and preferential sediment accumulation on the flanks of the paleo-Pass since the time of H8 (Figure 5.1 and Figure 5.29). The H7 to H8 interval thickens within the floor of the paleo-Pass towards the south (Figure 5.29). Another notable feature on the H7 depth structure map are the large scale troughs in the SE (Figure 5.28). These troughs are interpreted as sediment drift features formed by contour currents due to their smooth morphology shown in the seismic profile and on the depth structure map (Figure 5.28 and 5.30). Evidence of other bedforms to the NE support this interpretation (Figure 5.28).

Reflections below the H7 horizon are relatively low amplitude and faulted (Figure 5.30). Some faults extend through the H7 horizon, particularly in the base of Flemish Pass where the section is condensed. On the flanks of Flemish Pass, larger faults extend through or terminate at the H7 horizon. These larger faults are best represented

on the H7 dip of maximum similarity surface of Figure 5.31. Of particular note are larger apparent fault offsets in the northwest below the Sackville Spur (Figure 5.32).

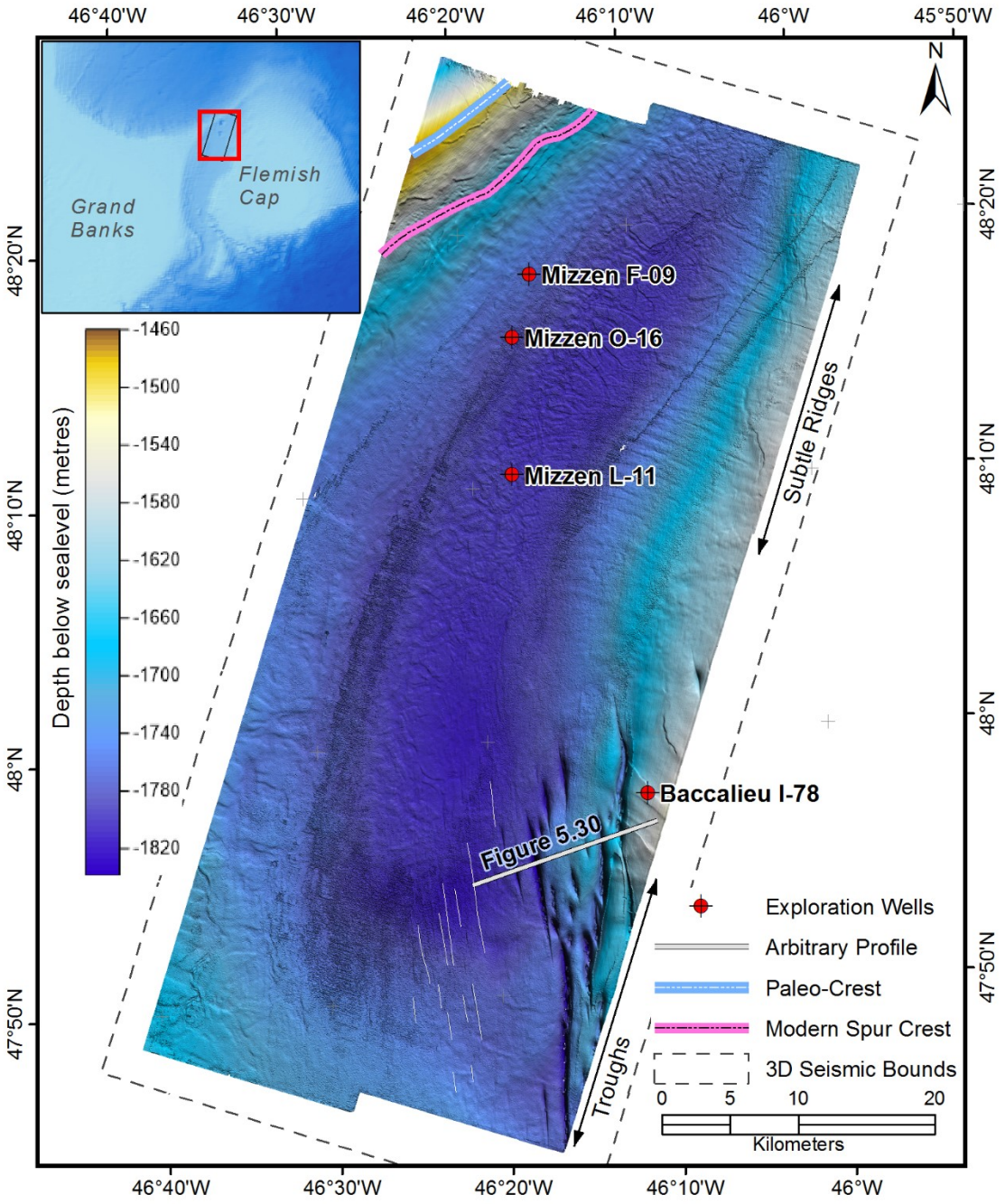

Figure 5.28 Depth structure along the H7 horizon. Subtle current scours are highlighted in the south.

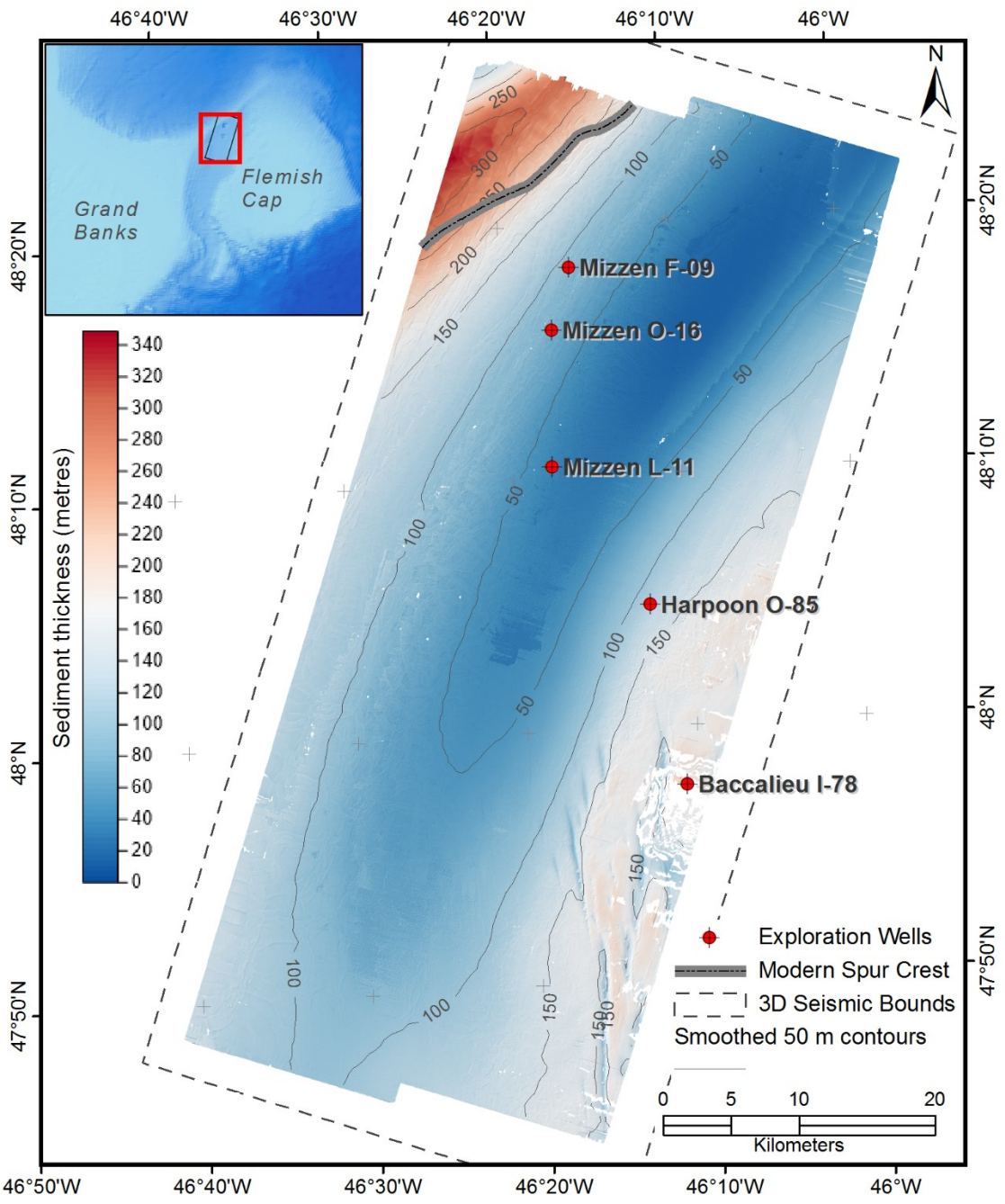

Figure 5.29 Isopach (thickness) map between the H8 and H7 horizons.

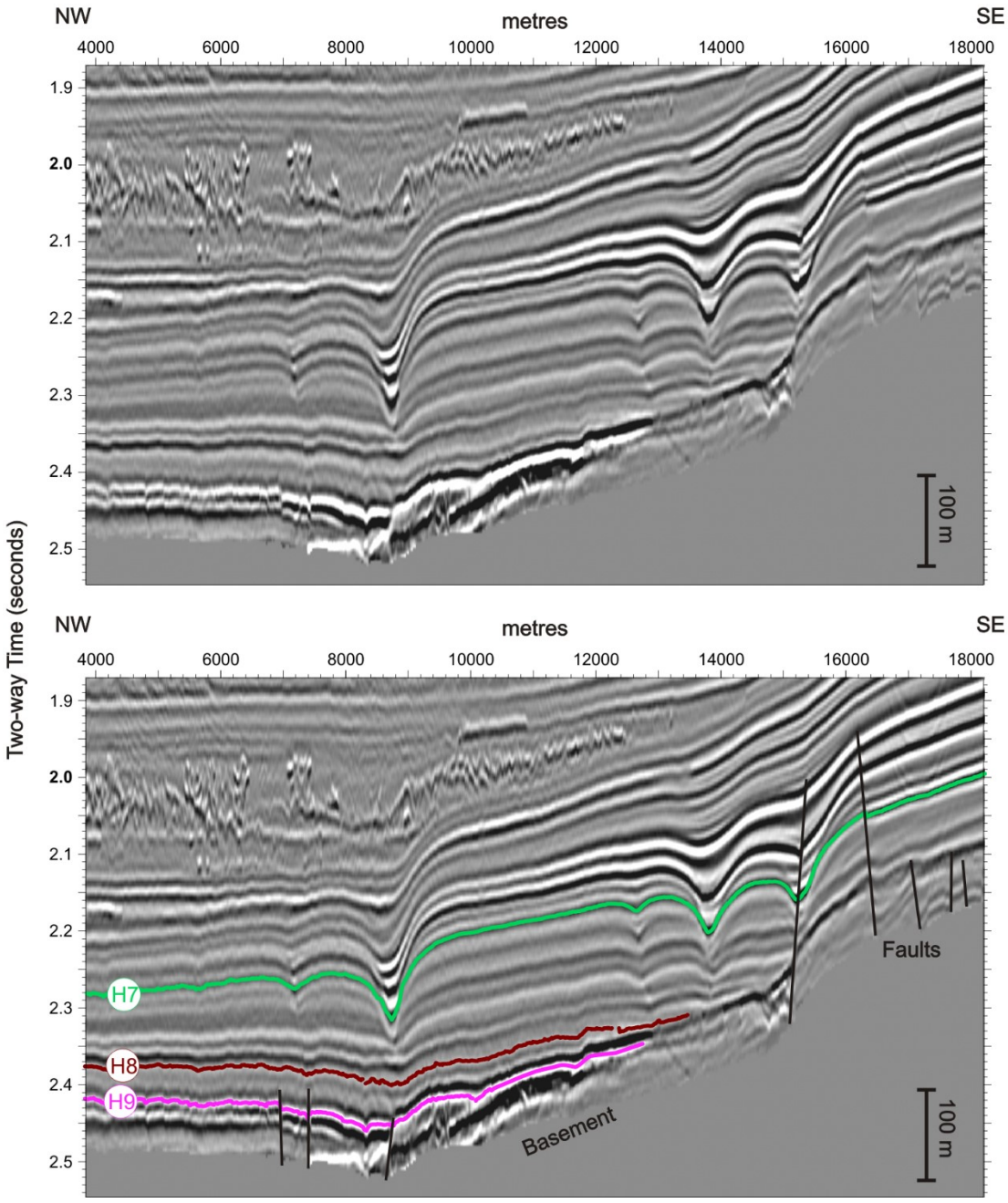

Figure 5.30 Arbitrary 3D seismic profile (uninterpreted above and interpreted below) through large scale sediment drift deposits along the H7 horizon. Refer to Figure 5.28 for the profile location.

Amplitudes along H7 are elevated below the Sackville Spur, are reduced in the Flemish Pass, and are highest on the eastern edge of the study area (Figure 5.33). The H7 instantaneous frequency surface shows frequencies decrease slightly in the area below the Sackville Spur where high amplitudes are observed along the horizon. The instantaneous phase along Horizon H7 shows no significant changes with only subtle varitaions corresponding to the reduced frequencies below the Sackville Spur.

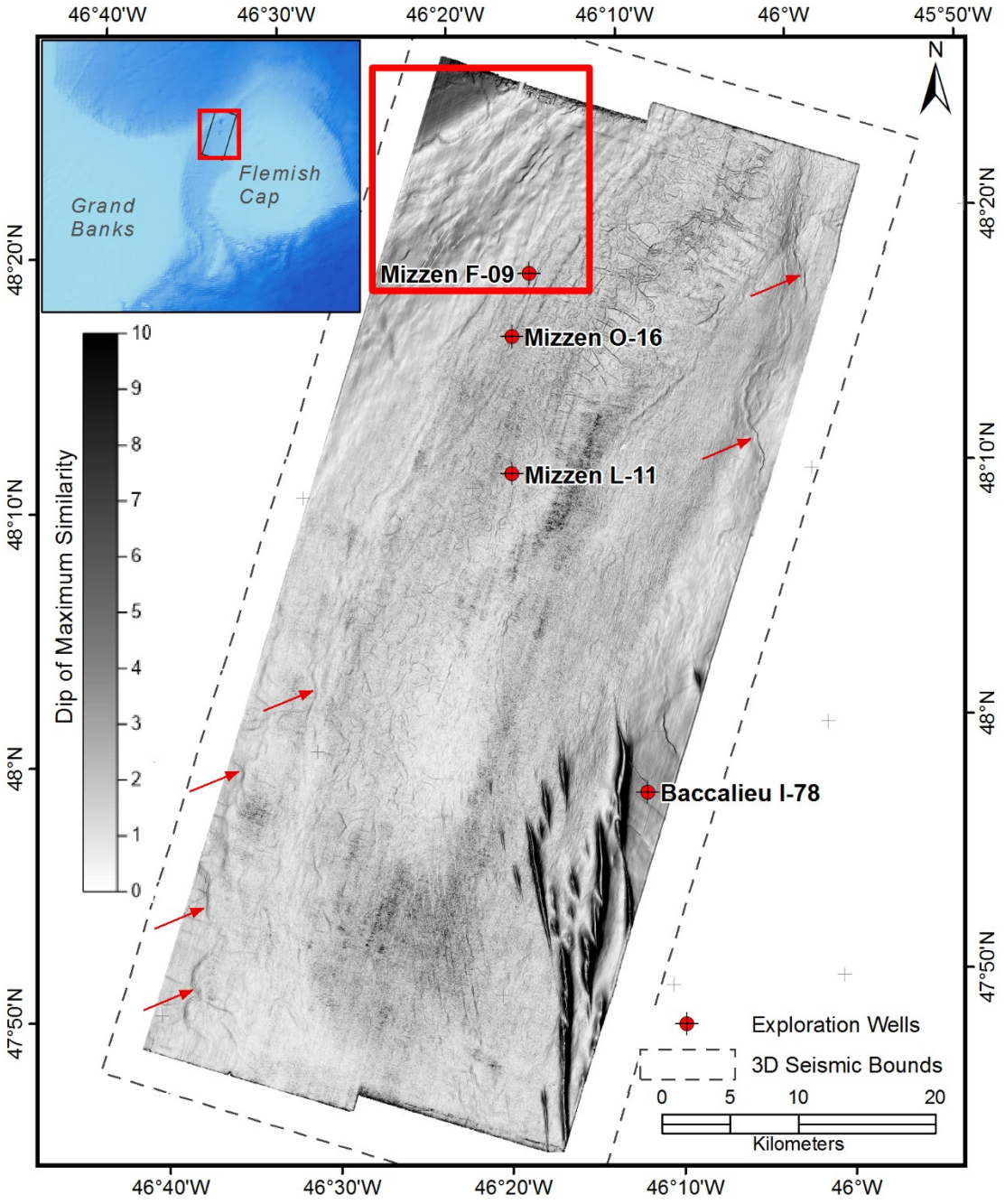

Figure 5.31 Dip of maximum similarity along the H7 Horizon with arrows identifying faults.

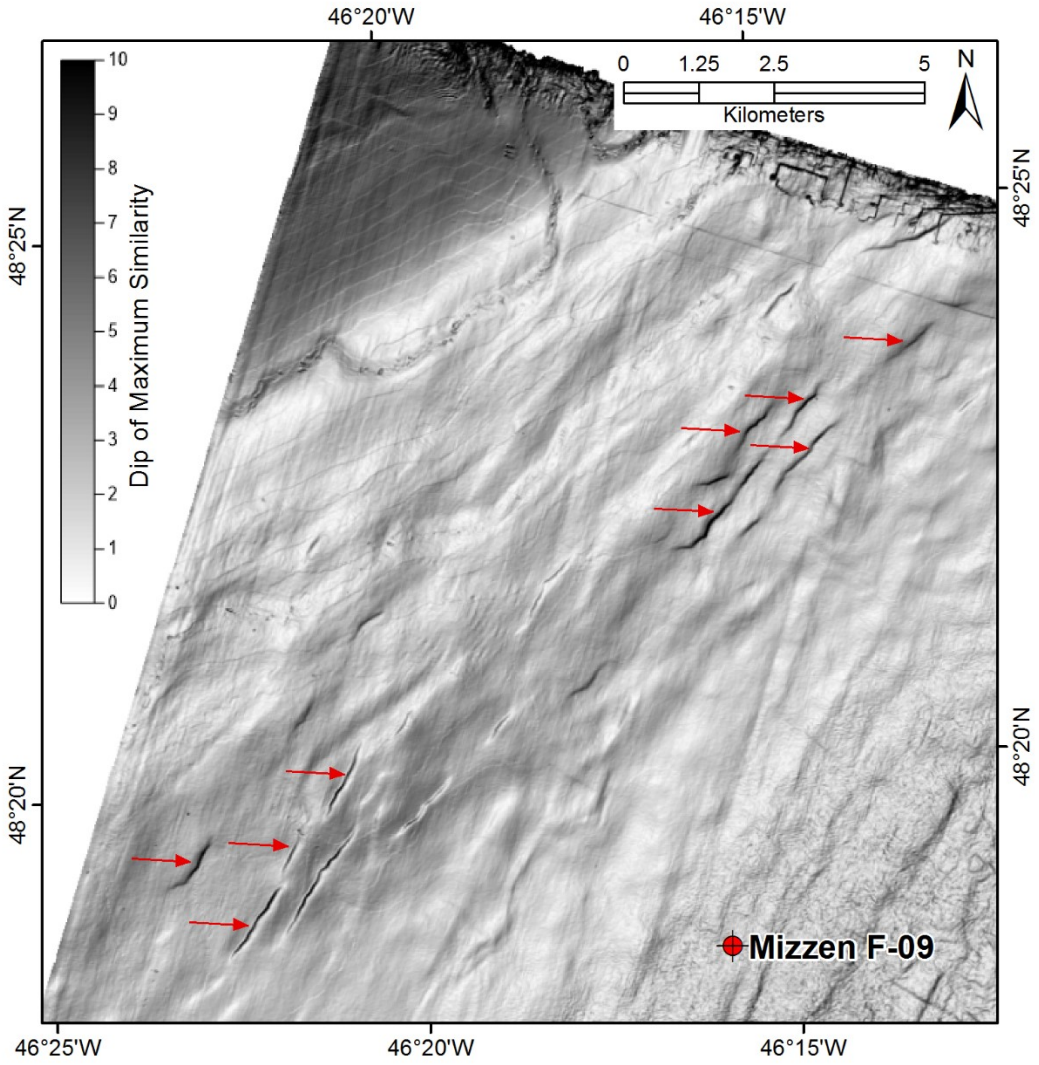

Figure 5.32 Zoomed map of the dip of maximum similarity along the H7 horizon with arrows highlighting faults. Refer to **Figure 5.31** for map location.

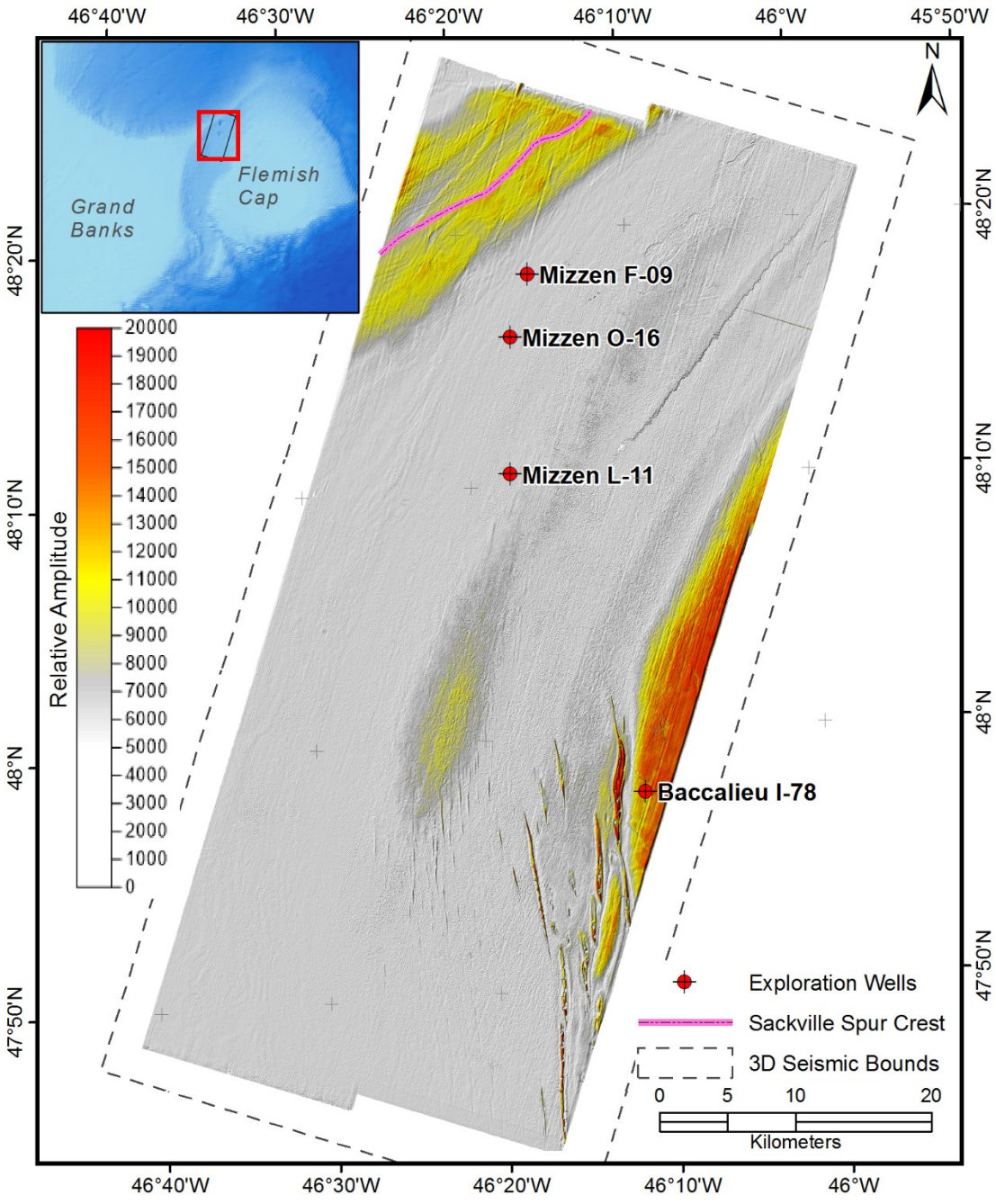

Figure 5.33 Relative amplitudes along the H7 horizon.

5.1.2.4 Horizon H6

Horizon H6 was interpreted over the western half of the survey area along a relatively high amplitude peak. The horizon could not be extended through the Flemish Pass where the reflections converge and eventually are not resolved (Figure 5.1). The depth structure along the horizon mimics that of the underlying H7 horizon; a broad paleo-drift the crest of which is north of the modern Sackville Spur's crest (Figure 5.34). Faults extend from depth and are visible on the H6 dip of maximum similarity surface (Figure 5.35), but are less abundant than the faults on the underlying H7 horizon, particularily below the Sackville Spur (Figure 5.31).

Amplitudes along the horizon are elevated in the northwest corner of the study area (Figure 5.36). Close inspection of the relative amplitudes show a broad band of elevated amplitudes where H6 intersects the second BSR and a distinct, lower amplitude, narrow band of slightly elevated amplitudes to the south (Figure 5.37). This narrow band corresponds with the poorly developed third BSR. The instantaneous frequency along H6 shows a subtle decrease in the vicinity of the high amplitude bands (Figure 5.38). A more restricted colour range shows a distinct zone of reduced frequencies bound to the south by the narrow band of high amplitudes and to the north by the the limits of the primary BSR (Figure 5.39). Instantaneous phase along H6 shows slightly more negative values between the two high amplitude bands (Figure 5.40).

Elsewhere within the 3D seismic volume, reduced frequencies extend in a band south from the Mizzen F-09 well (Figure 5.38). These reduced frequencies represent a tuning effect associated with constructive interference as straigraphic beds thin into Flemish Pass.

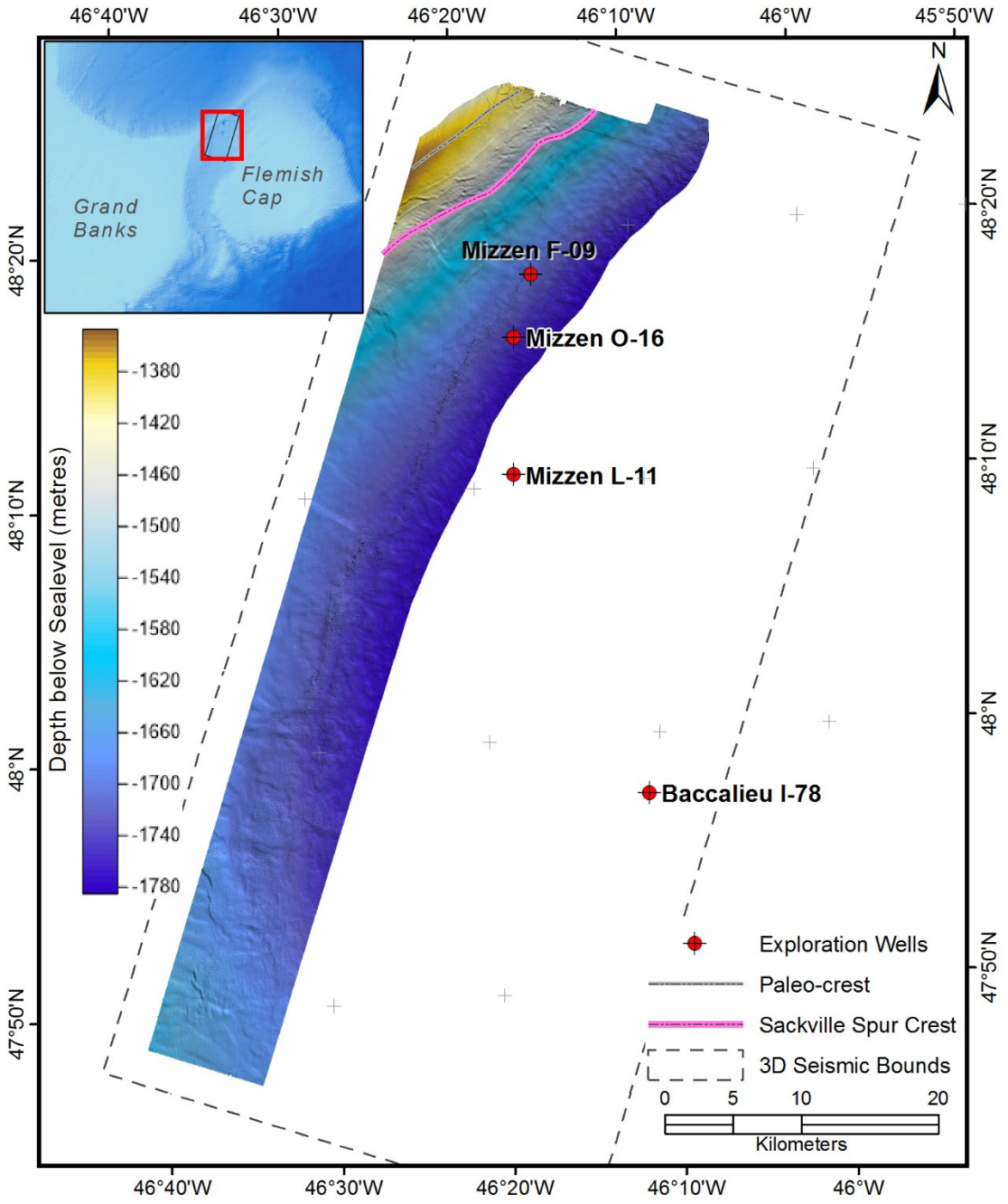

Figure 5.34 Depth structure along the H6 horizon.

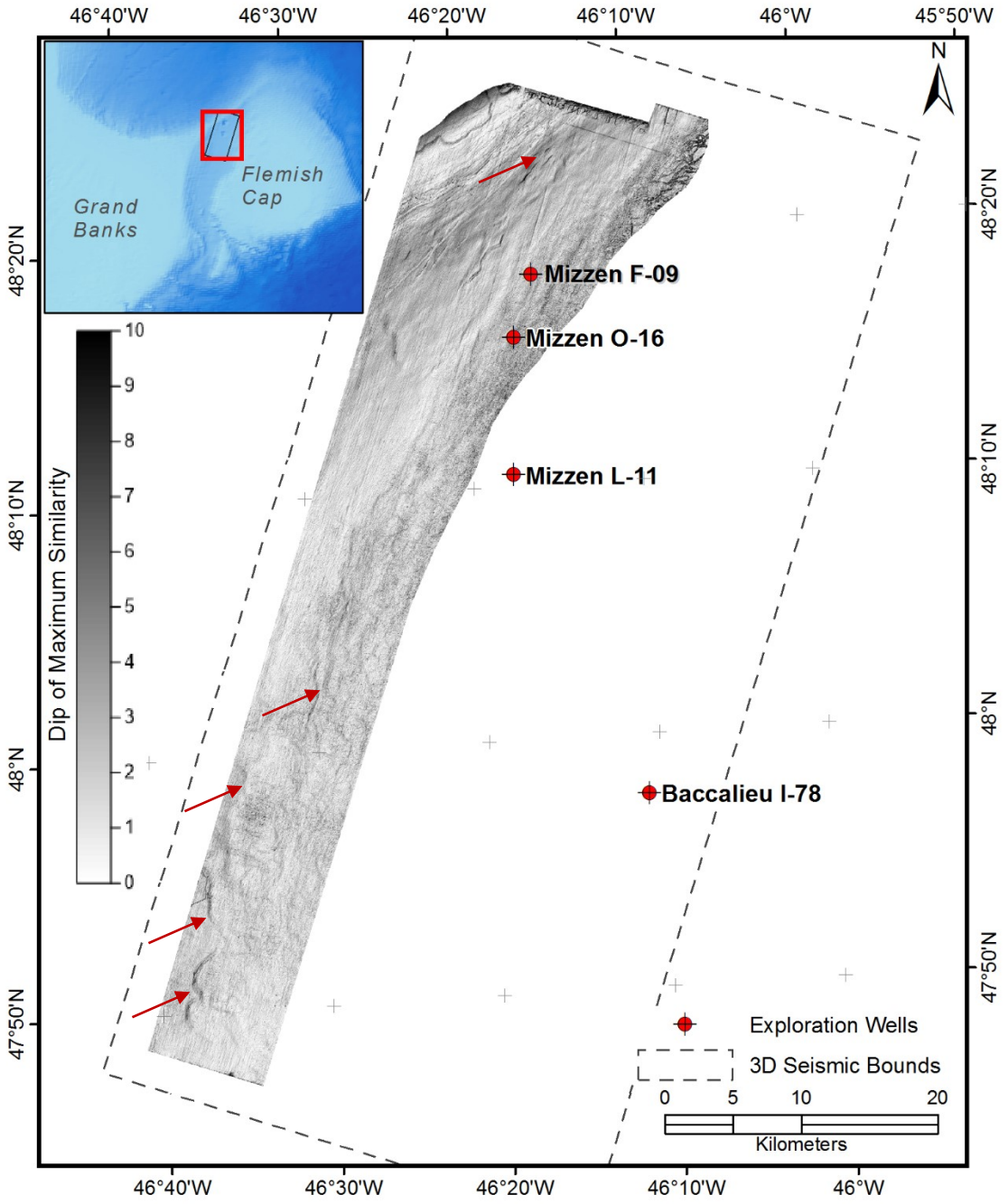

Figure 5.35 Dip of maximum similarity along the H6 horizon. The red arrows identify faults discussed in the text.

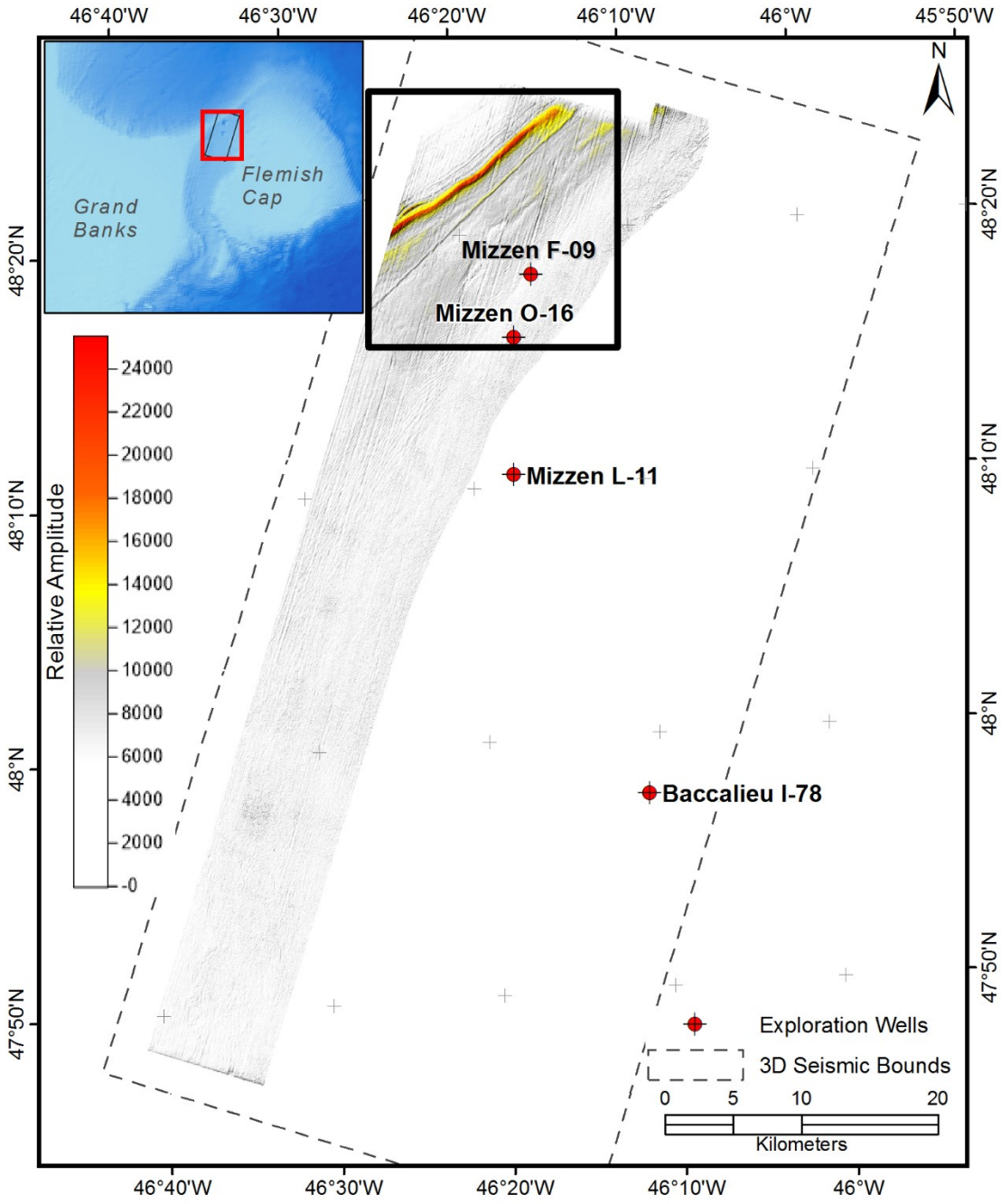

Figure 5.36 Relative amplitude along the H6 horizon.

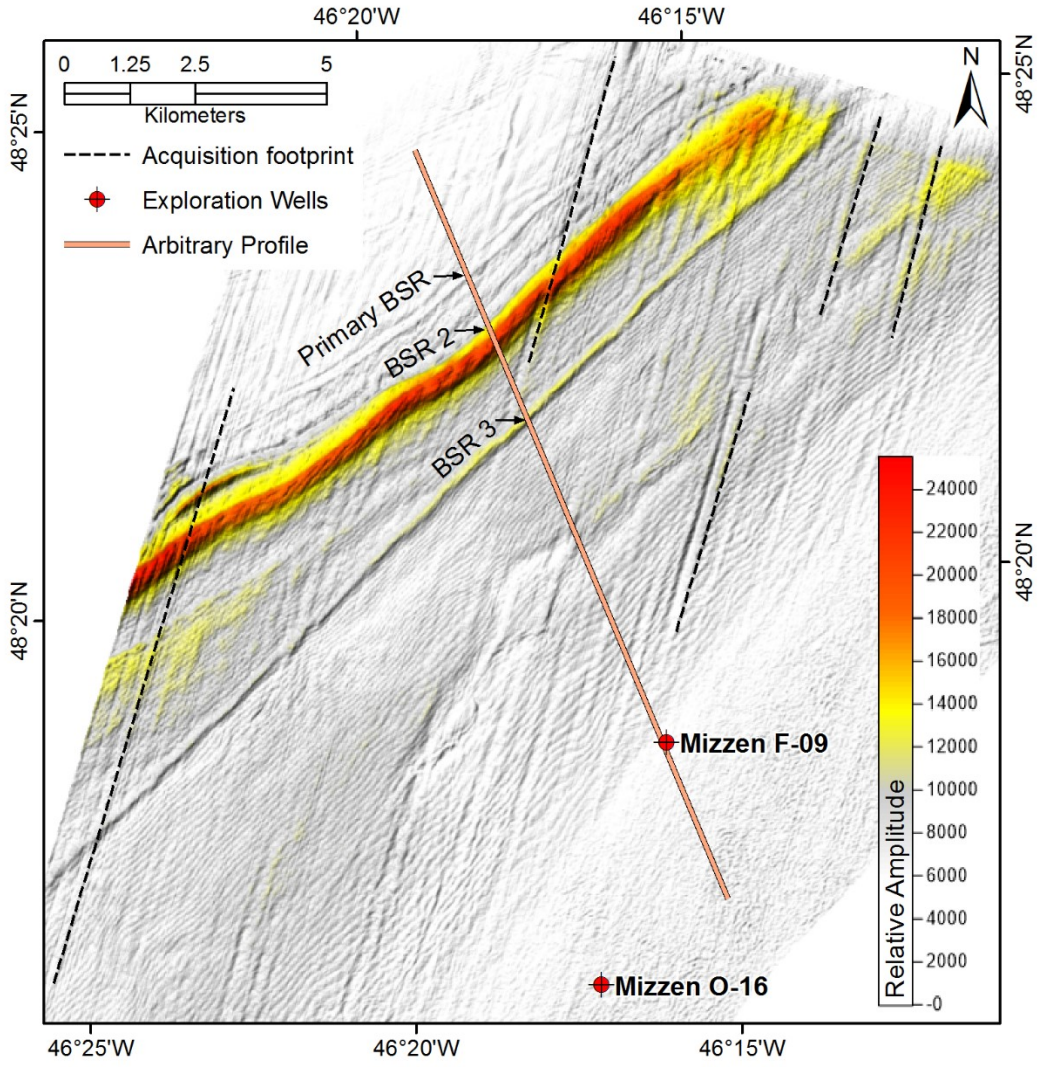

Figure 5.37 Detail of relative amplitudes along the H6 horizon. Refer to Figure 5.36 for map location. The arbitrary seismic profile is presented below in Figure 5.39.

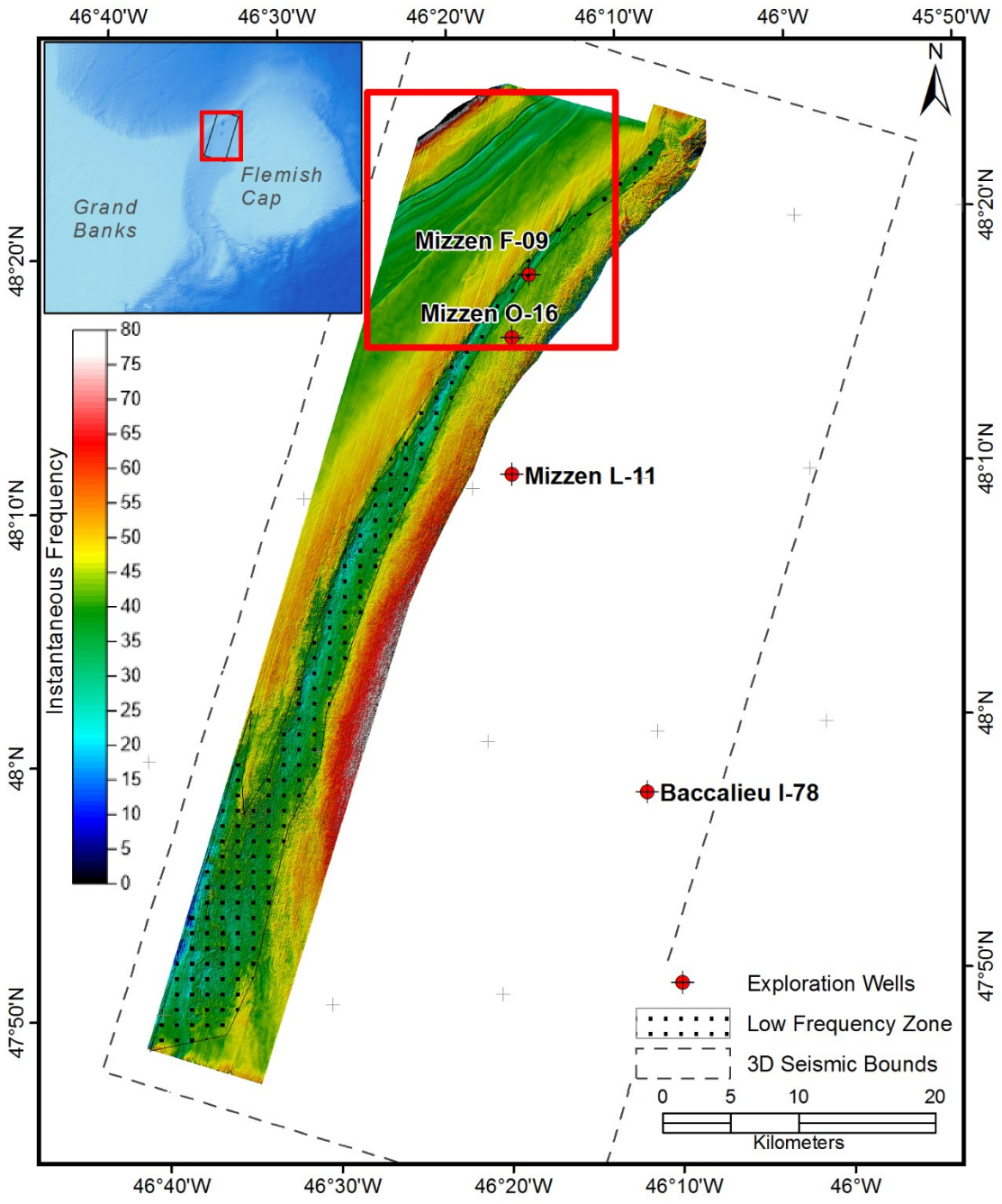

Figure 5.38 Instantaneous frequency along the H6 horizon highlighting the low frequency zone (tuning effect) discussed in the text. The red box represents the location of Figure 5.39 and Figure 5.40.

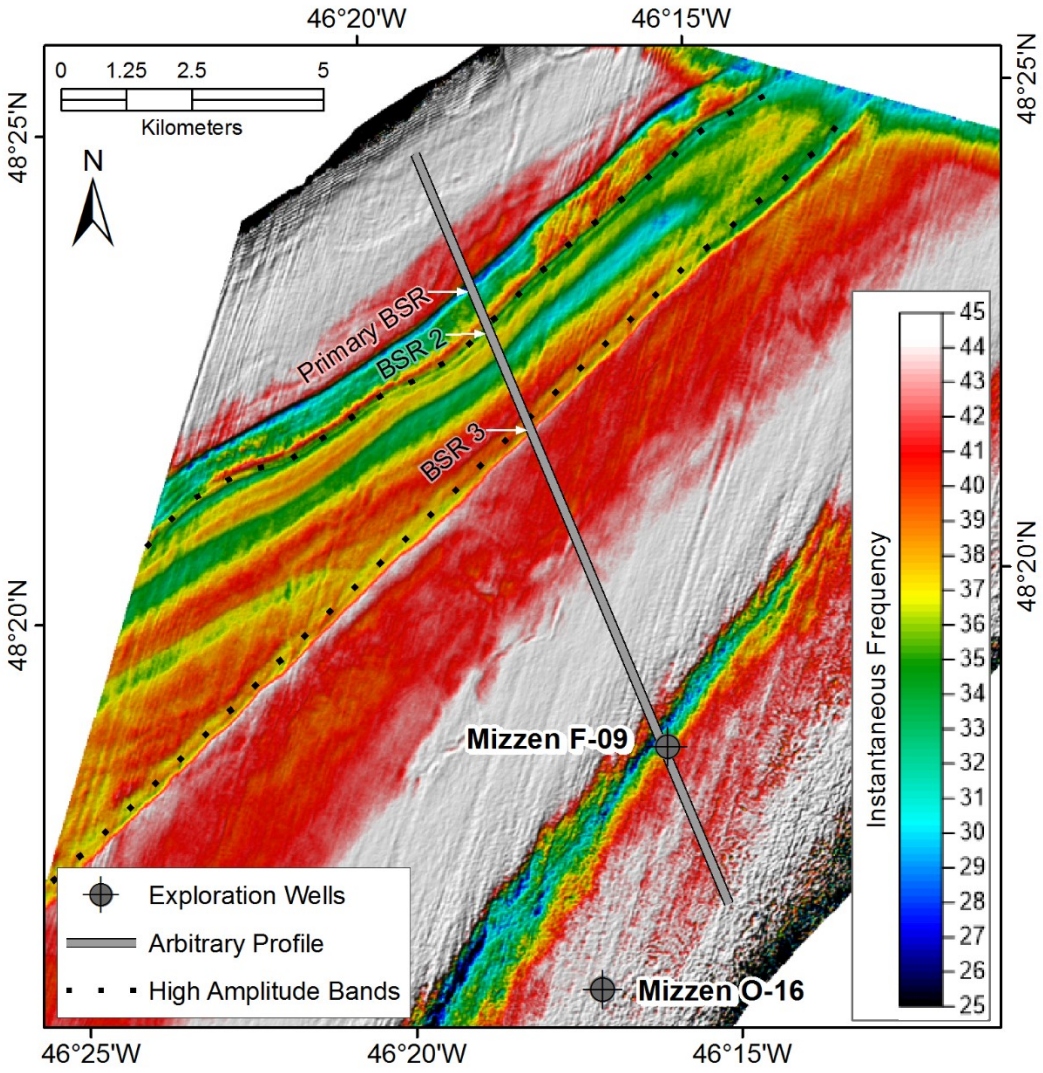

Figure 5.39 Detail of instantaneous frequency along the H6 horizon. Refer to Figure 5.38 for map location. The arbitrary seismic profile is presented below in Figure 5.39.

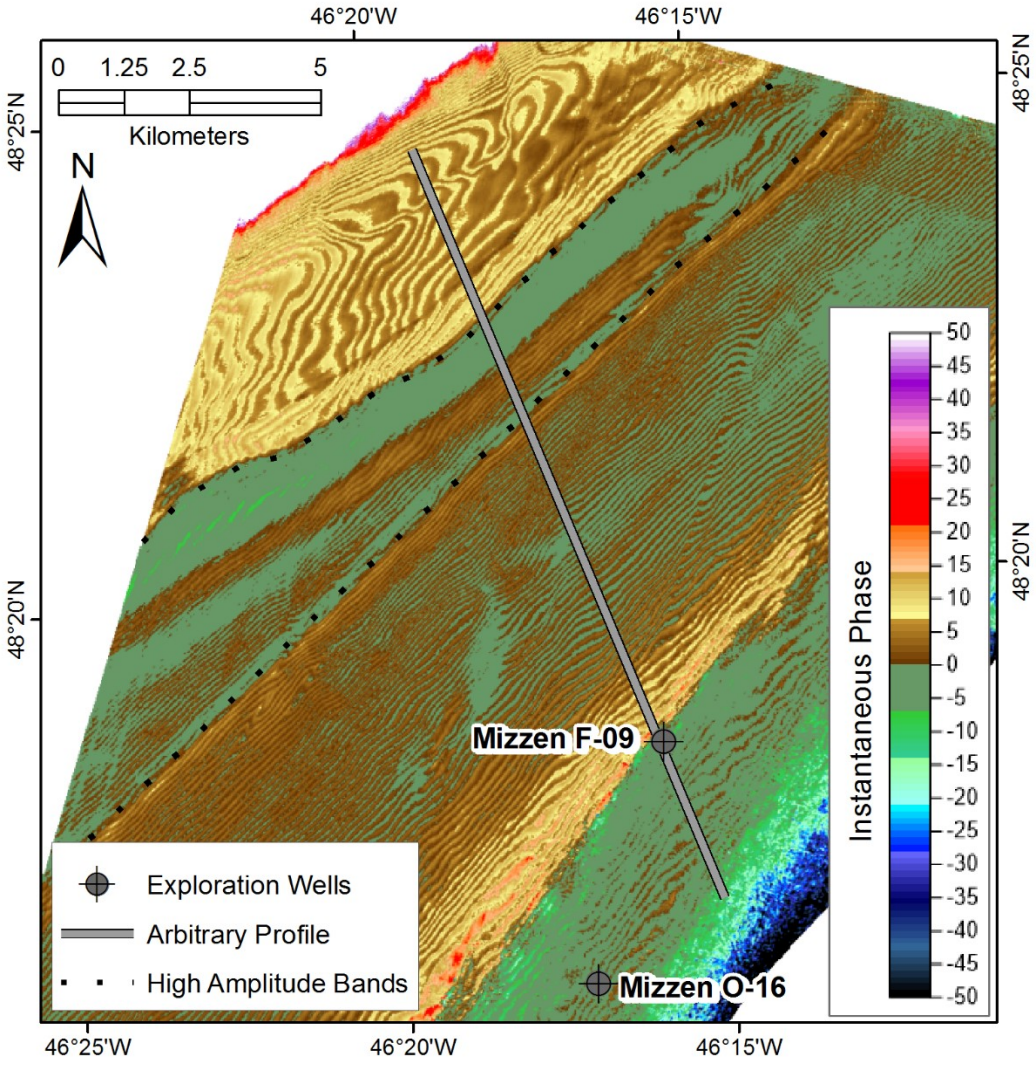

Figure 5.40 Detail of instantaneous phase along the H6 horizon. Refer to Figure 5.38 for map location. The arbitrary seismic profile is presented below in Figure 5.39

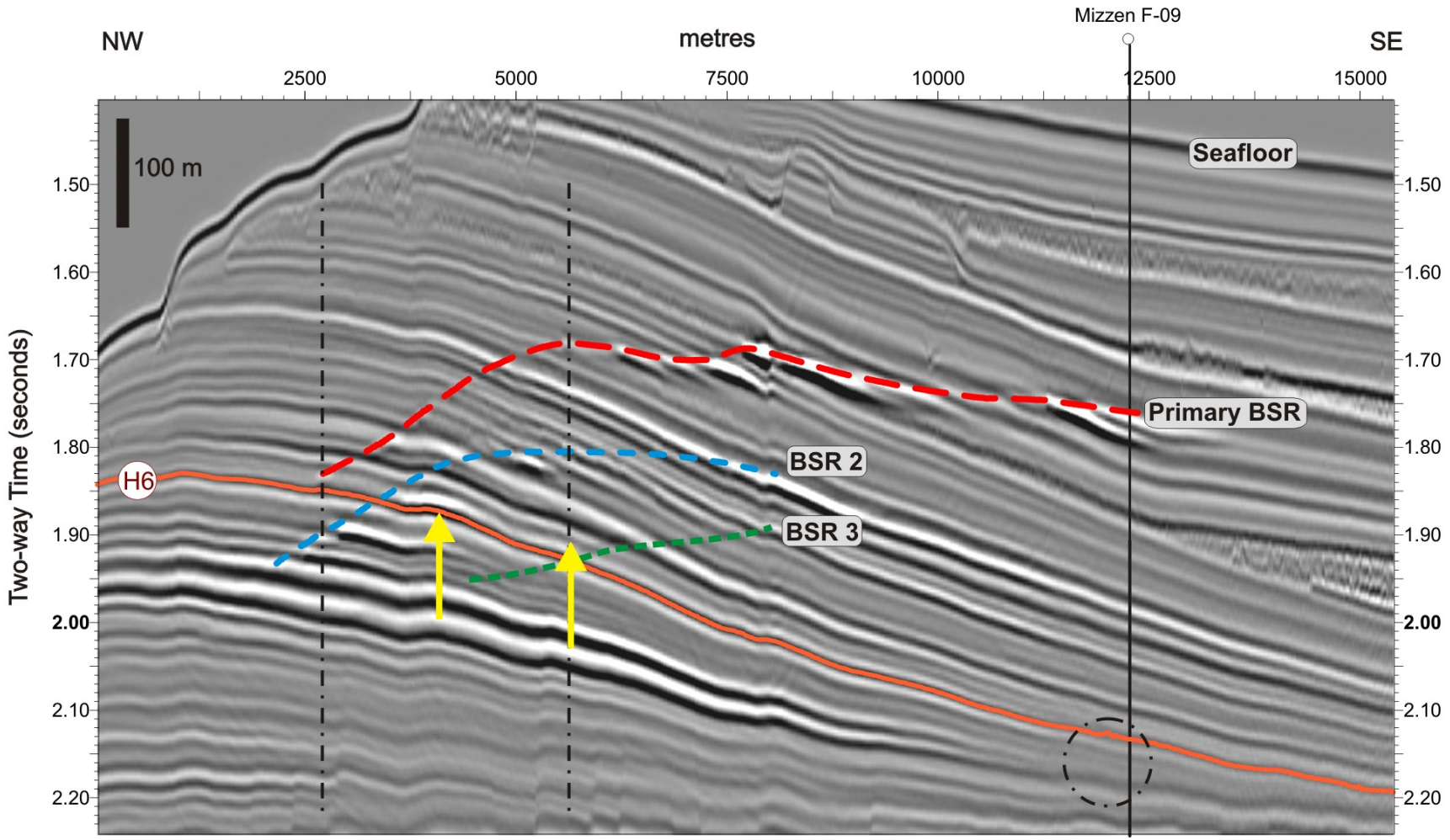

Figure 5.41 Arbitrary seismic profile through high amplitude, low frequency zones along the H6 horizon. The thin, vertical, dashed lines and dashed circle identify the areas of reduced frequencies discussed in the text. The yellow vertical arrows identify the high amplitude bands discussed in the text. Refer to Figure 5.39 and Figure 5.37 for profile location.

5.1.2.5 Horizon H5

Horizon H5 was interpreted along a continuous amplitude trough over most of the study area. In the northern most corner of the seismic volume, the H5 horizon has been disturbed or removed by sediment failures. Amplitudes along the horizon are elevated in the west and southeast (Figure 5.42) where troughs are visible on the depth structure map (Figure 5.43). An ovate area of high amplitudes below Flemsih Pass corresponds to a small basin that developed above the H5 horizon (Figure 5.51). The paleodrift structures observed along the underlying H7 horizon are apparent over the southeast portion of the H5 depth structure map (Figure 5.43). Along H5, the drift structures have less relief and are more subdued than along the H7 horizon indicating that the relief from the underlying morphological feature produced these troughs has been infilled compared to H7. The larger of the faults have minimal offsets along H5 although the fault traces are observed along the horizon's dip of maximum similary surface (Figure 5.44).

Small isolated pockmarks occur north of the modern crest of the Sackville Spur and on the flanks of the H5 paleo-crest (Figure 5.45 (A)). These pockmarks are also visible on the dip of maximum similarity surface (Figure 5.45 (B)).

The small basin or depocentre associated with elevated H5 amplitudes is more apparent on the instantaneous frequency map of Figure 5.46 where a second basin is visible to the north. Sediment failure tracks, visible in the northwest and southwest, appear to feed these basins (Figure 5.47 and Figure 5.48). The failure tracks are more abundant in the south where a thin MTD overlies H5 (Figure 5.49).

H5 marks a change in deposition with the onset of MTDs and increased deposition in the base of the Pass. Deposition was concentrated on the margins of the Pass below H5, particularily at the Sackville Spur, with thick drift deposits that thinned and pinched out within the Pass (Figure 5.50). Planar divergent reflections above H5 do thin from the flanks to the base of the Flemish Pass (Figure 5.51) but less dramatically as a lobe of MTD derived sediments (Figure 5.49) develops in the base of the Pass (Figure 5.52).

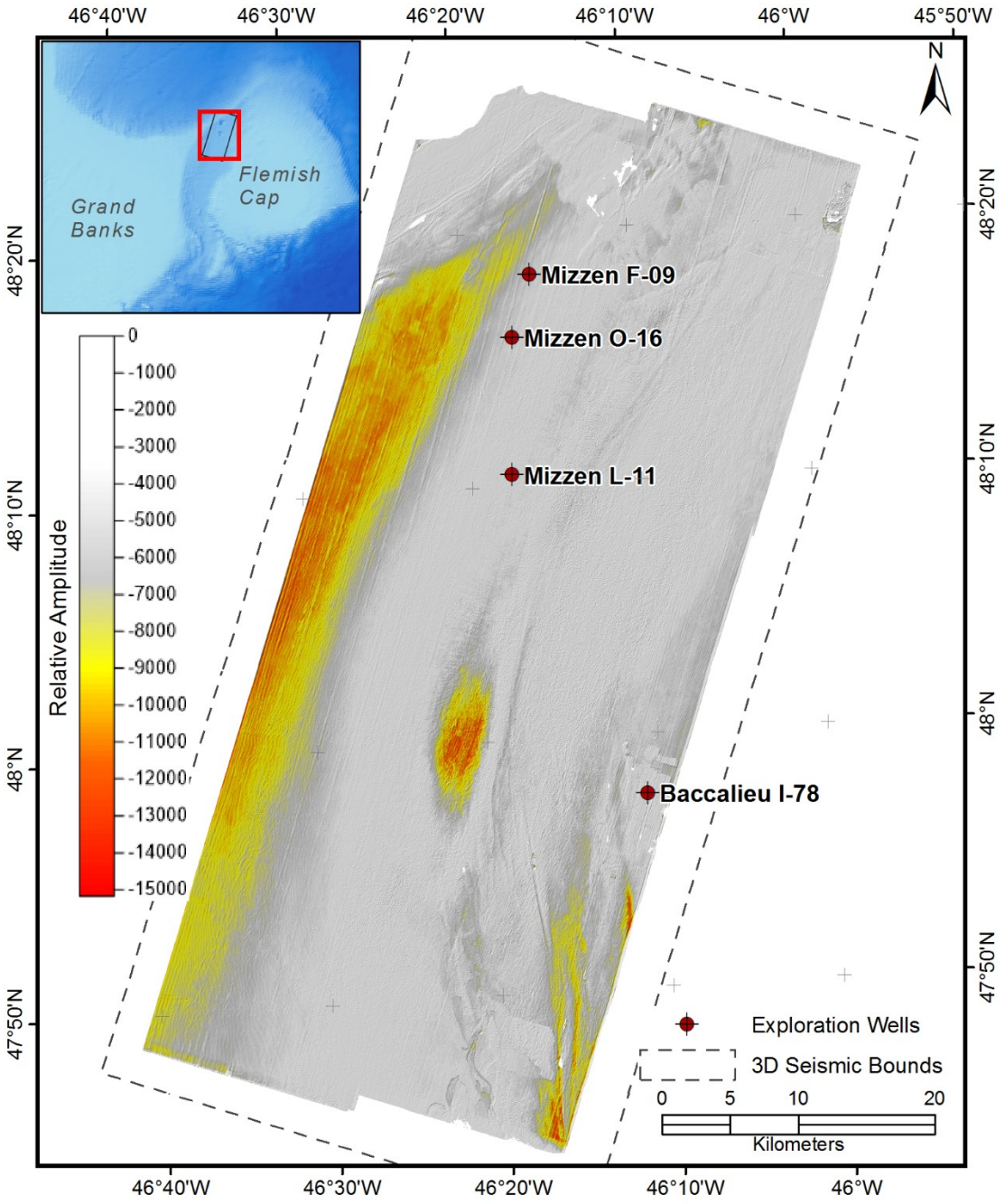

Figure 5.42 Relative amplitude along the H5 horizon.

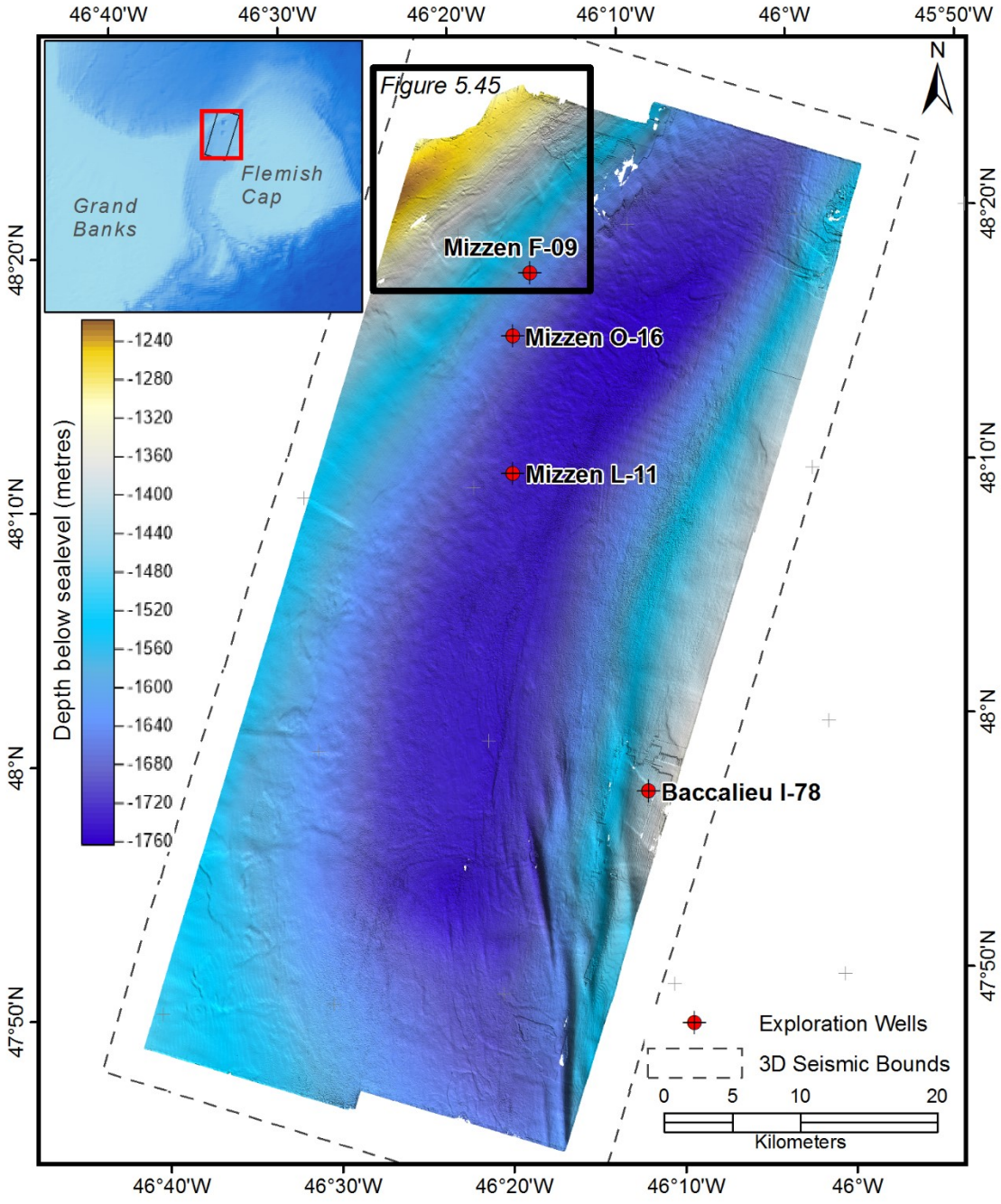

Figure 5.43 Depth structure along the H5 horizon.

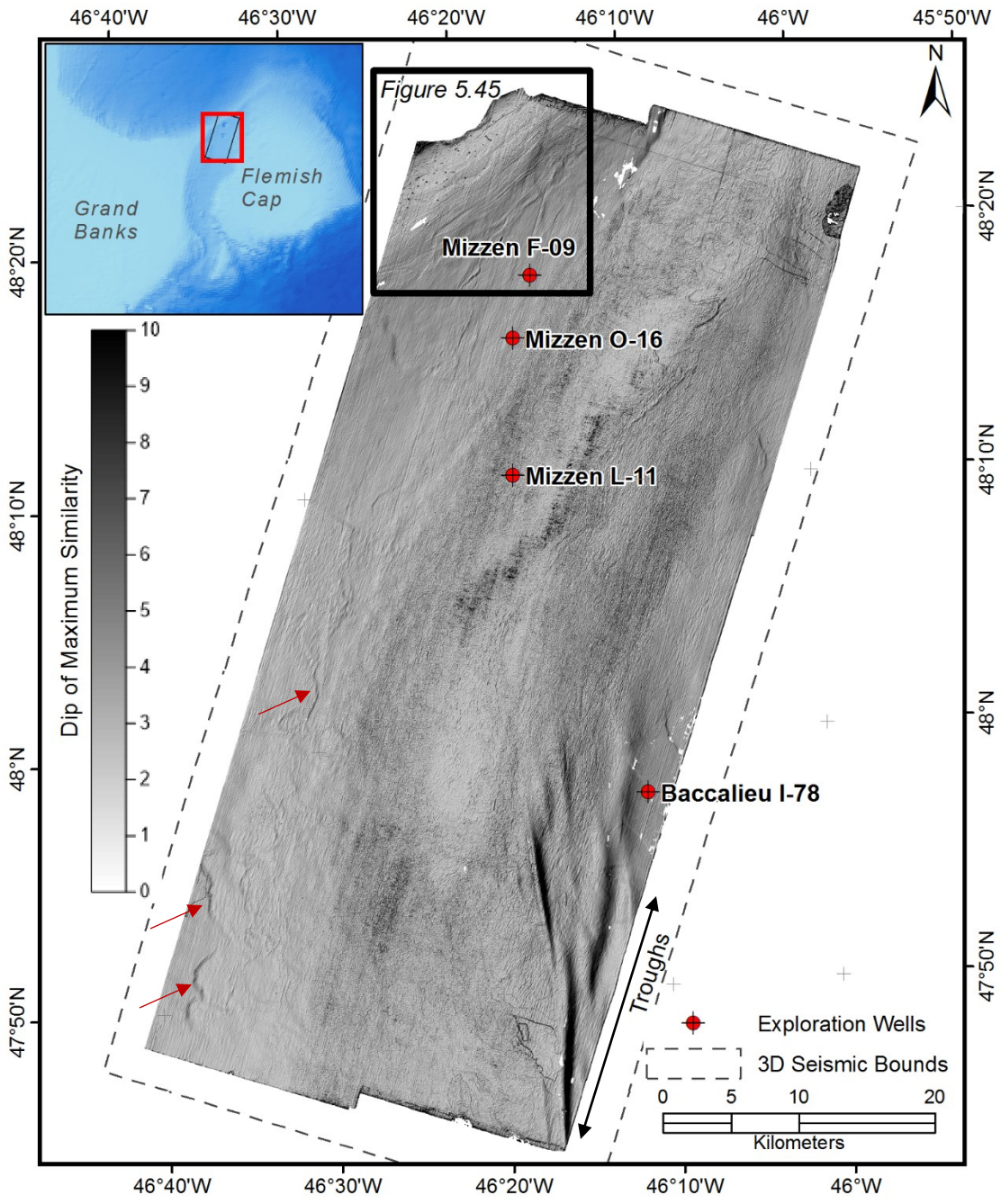

Figure 5.44 Dip of maximum similarity along the H5 horizon. The red arrows highlight faults discussed in the text. The black box delimits the area of Figure 5.45.

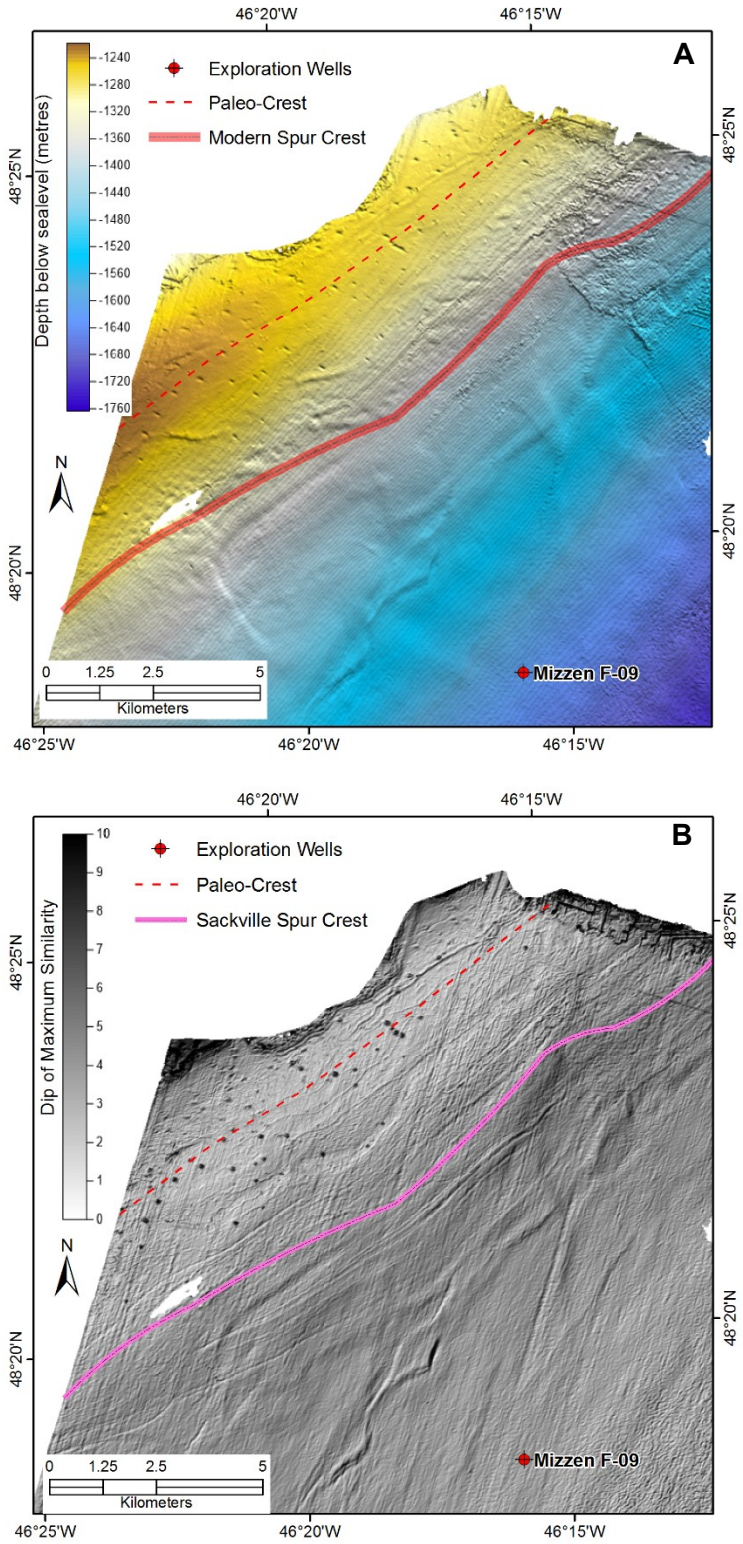

Figure 5.45 Detail of H5 depth structure (A) and dip of maximum similarity (B) showing pockmarks north of the modern crest of the Sackville Spur. Refer to **Figure 5.43** for map location.

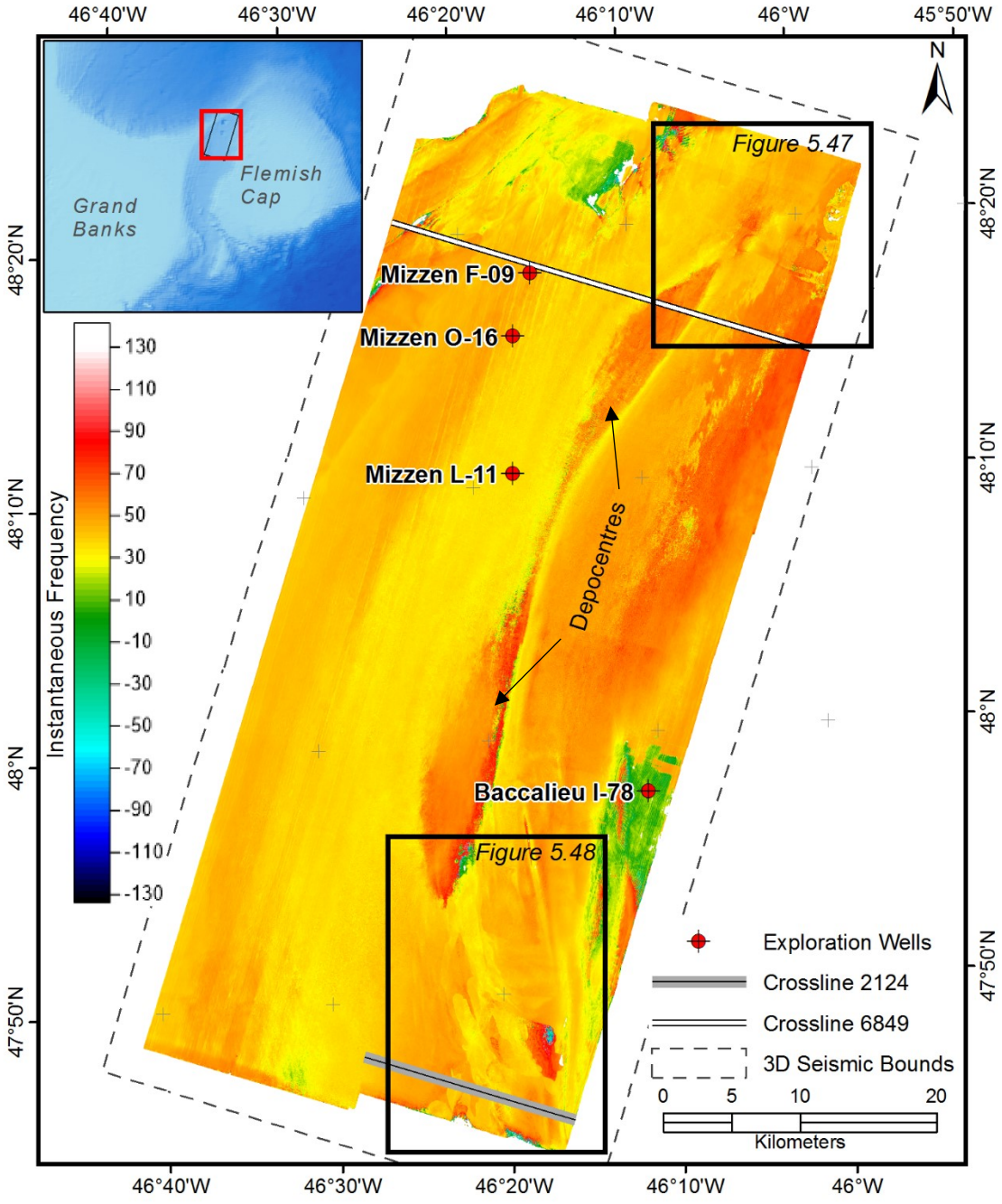

Figure 5.46 Instantaneous frequency along the H5 Horizon. The black rectangles delimit areas shown in **Figure 5.47** and Figure 5.48.

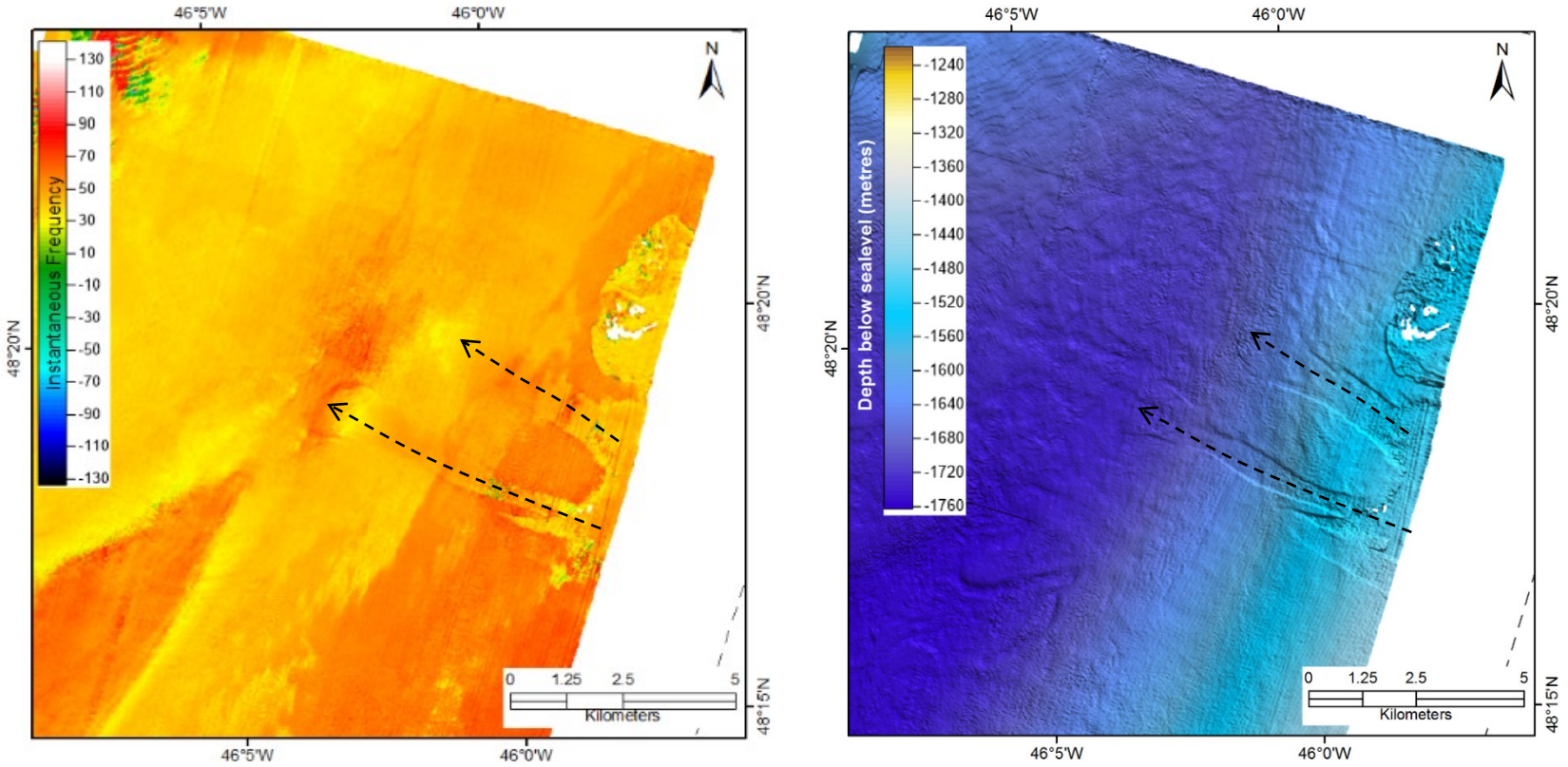

Figure 5.47 Detail of Instantaneous frequency (left) and depth structure (right) along the H5 horizon showing sediment failure tracks (black dashed arrows) over the NE portion of the 3D seismic. Refer to **Figure 5.46** for map location.

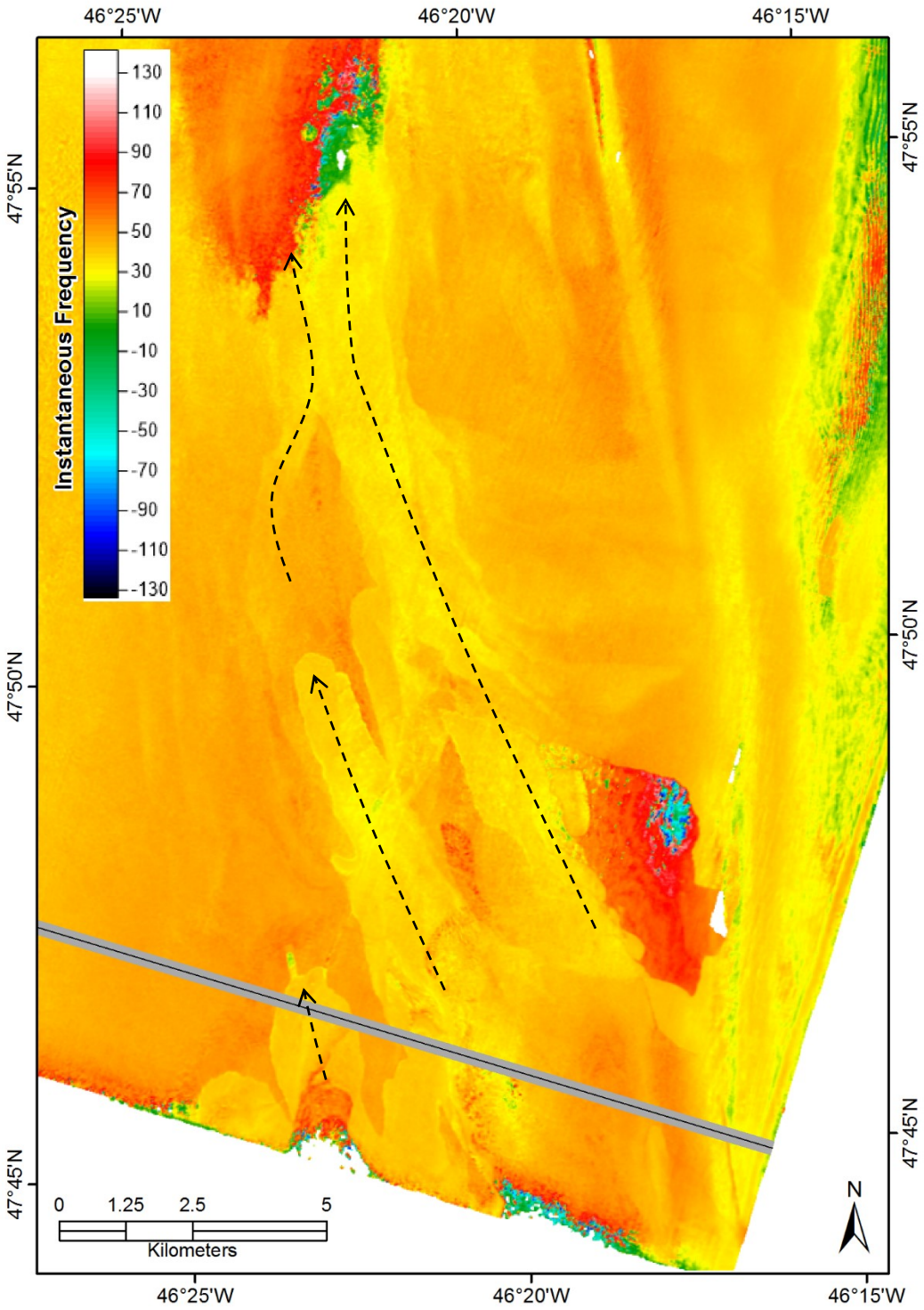

Figure 5.48 Detail of instantaneous frequency along the H5 horizon showing sediment failure tracks (black dashed arrows) in the SE corner of the 3D seismic volume. Refer to Figure 5.46 for map location. The grey line shows the location of the seismic profile presented in Figure 5.49.

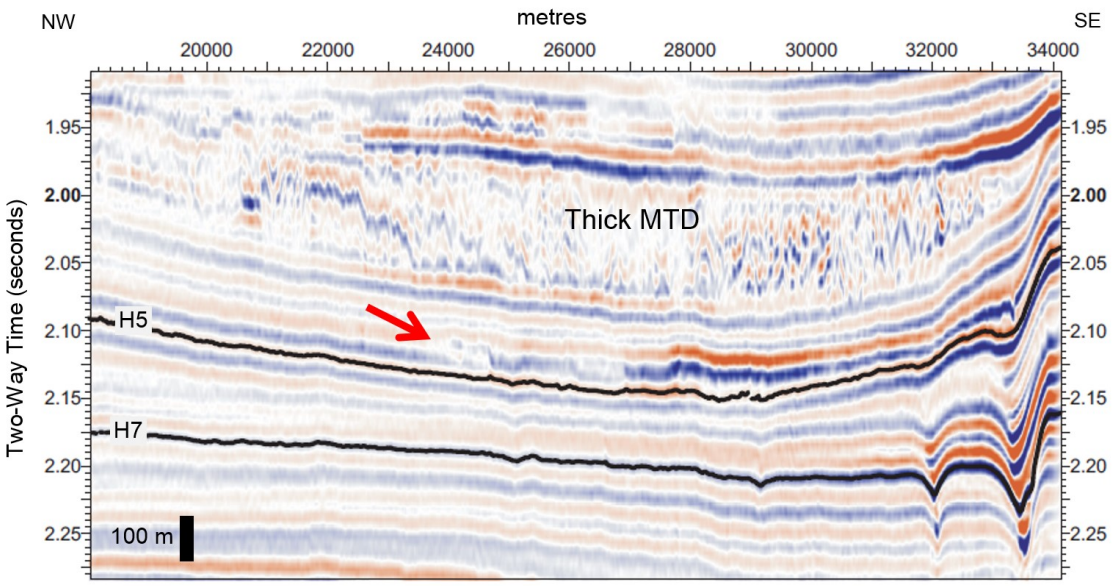

Figure 5.49 Portion of Crossline 2124 showing a thin MTD (red arrow) overlying the H5 horizon. A significantly thicker MTD is imaged above this thin MTD.. Refer to **Figure 5.46** for the profile location.

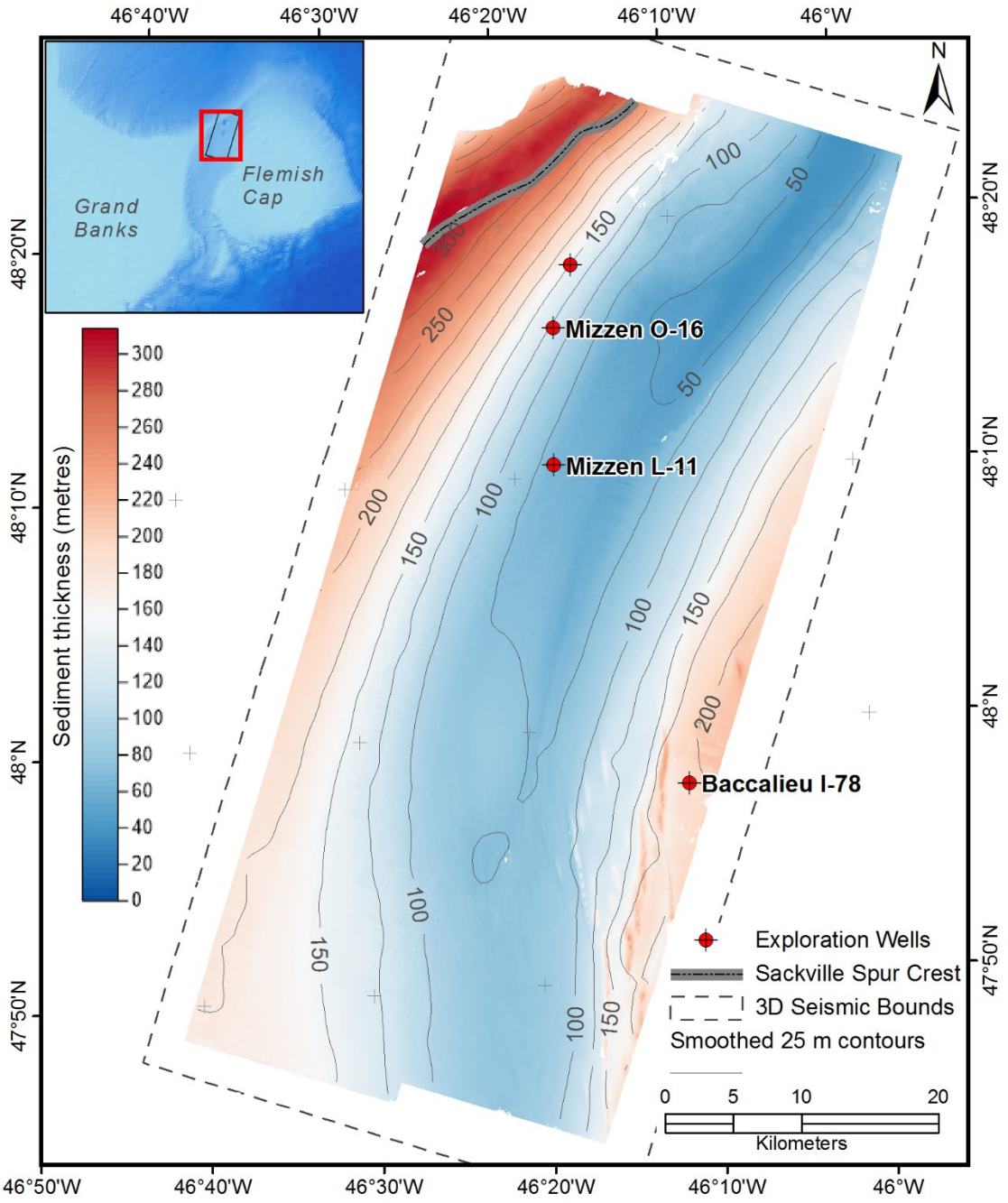

Figure 5.50 Isopach (thickness) map between the H7 and H5 horizons.

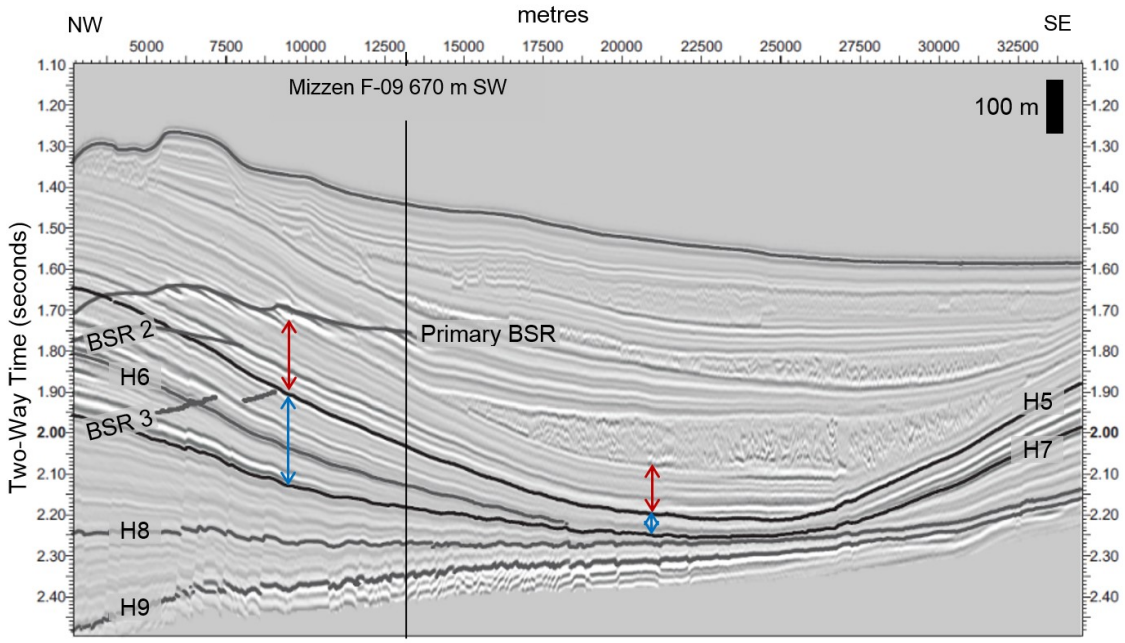

Figure 5.51 Crossline 6849 showing the increased accumulation in the Flemish Pass above the H5 horizon. Refer to **Figure 5.46** for the profile location.

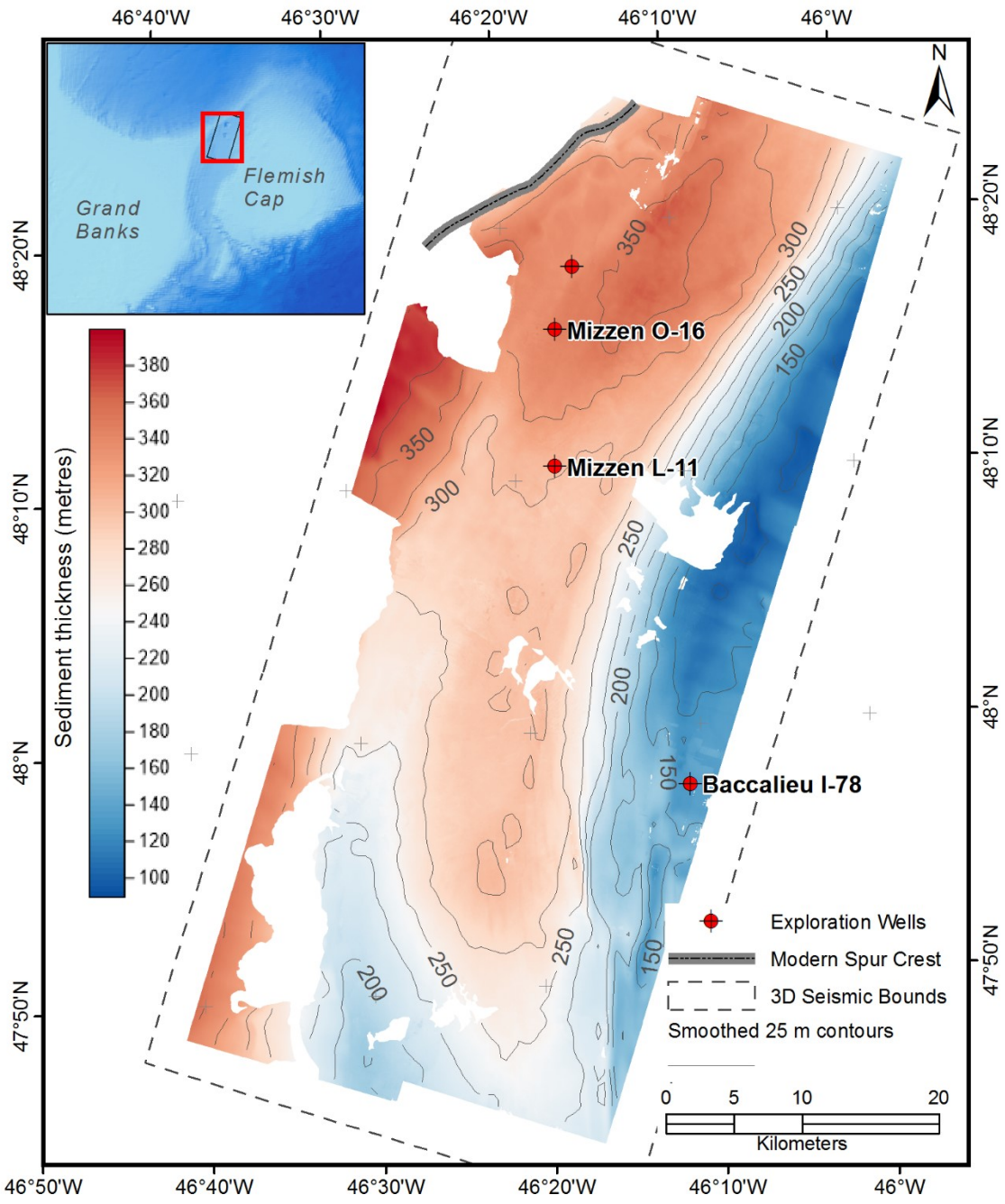

Figure 5.52 Isopach (thickness) map between the H5 and H1 horizons.

5.1.2.6 Horizon H4

Horizon H4 was interpreted along a high amplitude trough and is present over most of the 3D seismic volume. The horizon was eroded by mass transport deposits in the northwest corner of the study area. Below the western flank of Flemish Pass, mass transport scars are visible on the H4 depth structure map (Figure 5.53). Although not well developed, the sediment drift structures observed in the southeast along deeper horizons are still visible on the H4 depth structure map (Figure 5.53). Detailed inspection of the depth structure map shows pockmarks are present in the northwest corner of the study area, (Figure 5.54). The pockmarks are shown to extend further south on the H4 amplitude map of Figure 5.55.

An increased density of pockmarks are associated with an area of elevated amplitudes and reduced instantaneous frequencies (Figure 5.56). The decreased frequencies are roughly bound north and south by NE-SW lineations. On seismic profiles, this zone of decreased frequencies and elevated amplitudes is the result of reflection enhancement (constructive interference) associated with the three BSRs; the western lineation corresponds to the horizon's intersection with the primary BSR while the eastern lineation correlates with BSR 2 in the north and BSR 3 in the south.

Elsewhere within the 3D seismic volume, elevated amplitudes associated with thin mass movement events occur in the central and southeast portions of the study area (Figure 5.57) where MTD failure tracks occur on the underlying H5 horizon. Similarly in the north, sediment failure tracks represent the top of a thin mass transport deposit the base of which is observed along the H5 horizon (Figure 5.45). The H4 instantaneous frequency surface shows evidence of further sediment failures over the northeastern portion of the study area (Figure 5.58).

Below Flemish Pass there is an abrupt change to reduced frequencies (Figure 5.58) that corresponds to a change in texture on depth structure map (Figure 5.53). The western edge of the zone of reduced frequencies is very abrupt and is associated with a slight mistie where the horizon enters a basin at the base of Flemish Pass. This basin is larger and has more north-south continuity along the H4 horizon (Figure 5.58) than along the H5 horizon,

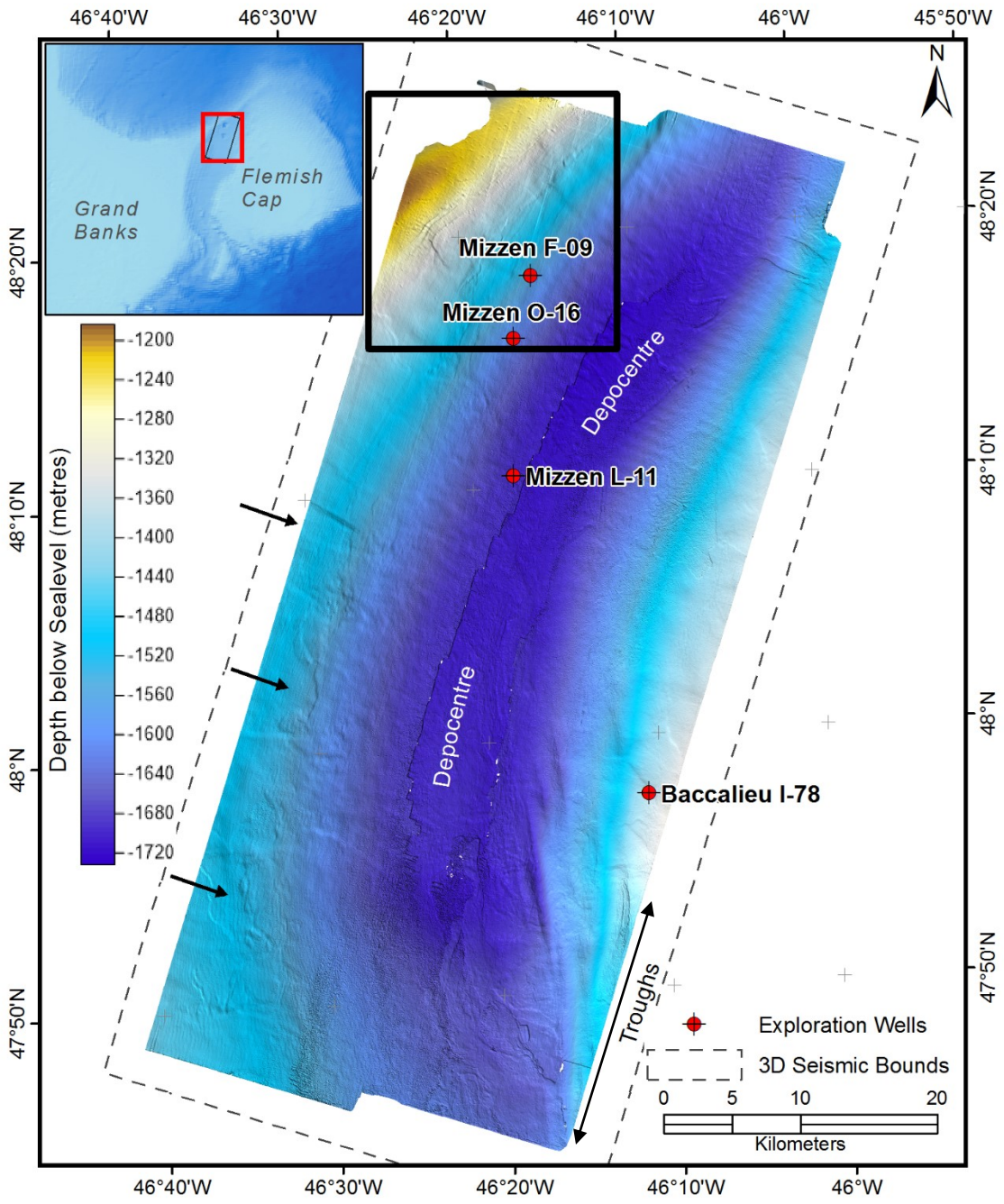

Figure 5.53 Depth structure along the H4 horizon. Black arrows highlight subtle mass transport deposits discussed in the text. Black box shows the location of Figure 5.54.

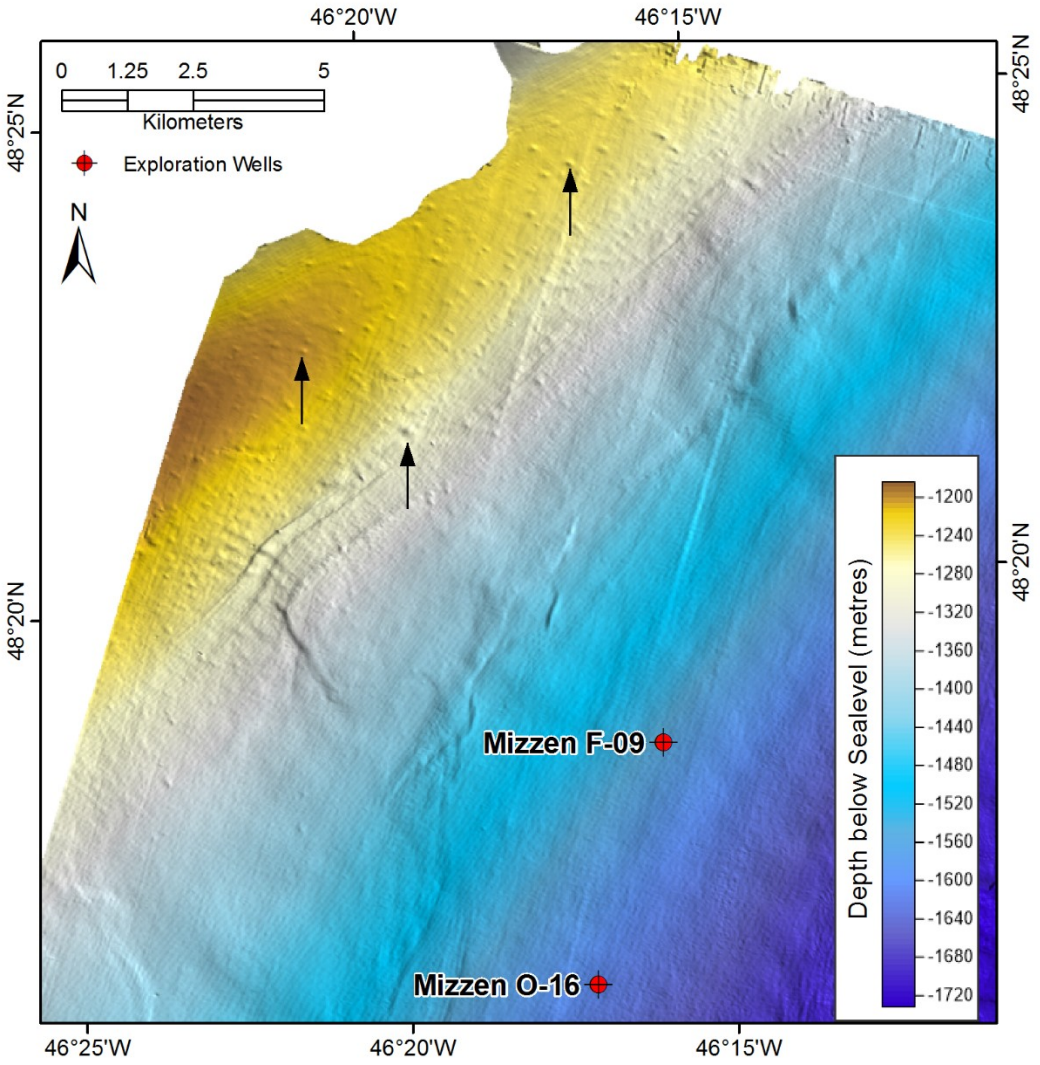

Figure 5.54 Detailed depth structure along the H4 Horizon. The white arrows highlight select pockmarks. Refer to **Figure 5.53** for map location.

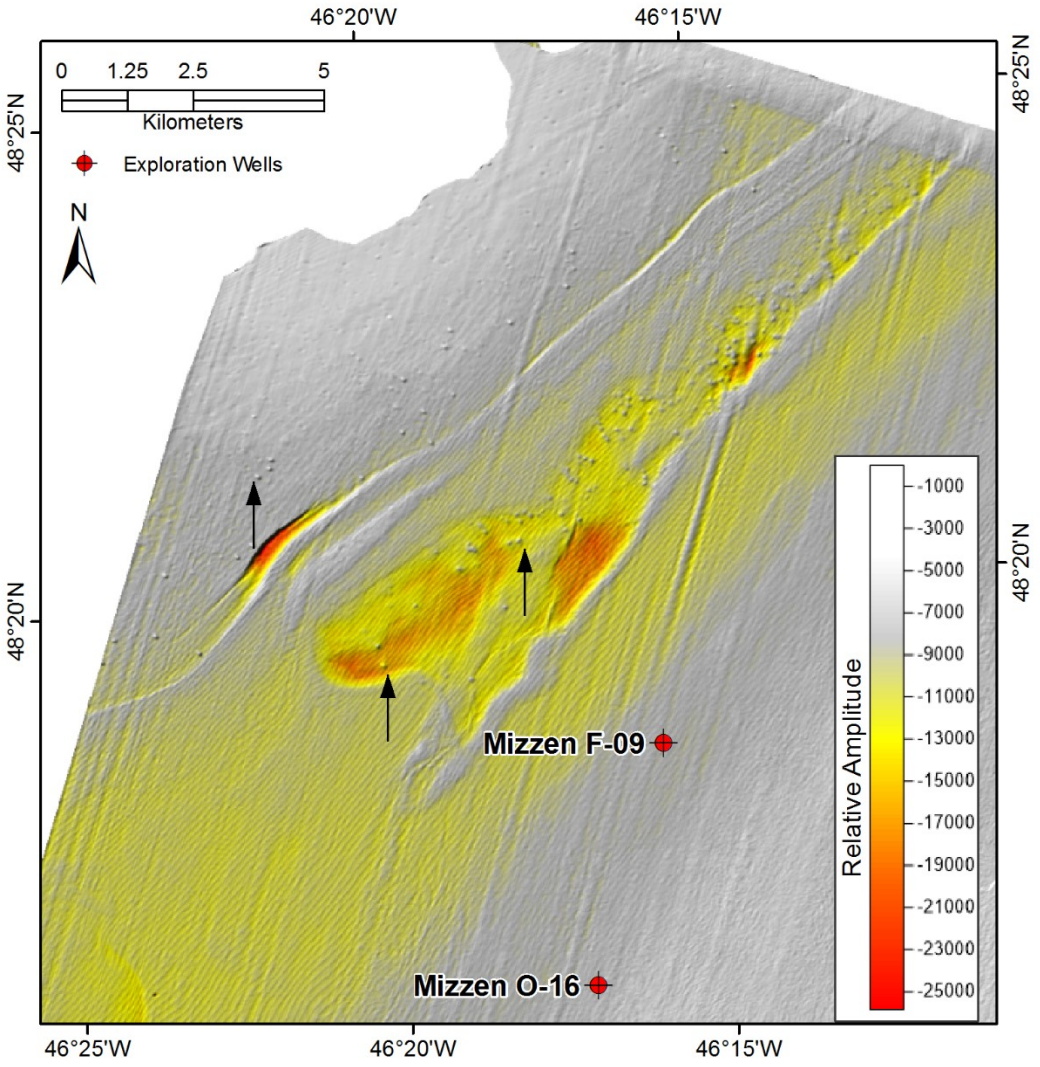

Figure 5.55 Detail of relative amplitudes along the H4 Horizon. The black arrows highlight select pockmarks. Refer to Figure 5.57 for map location.

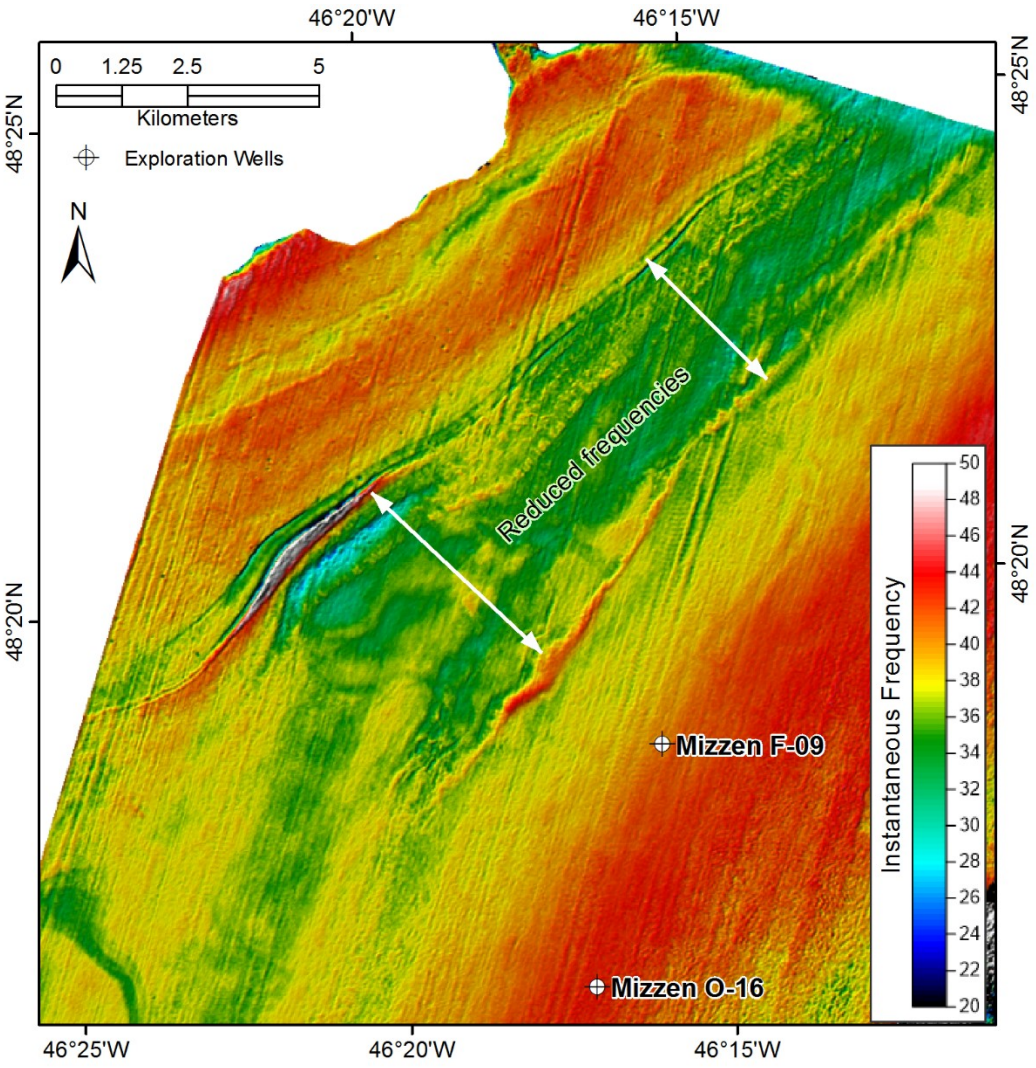

Figure 5.56 Detail of instantaneous frequency along the H4 horizon showing an area of reduced frequencies discussed in the text. Refer to Figure 5.58 for map location.

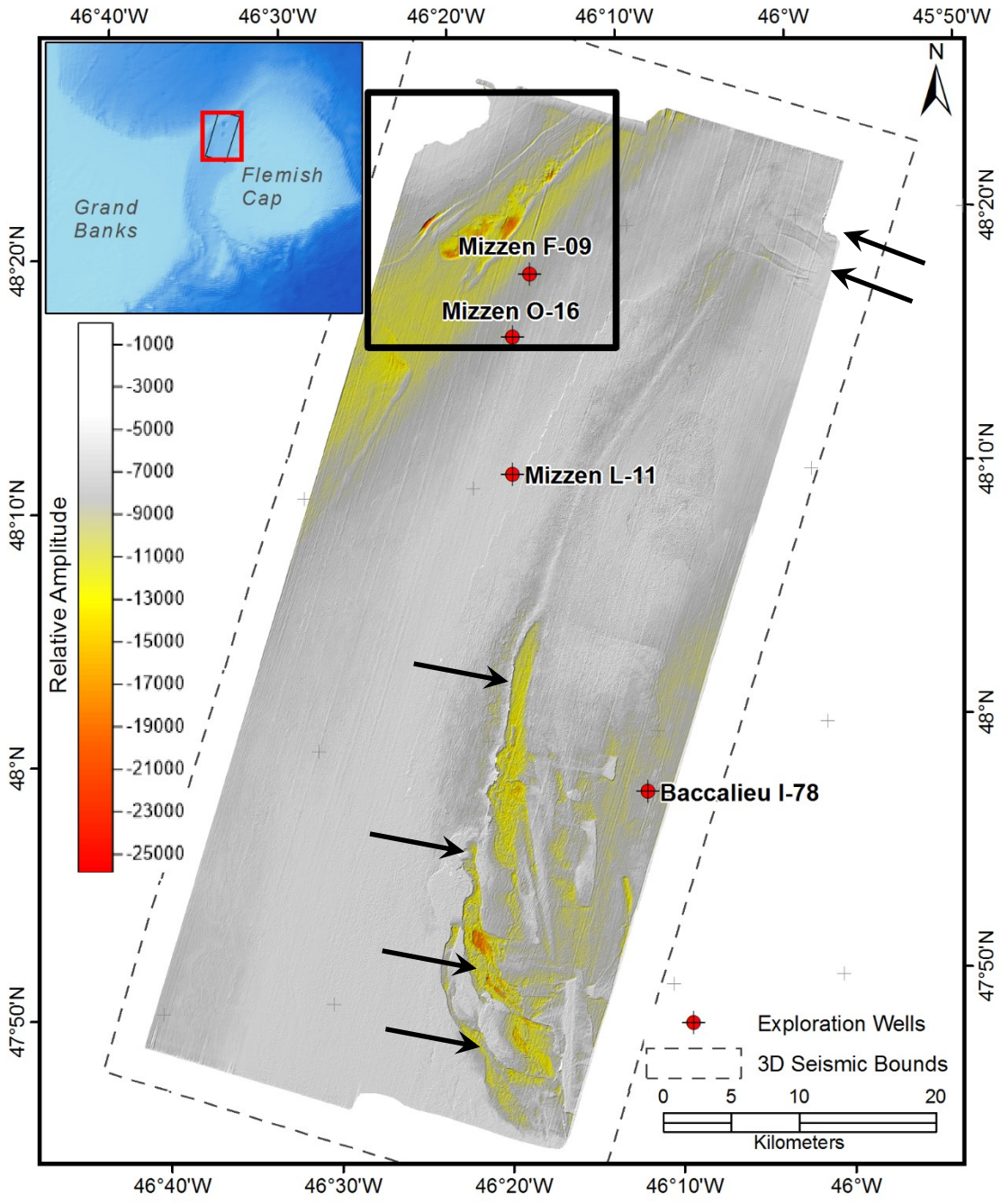

Figure 5.57 Relative amplitudes along the H4 Horizon. The black box shows the location of Figure 5.55. The black arrows highlight MTDs discussed in the text.

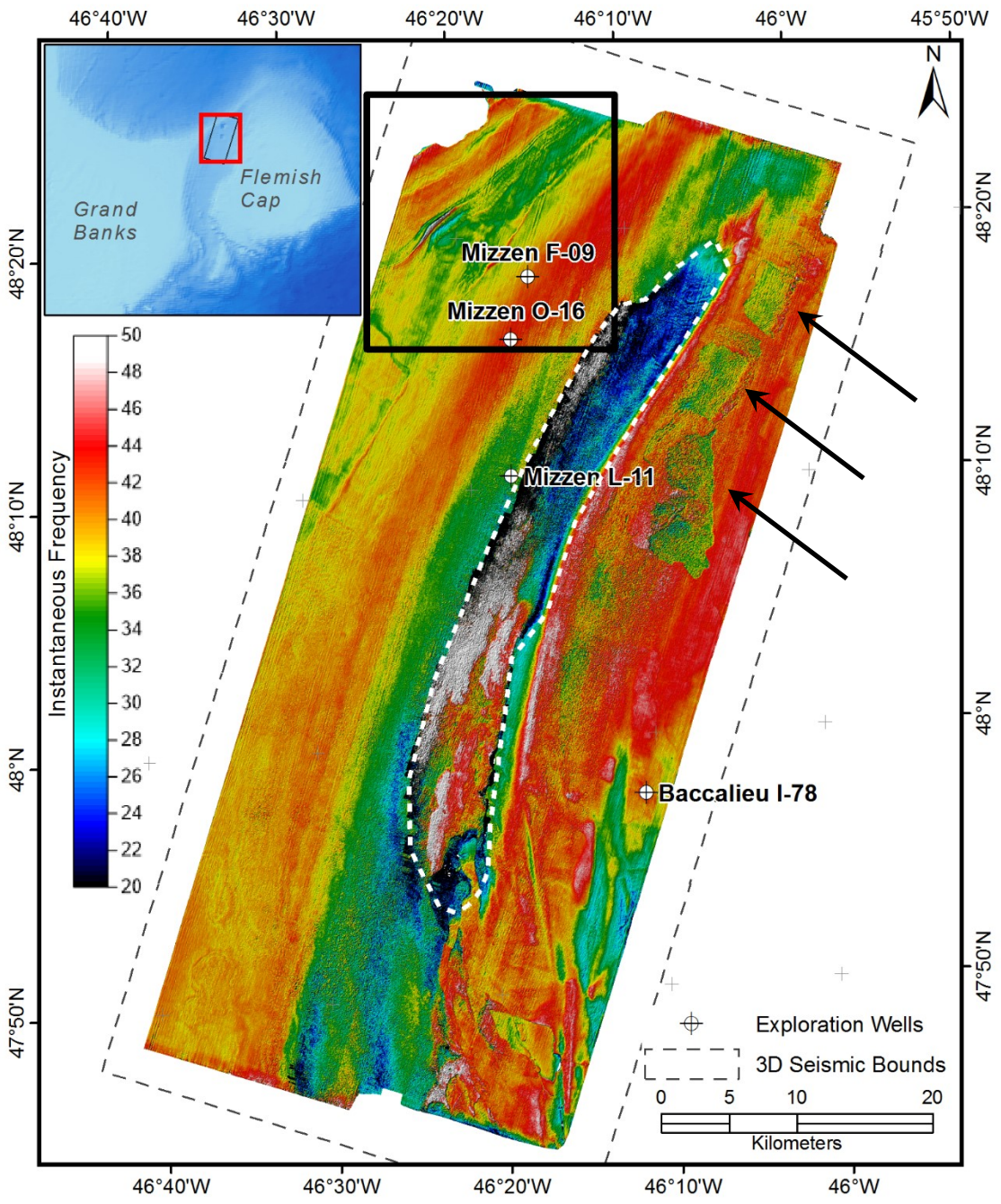

Figure 5.58 Instantaneous frequency along the H4 horizon. The black arrows highlight mass transport deposits discussed in the text while the white dashed line outlines the basin discussed in the text. The black box shows the location of Figure 5.56.

5.1.2.7 Horizon H3

Horizon H3 was interpreted along a low to moderate amplitude peak that is continuous in the west and becomes increasingly discontinuous to the east. The H3 horizon could not be mapped over the eastern half of the study area as the horizon was both removed by mass transport deposits and pinches out. Similarly, in the northwest corner of the 3D seismic, the horizon was eroded by mass transport deposits. Small data gaps are also present in the northwest where H3 intersects the BSR. The phase reversal associated with the BSR is so robust that the horizon could not always be picked through the BSR.

The depth structure along H3 mimics that of the underlying H4 horizon; a broad paleo drift the crest of which is north of the modern spur's crest (Figure 5.59). The isolated ovate area in the east represents the basin in Flemish Pass that is also observed on the underlying horizons (Figure 5.59). The size of the basin is reduced relative to the underlying H4 horizon.

Amplitudes along H3 are relatively low throughout the study area with bands of elevated values in the northwest where the horizon intersects the BSR (Figure 5.60). Instantaneous phase along H3 shows slightly positive phase increases where the horizon intersects the BSR (Figure 5.61). Amplitudes are also elevated in the east where H3 moves into the basin at the base of Flemish Pass (Figure 5.60).

Instantaneous frequencies along H3 show a distinct frequency change where the horizon intersects the BSR (Figure 5.62). Where this intersection occurs, the instantaneous frequencies are reduced in the north and elevated in the south (Figure 5.63). This narrow zone of distinct frequencies trends roughly NE-SW except where the low frequency bands form a SE protruding lobe. This lobe occurs where the BSR and H3 intersection extends further south (Figure 5.63).

Elsewhere along the H3 horizon, the instantaneous frequency map of Figure 5.62 shows elevated values north and south of the BSR intersection. These high values occur within the BSR extends. Elevated instantaneous frequency values over the eastern portion of the horizon are associated with a thick overlying MTD (Figure 5.1). The edges of the MTDs are well defined on the instantaneous frequency map (Figure 5.62) as well as the dip of maximum similarity map (Figure 5.64). Over the south-central portion of the horizon, it is disturbed by the overlying MTD and appears chaotic on all H3 maps. No evidence of pockmarks are imaged along the H3 horizon, although subtle current scours occur north of the horizon's intersection with the BSR (Figure 5.63).

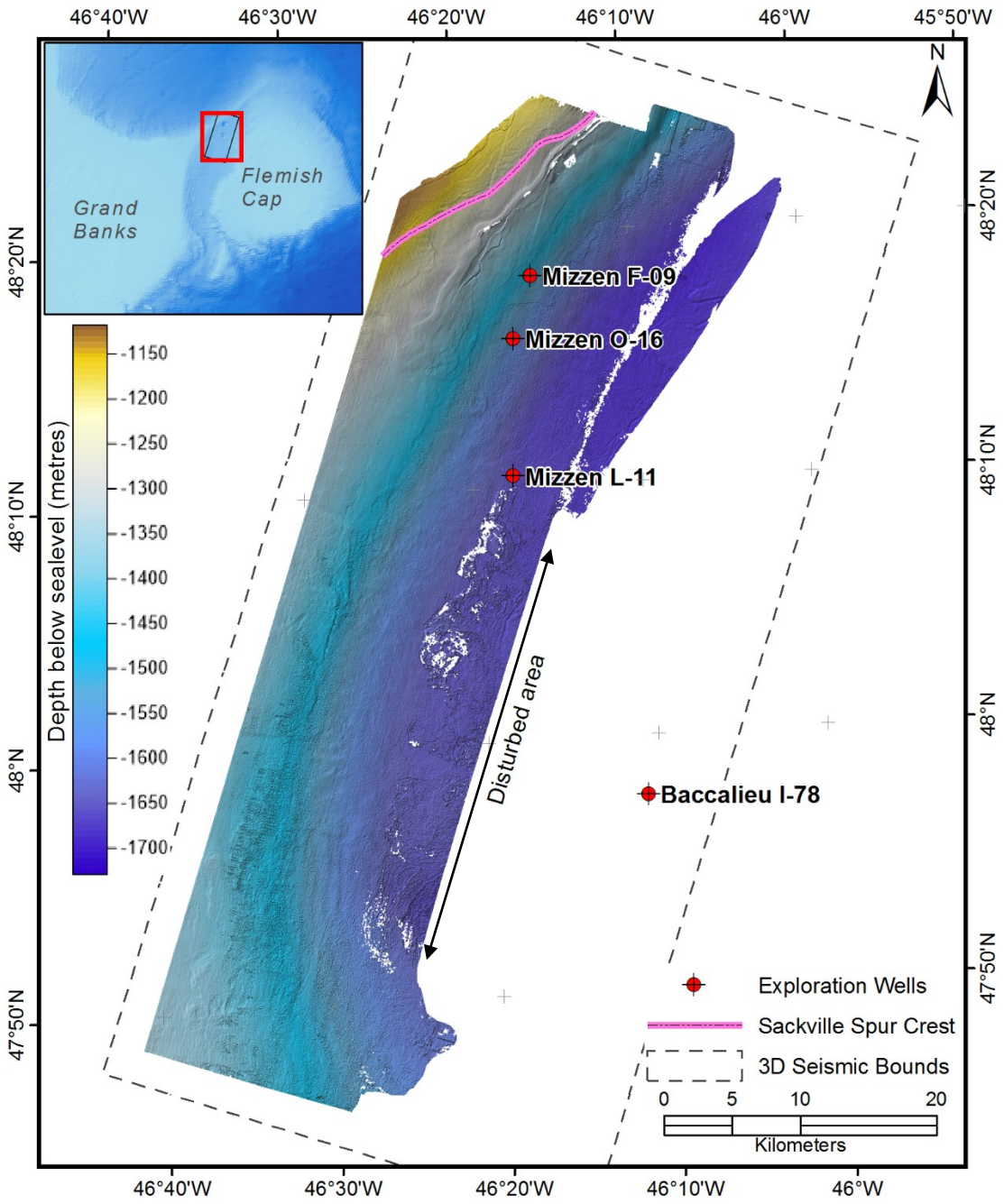

Figure 5.59 Depth structure along the H3 horizon.

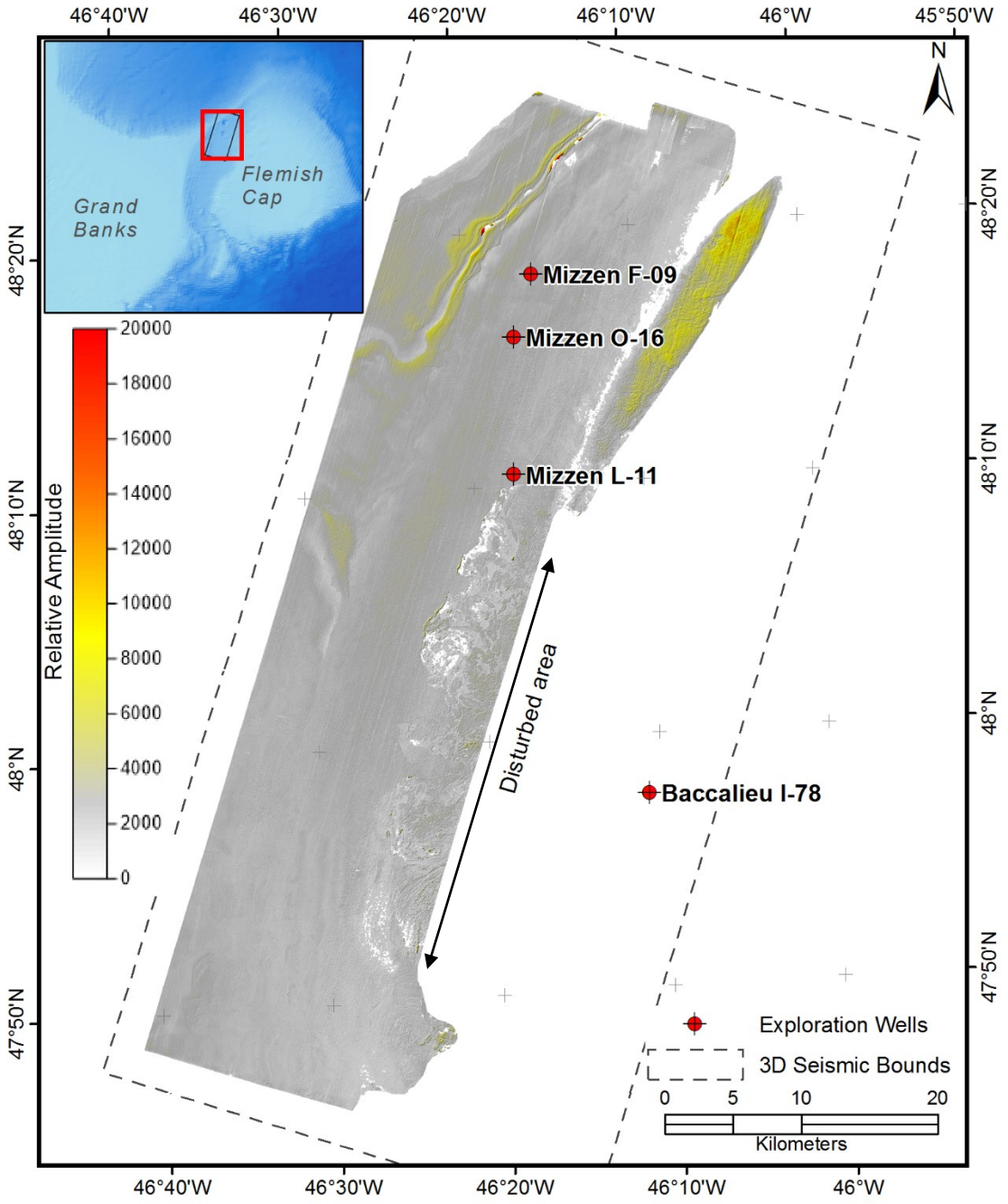

Figure 5.60 Relative amplitude along the H3 horizon.

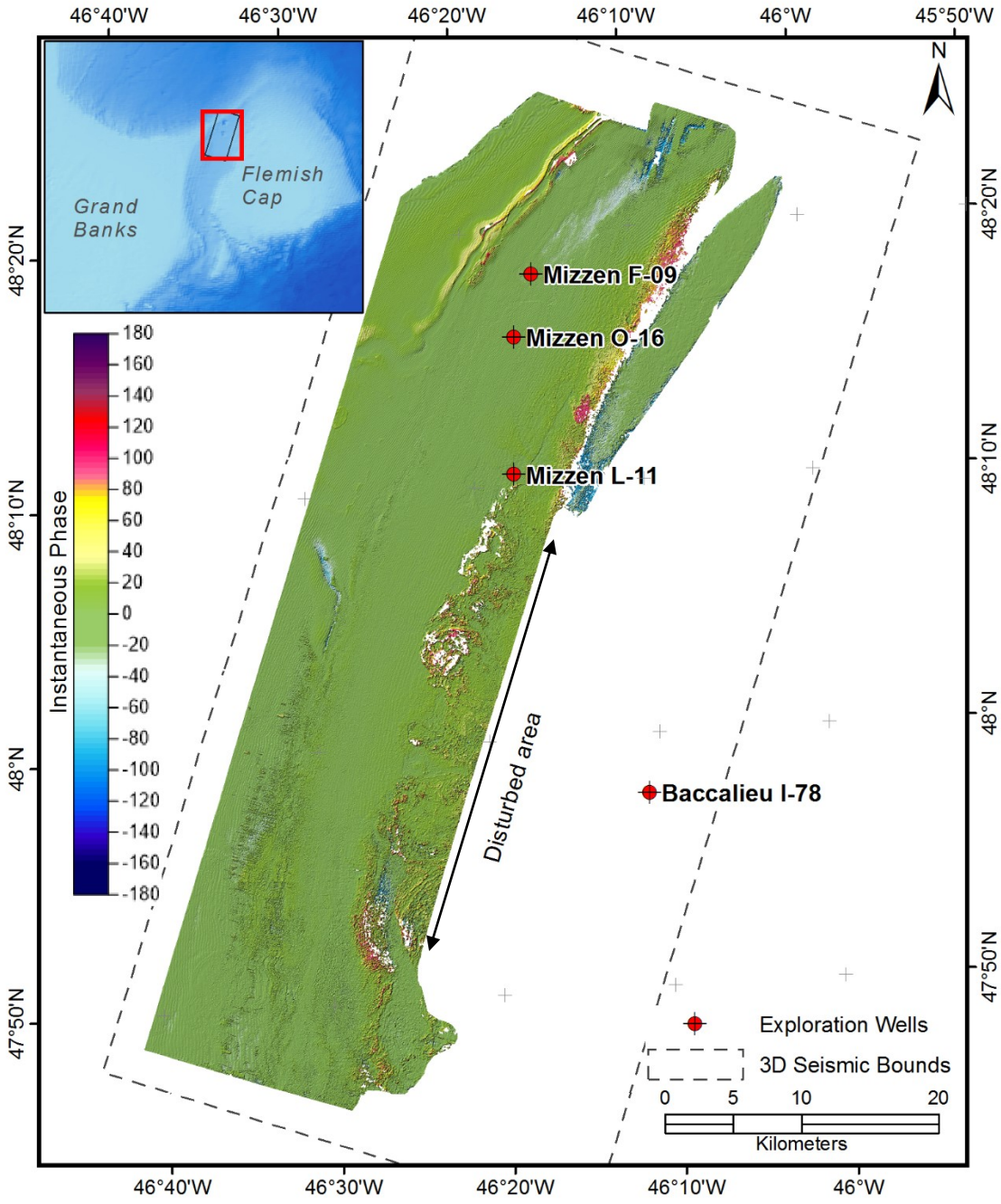

Figure 5.61 Instantaneous Phase along the H3 horizon.

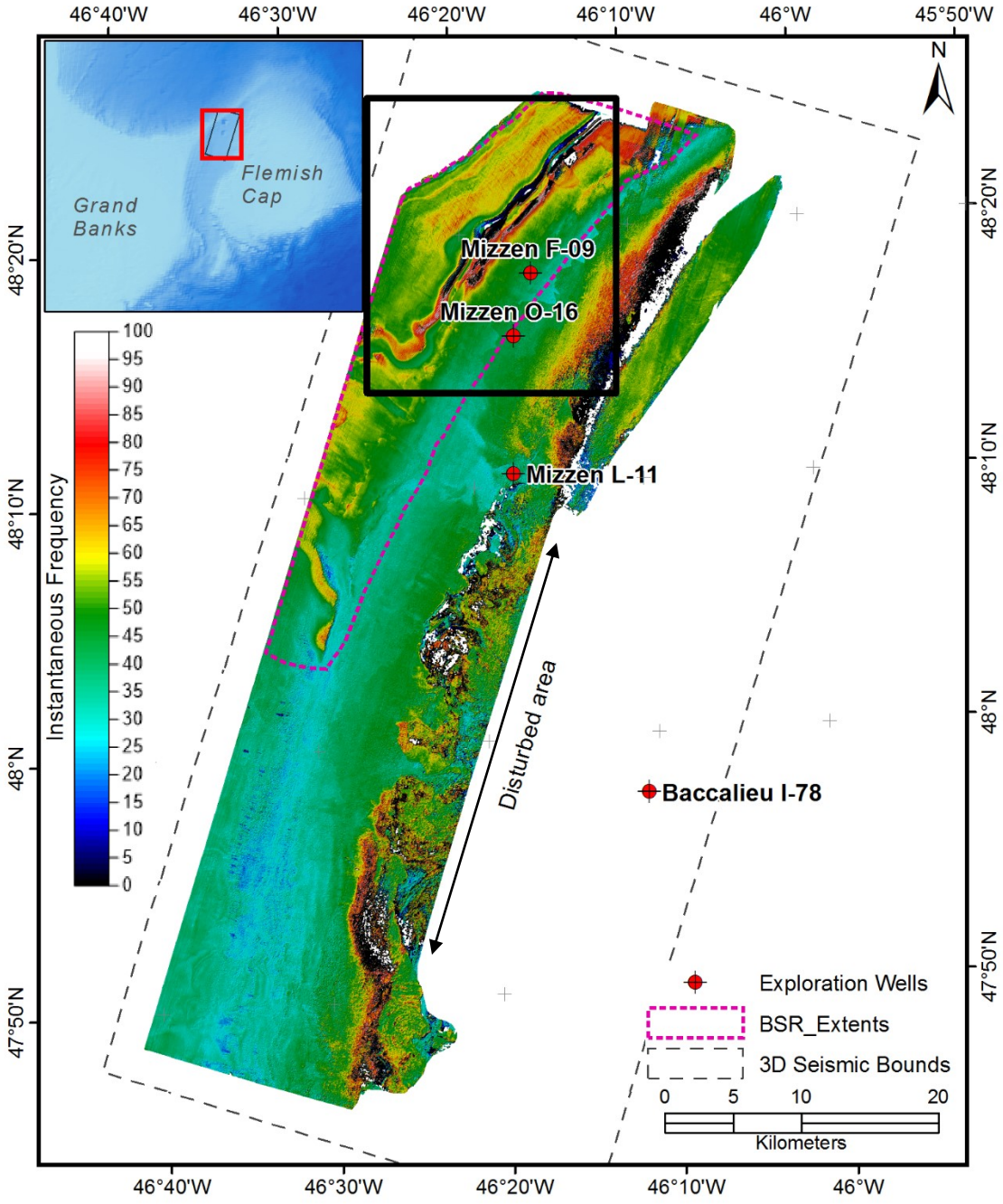

Figure 5.62 Instantaneous Frequency along the H3 Horizon. The black box shows the location of Figure 5.63.

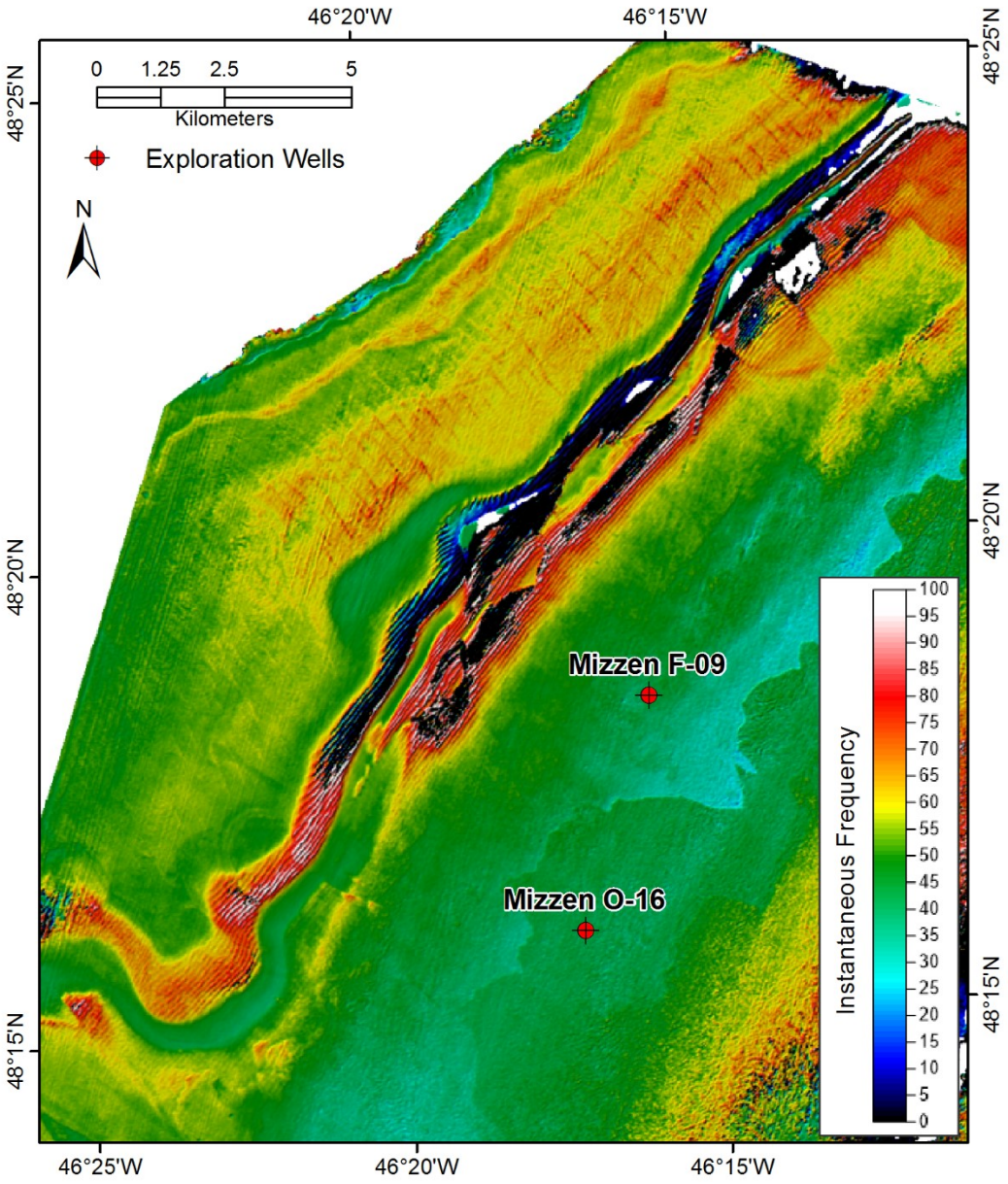

Figure 5.63 Detail of Instantaneous Frequency along the H3 Horizon. Subtle NW-SE trending lineations north of the band of reduced frequencies represent current scours. Refer to Figure 5.62 for map location.

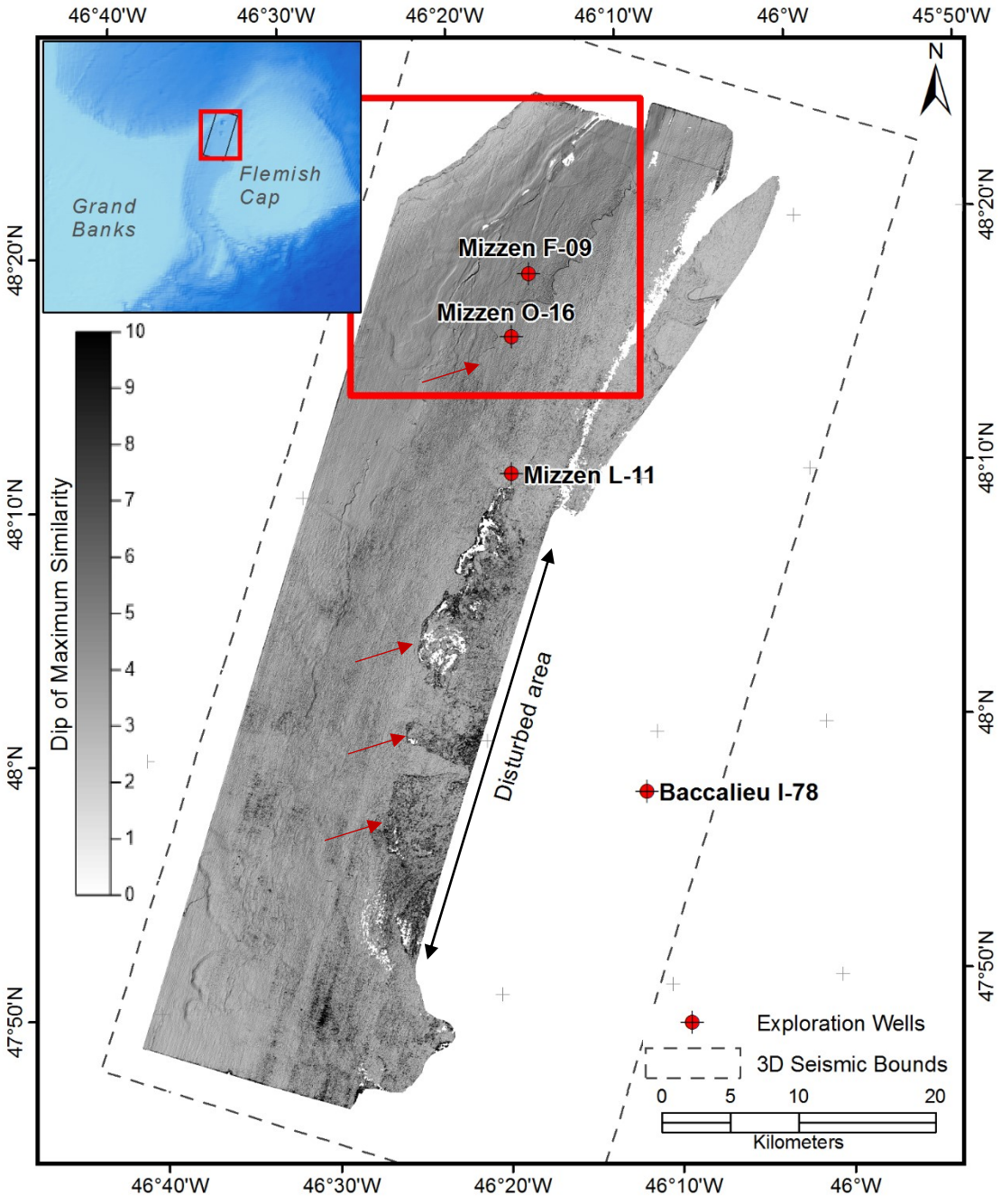

Figure 5.64 Dip of Maximum similarity along the H3 Horizon. Arrows highlight lineations marking the western limit of MTD-influenced sediments. The red box shows the location of Figure 5.65.

.

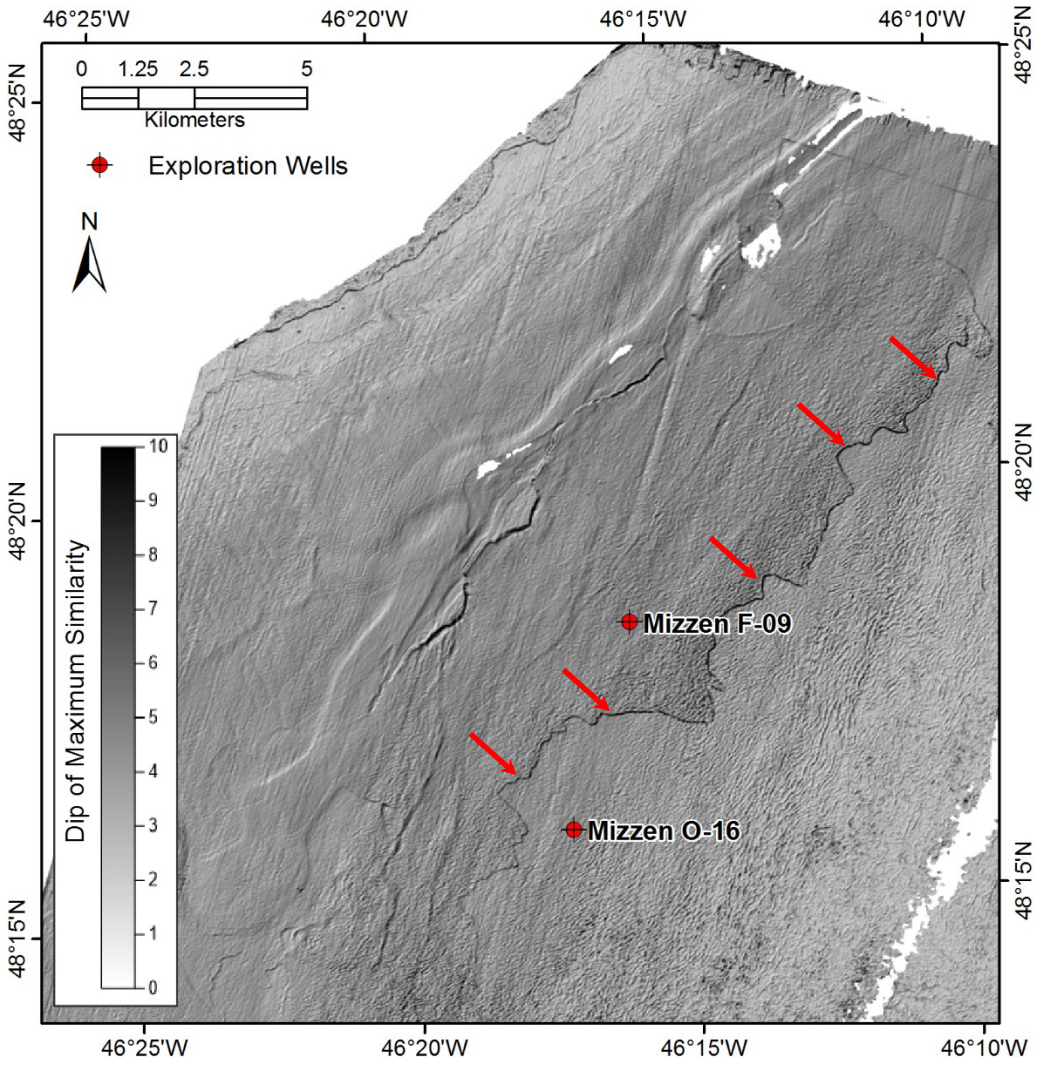

Figure 5.65 Detail of dip of maximum similarity along the H3 horizon Arrows highlight a lineation (escarpment) marking the western limit of MTD influenced sediments. Refer to Figure 5.64 for map location.

5.1.2.8 Horizon H2

The H2 horizon was interpreted over the northwestern portion of the 3D seismic volume along a continuous amplitude trough. H2 could not be extended through the Flemish Pass where horizons thin and are not resolved. Northwest of the exploration wells a distinct escarpment is apparent on the H2 depth structure map (Figure 5.66). 3D seismic profiles show chaotic reflections between H2 and the underlying H3 horizon that are interpreted as MTDs(Figure 5.67). The elevated areas northwest of this escarpment

represent remnants of original stratigraphy not removed by the MTD. H2 drapes these older failure scarps (Figure 5.67).

Pockmarks, visible on the depth structure (Figure 5.66) and dip of maximum similarity surfaces (Figure 5.69) are most abundant and largest northwest of the escarpment discussed above (Figure 5.68). The pockmarks are elongated and associated with lineations whose orientations parallel the pockmark's axis of elongation (Figure 5.68). Atop the paleo Spur, which is north of the modern Spur, the pockmarks and lineations trend NW-SE. The trend of the pockmarks and lineations shifts to N-S with increasing depth.

In addition to the pockmarks and lineations, the dip of maximum similarity shows a distinct line marking a change from greater similarity (darker colours) northwest of the F-09 well and reduced similarity (lighter colours) southeast of the F-09 well (Figure 5.69). This line corresponds to the inflection along H2 where dips decrease as the horizon goes into the paleo Flemish Pass. This line also corresponds to the primary BSR limits (Figure 5.69).

Amplitudes along H2 are low to moderate except for elevated bands associated with the intersection with the primary BSR (Figure 5.70). Low H2 amplitudes in the east and south correspond with reduced H2 instantaneous frequencies and occur where the sediments containing the H2 horizon thin into the Pass. Instantaneous frequencies decrease and become less consistent in the south (Figure 5.71). This area also has slightly elevated amplitudes and a rougher texture on the depth structure map (Figure 5.66) and similarity surfaces (Figure 5.69). 3D seismic profiles show these areas correspond to regions of underlying chaotic MTDs (Figure 5.67).

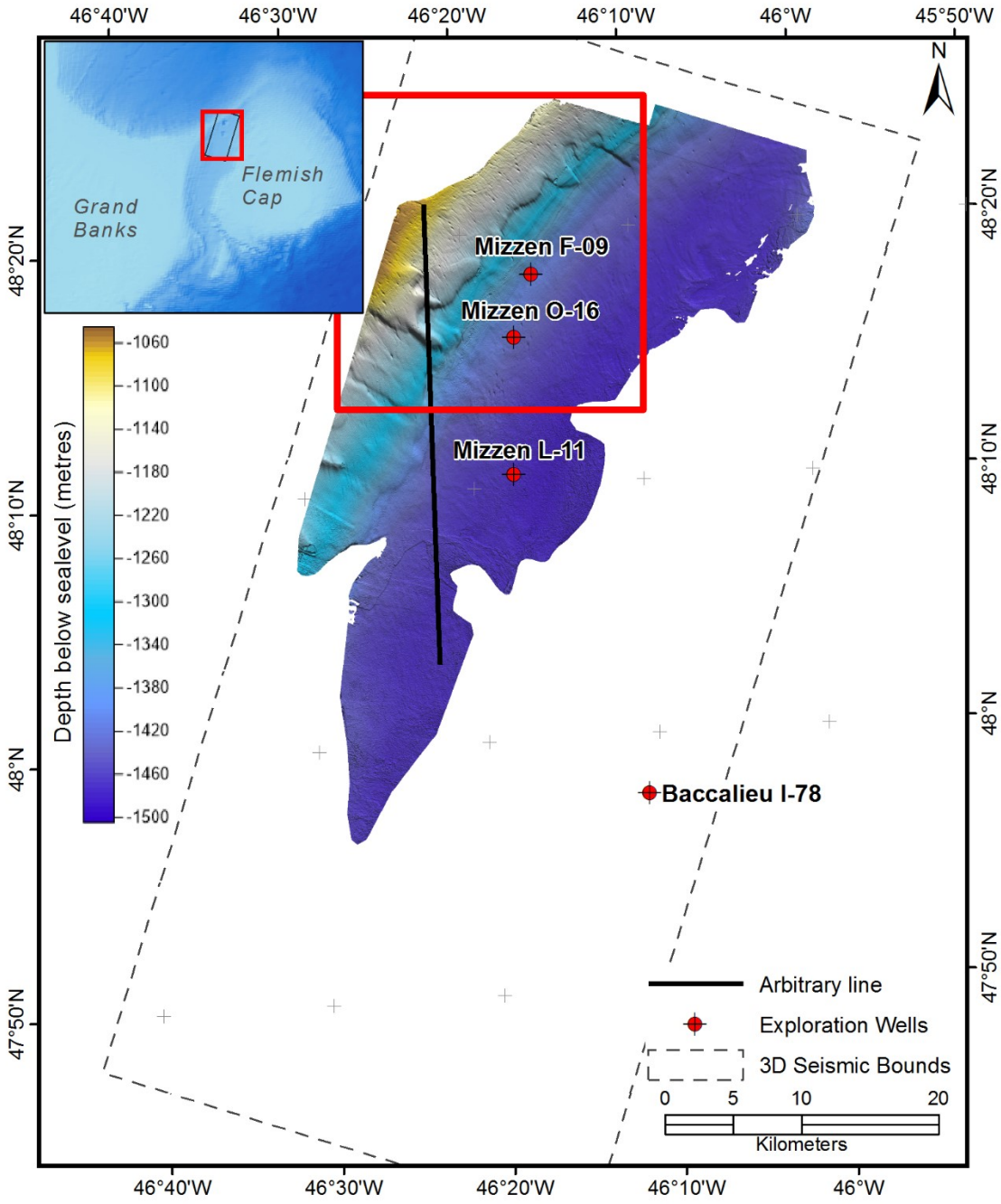

Figure 5.66 Depth structure along the H2 horizon.

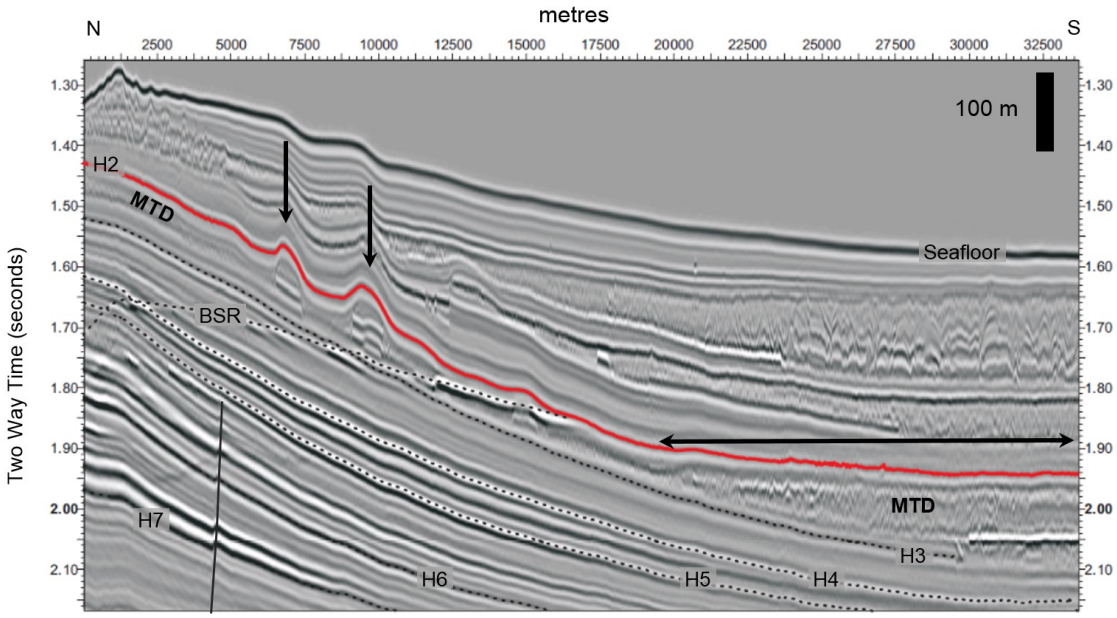

Figure 5.67 Arbitrary line with vertical arrows identifying sedimentary remnants below H2. The horizontal arrow identifies an area of reduced and inconsistent instantaneous frequencies and reduced amplitudes discussed in the text. Refer to Figure 5.66 for profile location.

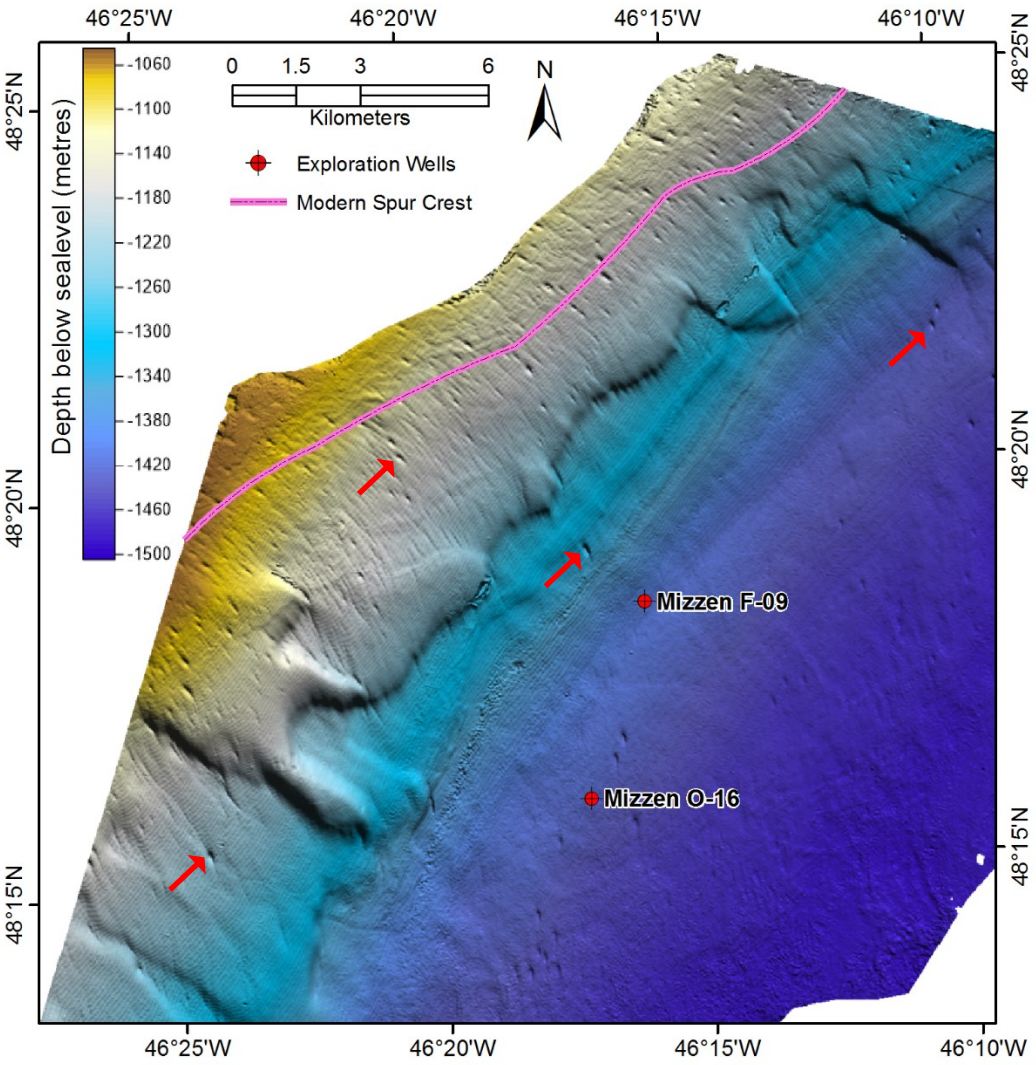

Figure 5.68 Detail of the H2 depth structure map. Refer to Figure 5.66 for map location. The red arrows highlight pockmarks.

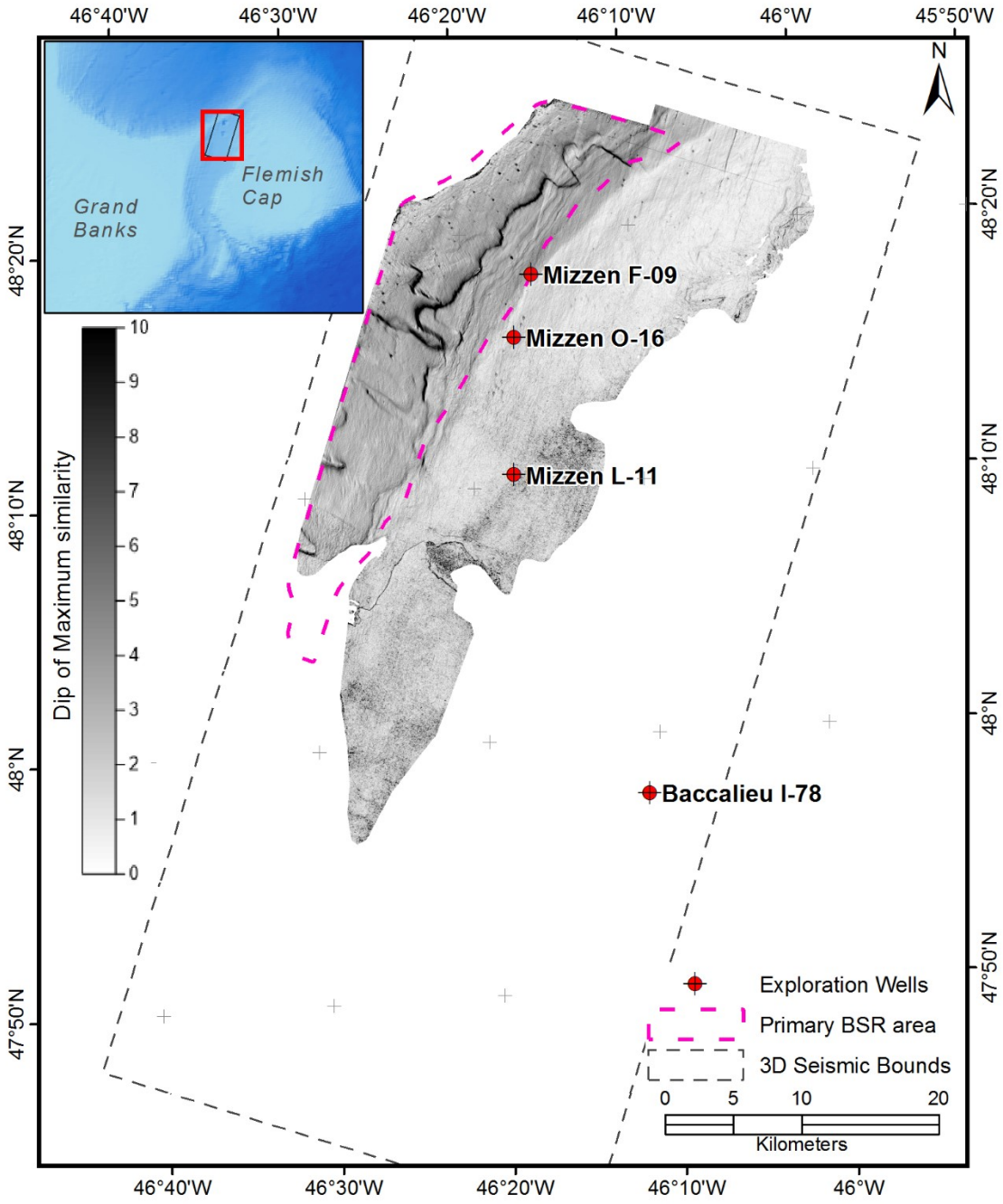

Figure 5.69 Dip of maximum similarity along the H2 horizon.

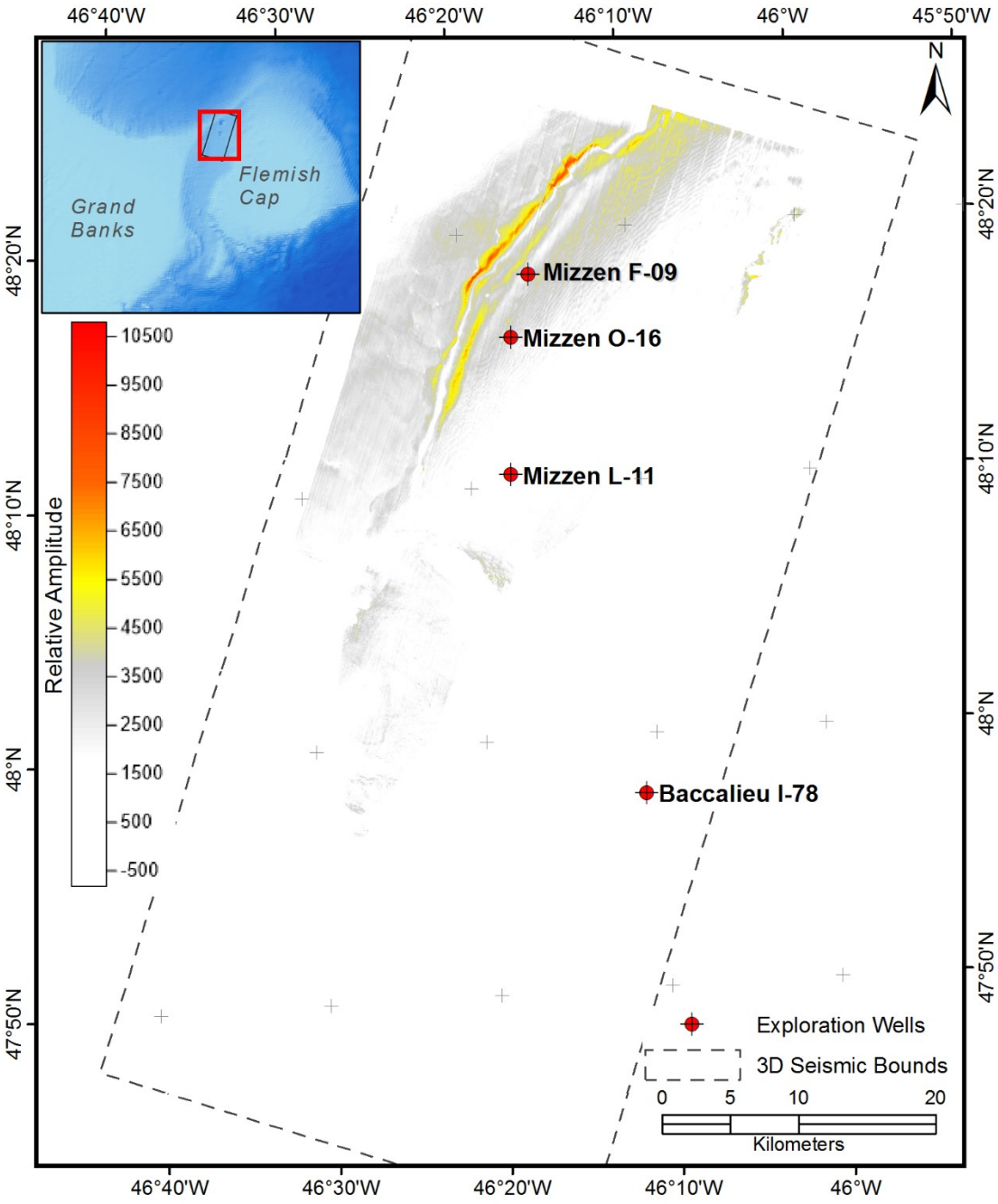

Figure 5.70 Relative amplitude along the H2 horizon.

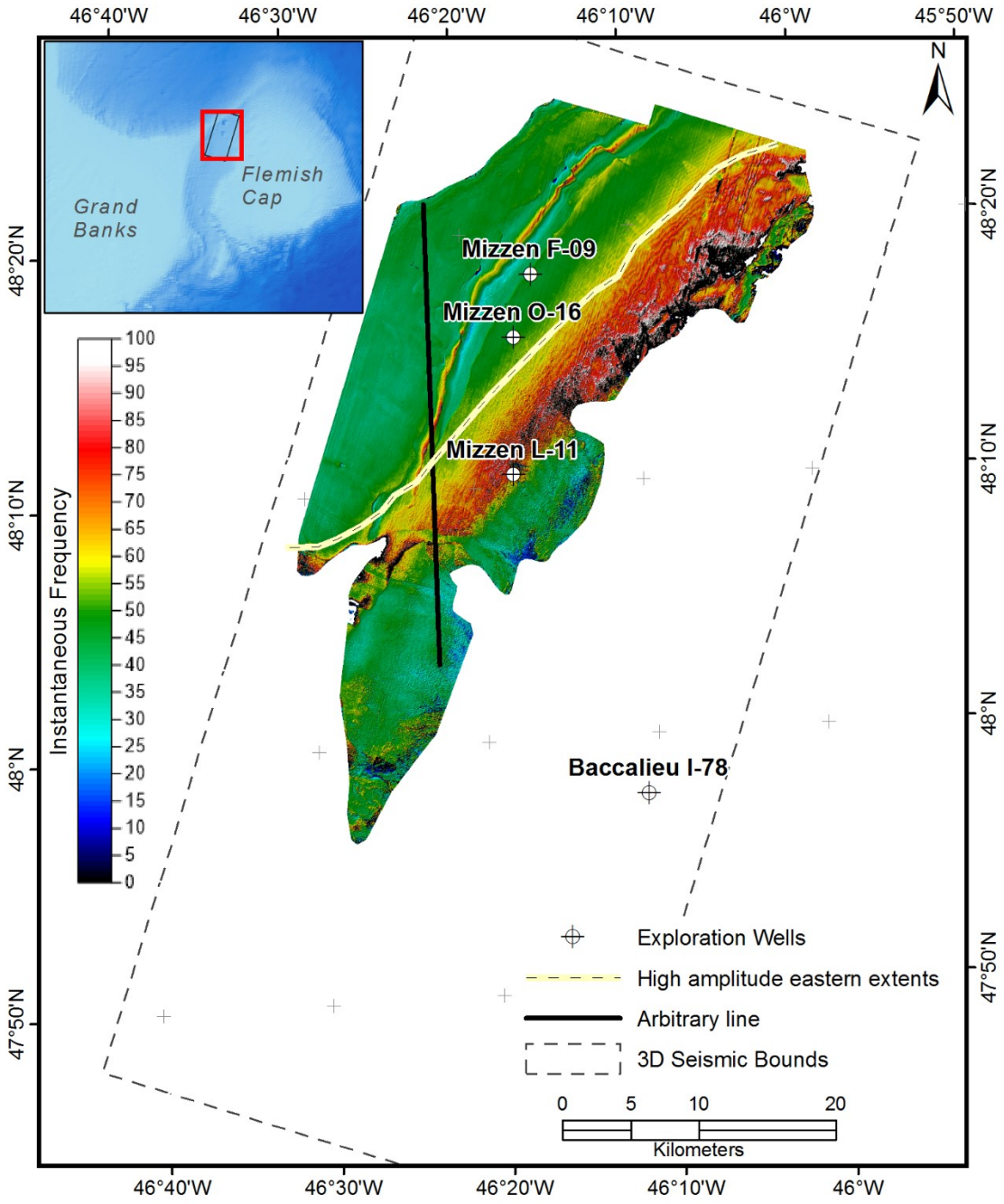

Figure 5.71 Instantaneous frequency along the H2 horizon.

5.1.2.9 Horizon H1

Horizon H1 was interpreted along a semi-continuous amplitude trough over most of the 3D seismic area. The horizon occurs above the BSR and is the shallowest horizon studied. H1 was modified and in various areas removed by younger mass movement events corresponding to data gaps along the horizon. The H1 depth structure map shows a broad depression in the Flemish Pass similar to that of the modern seafloor (Figure 5.72). The slopes on the flanks of the paleo-Flemish Pass are generally steeper along H4 than those of the modern seafloor. H4 amplitudes are higher in the north and are low to moderate elsewhere (Figure 5.73). Sediment failure tracks are visible on the amplitude and particularly the dip of maximum similarity maps (Figure 5.73 and Figure 5.74 respectively). From these surfaces, it appears that failures originate from both the eastern and western flanks of the paleo Flemish Pass.

Above H1 is an interval of chaotic reflections interpreted as a large MTD (Figure 5.75). This MTD is overlain by a unit of planar bedding that are is in turn overlain by another, larger MTD (Figure 5.75). In the SW this larger MTD removed sediment down to the H1 level (Figure 5.75). With time, the MTDs occur further east (Figure 5.1) with drift development focused below the Sackville Spur and restricted on the eastern flank of the Pass by the MTDs (Figure 5.76).

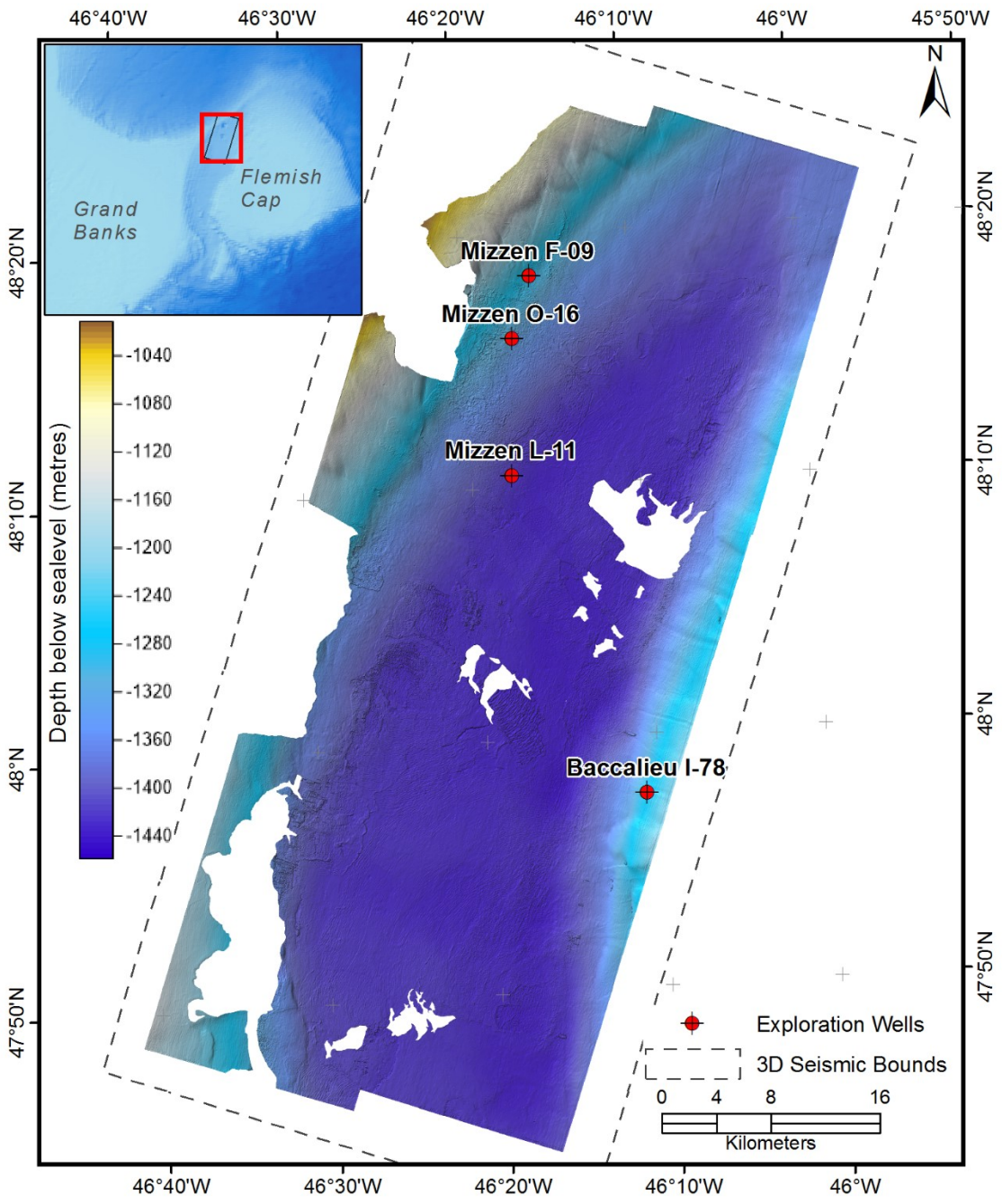

Figure 5.72 Depth structure along the H1 horizon.

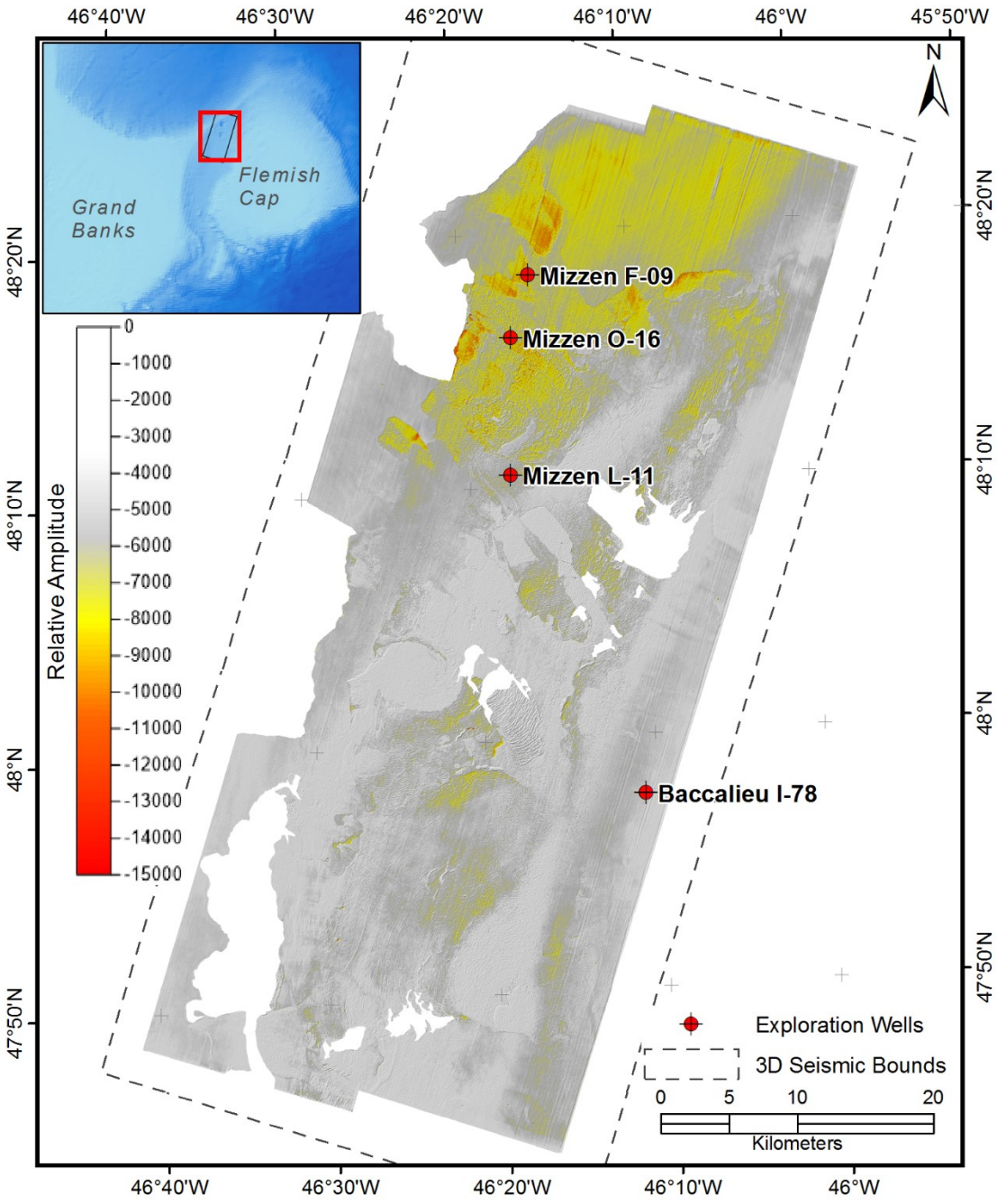

Figure 5.73 Relative amplitude along the H1 horizon.

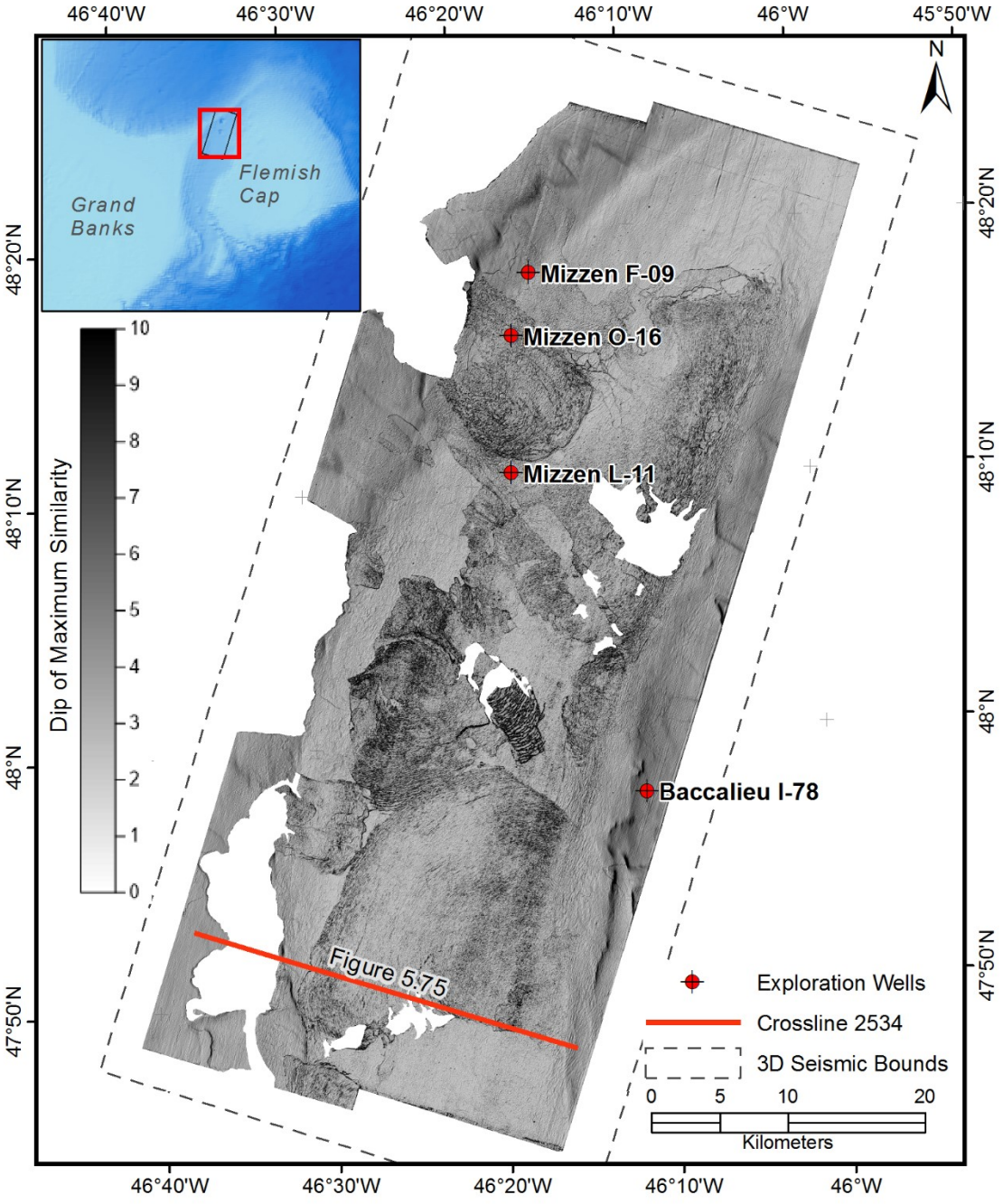

Figure 5.74 Dip of maximum similarity along the H1 horizon.

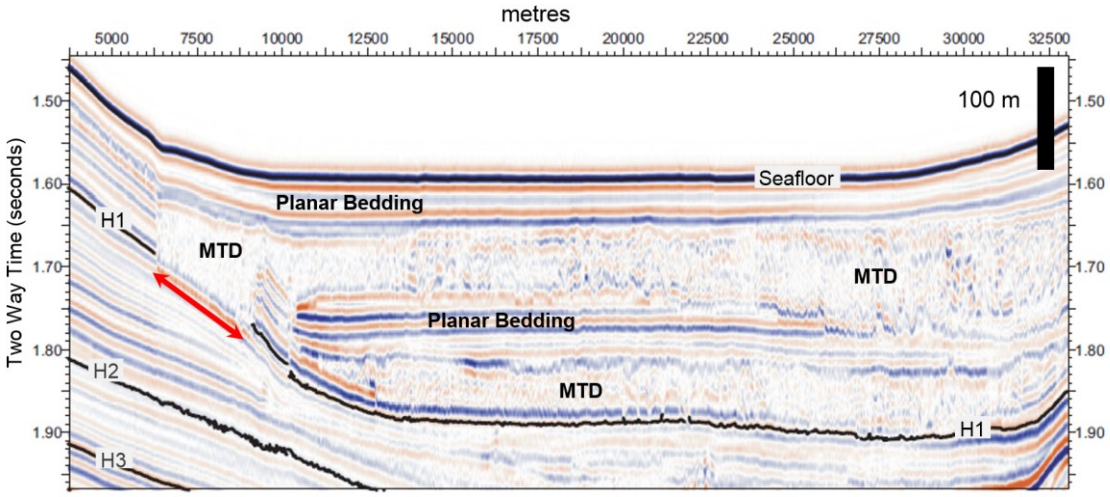

Figure 5.75 Portion of crossline 2534 showing the MTDs overlying the H1 horizon. The red arrow highlights where H1 was removed by the upper MTD. Refer to **Figure 5.74** for profile location.

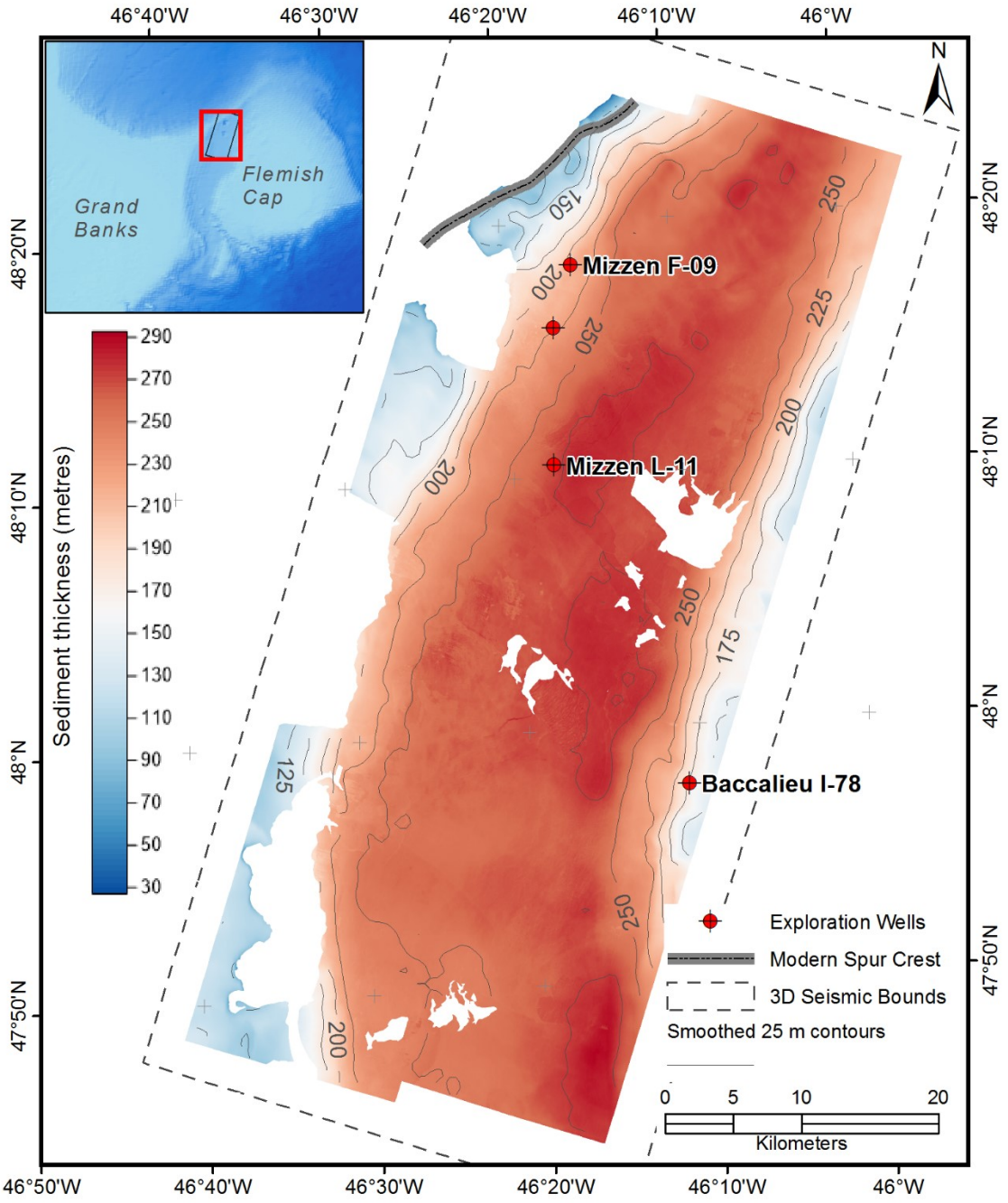

Figure 5.76 Isopach (thickness) map between the H1 horizon and the seafloor.

5.2 WELL CORRELATION

Well logs, well reports and biostratigraphic reports provide lithologic and age control for the seismic horizons described in the previous section.

5.2.1 Samples

Lithologic information from samples is limited for the younger strata studies in this thesis. No lithologic sample information is available for this study's interval of investigation at the Baccalieu I-78, F-09 or O-16 wells. The L-11 well reports were available and include cuttings summaries from the H4 horizon down (Deon and Timmons, 2003) (Figure 5.77. L-11 cuttings are described as predominately claystone between 1695 m (the start of sampling) and 1840 m (seismic limits). Limestone occurs in the strata below H9 (784-793 m (824-833 ms) bsf). H9 marks the onset of glauconite at L-11 (713 m (757 ms) bsf) while chert fragments are noted 1 m below H8 to 19 m below H9 (Figure 5.77). At L-11 strata between H5 and H4 contain 0.5-2 m thick sand dominated beds (543 m to 591 m (595-642 ms) bsf) (Deon and Timmons, 2003).

5.2.2 Age control

Age control, available for the O-16 (Fugro, 2009; Basin Database, 2017), L-11 (Fenton, 2003) and Baccalieu I-78 (CNLOPB, 2008; Robertson, 2002) wells, are correlated to the 3D seismic (Figure 5.77).

At the Baccalieu I-78 well the base Paleogene (CNLOPB, 2008) correlates on the 3D data to a basement high at 613 m (663 ms) below seafloor (bsf) that is onlapped by 104 m (100 ms) of Pliocene and possibly Pleistocene aged sediments (Robertson, 2002) (Figure 5.77). As previously noted, this basement is not regionally extensive and for most of the survey area dips below the available 3D data.

Strata below the H9 horizon vary in age from early Miocene (895 m (929 ms) bsf) at O-16 (Fugro, 2009) to middle Miocene (782-797 m (822-837 ms) bsf) at L-11 (Figure 5.77). Horizon H9 correlates to between the middle (835-865 m (872-901 ms) bsf) and late Miocene-Pliocene (775-805 m (816-844 ms bsf) (Fugro, 2009) at O-16 and to the late Miocene to early Pliocene (722-767 m (766-808 ms) bsf) (Fenton, 2003) at L-11 (Figure 5.77). At L-11, horizon H8 to H4 correlates to the Pliocene (Pleistocene?) (542-707 m (594-752 ms) bsf) (Fenton, 2003). No age calibration is available for strata above the H4 horizon.

At O-16 a late Miocene lithostratigraphic age (857 m (893 ms) bsf) (Basin Database, 2017) overlaps with the Middle Miocene biostratigraphic age (Fugro, 2009) (Figure 5.77). It is unclear what samples were used to acquire this lithostratigraphic age.

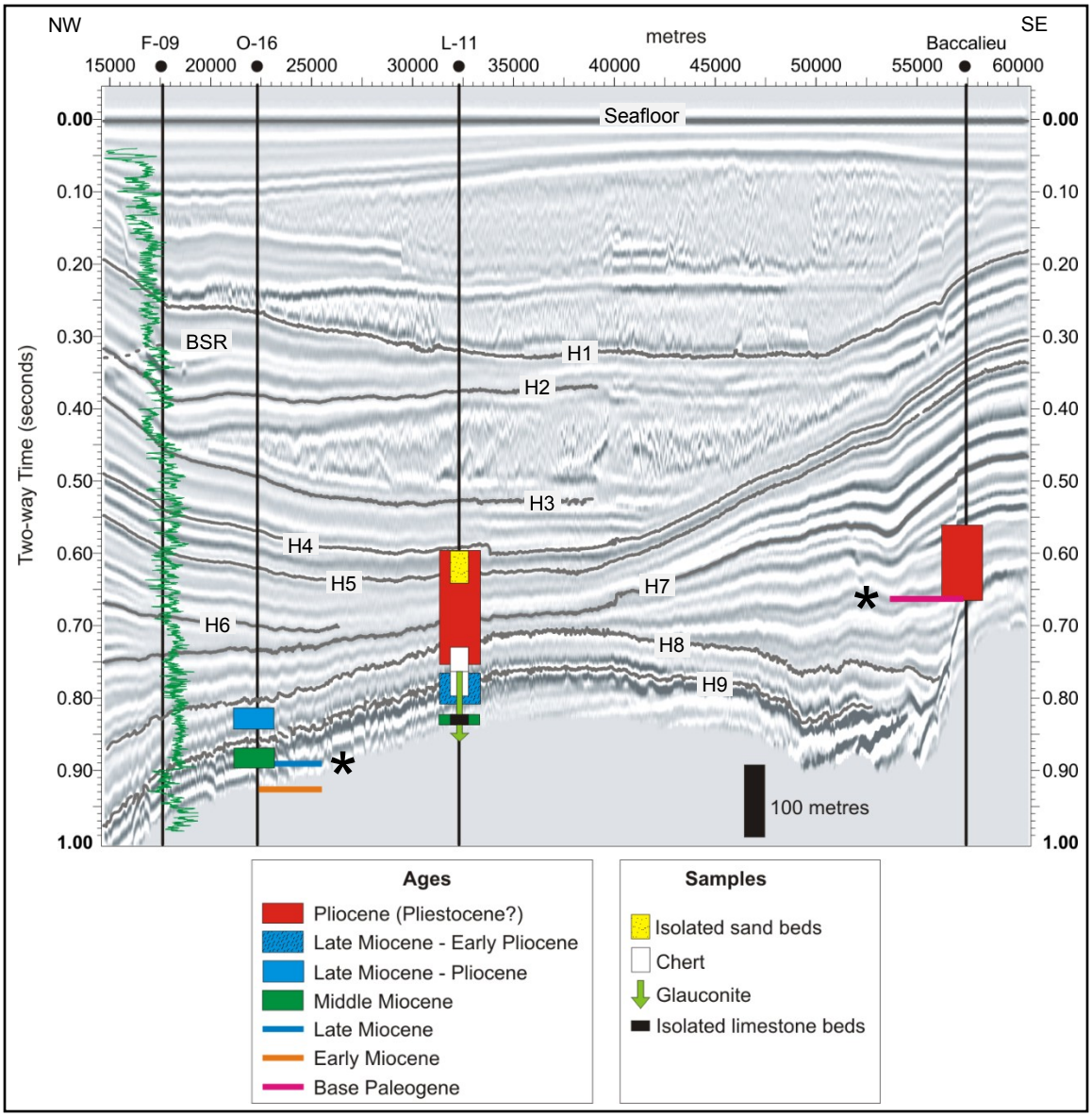

Figure 5.77 Seismic and well tie-line with ages and samples overlain. Wide boxes represent the stratigraphic extend for each age. Lines represent ages reported for a specific depth. The asterisks identify lithostratigraphic ages; all other ages are biostratigraphic. The F-09 gamma ray log is overlain. Horizontal scale is distance in metres.

5.2.3 Log descriptions

The F-09 well logs provide continuous vertical records through the depth interval represented on the 3D seismic volume. Four logging units are identified based on the F-09 well log responses and their correlation with the 3D seismic data (Figure 5.78).

The first unit is present from the H9 horizon to the H8 horizon. This unit marks an increase on the gamma ray, resistivity and sonic logs from the underlying deposits. Velocities increase from 1900 m/s below the H9 horizon to ~2300 m/s above the horizon. Unit 1 also marks a change to more consistent log values. The seismic response through Unit 1 is characterised by relatively low amplitude reflections. The top of Unit 1, marked by the H8 horizon, is not distinct on the well logs but is gradational and best defined by a significant reduction in densities above H8. A gap in the density log values correlates to chert recovery in the L-11 well, to faulted sediments on the seismic, and overlaps with the zone of low log values at the F-09 well.

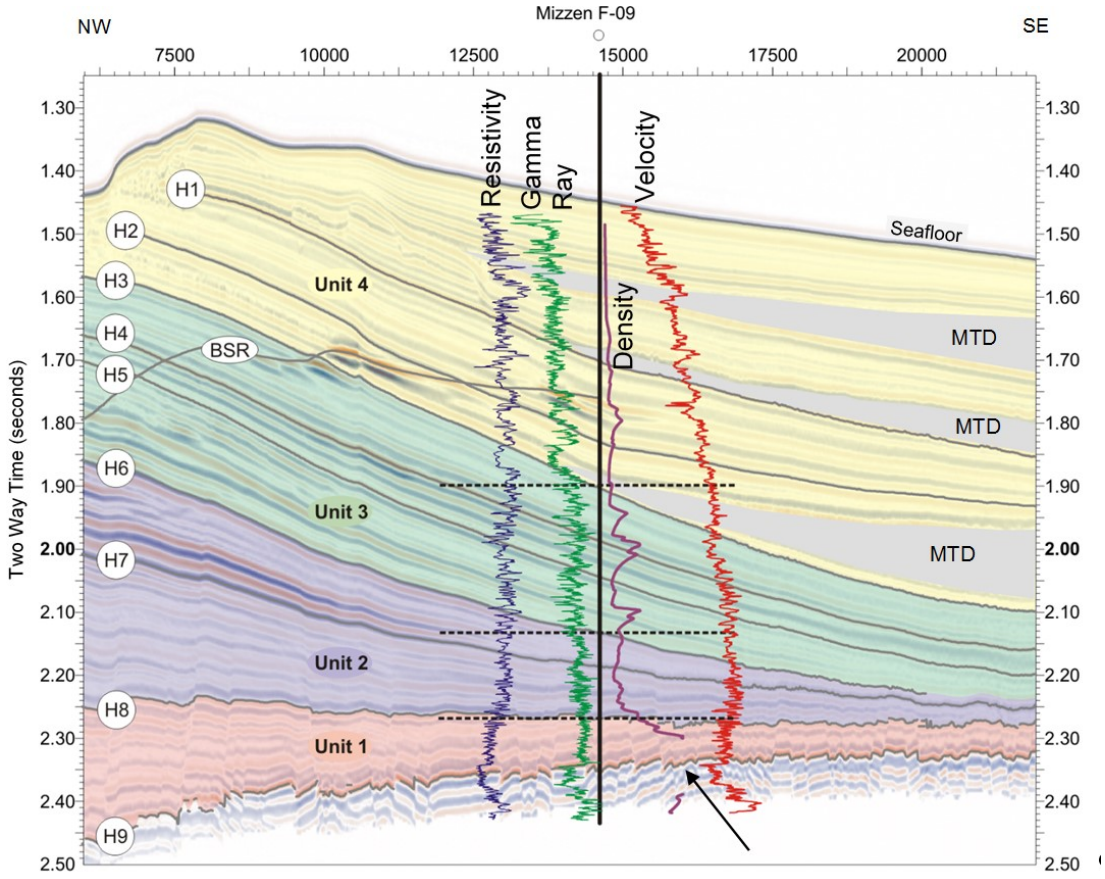

Figure 5.78 F-09 well logs overlain on the 3D seismic. The units described in the text are overlain and the lack dashed lines represent boundaries between these units at the F-09 well. The black arrow near the base of the seismic data identifies a gap in the density log. Horizontal units are in metres along line.

Unit 2 consists of two sub-units, the boundary between which is roughly marked by the H7 horizon. In the basal portion of Unit 2, the velocity and gamma ray log responses are variable while above H7 the log responses are moderately more consistent. At the F-09 well, the seismic profiles show higher amplitude reflections between H8 and H7 (the lower half of Unit 2) while in the upper half (between H7 and H6) amplitudes at F-09 reduce so that individual reflections are barely discernable. Resistivity values increase through Unit 2 relative to the underlying Unit 1 while density values through Unit 2 are consistently low.

H6 marks the base of Unit 3, which is characterised on the gamma ray and resistivity logs by increased variation; the highs are higher and the lows are lower than in the underlying units. Through Unit 3 discrete units of elevated log values become thicker and more easily discerned. Most notable are discrete intervals of increased density

values that correspond on the seismic data to elevated reflection amplitudes (Figure 5.78). The H3 horizon marks the top of Unit 3.

Unit 4, the shallowest and largest of the units, marks a change on both the gamma and resistivity logs to increased variability and the onset of distinct and relatively thick, packages of sediment with similar log responses. These discrete packages correlate on seismic profiles to intervals interpreted as MTDs (Figure 5.78). The Primary BSR intersects the F-09 well within Unit 4. The only definitive expression of the BSR on the well logs is a velocity reduction below the BSR. The seafloor marks the top of Unit 4.

5.3 BASE OF HYDRATE STABILITY

Theoretical base of gas hydrate stability depth surfaces were calculated from the intersection of four different hydrate stability functions with a local linear geothermal gradient. Predicted pressures and temperatures for hydrate stability were obtained using Sloan's (1998) CMDHyd software. These were compared to experimental values of Dickens and Quinby-Hunt (1994) fit to both a first and a second order polynomial. The final comparison applied the stability function of Majorowicz and Osadetz (2003), which they derived using output from Sloan's (1998) CMDHyd software. The various base of hydrate stability surfaces are presented in Figure 5.79.

It is apparent from Figure 5.79 that the surfaces generally agree well, with the Majorowicz and Osadetz (2003) surface being the most discordant. The CMDHyd (Sloan 1998) stability surface along with the first and second order polynomial fits of the Dickens and Quinby-Hunt (1994) experimental data were all corrected to account for the compression of seawater with increasing depth (pressure) and the change in gravitational strength with Latitude and depth. In contrast, the Majorowicz and Osadetz (2003) function used a simple hydrostatic gradient of 10 MPa/m for its pressure to depth conversion. To facilitate a proper comparison, stability depths were calculated using the stability function of Majorowicz and Osadetz (2003) and then converted back to pressures. The pressures were corrected for latitude and density variations then a new first order polynomial was defined. The resulting hydrate stability surface is presented in Figure 5.80 with the original Majorowicz and Osadetz (2003) for comparison. The corrected surface measures between 14.7m and 15.4 m deeper than the original with the greatest depth differences (15.4 m) below the crest of Sackville Spur.

A comparison of the corrected and uncorrected version of the second order polynomial fit to the experimental results of Dickens and Quinby-Hunt (1994) are also included in Figure 5.80. The depth variation is greater along the second order polynomial

surface varying between 10 and 19 m with the largest depth differences along the Spur's crest.

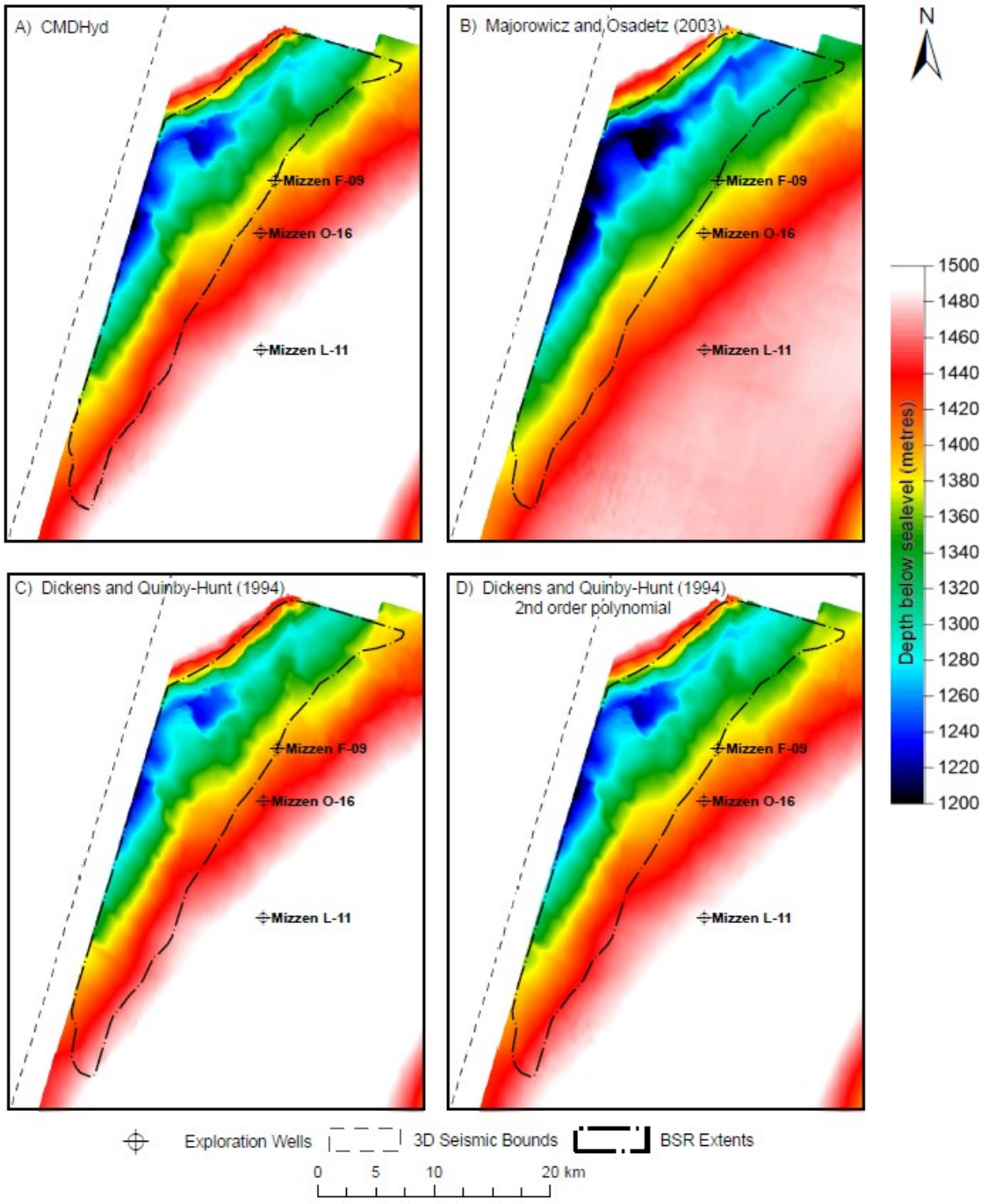

Figure 5.79 Base of hydrate stability surfaces using hydrate stability functions (A) from Sloan's (1998) CMDHyd software (B) as published by Majorowicz and Osadetz (2003) (C) from a first order polynomial fit of Dickens and Quinby-Hunt's (1994) experimental results as well as (D) to a second order polynomial (Dickens and Quinby-Hunt, 1994; Brown et al. 1996)

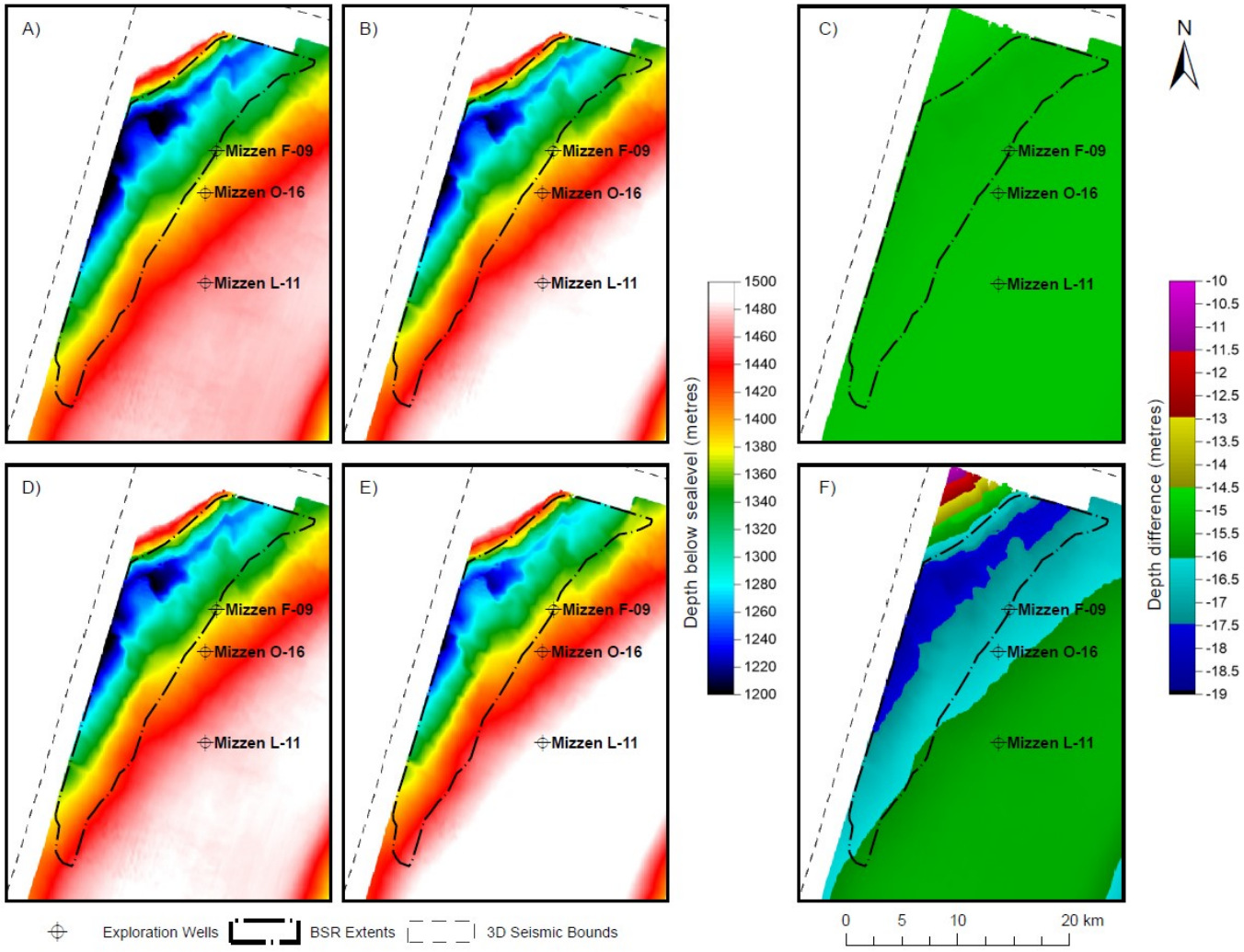

Figure 5.80 Depth difference (C) between Majorowicz and Osadetz (2003) base of hydrate stability surfaces using a hydrostatic gradient of 10kPa/m (A) and using the equation of state for seawater(B) to correct for density variations with depth as well as gravity variations with depth and latitude. Similarly, the depth difference for the Dickens and Quinby-Hunt (1994) third order polynomial surface uncorrected (D) and corrected for gravity and density variations.

A graphical representation of the different stability functions is presented in Figure 5.81. At low and high temperatures the Majorowicz and Osadetz (2003) stability function is concordant with the others. Through the depth of interest for this study, their stability curve diverges from the group. After correction for density and gravitational variations, the Majorowicz and Osadetz (2003) stability function moves closer to the other functions but is still in the range of curves not corrected for density and gravity variations.

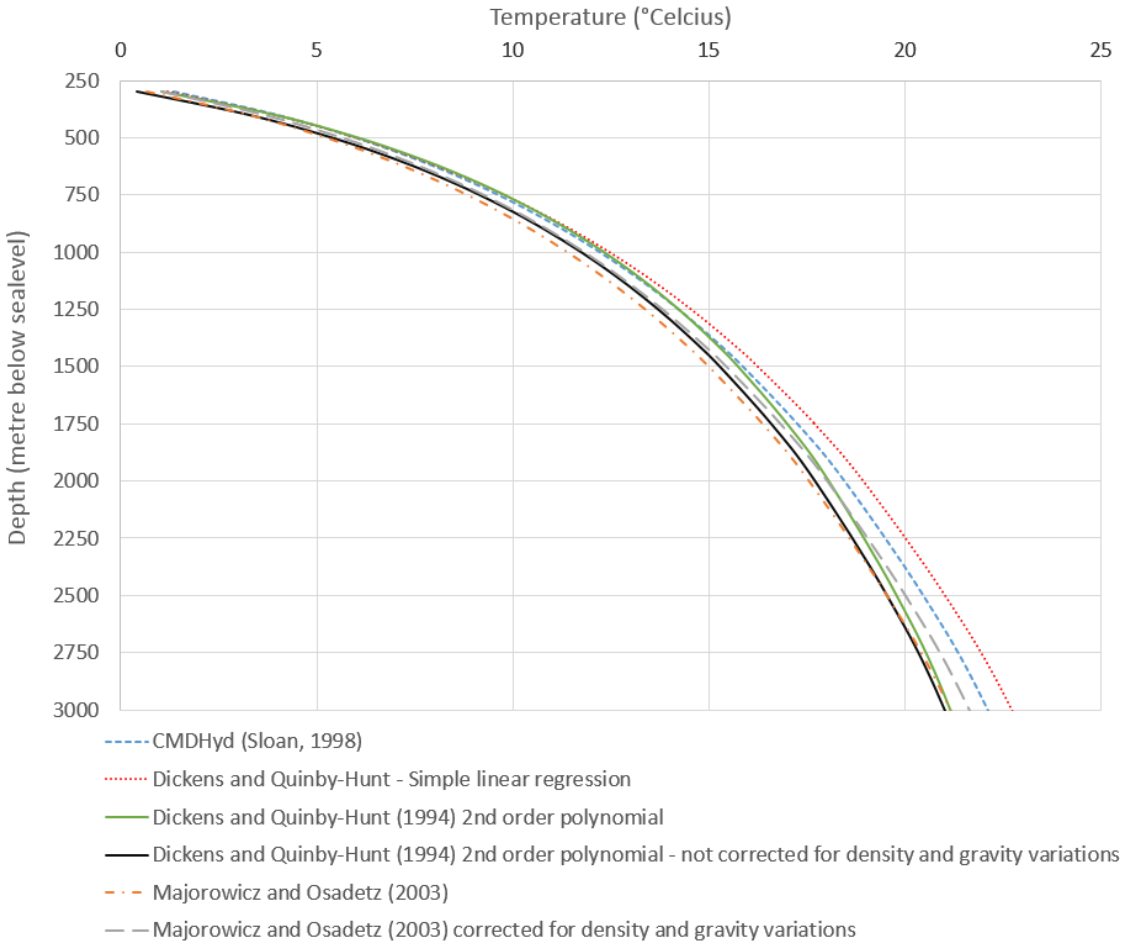

Figure 5.81 Graphical comparison of the various hydrate stability functions.

The Dicken-and Quinby Hunt (1994) second order polynomial agrees well with the CMDHyd (Sloan, 1998) function with some divergence at depth, as shown in Figure 5.82. Table 5.1 presents the depth differences for the various functions.

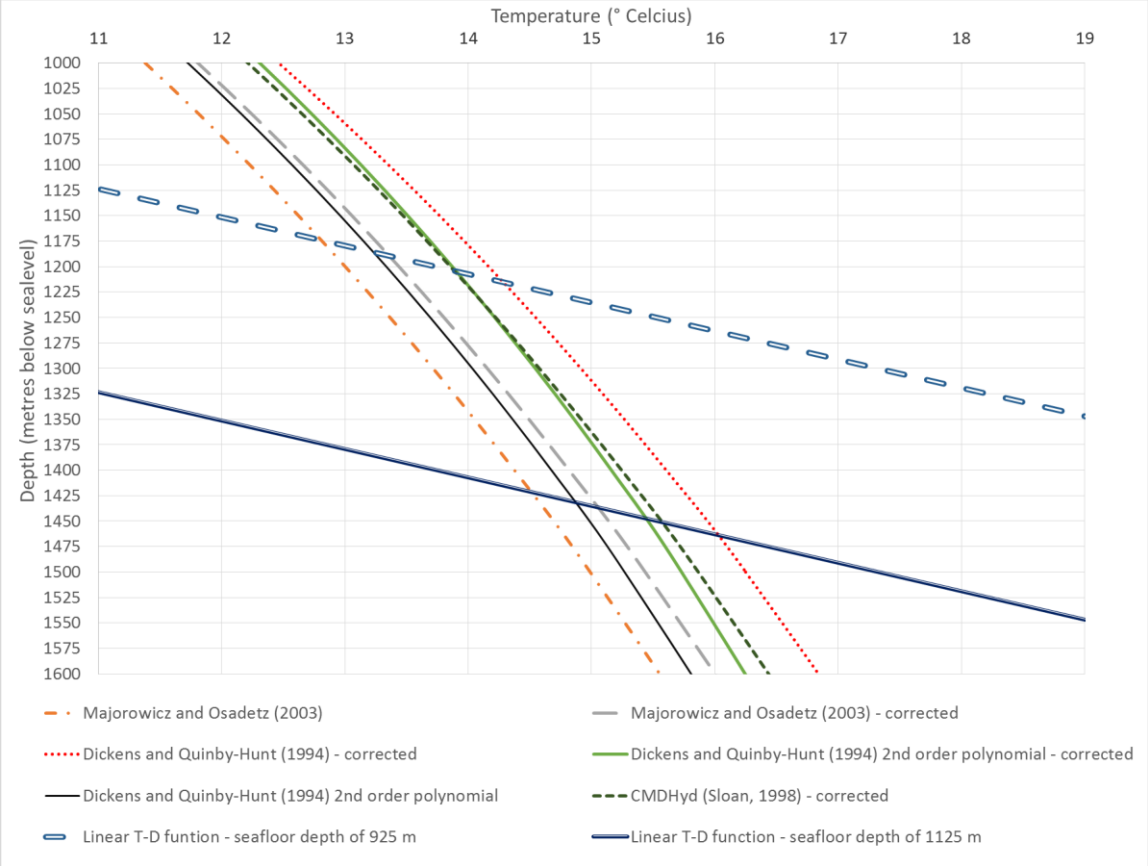

Figure 5.82 Base of hydrate stability curves with linear geothermal gradient function overlain. The functions that are adjusted for density and gravitational variations include the word 'corrected' in the legend. The linear functions for 925 m and 1125 m represent the shallowest and deepest water depths above the Primary BSR. The intersection of the linear and stability functions represents the depth to the base of the hydrate stability zone. The linear functions assume a seafloor temperature of 3.9°C and a geothermal gradient of 35.8°C/km (as observed in the Bacceleau well).

There is a maximum depth difference of 42 m between the uncorrected Majorowicz and Osadetz (2003) and the first order polynomial fit to the corrected Dickens and Quinby-Hunt (1994) data (Table 5.1). In the area of the BSR, the thickness of the hydrate stability zone varies between 249-290 m in water depths of 925 m to 338-380 m in water depths of 1125 m. These depth differences equate to temperatures at the base of hydrate stability between 12.8-14.5°C in water depths of 925 m and 14.3-16 °C in water depths of 1125 m.

Table 5.1 Depth to the base of hydrate stability for the shallowest and deepest water depths within the Primary BSR area using the various functions presented in Figure 5.81.

	Depth below sea level (metres)		Thickness of the hydrate stability zone
	Shallowest	Deepest	
Seafloor from 3D seismic	**925**	**1125**	**NA**
Majorowicz and Osadetz (2003)	1174	1422	249-338
Majorowicz and Osadetz (2003) - corrected	1189	1437	264-353
CMDHyd (Sloan, 1998) - corrected	1204	1451	279-367
Dickens and Quinby-Hunt (1994) - corrected	1215	1464	290-380
Dickens and Quinby Hunt (2003) second order polynomial (Brown et al. 1996)	1186	1432	261-348
Dickens and Quinby Hunt (2003) second order polynomial (Brown et al. 1996) - corrected	1205	1448	280-364

The manually interpreted Primary BSR lies between 307 and 400 m below the seafloor. The differences between the theoretical bases of hydrate stability zone and the depth to the Primary BSR are shown in Figure 5.83. The CMDHyd (Sloan, 1998) and Dickens and Quinby-Hunt (1994) second order polynomial models, both of which are corrected for density and gravity variations, are the closest to the observed BSR depths. Discrepancies increase with water depth with some variability based on location. Discordances near the crest of the Spur are associated with the failure scars at the seabed that are reflected in the stability but not the BSR surface. The stability functions of CMDHyd and the second order polynomial of Dickens and Quinby-Hunt (1994) diverge slightly with increasing depth (Figure 5.81). The Dickens and Quinby-Hunt (2003) first order polynomial function agrees well with the BSR in shallow waters but at greater water depths becomes increasingly discordant, mapping too deep relative to the BSR.

The uncorrected Majorowicz and Osadetz (2003) stability surface diverges the most from the observed BSR particularly in the shallow water areas where it maps up to 77m shallower than the BSR. Unlike the other functions, this function matches best at depth. Even after correction for density and gravitational variations, the corrected Majorowicz and Osadetz (2003) stability surface still maps too shallow relative to the BSR over most of the BSR area.

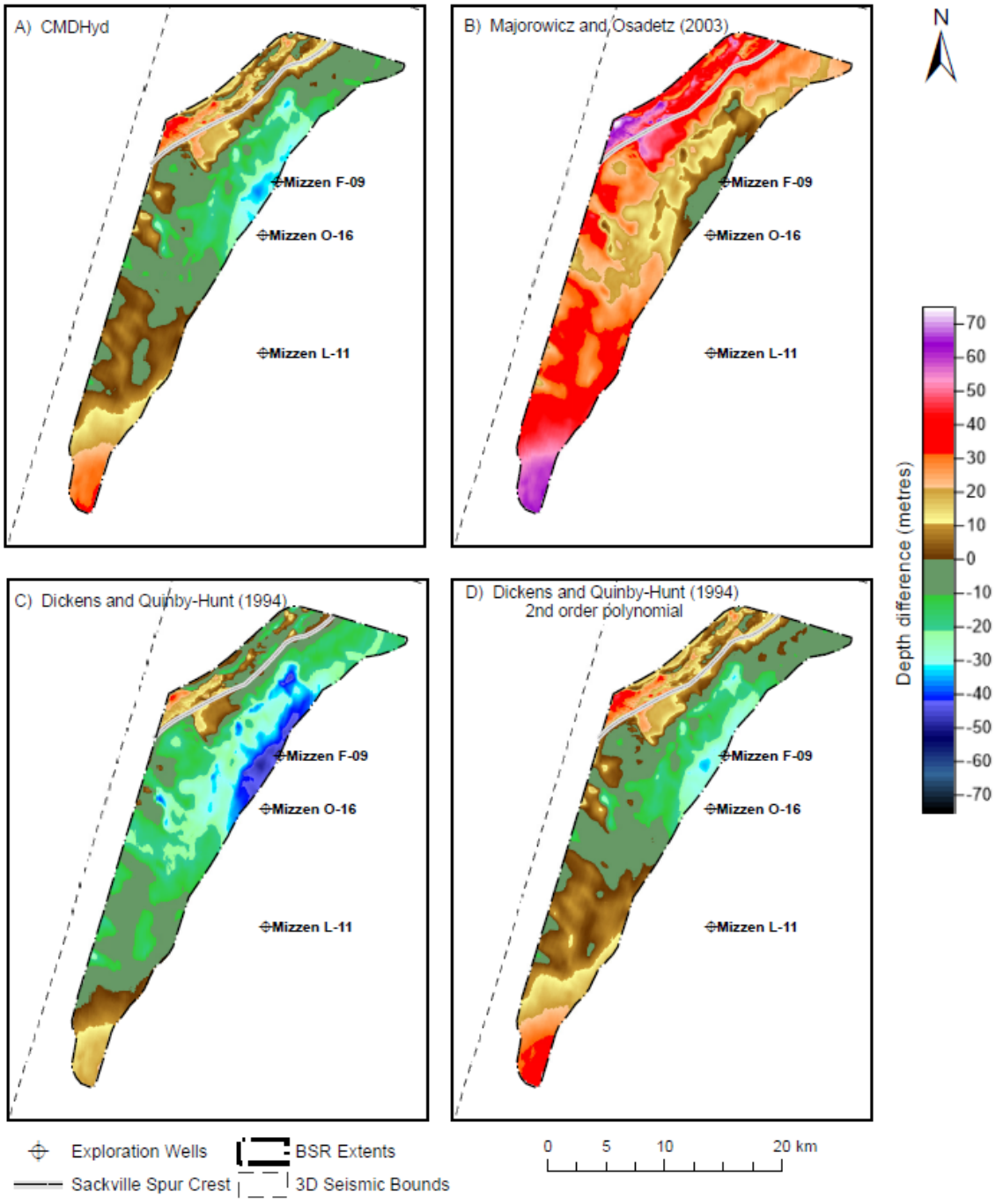

Figure 5.83 Depth difference surfaces between the manual Primary BSR and the different hydrate stability depth surfaces. All hydrate stability surfaces have been corrected for density and gravity variations except for (B).

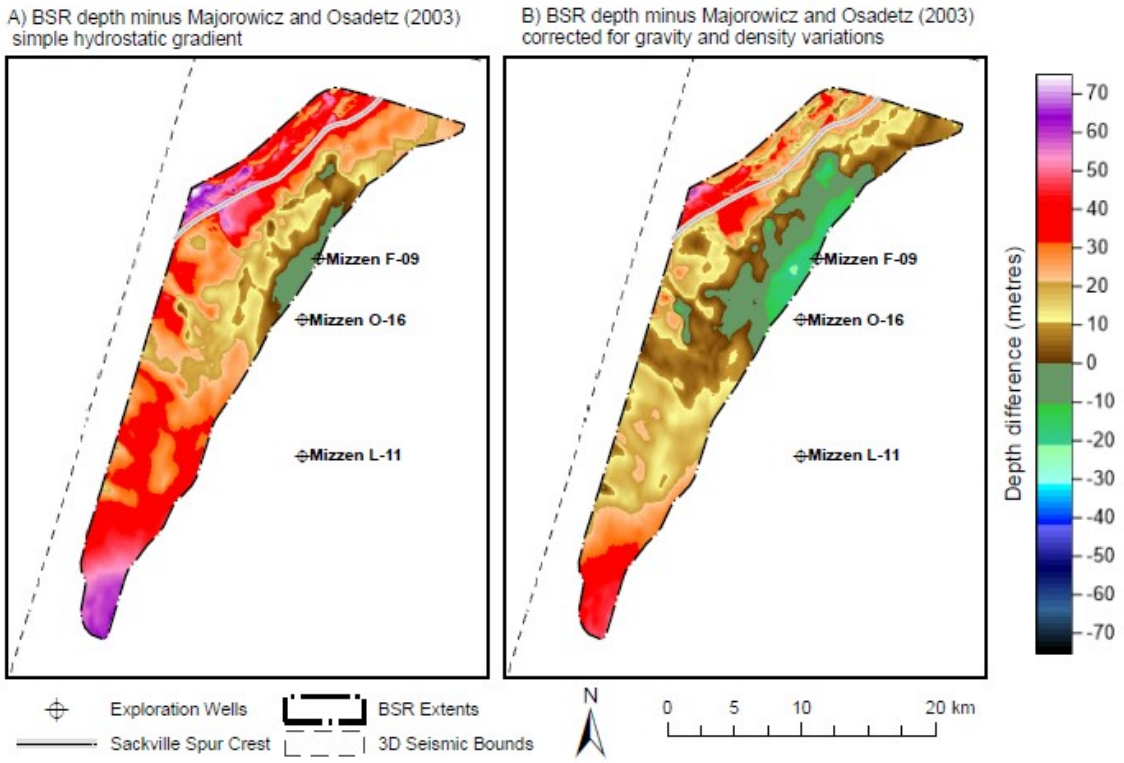

Figure 5.84 Comparison of depth difference surfaces between the manual Primary BSR and the Majorowicz and Osadetz (2003) uncorrected (A) and corrected (B) base of hydrate stability surfaces.

5.3.1 Sensitivity Analysis

Seafloor temperature and geothermal gradient, constants in the linear temperature depth function, were varied by 20% to assess the resulting effect on the base of hydrate stability depth. These 20% variations represent a range of values that are reasonable for the area. The results of this sensitivity analysis show that the seafloor temperature has less effect on the final stability depth than the geothermal gradient (Table 5.2). Unlike the seafloor temperatures, whose 20% variance generally result in the same absolute percent change in stability depth, geothermal gradient reductions have a higher per cent change in stability depth than gradient increases. As the stability curve becomes more vertical with increasing depth and temperature there is more depth variation over the same temperature interval.

Table 5.2 Results of the sensitivity analysis on the linear temper-depth function. The CMDHyd stability function was used along with a seafloor temperature of 3.9 °C and a geothermal gradient of 35.8 °C/km.

Seafloor Depth of 925 m				
	20% Increase		20% Decrease	
	Hydrate Stability Depth	% Change from Standard Stability Depth (1204 m)	Hydrate Stability Depth	% Change from Standard Stability Depth (1204 m)
Seafloor Temperature	1176 m	-2.4	1231 m	2.3
Geothermal Gradient	1147 m	-4.7	1298 m	7.8

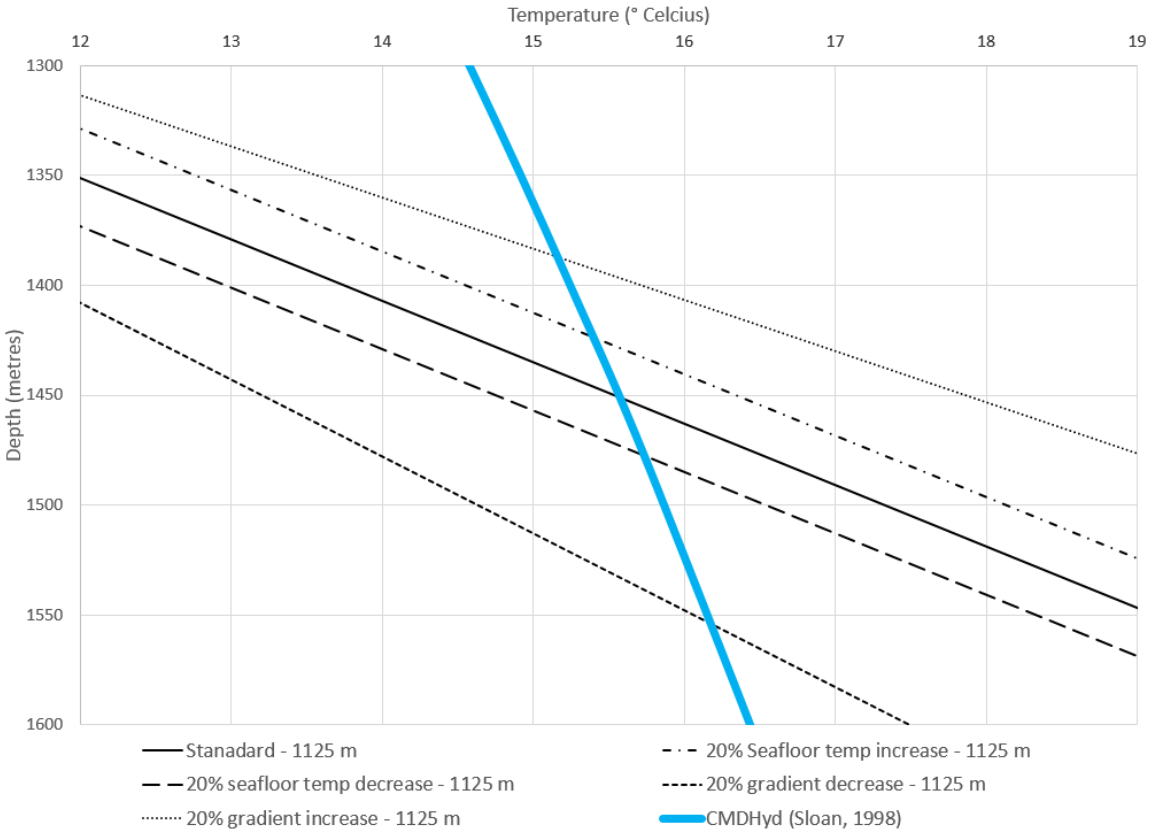

Figure 5.85 Chart showing the effect of varying the seafloor temperature and geothermal gradient on the depth to the base of hydrate stability (the intersection of the linear function with the hydrate stability curve) for the deepest waters in the Primary BSR area. The standard calculations are those used in this study, a seafloor temperature of 3.9°C and a geothermal gradient of 35.8°C/km. Refer to Table 5.2 for quantitative results from the sensitivity analysis.

5.3.2 Salinity Variations

A salinity of 35‰ NaCl was assumed for the CMDHyd calculations as well as for the pressure to depth calculations. Dickens and Quinby-Hunt (1994) used seawater with a salinity of 33.5‰ representing seawater from the Pacific Ocean, for their laboratory experiments. They note that for the natural salinity range for seawater, 33-37‰ there is little effect on the temperature and hence pressure of hydrate formation (Dickens and Quinby-Hunt, 1994).

Comparison of stability functions for salt water with 35‰, 40‰ and 100‰ NaCl as calculated in CMDHyd (Sloan, 1998) with the experimental values of Dickens and Quinby-Hunt (1994) shows the 35‰ and 40‰ agree well with and overlap onto the 33.5‰ salinity curve. The 0.5 ‰ increase in salinity from 3.5‰ to 4.0‰ changes the resulting depth to the base of hydrate stability by 1 m thus demonstrating that exact salinities are not critical in determining reasonable accurate (less than the seismic resolution) base of hydrate stability depths.

The freshwater stability curve clearly lies above the other stability functions (gas hydrates will form at higher temperatures and pressures) while the 10% NaCl curve lies distinctly below (lower temperatures and pressures for hydrate formation) (Figure 5.86).

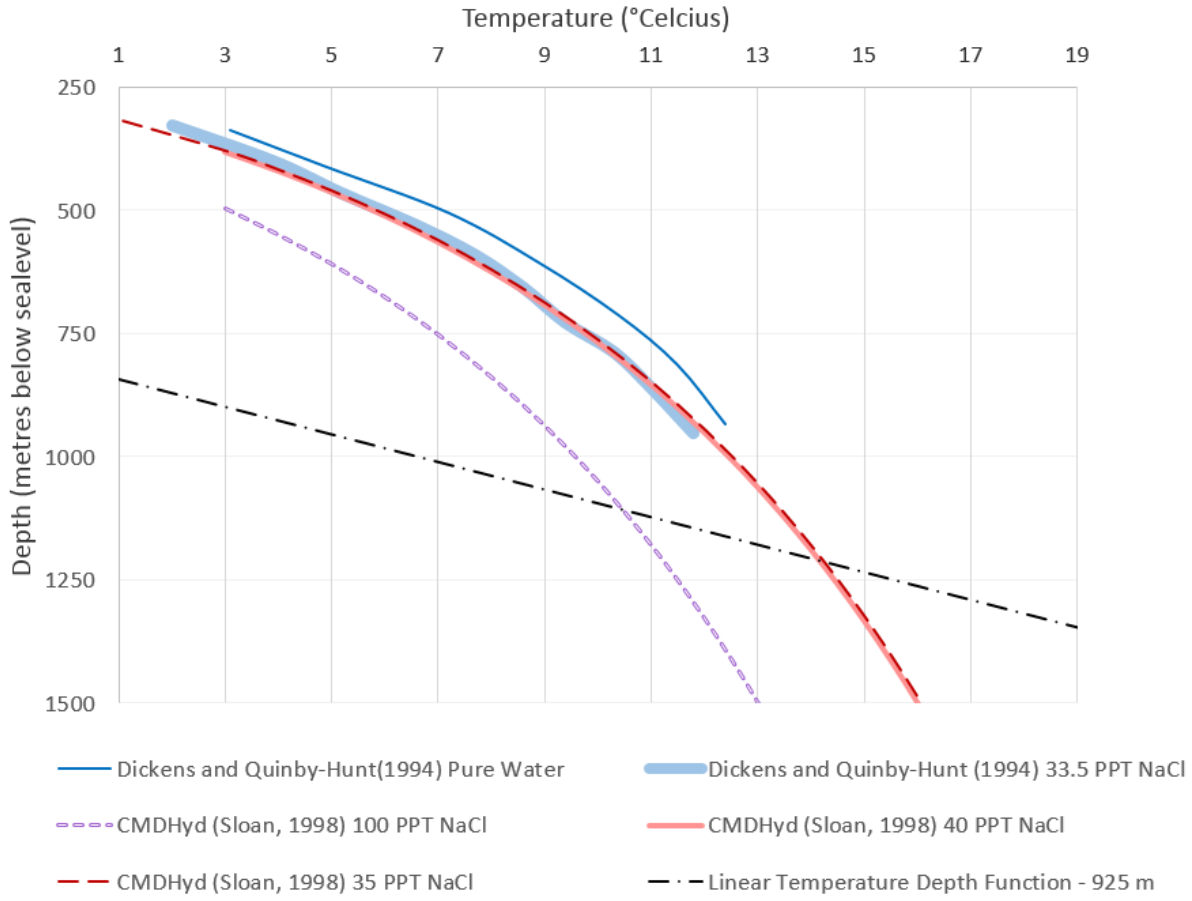

Figure 5.86 Effects of sanity changes on the hydrate stability function.

5.4 EFFECTIVE MEDIUM MODELLING

In the sediments above the BSR there are two zones of elevated F-09 velocities with corresponding elevated resistivity values indicative of gas hydrate in the sediments. These zones correspond to MTDs on the seismic profiles which in turn are associated with sandier sediments as indicated by reduced gamma ray values. Coarser grained, sandy sediments would typically have reduced resistivity values because of the increased water content. Gas in the sediment underlying the BSR is suggested by reduced F-09 velocities in both the F-09 well log and the OBS data. The two velocities compare well both recording a 30 m low velocity zone with an 11-12 % decrease in velocity values. These values are similar to those recorded on the western Atlantic passive margin (Schlesinger et al. 2012; Helgerud et al. 1999). Using the effective medium model of Helgerud et al. (1999) hydrate and gas concentrations have been estimated.

5.4.1 Velocities

Measured velocities from the Mizzen F-09 well and modelled OBS velocities are overlain on and compared with velocities for various gas and gas hydrate concentrations calculated using the effective medium model of Helgerud et al. (1999). Helgerud et al. (1999) provide methodology to model hydrate and homogeneous gas in the pores (Figure 5.87) and to model hydrate as part of the frame with patchily distributed pore gas (Figure 5.88).

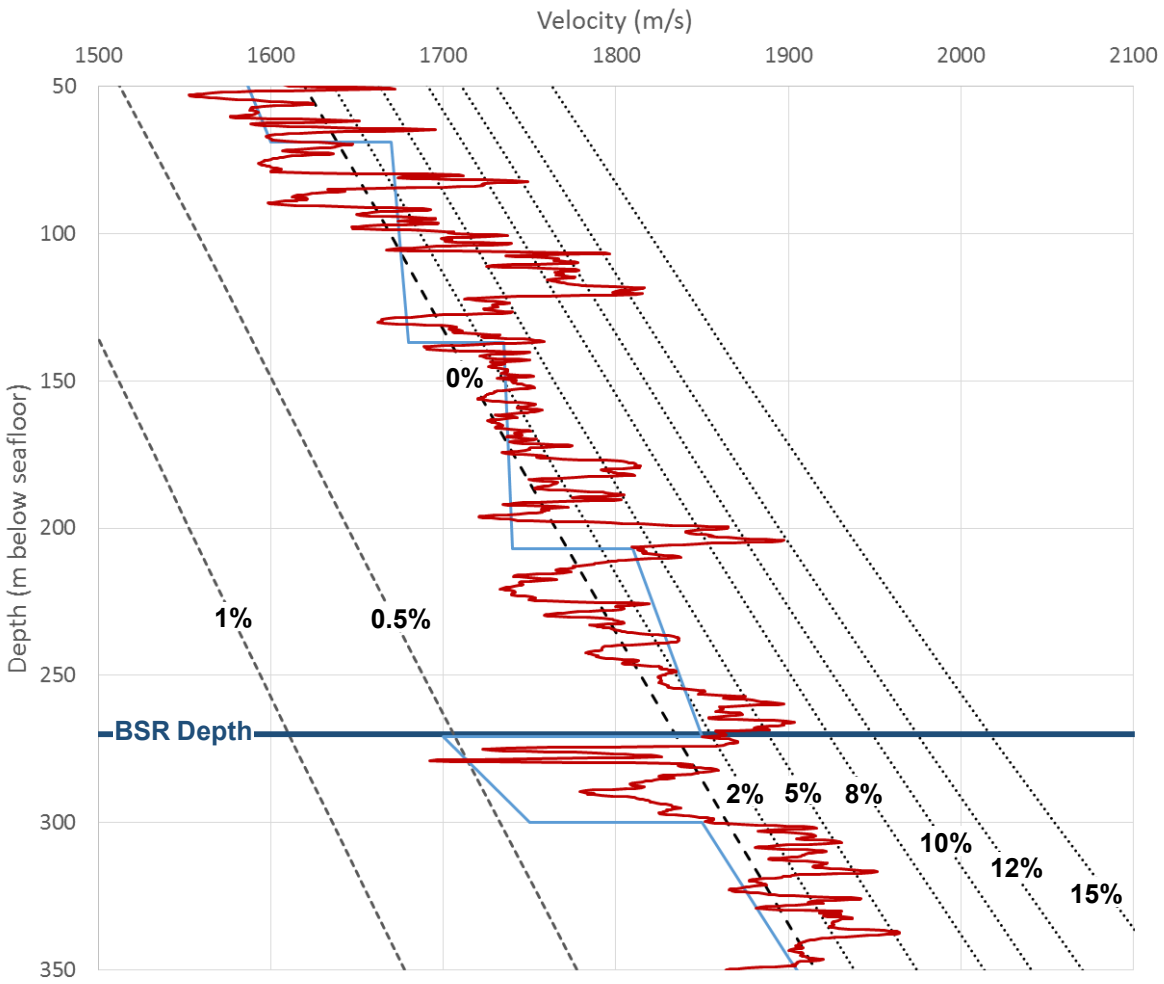

Figure 5.87 Hydrate and gas concentrations with hydrate (dotted lines to the right) and homogeneously distributed gas (dashed lines to left) in the pore fluids. Overlain are downhole velocities from the F-09 well (red solid line) and OBS velocities (light blue solid line). Note that the blocky, low resolution of the OBS velocities (Chian 2008) do not capture the high velocity zones above the BSR but do model the low velocity unit underlying the BSR.

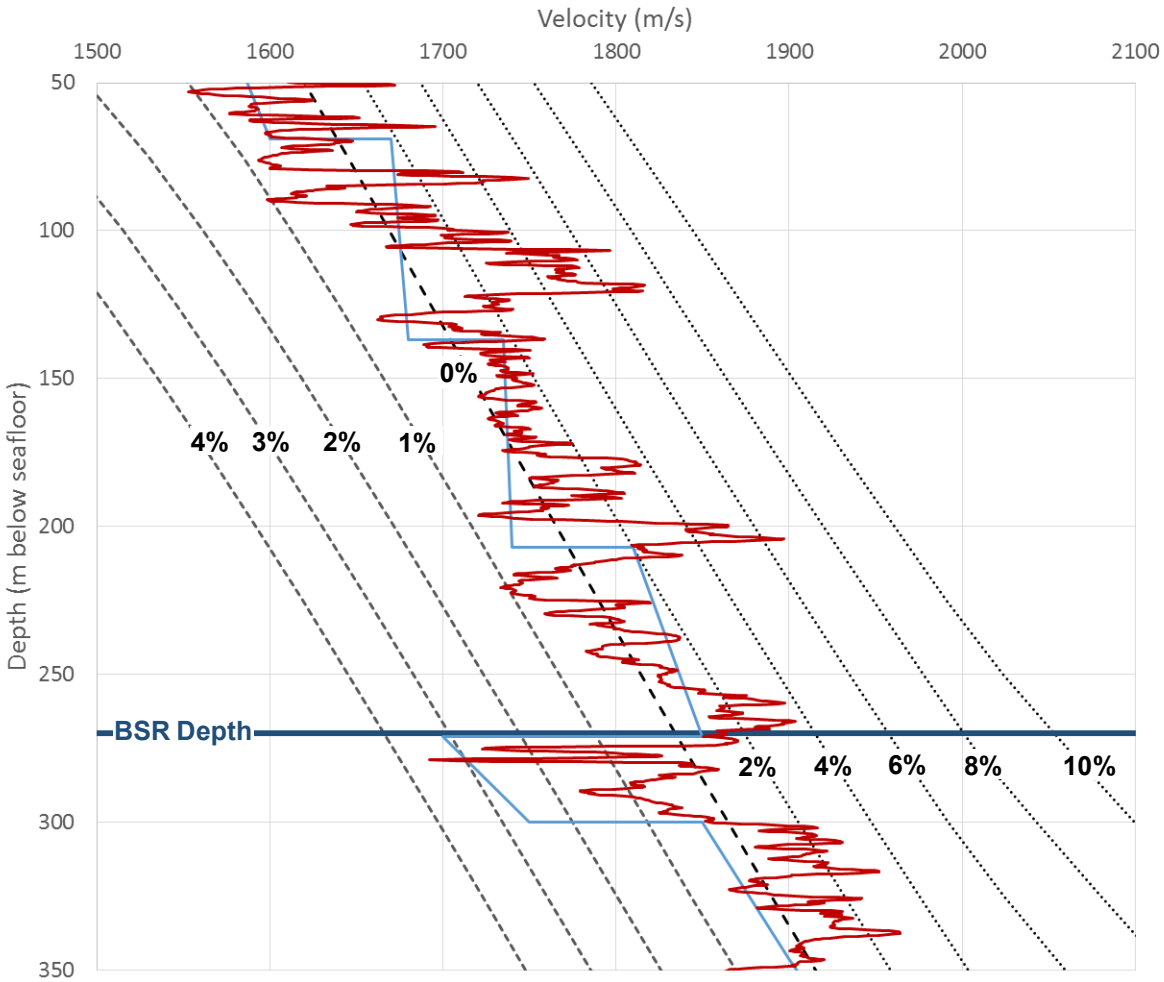

Figure 5.88 Hydrate and gas concentrations with hydrate as part of the sediment frame (dotted lines to the right) and gas patchily distributed in the pore fluids (dashed lines to left). Overlain are downhole velocities from the F-09 well (red solid line) and OBS velocities (light blue solid line). Note that the blocky, low resolution of the OBS velocities (Chian, 2008) do not capture the high velocity zones above the BSR but do model the low velocity unit underlying the BSR.

There is a distinct 30 m zone of low velocities below the BSR on the F-09 velocity log. These reduced velocities correspond with the elevated seismic amplitudes that define the BSR. Comparison with the modeled velocities shows the sub-BSR low velocities correspond to gas concentrations up to 0.5% for homogenously distributed gas (Figure 5.87) and up to 3% for gas patchily distributed in the pores (Figure 5.88).

The manual BSR maps six metres above the low velocity zone (Figure 5.87 and Figure 5.88). Seismic profiles show the low velocity zone corresponds with the depth of the snapped BSR (Figure 5.89).

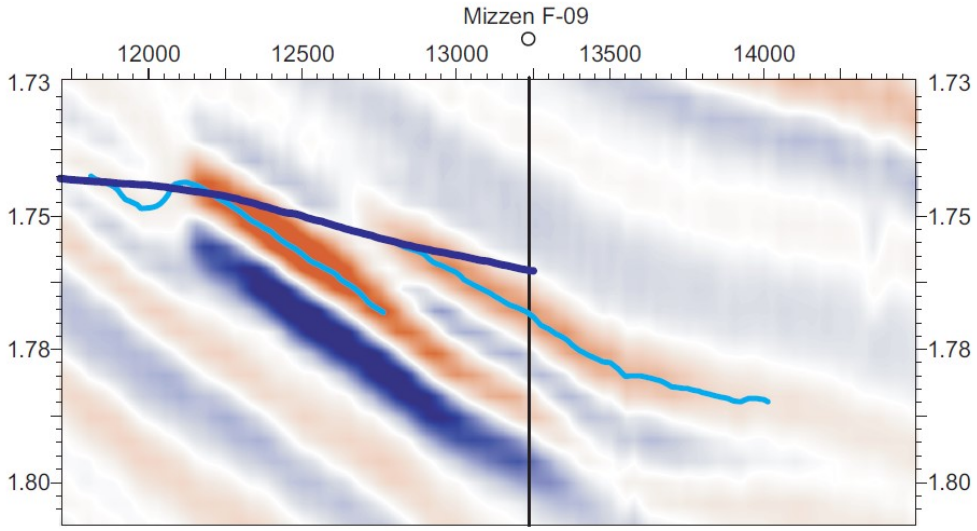

Figure 5.89 Crossline through the Mizzen F-09 well showing the offset between the manual and snapped BSR.

Elevated velocities above the BSR through the depth intervals of 106-120 m and 198-210 m sub-seafloor are associated with possible hydrate concentrations on the order of 12% for hydrate in the pores and 7% for hydrate as part of the sediment frame. Velocities through these two zones are higher than those below the BSR but are not distinctly elevated compared to other gas hydrate deposits such as the Blake Ridge (Collett and Ladd 2000).

5.4.2 Sensitivity analysis

The porosity function in the effective medium model defines the shape and position of the velocity functions. Changing the initial porosity values results in an offset of the velocity function while modifying the decay constant changes the slope of the curve. A 5% decrease in the initial porosity increases the modeled velocity by 50 m/s in 300 m of water while increasing the decay constant by 100 decreases the modeled velocity by 25 m (Figure 5.90).

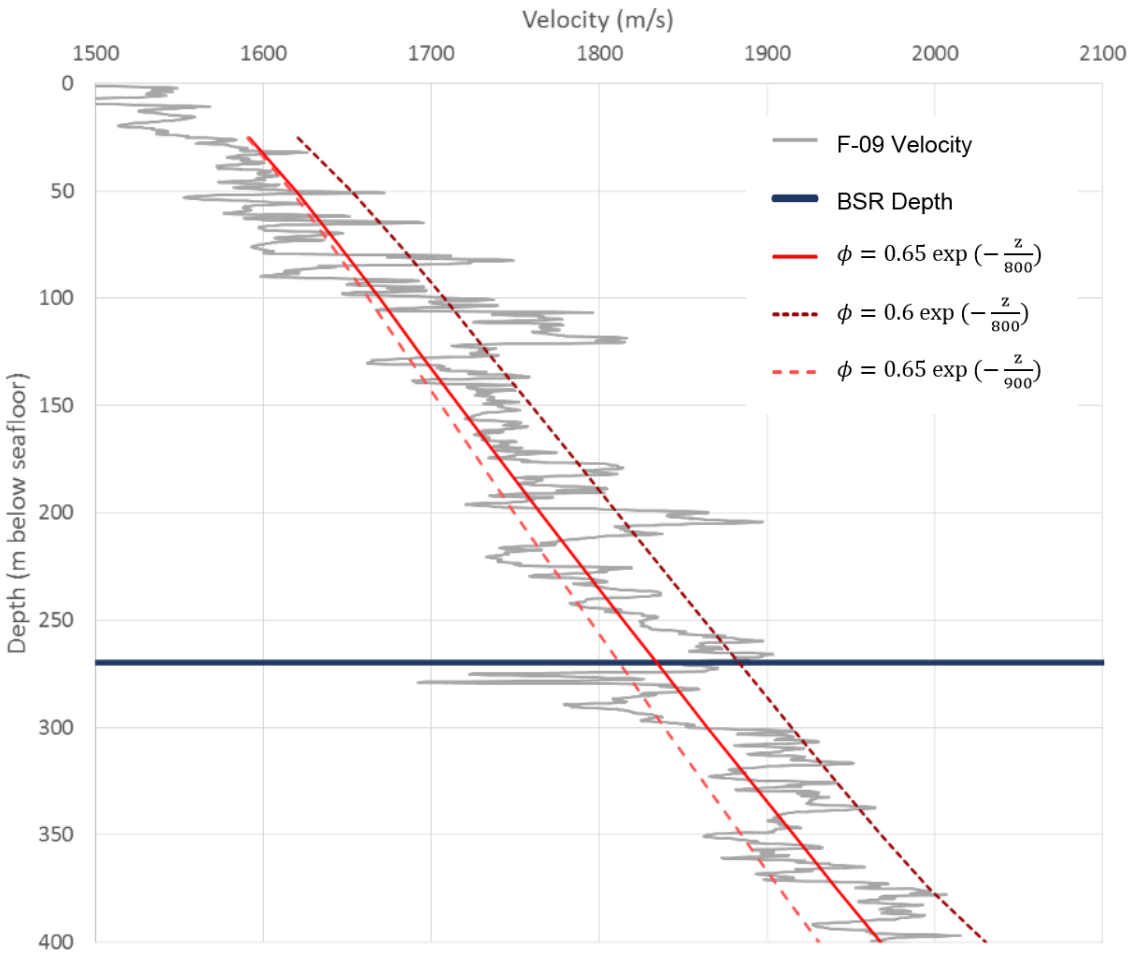

Figure 5.90 Effects of porosity function on the modeled velocities

Surface porosities predicted from the exponential porosity function although slightly higher, generally agree well with those from the 2001045-14 surface core (Figure 5.91).

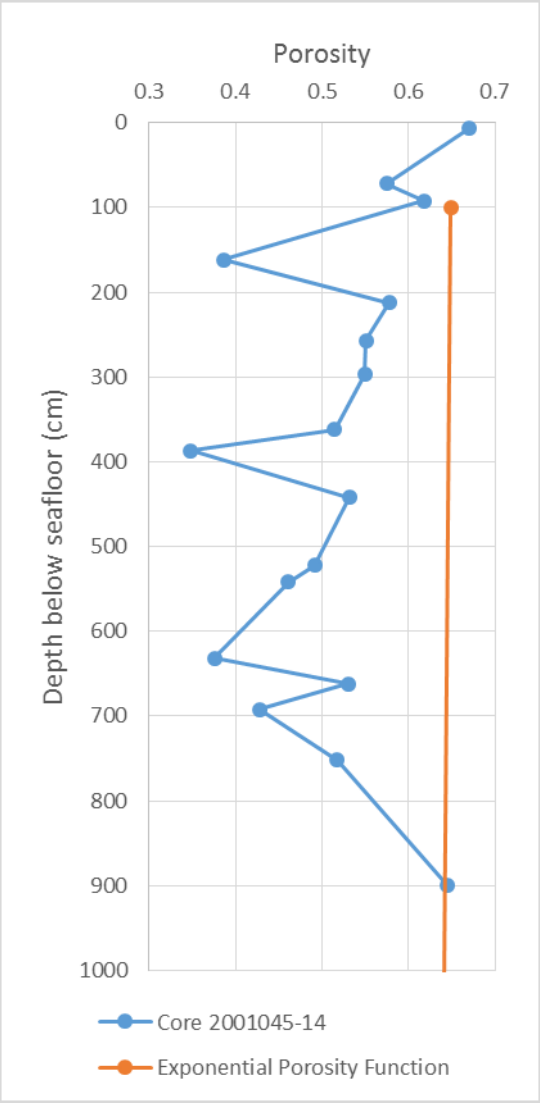

Figure 5.91 Comparison of predicted porosities calculated from the exponential porosity function $0.65*e^{(-z/800)}$ with porosities from the 2001043-14 Core. See **Figure 4.18** for the piston core location.

5.5 ARCHIE'S QUICK LOOK METHOD

Zones of increased electrical resistivity, which can be an indicator of gas hydrate, occur above the BSR in the F-09 well. The baseline or R_0 value determined for the F-09 well is presented below in Figure 5.92. Included on the figure is the equation for the R_0 line, which is the background resistivity value if only sea water were in the pores. Unlike the resistivity logs of Collect and Ladd (2000) from Blake Ridge, F-09 does not have a distinct hydrate zone (a zone of distinct and sustained elevated resistivity values) above the BSR making the positioning of the R0 line subjective.

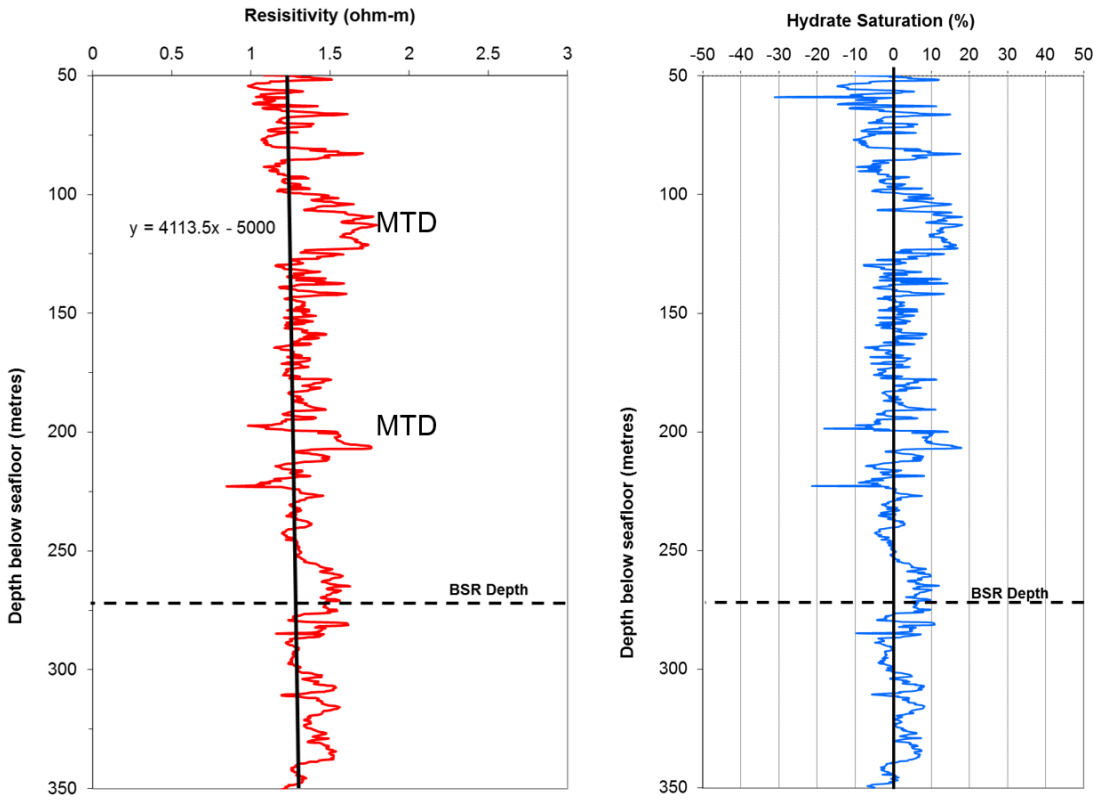

Figure 5.92 Resistivity versus depth plot at the F-09 well showing the chosen R_0 line used in Archie's Quick Look method. Gas hydrate saturations as determined from the F-09 resistivity log. Hydrate saturation is expressed as a percent of the total pore fluids.

Gas hydrate saturations were determined for the F-09 well, based on the R_0 line of Figure 5.92. In the hypothesized hydrate zone above the BSR there are calculated gas hydrate saturations up to 18%. A 30 m zone of consistently elevated gas hydrate saturations occurs between 1180 m and 1210 m below-sea-level (115-145 m bsf). A smaller zone of consistently elevated hydrate saturations occurs between 1283 m and 1291 m below sea-level (218-226 m bsf). Both of these zones can be tied to MTDs imaged on the 3D seismic and are associated with increased compressional velocities. A zone of increased hydrate saturations occur at the BSR depth and below, which is theoretically not possible. Hydrates should not occur below the BSR, which marks the base of hydrate stability. Elevated saturations extend to a depth of 1368 m, 18 m below the BSR. This suggests the resistivity variation is not a product of hydrate in the sediments.

CHAPTER SIX: DISCUSSION

6.1 STRATIGRAPHY

The stratigraphic evolution of the Sackville Spur is divided into four units outlined in Figure 6.1. These four units are discussed below.

6.1.1 Unit 1 – Upper Miocene to Pliocene

The Base of Unit I, marked by the unconformable H9 horizon (Figure 6.1A), corresponds to the boundary between Kennard et al. (1990) stratigraphic units 1 and 2 as well as to Deptuck's (2003) T80 seismic marker representing the base of his Unit 4. Kennard et al. (1990) interpreted this unconformity to be near the Pliocene-Miocene boundary and suggested it is equivalent to the regional Merlin unconformity on the US Atlantic margin that formed as a result of intensification of bottom currents in the Late Miocene (Mountain and Tucholke 1985). More locally, Deptuck (2003) interpreted the central Flemish Pass unconformity to be Middle miocene aged based on seismic and well correlations. Piper and Normark (1989) and Marshal et al. (2014) identified a Mid-Miocene unconformity in southern Flemish Pass based on correlation with ages from the Gabriel C-60 well. These ages agree well with the middle to late Miocene H9 horizon age correlations at the O-16 and L-11 wells. Both Miocene aged sediments and the H9 horizon are absent at the Baccalieu I-78 well.

Around this time period, biogenic silica deposition is reported in the Labrador Sea (Bohrmann and Stein, 1989) and inferred throughout the study area based on the correlation between chert recovered in the L-11 well and the polygonal faults imaged on the seimsic data. Deposition of Unit 1 was unconfined to the north, into Orphan Basin (Deptuck 2003) while currents restricted deposition on the eastern flank of the paleo Flemish Pass as evidenced by sediment waves in the NE and moating around the Mesozoic basement high in the SE. Similar moating around basement highs was noted in the Flemish Pass by Deptuck (2003). A system of polygonal faults developed within these silicous Miocene sediments through the process of diagenetically induced shear failure (Cartwright 2011),. The presence of limestone, glauconite, and chert below H9 suggest the horizon represents the top of a middle to late Miocene diagenetic front. In a study of glauconite, Amorosi (1995) noted that sediment starvation creates the conditions most favorable for the mineral's formation. As such, glauconite is most commonly associated with condensed sections (Amorosi 1995), which in turn often occur as zones of burrowed slightly lithified beds or as marine hardgrounds (Loutit et al.

1988). Increased density as reported in L-11 samples and in the F-09 density log, correlate with increased seismic amplitudes.

In the Pliocene, increased sediment supply and potential slowing of or change in the Labrador Current allowed a large drift deposit to form north of the modern Sackville Spur while deposition remained restricted along the flank of Flemish Cap (Figure 6.1B). Deposition rates were relatively lower in the paleo Flemish Pass as evidenced by the thin seismic sequence and the abundance of glauconite in the L-11 well.

H8 marks the top of Unit 1 which correlates with Campbell's (2014) Cenozoic seismic stratigraphic Unit 3 of the western North Atlantic margin. Campbell (2014) describes his Unit 3 as Oligocene-middle Miocene with a predominance of contourite drift development.

6.1.2 Unit 2 - Pliocene

Drift development on the flanks of Flemish Pass dominated in the Pliocene. Drifted sediment accumulated below the Sackville Spur and on the eastern flank of Flemish Cap including the moated area of Unit 1 (Figure 6.1C). The moated area of Unit 1 is replaced first by sheet drifts then by large current parallel troughs within the drifted sediments (Figure 6.1C). Deposition at the base of the Pass was restricted even more than in Unit 1 although the well logs indicate increased lithologic variation in Unit 2, suggesting periodic pulses of coarser sediment into the Pass or winnowing from increased currents. Elevated amplitudes along the H7 horizon, which are concentrated below the Spur and on the eastern flank of the pass, likely reflect winnowed drift sediments with a higher coarse fraction and potentially free gas.

The L-11 well report describes Unit 2 as claystone with varying amounts of well cement, attesting to the reduced lithification of the unit (Datalog 2003). Faults extend from the system of polygonal faults into Unit 2 with select faults extending into the sediments below the Sackville Spur, potentially providing conduits for gas and fluids to migrate from depth.

6.1.3 Unit 3 – Plio-Pleistocene

Unit 3 marks a significant change in deposition style with the onset of MTDs that Piper and Normark (1989) correlate with the onset of Pleistocene glaciation. The well

logs show increased variation representing influxes of coarser sediments into the Pass by MTDs. Drift development became focused at Sackville Spur with thinner sheet drifts over the Pass's eastern flank (Figure 6.1D). In the base of the Pass, a small basin fed by MTDs developed, sourced from the flanks of the Pass. Sediment accumulation in the Pass and on the Spur become more concordant (Figure 6.1D) suggesting a change in the Labrador Current. Faults generally do not extend from the underlying polygonal fault system into Unit 3 except for a select number below the western flank of the Pass including below Sackville Spur. These observations agree with a global study by Cartwright and Dewhurst (1998) who consistently observed layer bound polygonal faults overlain by unfaulted Pleistocene sediments dominantly composed of MTDs. Although the faults are limited, the upward migration of fluids and gases and their release on the paleo seafloor is documented by a series of pockmarks on the H5, H4 and H2 surfaces.

6.1.4 Unit 4 - Pleistocene

As Pleistocene glaciation continued, large portions of the Sackville Spur sediments were removed by MTDs and deposited in the Pass with three large MTD deposits imaged on the 3D seismic volume (Figure 6.1E). Drift development, focused on the western flank of the Pass, continued between MTD events. MTDs, emplaced progressively east, filled and widened the Pass (Figure 6.1E). The well logs show significant variation attesting to the increased coarse fraction supplied by the MTDs. No faults occur in Unit 4 but pockmarks are observed. The elongation and current scouring of these pockmarks (Figure 5.68) in addition to current striations that pass over Sackville Spur (Figure 5.63) record periods of increased Labrador Current velocities. Winnowing would increase during such periods creating sandier, more porous beds in which hydrate and gas preferentially accumulate. Within Unit 4, MTD deposition in the base of the Pass outpaces drift deposition on the flanks of the Pass (Figure 6.1E). Through time, these MTDs fill and widen the Pass (Figure 6.1E).

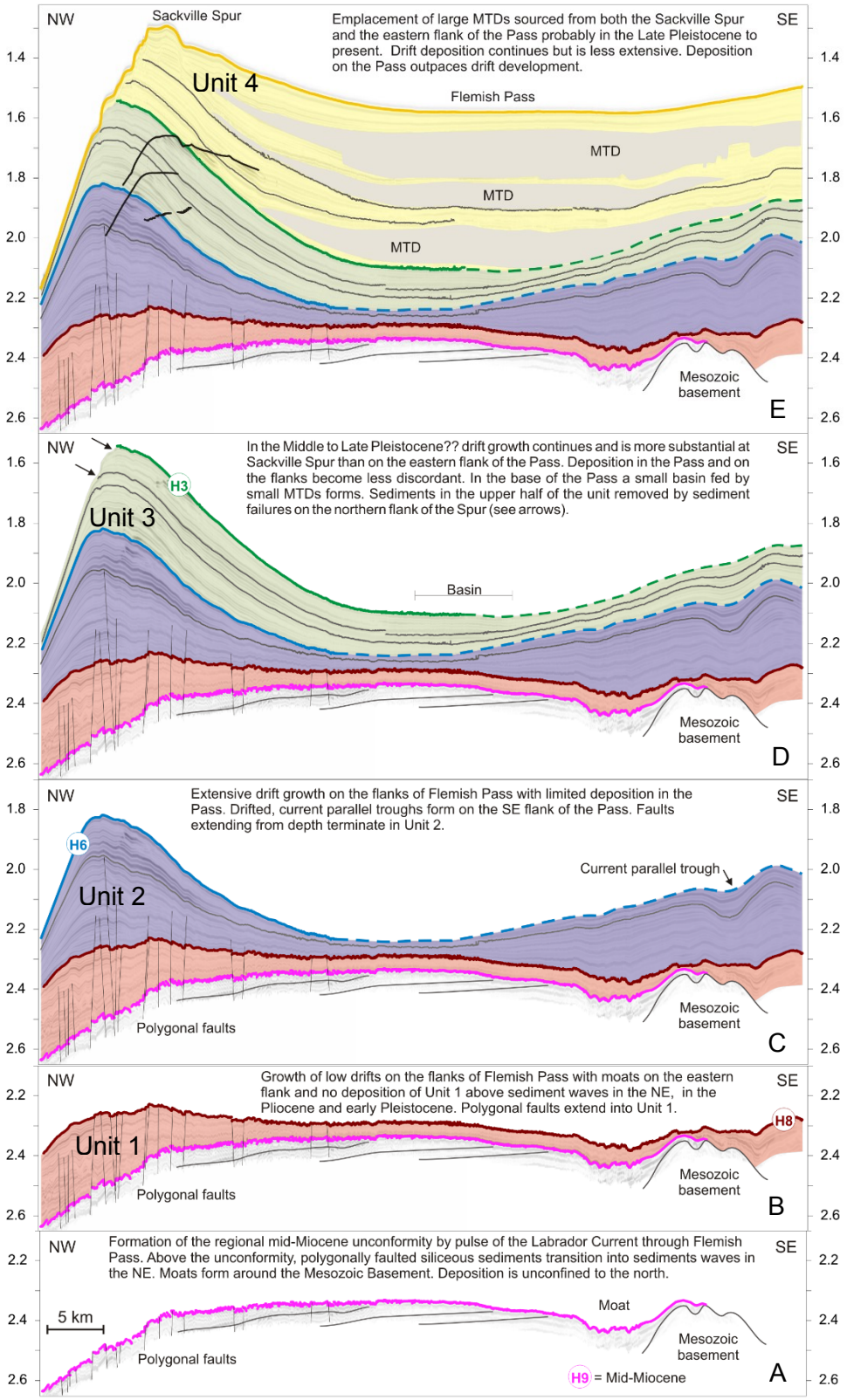

Figure 6.1 An annotated arbitrary NW-SE 3D seismic profile through the Sackville Spur and Flemish Pass showing the stratigraphic evolution of the area. Vertical units are two-way time in seconds.

6.2 ORIGIN OF THE SACKVILLE SPUR BSR

6.2.1 Gas Hydrate BSR

The Sackville Spur BSR was first reported by Mosher (2011) who, based on its cross-cutting nature and correlation with base of hydrate stability depths, related the BSR to the presence of gas hydrates. Conversely, consultants hired by the operators of the lease block interpreted the origin of the BSR to the diagenetic transition of silica (E. Stacey, personal communication 2011). They likened the BSR to the Qulleq-1 exploration well drilled in the Davis Strait off western Greenland (Pegrum et al. 2001) where a high amplitude, cross cutting reflector (CCR) imaged on various seismic profiles was interpreted as a water on gas contact. Once drilled, examination of side cores determined that the flat spot was not a water gas contact but instead represented the diagenetic transition of opal CT to microquartz (Pegrum et al. 2001).

Unlike the Quelleq-1 CCR, which was continuous and had normal polarity, the Sackville Spur BSR is characterized by reversed polarity along abruptly terminated, high-amplitude reflections. In addition, the F-09 resistivity, density and gamma ray logs show no indication of a lithological change or a significant density increase across the BSR(s) as occurs across a diagenetic BSR (Nobes et al. 1992). These observations along with the strong correlation between base of hydrate stability and Primary BSR depths, indicate a hydrate origin for the BSR. That being said, the acoustic impedance contrast that produces the BSR is not solely related to the change from hydrate-bearing to non-hydrate-bearing beds. Instead, it results from accumulation of gas in the more porous beds below the hydrate bearing sediments.

Once in the hydrate stability zone, the beds become hydrated and prevent further gas ascension as described by Bouriak et al. (2000) on the mid Norwegian margin. This process is suggested at the F-09 well where a zone of reduced resistivities and gamma ray values that are indicative of increased water content and increased sand content (hence increased porosity) correlates updip on the seismic data with elevated BSR amplitudes (2 of Figure 6.2). Units with elevated gamma ray and resistivity values correspond on the seismic to less elevated updip BSR amplitudes (Figure 6.2). Gas as the origin of the BSR is further supported by a correlation between reduced velocities at the F-09 exploration well and elevated BSR amplitudes on the 3D seismic. A similar decrease in velocity is observed on the 2D refraction profile acquired by NRCan (Chian 2008).

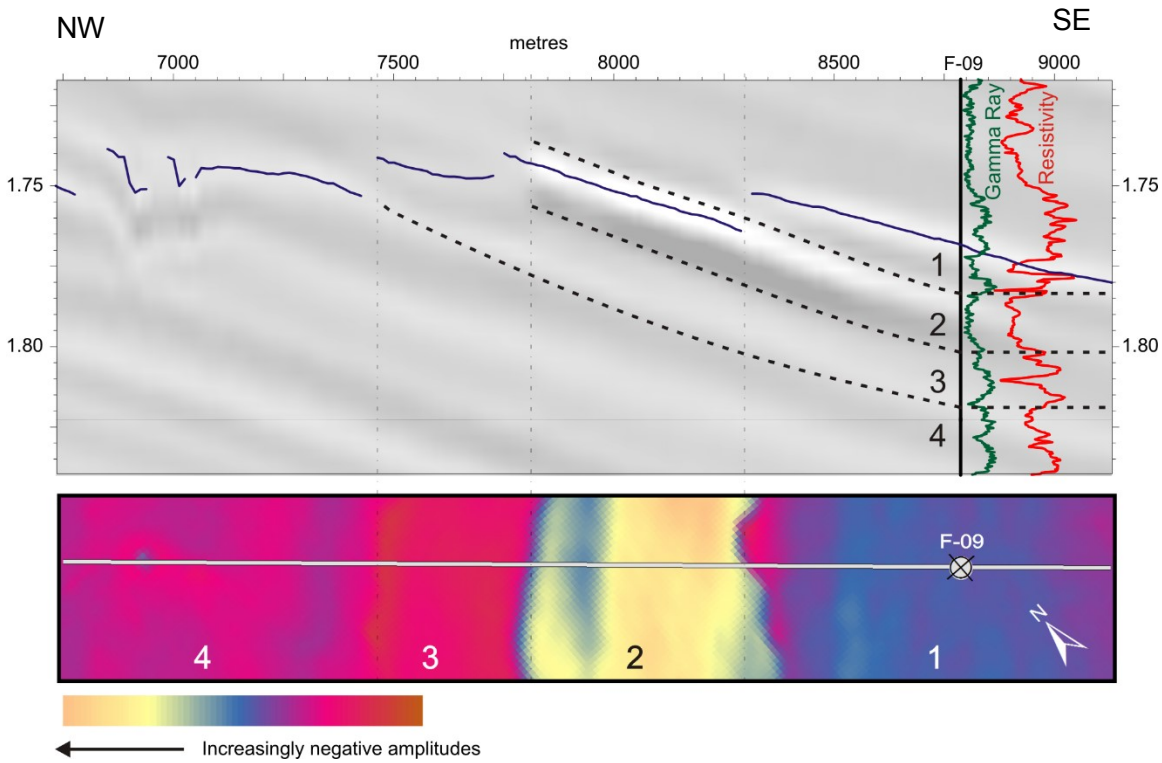

Figure 6.2 A 2 km arbitrary seismic profile through the F-09 well showing the correlation between increased BSR amplitudes and resistivity and gamma ray log responses at the F-09 well. The location of the upper seismic profile is overlain in grey on the BSR amplitude surface. The highest BSR amplitudes correlate to a unit with consistency low log values (2) which are interpreted as porous sands. BSR segments with reduced amplitudes correlate with higher log values interpreted as sediments with greater amounts of silt and clay.

Further evidence against a potential diagenetic origin is the age of the sediments at the depth of the BSR. Miocene and older ages, which are reported for diagenetic boundaries in the Labrador Sea (Thein and von Rad, 1987, Bohrmann, and Stein 1989), on the New Jersey margin (Vecsei and Hoppie 1996), and on the mid Norwegian margin (Bouriak et al. 2000), are older than Pliocene and younger sediments that are host to the Sackville Spur BSR. Post-rift sediments on the Newfoundland margin show no evidence of an elevated geothermal gradient (Wielens and Jauer 2001) or volcanic eruptions that could accelerate silica diagenesis. Additionally, given the margin's mature passive tectonic setting, it is unlikely that a significantly elevated geothermal gradient has occurred since the Pliocene. Chert, a diagenetic silica, was reported in the L-11 well below the H8 horizon, 365-660 m below the BSR. The onset of chert is associated with a

significant increase in density at the F-09 well and to well-developed polygonal faults on the seismic profiles, both of which are characteristic of a diagenetic front (Neagu 2011). Based on these associations, the H9 horizon is interpreted to mark the top of the opal-A to opal-CT diagenetic front.

The H9 horizon is associated with an underlying low velocity zone. At the Monterey Formation in California, polygonal faults brecciated the dense and brittle diagenetic sediments thus increasing the deposit's permeability and allowing upward migrating gas and fluids into the shallow sediments (Behl 1998). The fluids may also be the result of dewatering during silica diagenesis. Below the Sackville Spur, faulting of the H9 horizon could increase the permeability and porosity of the sediments creating space to capture gas and fluids migrating up from the underlying hydrocarbon reservoir.

Key factors for distinguishing between gas hydrate and silica diagenetic BSRs in the western North Atlantic, based on observations at the Sackville Spur BSR are summarized in Table 6.1.

Table 6.1 Key factors for distinguishing BSRs in the western North Atlantic.

	Gas Hydrate Origin	Diagenetic Silica Origin
Sediment Age	Relatively modern (Pleistocene and younger) sediments - at increased burial depths (increased pressures and temperatures) hydrates dissociate	Miocene and older
Seismic	Frequency and amplitude anomalies along and underlying the BSR Frequency shadows underlying the BSR Indications of fluid and gas flux such as pockmarks Defined by abruptly terminated high amplitude, phase reversed reflections Relatively parallel to modern seafloor	High amplitude reflection associated with small offset, layer bound, polygonal faults Horizon may or may not be phase reversed. Parallel to paleo-seafloor
Environment	Typically contained within drift deposits and associated with fluid evacuation structures Overlie conventional hydrocarbon fields	Large periods of global deposition Deposition and preservation is controlled by silica saturation in the oceans
Well Logs	Underlying low velocity zone Overlying resistivity increases	Significant density increases
Hydrate stability	Correlated with the base of hydrate stability	No correlation with base of hydrate stability
Samples and cuttings	Porous, unlithified silt and sand	Chert, ash or other siliceous sediments

6.2.2 Evidence of Gas

Horizons underlying the BSR(s) show subtle instantaneous frequency reductions (e.g. Figure 5.39). This phenomenon is reported below gas hydrate BSRs of other margins including the Blake Ridge, (Taylor et al. 2000), the mid-Norwegian margin (Berndt et al. 2004) and on both the western and eastern margins of India (Satyavani et al. 2008 and Satyavani et al. 2005). At these locations, the authors attributed the reduced frequencies to attenuation (or absorption) of the high frequency component of the seismic energy by free gas in the sediments. At the Sackville Spur, the reduced seismic frequencies occur below the high amplitude portions of the Primary BSR as well

as surrounding and below the two secondary BSRs. Reduced frequencies coupled with increased amplitudes along the H7 Horizon, which underlies all three BSRs, are spatially associated with reduced amplitudes on the underling H9 horizon. This type of amplitude shadow is commonly reported below gas bearing beds (Spence et al. 2011).

The presence of pockmarks, which form when gas and fluids are abruptly released from the sediments, provides evidence of shallow gas in the subsurface (Hovland and Judd 1988). Upward migration along permeable beds is suggested by pockmarks concentrated below the crest of the Spur, updip of the Primary BSR, and with the lack of observed fluid migration structures such as chimneys. Cathles et al.(2010) suggest pockmarks form when gas accumulates below a seal of fine grained sediment or sediment whose pores have been reduced by hydrate crystallization. As the gas accumulates, pore pressures increase until the fine grained seal breaks and the pressurized gas and fluids are release at the seabed.

The pockmarks' spatial association with the primary BSR suggests a causational relationship between hydrate dissociation and pockmark formation. Reduced pore pressures or increased temperatures in the shallow sediments can lead to hydrate instability with increased sensitivity to temperature over pressure (Sloan 2003). Reductions in pressure are easily accounted for by changes in sealevel during glacial periods. During the LGM water depths were 120 m shallower than at present although the isostatic adjustments of the study area are unknown (King and Sonnichsen, 1999). A 120 m lowering of the modern sealevel would result in a maximum 140 m shallowing of the hydrate stability field. This would reduce the hydrate stability zone by 40 km^3.

Temperature increases, if they occurred, presumably resulted from changes in ocean circulation. Pleistocene changes in the Labrador Current are evidenced in this study by the appearance of current scours along the H3 and H2 horizons. This observation agrees with work by Li and Piper (2015) who used the sortable silt proxy in cores from Flemish Pass to identify enhancement in the Labrador Current strength in Heinrich Event 1 and the Younger Dryas, both of which were related to increased meltwater supplies. Lazier and Wright (1993) showed that through increased freshwater supply from rivers, the strength of the modern Labrador Current is enhanced in the summer. In the southern Flemish Pass, through correlation of cores with seismic stratigraphy, Marshal et al. (2014) identified three periods of long term flow variations in at least the past 29 ka. In a regional study of seismic lines from the Labrador Sea, Myers

and Piper (1988) noted that deep circulation was slowed or ceased by permanent ice cover during times of glacial maxima.

Changes in ocean current speed could also be associated with alteration in the course of the current whether onto the Grand Banks or into deeper waters. A diversion of the cold Labrador Current could change the seafloor and shallow sediment temperature regime potentially leading to sediment warming and subsequent hydrate dissociation. At the Sackville Spur, a 2°C seafloor temperature increase equates to a ~70m shallowing of the hydrate stability field.

Hydrate dissociation can also result in sediment instability and ultimately in sediment failure. Piper et al.(2012) note that sediment failures are commonly associated with pockmarks and sub-surface gas hydrates. This is observed in the study area where the BSR and failure scarps are spatially associated and the onset of pockmarks and of failure scarps are stratigraphically correlated. Conversely, the onset of pockmarks is stratigraphically correlated with the onset of MTDs but the two are not spatially associated. Based on these observations hydrate dissociation is associated with sediment failures but is likely not their primary trigger. Other potential preconditioning factors that may have acted to trigger sediment failure include steepening and loading of the seabed, increased sedimentation rates resulting in under-consolidation (Piper et al. 2012) and loading by grounded ice or rising sea level (Mulder and Moran 1995). In a study of a geologically recent failure complex in northern Flemish Pass, Cameron et al.(2014) correlated slope failure events with glacial maximum and retreat owing the failure's formation to seismic activity with a minimum reoccurrence interval of ~10^4 years. Cameron et al.(2014) went on to suggest this seismic activity was related to isostatic adjustments resulting from the unloading by recession of the heavy ice sheet.

6.2.3 Gas Origin

Headspace gas analysis, a standard method for distinguishing biogenic versus thermogenic gases, was not undertaken within the study area. Natural gas hydrates encountered in shallow marine sediments are typically associated with biogenic methane produced by bacterial break-down of organic matter. Organic- carbon values in Eocence to Holocene aged Labrador Sea drifted sediments range from 0.1% to 0.75% (Stein et al. 1989). A minimum of 0.5% total organic-carbon is required in sediments for gas hydrates to form from in situ bacterial methane production (Waseda 1998).

The two deeper BSRs imaged on the Baynord 3D seismic profiles suggest an alternative gas origin. These BSR depths compare well with theoretical base of hydrate stability depths for gas mixtures with variable amounts of methane, ethane and propane (Figure 6.3). This correlation suggests a thermogenic gas contribution. Faults extending from depth along with the polygonal faults provide a potential conduit for gas migration. Multiple BSRs have been reported in the Black Sea (Popescu et al. 2006) and Nankai Trough (Golmshtok and Soloviev 2006), where well defined double BSRs record abrupt changes in pressure and temperatures. Such dramatic temperature and sea-level changes are not documented on the western North Atlantic's passive margin and the poorly developed, discontinuous BSR 2 and BSR 3 resemble a second BSR in Antarctica's Ross Sea that is attributed to thermogenic gas (Geletti and Busetti 2011). At Blake Ridge, Paull et al. (2000) identified ethane within the hydrate bearing zone. A thermogenic contribution to the Sackville Spur and other hydrate bearing sediments could explain the common correlation along Canada's Atlantic margin between BSRs and underlying conventional hydrocarbon deposits (Mosher 2011).

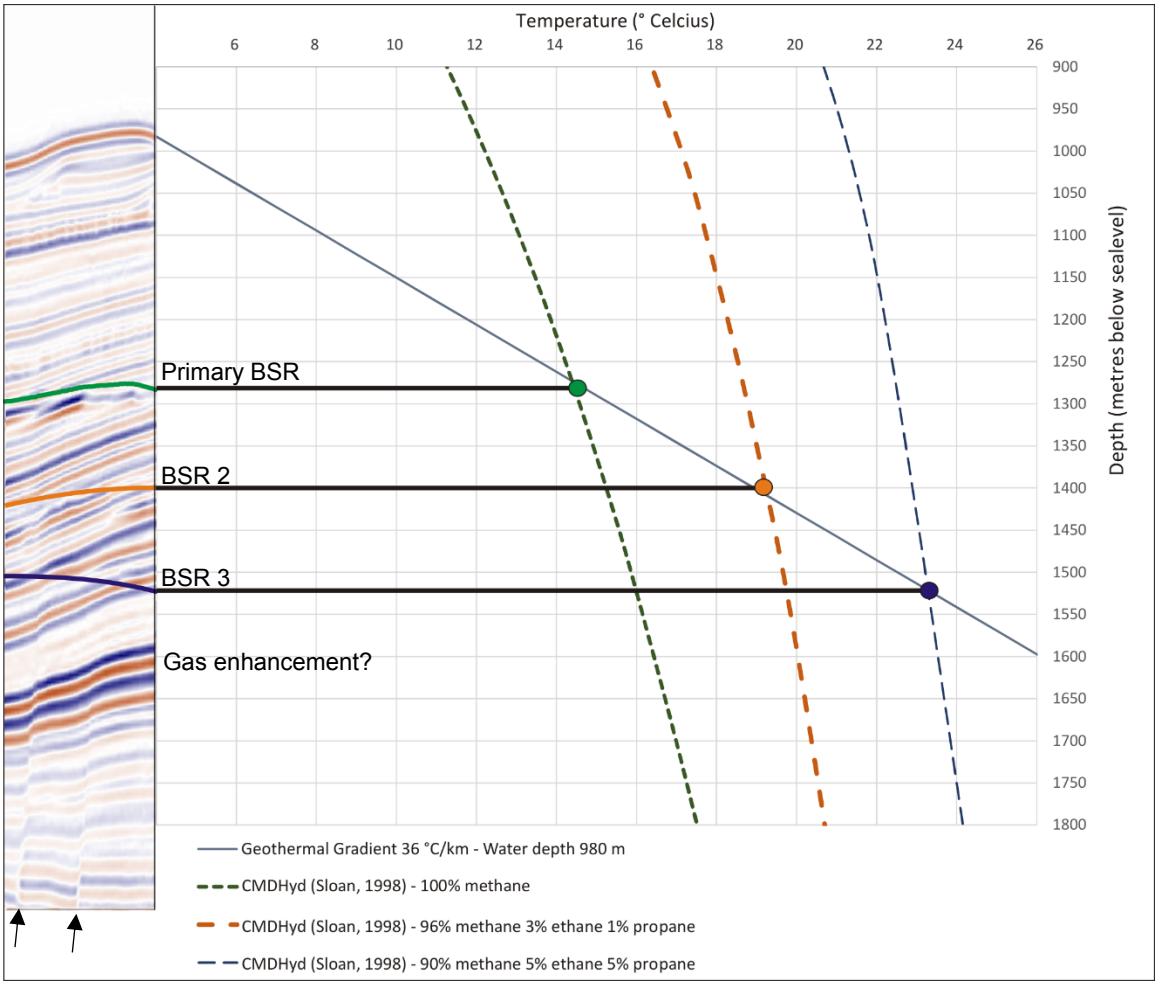

Figure 6.3 Hydrate stability depths for gas compositions with variable amount of thermogenic ethane and propane compared with the various BSR depths.

6.2.4 Gas Hydrate and Free Gas Concentrations

The F-09 well was drilled on the edge of the BSR where elevated seismic amplitudes that define the BSR are low compared to elsewhere below the Spur (Figure 5.5). As such, estimates of free gas and hydrate concentrations at the F-09 represent minimal values. Both the Quick Look and effective medium model suggest elevated hydrate concentrations occur in MTDs overlying the BSR. MTDs associated with distinctly elevated resistivities and velocities occur in the Ulleung Basin offshore Korea (Riedel et al. 2012). Riedel et al. (2012) identified fracture filling hydrates that created anisotropy not accounted for in Archie's Quick Look method and the effective medium model, both of which assume sediment isotropy. This assumption can result in inflated hydrate concentrations. Low hydrate concentrations are not well suited to Archie's quick

look method. Lithologic variations become difficult to distinguish from the hydrate response on the resistivity log and as such the background value, or R_0 line, becomes increasingly subjective. At the F-09 well, hydrate concentrations estimated from the Quick Look method are significantly higher than those estimated using the effective medium modelling.

The concentrations estimated using the effective medium model agree well with Schlesinger et al.(2012) who used the effective medium model of Helgerud et al. (1999) to estimate bulk hydrate concentrations of 2-18% on the Scotian margin. Unlike at the F-09 well, hydrate accumulations on the Scotian margin are represented by increased velocities directly above the BSR. For the BSR to form there must be hydrate to trap ascending gas. At the Sackville Spur BSR, the beds with the highest gas saturation are associated with increased porosity and permeability and presumably in turn with increased hydrate concentrations. The F-09 well intersects a low amplitude reflection above the BSR that is not particularly sandy (Figure 6.2) although a subtle 20 m zone of increased velocity and resistivity does occur above the BSR (Figure 5.87, Figure 5.88, and Figure 5.92). This zone is associated with hydrate concentrations on the order of 2-7% for the effective medium model (Figure 5.87and Figure 5.88) and ~10% using the Quick Look method (Figure 5.92).

6.3 HYDRATE STABILITY

The CMDHyd and second order polynomial provide the best fit of the three hydrate stability functions the observed BSR (Figure 5.79). Majorowicz and Osadetz's (2003) stability curve does not match the output from Sloan's (1998) hydrate stability program and even after correcting for gravity and density variations, it produces base of hydrate stability depths that are the most discordant from the BSR depths.

Southeast into the Flemish Pass the BSR is shallower than the CMDHyd and second order polynomial base of stability depth surfaces. North of the Spur's crest, the BSR is deeper than these modelled base of hydrate stability depths (Figure 5.83). These discrepancies likely reflect seabed temperature variations with reduced temperatures to the north where the Deep Western Boundary Current sweeps the Spur's northern flank. South of the crest where the base of hydrate stability is deeper than the BSR, temperatures are likely greater than the average 3.9°C used in the stability calculations. It is also possible that spatial variations in the geothermal gradient occur and contribute to the discrepancies between the BSR and hydrate stability depths.

CHAPTER SEVEN: CONCLUSIONS

This thesis tested the hypothesis that the Sackville Spur BSR is the product of free gas trapped below gas hydrate bearing sediments. The results have not falsified the hypothesis. The alternative hypothesis tested was that the BSR represented the diagenetic transition of opal-A to opal-CT in siliceous sediments. The results of this research have falsified this hypothesis.

The Sackville Spur BSR is the result of free gas trapped below gas hydrate bearing sediments. This conclusion is based on the following observations which form key features for distinguishing between silica diagenetic and gas hydrate BSRs.

1. The modelled base of hydrate stability depths have a strong correlation with depths to and the Primary BSR.
2. Gas in the sediments is inferred by amplitude and frequency anomalies below and between the BSR(s).
3. The Pliocene and younger sediments containing the BSR are silica poor making silica diagenesis unlikely.
4. The two deeper BSRs correlate with the base of hydrate stability for gas mixes with variable methane and ethane thermogenic gas contributions.

Based on the following evidence, the silica diagenetic front occurs along the basal H9 horizon 365-660 m below the Primary BSR.

1. Correlation of the L-11 exploration well to the seismic data show that the H9 horizon correlates with chert, which is a product of silica diagenesis.
2. The middle to late Miocene age of the sediments at the depth of H9 correlates to regionally abundant siliceous sediments. Silica production and/or preservation in the western North Atlantic were poor in Pliocene and younger sediments (Bohrman and Stein 1989; Mountain and Tucholke 1985).
3. The layer bound, small offset polygonal faults, which affect the H9 horizon, are associated with siliceous diagenetic fronts in the North Atlantic (Cartwright 2011).
4. The increase in density across the H9 horizon is a characteristic product of the volume reduction that occurs during the diagenetic transition of opal-A to opal-CT.

Gas hydrates and underlying free gas preferentially occur in the permeable beds of Pliocene and younger drift deposits of the Sackville Spur. Free gas concentrations in the permeable beds defining the BSR have probable minimal values of 0.5%. At the F-

09 well, hydrates are present in a 20 m zone above the BSR in concentrations between 2% and 7%.

There is no clear spatial association between the BSRs and MTDs at the Sackville Spur although the MTDs are spatially associated with failure scarps. Fluid and gas flux potentially associated with periods of hydrate dissociation are recorded by pockmarks along beds updip of the BSRs. The onset of these pockmarks is contemporaneous with the appearance of MTDs and failure scarps while the BSRs are spatially associated with failure scarps but not with the MTDs. These observations suggest that hydrate dissociation and sediment failures are related but that there is no conclusive evidence that the latter is triggered by the former. It is possible that the appearance of significant northern hemisphere ice sheets reduced sealevels leading to hydrate dissociation. While at the same time glacial unloading resulted in earthquakes that triggered the MTDs. These earthquakes could reactivate deeper faults in the Cumberland Belt Transfer Zone increasing the flux of gas and fluids to the shallow sediments.

The stratigraphic evolution of the Sackville Spur and northern Flemish Pass agrees well with that of the Beothuk Drift (Deptuck 2003) in southern Flemish Pass (Marshal et al. 2014) and supports observations made elsewhere along the margin (Tucholke and Mountain 1986; Piper and Normark 1989; Campbell and Mosher 2016). A pulse of the Labrador Current is recorded by a mid- to late-Miocene erosional unconformity that is characterized on seismic profiles by polygonal faults that transition to sediment waves. In the late Miocene and early Pliocene, deposition began as the current waned and a precursor spur north of the modern Sackville Spur's crest formed. Deposition was restricted in the NE quadrant of the study area and around the Mesozoic basement high where moating records increased current. Increased sediment supply and/or a change in the current regime is recorded in the Pleistocene by increased drift deposition on both flanks of the Pass and limited deposition above the floor of the Pass. Periodic increases in the Labrador Current velocity are recorded by current striations and elongated pockmarks along stratigraphic surfaces of the Sackville Spur. The Labrador Current waned further and deposition was once again focused below the Sackville Spur. In the middle to late Pleistocene, MTD deposition in the Pass outpaced drift development on the flanks of the Pass filling and broadening the Flemish Pass.

Knowledge and understanding of the hydrate bearing sediments at Sackville Spur are critical for the safety of future hydrocarbon drilling and development operations in the northern Flemish Pass.

REFERENCES

Amorosi, A. 1995. Glaucony and sequence stratigraphy: a conceptual framework of distribution in siliclastic sequences. Journal of Sedimentary Research, **B65**: 419-425.

Andrews, J.T., Jennings, A.E., Coleman, C., and Eberl, D.D. 2010. Holocene variations in mineral and grain-size composition along the East Greenland glaciated margin (ca 67°-70°N): Local versus long-distance sediment transport, Quaternary Science Reviews, **29**: 2619-2632.

Arthur, M.A., Srivastava, S.P., Kaminski, M., Jarrard, R., and Osler, J. 1989. Seismic Stratigraphy and history of deep circulation and sediment drift development in Baffin Bay and the Labrador Sea. Proceedings of the Ocean Drilling Program, Scientific Results, **105**: 957-988.

Bahorich, M. and Farmer, S. 1995. The coherence cube. The Leading Edge, **14**: 1053-1058.

Barnes, A.E. 1998. The complex seismic trace made simple. The Leading Edge, April, 1998. Society of Exploration Geophysicists.

Barnes, A.E. 2001. Seismic attributes in your facies. CSEG Recorder, September 2001: 41-47.

Basin Database, Natural Resources Canada. Strickland, Roland Stride Consulting - O-16 lithostratigraphic ages.
http://basin.gdr.nrcan.gc.ca/wells/single_lithostrat_e.php?type=picks&well=N342
[accessed March 2, 2017]

Behl, R.J., 1998. Relationships between silica diagenesis, deformation, and fluid flow in Monterey Formation cherts, Santa Maria Basin, California. *In* Diagenesis, deformation, and fluid flow in the Miocene Monterey Formation. *Edited by* P. Eichhubl. Special Publication Pacific Section SEPM: Society for Sedimentary Geology, **83**: pp. 77-83.

Berndt, C., Bünz, S., Clayton, T., Mienert, J., and Saunders, M. 2004. Seismic character of bottom simulating reflectors: examples from the mid-Norwegian margin. Marine and Petroleum Geology, **21**: 723-733.

Best, A.I., Priest, J.A., Clayton, C.R.I. and Rees, E.V.L., 2013. The effect of methane hydrate morphology and water saturation on seismic wave attenuation in sand under shallow sub-seafloor conditions. Earth and Planetary Science Letters, **368**: 78-87.

Birchwood, R., Noeth, S., Jones, E., 2008. Safe drilling in gas-hydrate prone sediments: Findings from the 2005 drilling campaign of the Gulf of Mexico gas hydrates Joint Industry Project (JIP): USDOE-NETL Fire in the Ice Newsletter, Winter 2008, pp. 1-4.

Bohrmann, G. and Stein, R. 1989. Biogenic silica at ODP Site 647 in the southern Labrador Sea: Occurrence, diagenesis, and paleoceanographic implications. Proceedings of the Ocean Drilling Program, Scientific Results, **105**: 156-170.

Borowski, W.S. 2004. A review of methane and gas hydrate in the dynamic, stratified system of the Blake Ridge region, offshore southeastern North America. Chemical Geology, **205**: 311-346.

Borwski, W.S., Paull, C.K., and Ussler III, W. 1999. Global and local variations of interstitial sulfate gradients in deep-water, continental margin sediments: Sensitivity to underlying methane and gas hydrates. Marine Geology, **159**: 131-154.

Boswell, R. and Collett, T.C. 2011. Current perspectives on gas hydrate resources, Energy & Environmental Science, **4**: 1045-1528.

Bouriak, S., Vanneste, M., Soutkine, A., 2000. Inferred gas hydrates and clay diapirs near the Storegga Slide on the southern edge of the Vøring Plateau, offshore Norway. Marine Geology, **163**: 125–148.

Brackenridge, R., Stow, D.A.V., and Hernández-Molina, F.J. 2011. Contourites within a deep-water sequence stratigraphic framework. Geo-Marine Letters, **31**: 343–360.

Brown, A R. 2011. Interpretation of Three-dimensional Seismic Data. 7th ed. AAPG Memoir; 42. Published Jointly by American Association of Petroleum Geologists and the Society of Exploration Geophysicists. Tulsa, OK U.S.A.

Buffett, B. and Archer, D. 2004. Global Inventory of Methane Clathrate: Sensitivity to Changes in the Deep Ocean, Earth and Planetary Science Letters, **227** (3-4): 185–199.

Cameron, G.D.M., Piper, D.J.W., and MacKillop, K. 2014. Sediment failures in northern Flemish Pass. Geological Survey of Canada Open file 7655, pp. 1-141.

Campbell, D.C. and MacDonald, A.W.A. 2017. Preliminary results of investigations of seabed cold seeps along the outer continental margin south of Nova Scotia. AGS Conference, Fredericton New Brunswick, Canada

Campbell, D.C., Piper, D.J.W., Douglas, E.V. and Migeon, S. 2002. Surficial Geology of Flemish Pass: Assessment of hazards and constraints to development, Geological Survey of Canada, Open File 1454, pp. 1-61.

Campbell, D.C. 2014.Comparison of large contourite drifts in the western North Atlantic, 2nd Deep-Water Circulation Congress, 10-11 Sept. 2014, Ghent, Belgium.

Campbell, D.C. & Mosher, D.C. 2016. Geophysical evidence for widespread Cenozoic bottom current activity from the continental margin of Nova Scotia, Canada. Marine Geology, **378**: 237-260.

Cant, D.J. 1986. Diagenetic traps in Sandstone. AAPG Bulletin, **70**: 155-160.

Carroll, J. 2009. Natural gas hydrates. Gulf Professional Publishing, Boston.

Cartwright, J. 2011. Diagenetically induced shear failure of fine-grained sediments and the development of polygonal fault systems. Marine and Petroleum Geology, **28**(9): 1593-1610.

Cartwright, J.A. and Dewhurst, D.N. 1998. Layer-bound compaction faults in fine-grained sediments. GSA Bulletin, **110**(10): 1242-1257.

Castellani, B., Filipponi, M., Nicolini, A., Cotana, F., and Rossi, F. 2013. Carbon dioxide capture using gas hydrate technology, Journal of Energy and Power Engineering, **7**: 883-890.

Cathles, L.M., Su, Z., and Chen, D. 2010. The physics of gas chimney and pockmark formation, with implications for assessment of seafloor hazards and gas sequestration. Marine and Petroleum Geology, **27**(1): 82-91.

Chand, S., and Minshull, T.A., 2004. The effect of hydrate content on seismic attenuation: a case study for Mallik 2L-38 well data, Mackenzie delta, Canada. Geophysical Research Letters, **31**: L14609-L14609.

Chian, D., 2008. Hud2004-024 Ocean Bottom Seismometer Data Analysis: Sackville Spur Bottom Simulating Reflector (BSR), Unpublished report to Geological Society of Canada – Atlantic, Dartmouth, NS (D. Mosher).

Chopra, S. 2002. Coherence Cube and Beyond. First Break, **20**(1): 27-33.

Christiansen, F.G. et al. 2001. Petroleum Geological Activities in West Greenland 2000. Geology of Greenland Survey Bulletin, **189**: 24-33.

CNLOPB Publication. 2008. Schedule of Wells: Newfoundland and Labrador Offshore Area.

Colbourne, E.B. and Foote, K.D., 1994. Spatial Temperature and salinity fields over the shelves of Newfoundland and Labrador. Canadian Technical Report of Hydrography and Ocean Sciences, No. 160, 1-128.

Collett, T.S. and Ladd, J. 2000. Detection of gas hydrate with downhole logs and assessment of gas hydrate concentrations (saturations) and gas volumes on the Blake

Ridge with electrical resistivity log data. *In* Proceedings of the Ocean Drilling Program, Scientific Results, Leg 164: pp. 179-191.

Collett, T., Lee, M., Lewis, R., Mrozewski, S., Guerin, G., Goldberg, D., Cook, A., 2012. Gulf of Mexico gas hydrate joint industry project Leg II logging-while-drilling data acquisition and analysis. Journal of Marine and Petroleum Geology, **34**: 41-61.

Cressie, N. A. C. 1990. The Origins of Kriging. Mathematical Geology, **22**: 239-252.

Cullen, J., Mosher, D.C., and Louden, K. 2008. The Mohican Channel gas hydrate zone, Scotia Slope: Geophysical structure. *In* Proceedings of the 6th International Conference on Gas Hydrates Vancouver, B.C. Canada July 6-10.

Cyranoski, D. 2013. Japanese test coaxes fire from ice. Nature, **496** (7446): 409.

Datalog, 2003. End of Well Report, Petro-Canada, Mizzen L-11.

Davy, H. 1811. On some of the combinations of oxy-muriatic gas and oxygen, and on the chemical relations of the principles to inflammable bodies. Philosophical Transactions of the Royal Society, **101**: 1-35

Deon, G. anfd Timmons, G. 2003. Geologic Report on Petro-Canada et al Mizzen L-11 N. Flemish Pass for Petro Canada Oil & Gas. DMA Geological and Timmons Consulting. UWI 300L11-4820-04615-01.

Deptuck, M.E. 2003. Post-rift geology of the Jeanne d'Arc Basin with a focus on the architecture and evolution of early Paleogene submarine fans, and insights from modern deep-water systems. Ph.D. thesis, Dalhousie University.

DeSilva, N.R. 1997. Flemish Pass Basin: Hydrocarbon Prospectively and Potential Deep Water Development. Annual Technical Meeting June 8-11 Calgary Alberta, Petroleum Society of Canada.

Dickens, G.R. and Quinby-Hunt, M.S. 1994. Methane hydrate stability in seawater. Geophysical Research Letters, **21**(19): 2115-2118.

Dickens, G.R., O'Neil, J.R., Rea, D.K., and Owen, R. M.1995. Dissociation of oceanic methane hydrate as a cause of the carbon isotope excursion at the end of the Paleocene. Paleoceanography, **19**: 965–971.

Dickens, G.R. 2011. Down the Rabbit Hole: toward appropriate discussion of methane release from gas hydrate systems during the Paleocene-Eocene thermal maximum and other past hypothermal events. Climate of the Past, **7**: 831-846.

Dvorkin, J., Prasad, M., Sakai, A., and Lavoie, D. 1999. Elasticity of marine sediments: Rock physics modeling. Geophysical Research Letters, **26** (12): 1781-1784.

Eberl, D.D. 2003. User guide to RockJock: a program for determining quantitative minerology from X-ray diffraction data. United States Geological Survey, Open File Report 03-78. Washington, DC, pp. 40.

Enachescu, M.E., Hogg, J.R., Fowler, M., Brown, D.E., and Atkinson, I. 2010. Late Jurassic Source Rock Super-Highway on Conjugate Margins of the North and Central Atlantic (offshore East Coast Canada, Ireland, Portugal, Spain and Morocco). Central & North Atlantic Conjugate Margin Conference, Lisbon 2010.

Ersland, G., Husebø, J., Graue, A., and Kvamme, B. 2009. Transport and storage of CO_2 in natural gas hydrate reservoirs. Energy Procedia, **1**: 3477-3484.

Falkowski, P.G., Katz, M.E., Knoll, A., Quigg,A., Raven, J.A. Schofield, O., and Taylor, M., 2004. The evolutionary history of eukaryotic phytoplankton. Science, **305**: 354-360.

Faugères, J.C., and Stow, D.A.V. 2008. Contourite drifts: Nature, evolution and controls. *In* Contourites. *Edited by* M. Rebesco, and A. Camerlenghi. Elsevier Science, Boston, Mass. pp. 143-156.

Fenton, J.P.G. 2003. Petro-Canada Mizzen L-11 Well, Flemish Pass Area, Offshore Newfoundland - Biostratigraphy of the Interval 1695m - 3823m TD. Robertson Research International Limited, Llandudno, North Wales, UK. Report Number 6533/Ib.

Fisheries and Oceans Canada, 2011. Newfoundland Shelf Climatology (Data File). Retrieved from http://www2.mar.dfo-mpo.gc.ca/science/ocean/tsdata.html.

Fofono, N. P., and R. C. Millard, 1983. Algorithms for computations of fundamental properties of seawater. Unesco Technical Papers in Marine Science No. 44, 53 pp.

Foster, D. G., and A. G. Robinson, 1993. Geological history of the Flemish Pass Basin, offshore Newfoundland. AAPG Bulletin, **77**: 588–609.

Frakes, L.A. 1979. Climates throughout geologic time. Elsevier Scientific Publishing Company, New York.

Froján, C.R.S.B., MacIsaac, K.G., McMillan, A.K., Cuadrado, M. M. S., Large, P.A., Kenny, A.J., Kenchington, E., and González. 2012. An evaluation of benthic community structure in and around the Sackville Spur closed area (Northwest Atlantic) in relation to the protection of vulnerable marine ecosystems. ICES Journal of Marine Science, **69**: 213-222.

Frye, M., Shedd, W., Godfriaux, R., Collet, T., Lee, M., Boswell, R., Dufrene, R., and McConnell, D. 2009. Gulf of Mexico Gas Hydrate Joint Industry Project Leg II: Alaminos Canyon 21 Site Summary. U.S. Department of Energy, Proceedings of the Drilling and Scientific Results of the 2009 Gulf of Mexico Gas Hydrate Joint Industry Project Leg II.

Fugro Robertsom Limited, 2009. StatoilHydro Mizzen O-16 Well, Flemish Pass Area, Offshore Newfoundland - Biostratigraphy of the Interval 1870m-3758.5 m TD. Fugro Robertson Limited, Llandudno, North Wales, UK. Report Number 7038(C-NLOPB)/Ib, August 2009. Prepared for StatoilHydro Canada Limited, Calgary, Alberta.

Gabitto, J.F. and Tsouris, C. 2010. Physical properties of gas hydrates: A review. Journal of Thermodynamics, **2010**: 1-12.

Gacal-İşler, B. 2009. Mesozoic Tectonic and Stratigraphic Evolution of the Orphan Basin, with Special Emphasis on Regional Correlations with Flemish Pass and Northern Jeanne d'Arc Basins, Grand Banks of Newfoundland. Masters thesis, Memorial University of Newfoundland.

Geletti, R. and Busetti, M. 2011. A double bottom simulating reflector in the western Ross Sea, Antarctica. Journal of Geophysical Reaserch, **116**: 1-15.

Giavarini, C. and Hester, K., 2011. Gas Hydrates, Immense Energy Potential and Environmental Challenges. Springer, New York.

Golmshtok, A.Y. and Soloview, V. A. 2006. Some remarks on the thermal nature of the double BSR, Marine Geology, **229**: 187-198.

Grant, A.C. and McAlpine, K.D., 1990. The Continental Margin Around Newfoundland. *In* Geology of the Contienntal Margin of Eastern Canada. *Edited by* M.J. Keen and G.L. Williams. Geological Survey of Canada, Geology of Canada Series no. 2, 239-292.

Haacke, R.R., Westbrook, G.K., and Hyndman, R.D. 2007. Gas hydrate, fluid flow and free gas: Formation of the bottom-simulating reflector. Earth and Planetary Science Letters, **261**: 407-420.

Hammerschmidt, E.G. 1934. Formation of gas hydrates in natural gas transmission lines. Industrial Engineering Chemistry, **26**: 851-855.

Hein, J.R., Scholl, D.W., Barrow, J.A., Jones, M.G., and Miller, J. 1978. Diagenesis of late Cenozoic deposits and formation of the bottom simulating reflector in the southern Bering Sea. Sedimentology, **25**: 155-181.

Helgerud, M.B., Dvorkin, J., Nur, A., Sakai, A., and Collet, T. 1999. Elastic-wave velocity in marine sediments with gas hydrates: Effective medium modeling. Geophysical Reasearch Letters, **26** (13): 2021-2024.

Henry, S.G., 1997. Catch the (Seismic) Wavelet. AAPG Explorer.

Hill, R. 1952. The elastic behavior of crystalline aggregate. Proceedings of the Physical Society of London, **A65**: 349-354.

Hovland, M. and Gudmestad, O.T. 2001. Potential Influence of Gas Hydrates on Seabed Installations, *in* Natural Gas Hydrates: Occurrence, Distribution, and Detection. *Edited by* W.P. Dillion and C.K. Paull, American Geophyscial Union, Washington DC, 307-315.

Hovland, M. and Judd, A.G. 1988. Seabed Pockmarks and Seepages. Impact on Geology, Biology and the Marine Environment, Graham and Trotman Limited, London.

Huppertz, T.J. 2007. Late Quaternary history of Flemish Pass, southeast Canadian continental margin. MSc Masters thesis Dalhousie University.

Huppertz, T.J. and Piper, D.J.W. 2009. The influence of shelf-crossing glaciation on continental slope sedimentation, Flemish Pass, eastern Canadian continental margin, Marine Geology, **256**: 67-85.

Husebø, J., Ersland, G., Graue, A., and Kvamme, B. 2009. Effects of salinity on hydrate stability and implications for storage of CO_2 in natural gas hydrate reservoirs, Energy Procedia, **1**: 3731-3738.

Hyndman, R.D. and Davis, E.E., 1992. A mechanism for the formation of methane hydrate and seafloor bottom-simulating reflectors by vertical fluid expulsion. Journal of Geophysical Research, **97**(B5): 7025-7041.

Jadhawar, P., Mohammadi, A.H., Yang, J., and Tohidi, B. 2006. Subsurface carbon dioxide storage through clathrate hydrate formation. *In* Advances in the Geological Storage of Carbon Dioxide: International Approaches to Reduce Anthropogenic Greenhouse Gas Emissions. *Edited by* S. Lombardi, L.K. Altunina, and S.E. Beaubien. Springer, Netherlands, pp. 11-126.

Jansa, L.F., and Wade, J.A. 1975. Geology of the continental margin off Nova Scotia and Newfoundland. *In* Offshore Geology of Eastern Canada. *Edited by* W.J.M. Van Der Linden and J.A. Wade. Geological Survey of Canada Paper 74-30, vol.2., pp.51-105.

Jansa, L.F., Remane, J., and Ascoli, F. 1980. Calpionellid and foraminiferal-ostracode biostratigraphy in the Jurassic/Cretaceous boundary, offshore Eastern Canada. Rivista Italiana Paleontology, **86**(1): 67-126.

Japan Oil, Gas and Metals National Corporation (JOGMeC). Gas Production from Methane Hydrate Layers Confirmed. News Release, 12.03.13 (2013), pp. 1–3. Accessed from https://www.jogmec.go.jp/english/news/release/release0110.html on 2/15/2016.

Kastner, M., Keene J.B., and Gieskes, J.M. 1977. Diagenesis of Siliceous Oozes .1. Chemical Controls on Rate of Opal-a to Opal-CT Transformation - Experimental-Study. Geochimica Et Cosmochimica Acta, **41**: 1041-1059.

Katz, M.E., Wright, J.D., Miller, K.G., Cramer, B.S., Fennel, K., and Falkowski, P.G. 2005. Biological overprint of the geological carbon cycle. Marine Geology, **217**: 323-338.

Kennard, L. Schafer, C., and Carter, L. 1990. Late Cenozoic evolution of Sackville Spur: a sediment drift on the Newfoundland continental slope. Canadian Journal of Earth Sciences, **27**: 863-878.

Kim, H.-J.; Jou, H.-T.; Kang, S.-G.; Lee, G. H.; Yi, B. Y.; Yoo, D.-G. ; Ryu, B.-J.; Shin, C. 2013. Seismic characterization and imaging of a gas hydrate deposit in the western part of the Ulleung Basin, the East Sea (Japan Sea). Marine and Petroleum Geology, **47**: 214-221.

King, E.L. and Sonnichsen, G.V. 1999. Characterization of near-surface seismostratigraphy and features of Northeastern Grand Bank: sea level fluctuations, glaciation and slope stability. Open File 3886, Geological Survey of Canada, Ottawa.

Kingdom®, Version 8.8. [Computer software] HIS.

Klauda, J.B. and Sandler, S.I., 2005. Global Distribution of Methane Hydrate in Ocean Sediment. Energy and Fuels, **19**: 469-470.

Kvenvolden, K.A. and Barnard, L.A., 1983. Gas Hydrates of the Blake Outer Ridge Site 533, Deep Sea Drilling Project Leg 76. *In* Initial Reports DSDP 76. *Edited by* R.E Sheridan, F. Gradstien et al. PP. 353-365.

Lazier, J.R.N. and Wright, D.G. 1993. Annual Velocity Variations in the Labrador Current, Journal of Physical Oceanography, **23**: 659-678.

LeBlanc, C., Louden, K., and Mosher, D. 2007. Gas hydrates off Eastern Canada: Velocity models from wide-angle seismic profiles on the Scotia Slope. Marine and Petroleum Geology, **24**(5): 321-335.

Lee, H.J. 2009. Timing of occurrence of large submarine landslides on the Atlantic Ocean margin. Marine Geology, **264**(1-2): 53-64.

Lee, M.W., Hutchinson, D.R., Agena, W.F., Dillion, W.P., Miller, J.J., and Swift, B.A. 1994. Seismic character of gas hydrates on the southeastern U.S. continental margin. Marine Geophysical Researches, **16**: 163-184.

León, R. Somoza, L., Giménez-Moreno, C.J., Dabrio, C.J., Ercilla, G., Praeg, D., Díaz-del-Río, V., and Gómez-Delgado, M. 2009. A predictive numerical model from potential mapping of the gas hydrate stability zone in the gulf of Cadiz. Marine and Petroleum Geology, **26**: 1564-1579.

Li, G. and Piper, D.J.W. 2015. The influence of meltwater on the Labrador Current in Heinrich event 1 and the Younger Dryas, Quaternary Science Reviews, **107**: 129-137.

Liner, C.L. 2004. Elements of 3D seismology, 2nd edition PennWell Publishing, Tulsa, OK U.S.A.

Loutit, T.S., Hardenbol, J., Vail, PR. and Baum, G.R., 1988. Condensed sections: the key to age determination and correlation of continental margin sequences. *In* Sea-Level Changes: An Integrated Approach. *Edited by* C.K. Wilgus, B.S. Hastings et al., Special Publication, Society of Economic and Paleontological Mineralogy, **42**: pp. 183-213.

Lowe, D.G., Sylvester, P.J. and Enachescu, M.E. 2011. Provenance and paleodrainage patterns of Upper Jurassic and Lower Cretaceous synrift sandstones in the Flemish Pass Basin, offshore Newfoundland, east coast of Canada. AAPG Bulletin, **95**(8): 1295-1320.

Majorowicz, J.A. and Osadetz, K.G. 2003. Natural Gas Hydrate Stability in the East Coast Offshore-Canada. Natural Resources Research, **12**(2): 93-104.

Malone, R., 1985. Gas hydrates topical report, Tech. Rep. DOE/METC/SP-218 (DE85001986), Department of Energy, Morgantown Energy Technology Center, Morgantown, WVa, USA.

Manspeizer, W., 1988. Triassic-Jurassic rifting: Continental breakup and the origin of the Atlantic Ocean and passive margins. Developments in Geotectonics, **22**: 41-80.

Markl, R.G., Bryan, G.M., and Ewing, J.I. 1970. Structure of the Blake-Bahama Ridge. Journal of Geophysical Research, **75**: 4539-4555.

Marfart, K.J., Kirlin, R.L., Farmer, S.L. and Bahorich, M.S. 1998. 3-D seismic attributes using a semblance-based coherency algorithm. Geophysics; **63** (4): 1150-1165.

Marfurt, K.J., Sudhaker, V., Gersztenkorn, A., Crawford, K.D., and Nissen, S.E. 1999. Coherency calculations in the presence of structural dip: Geophysics, **64**: 104-111.

Marshall, N.R., Piper, D.J.W., Saint-Ange, F., and Campbell, D.C. 2014. Late Quaternary history of contourite drifts and variations in Labrador Current flow, Flemish Pass, offshore eastern Canada. Geo-Marine Letters, **34**: 457-470.

Mavko, G., Mukerji, T., and Dvorkin, J. 2009. The Rock Physics Handbook, Cambridge University Press, New York, pp. 511.

Max, M.D. and Johnson, A.H., 2014. Hydrate petroleum system approach to natural gas hydrate exploration, Petroleum Geoscience, **20**: 187-199.

McConnel, D. and Kendall, B. 2001. Images of the base of hydrate stability, Northwest Walker Ridge, Gulf of Mexico. OTC Paper #14103.

McConnell, D.R., Zhang, Z., and Boswell, R. 2012. Review of progress in evaluating gas hydrate drilling hazards. Marine and Petroleum Geology, **34**: 209-223.

Meadows, D. and Davies, R.J. 2010. The limited suitability of silica diagenetic boundaries as isothermal markers: Insights from seismic reflection imaging, Offshore Sakhalin, Russian Far East. Marine and Petroleum Geology, **27**:1028-1039.

Miller, K.G., Wright, J.D., Katz, M.E., Wade, B.S., Browning, J.V., Cramer, B.S., and Rosenthal, Y. 2009. Climate threshold at the Eocene-Oligocene transition: Antarctic ice sheet influence on ocean circulation. *In* The Late Eocene Earth—Hothouse, Icehouse, and Impacts: Geological Society of America Special Paper 452. *Edited by* C. Koeberl, A. Montanari, p. 169–178.

Milkov, A.V. and Sassen, R., 2002. Preliminary assessment of resources and economic potential of individual gas hydrate accumulations in the Gulf of Mexico continental slope, Marine and Petroleum Geology, **20** (2): 111-128.

Mitchum, R.M., Vail, P.R., and Sangree, J.B. 1977. Seismic stratigraphy and global changes of sea level, Part 6: stratigraphic interpretation of seismic reflection patterns in depositional sequences. *In* Seismic Stratigraphy – Applications to Hydrocarbon Exploration. American Association of Petroleum Geologists Memoir 26. *Edited by* C.E. Payton, 117-133.

Moridis, G.J., Collett, T.S., Dallimore, S.R., Inoue, T., and Mroz, T., 2005. Ananlysis and interpretation of the thermal test of gas hydrate dissociation in the JAPEX/JNOC/GSC et. Mallick 5L-38 gas hydrate production research well. *In* Scientific Results from the Mallik 2002 Gas Hydrate Production Research Well Program, Mackenzie Delta, Northwest Territories, Canada. Edited by S.R. Dallimore and T.S. Collett: Geological Survey of Canada, Bulletin 585, 1-21.

Mosher, D.C., Bigg, S., and LaPierre, A. 2006. 3D seismic versus multibeam sonar seafloor surface renderings for geohazard assessment: Case examples from the central Scotian Slope. The Leading Edge, **25**: 1484-1494.

Mosher, D.C. 2011. A margin-wide BSR gas hydrate assessment: Canada's Atlantic margin. Marine and Petroleum Geology. **28**: 1540-1553.

Mountain, G.S. and Tucholke, B.E. 1985. Mesozoic and Cenozoic Geology of the U.S. Atlantic Continental Slope and Rise. *In* Geologic Evolution of the U.S. Atlantic Margin. *Edited by* Poag, C.W., Van Nostrand Reinhold, pp. 293-341.

Mulder, T. and Moran, K. 1995. Relationship among submarine instabilities, sea level variations, and the presence of an ice sheet on the continental shelf: An example from the Verrill Canyon Area, Scotian Shelf. Paleoceanography, **10**: 137-154.

Muller-Michaelis, A. and Uenzelmann-Neben, G. 2014. Development of the Western Boundary Undercurrent at Eirik Drift related to changing climate since the early Miocene, Deep Sea Research Part 1: Oceanographic Research Papers, **93**: 21-34.

Murphy, W.F. III, 1982. Effects of Microstructure and Pore Fluids on the Acoustic Properties of Granular Sedimentary Materials. Ph.D. Dissertation, Stanford University.

Myers, R.A. and Piper, D.J. 1988. Seismic Stratigraphy of late Cenozoic sediments in the northern Labrador Sea: a history of bottom circulation and glaciation. Canadian Journal of Earth Science, **25**: 2059-2074.

Neagu, R.C. 2011. The relationship between biogenic silica diagenesis and the physical properties of sediments studied using seismic and well data. Ph.D Dissertation, Cardiff University

Nierenberg, W.A. and Peterson, M.N.A. 1971. Deep Sea Drilling Project Technical Report No. 1, Scripps Institution of Oceanography, University of California at San Diego. Operations Resumes Leg 1 through Leg 18 August 11, 1968 through July 19, 1971.

Nobes, D.C., Murray, R.W., Kuramoto, S., Pisciotto, K.A., and Holler, P. 1992. Impact of silica diagenesis on physical property variations. *In* Proceedings of the Ocean Drilling Program, Scientific Results, Leg 127/128 part 1: pp. 3-31.

Nur, A., Mavko, G. Dvorkin, J., and Galmudi, D. 1998. Critical Porosity: A Key to Relating Physical Properties to Porosity in Rocks. The Leading Edge, **17**: 357-362.

Owen, M., Day, S. and Maslin, M. 2007. Late Pleistocene submarine mass movements: occurrence and causes. Quaternary Science Review, **26**: 958-978.

Paull, C.K., Lorenson, T.D., Dickens, G., Borowski, W.S., Ussler III, W., and Kvenvolden K. 2000. Comparisons of *In Situ* and Core Gas Measurements in ODP Leg 164 Bore Holes. Annals of the New York Academy of Sciences, **912**: 23-31.

Paull, C.K., Ussler, W., and Borowski, W.S., 1994. Sources of Biogenic Methane to Form Marine Gas Hydrates, Annals of the New York Academy of Sciences, **715**: 392-409.

Pearson, C.F., Halleck, P.M., McGuire, P.L., Hermes, R., and Mathews, M., 1983. Natural gas hydrate deposits: a review of in-situ properties. Journal of Physical Chemistry, **87**: 4180–4185.

Pegrum, R.M., Ødegård, T., Bonde, K., and Hamann, N.E. 2001. Exploration in the Fylla Area, SW. AAPG Regional Conference, St Petersburg Russia.

Penman, D.E., Turner, S.K., Sexton, P.F., Norris, R.D., Dickson, A.J., Boulila, S., Ridgwell, A., Zeebe, R.E., Zachos, J.C., Cameron, A., Westerhold, T., and Rohl, U. 2016. An abyssal carbonate compensation depth overshoot in the aftermath of the Palaeocene-Eocene Thermal Maximum. Nature Geoscience, **9**(8): 575-581.

Pecher,I.A., and Holbrook, W.S., 2003. Seismic methods for detecting and quantifying marine methane hydrate/free gas reservoirs. *In* Natural Gas Hydrate in Oceanic and Permafrost Environmnets. *Edited by* M.D. Max. Kluwer Academic Publishers, Boston, Mass., pp. 275-294.

Phrampus, B.J. and Hornbach, M.J. 2012. Recent changes to the Gulf Stream causing widespread gas hydrate destabilization, Nature, **490** (7421): 527-530.

Piper, D.J.W., Deptuck, M.E., Mosher, D.C., Hughes-Clarke, J.E., and Migeon, S. 2012. Erosional and depositional features of glacial meltwater discharges on the eastern Canadian continental margin. *In*: Application of the Principles of Seismic Geomorphology to Continental Slope and Base-of-slope Systems: Case Studies from Seafloor and Near-Seafloor Analogues. *Edited by* B. Prather, M. Deptuck, D. Mohrig, B. van Hoorn, and R. Wynn. SEPM Special Publication **99**, Tulsa, OK U.S.A. pp. 61-80.

Piper, D.J.W. and Normark, W.R. 1989. Late Cenozoic sea-level changes and the onset of glaciation - impact on continental-slope progradation off eastern Canada. Marine and Petroleum Geology, **6** (4): 336-347.

Piper, D.J.W. and Pereira, C.P.G., 1992. Late Quaternary sedimentation in central Flemish Pass, Canadian Journal of Earth Sciences, 29, 535-550.

Popescu, I., DeBatist, M., Lericolais, G., Nouzé, H., Poort, J., Panin, N., Versteeg, W., and Gillet, H. 2006. Multiple bottom-simulating reflections in the Black Sea: Potential proxies of past climate conditions. Marine Geology, **227**(3): 163-176.

Priest, J.A., Best, A.I., and Clayton, C.R.I., 2006. Attenuation of seismic waves in methane gas hydrate-bearing sand. Geophysics Journal International, **164**: 149-159.

Riech, V. and von Rad, U. 1979. Eocene porcellanites and Early Cretaceous cherts from the western North Atlantic Basin. *In* Initial Reports of the Deep Sea Drilling Project (DSDP): Leg 43. *Edited by* B.E. Tucholke,.P.R.Vogt, et al. pp. 437-455.

Riedel, M., Bahk, J.-J., Ryu, B.-J., Yoo, D.-G., Kim, W., and Kim, G.Y. 2012. Mass-transport deposits and gas hydrate occurances in the Ulleung Basin, East Sea – Part 2: Gas hydrate content and fracture-induced anisotrophy, Marine and Petroleum Geology, **35**: 75-90.

Riedel, M., Willoughby, E.C., and Chopra. S. 2010. Geophysical characterization of gas hydrates. Society of Exploration Geophysicists, Tulsa, OK U.S.A.

Robertson Research International Limited, 2002. Stratigraphic correlation of Baccalieu I-78, Gabriel C-60, Lancaster G-70 and South Tempest G-88 wells. Robertson Research International Limited Report Number 6268/Ib.

Ruppel, C., Boswell, R., Jones, E. 2008. Scientific results from Gulf of Mexico gas hydrates joint industry project Leg 1 drilling: introduction and overview. Journal of Marine and Petroleum Geology, 25: 819-829.

Sain, K., Singh, A.K., Thakur, N.K., and Khanna, R. 2009. Seismic quality factor observations for gas-hydrate-bearing sediments on the western margin of India. Marine Geophysical Research, **30**: 137-145.

Satyavani, N., Sain, K., Lall, M., and Kumar, B.J.P. 2008. Seismic attribute study for gas hydrates in the Andaman Offshore India, Marine Geophysical Research, **29**: 167-175.

Satyavani, N., Thakur, N.K., Aravind Kumar, N., and Reddi, S.I. 2005. Migration of methane at the diapiric structure of the western continental margin of India – insights from seismic data. Marine Geology, **219**(1): 19-25.

Saunders, P. M. and Fofono, N. P. 1976. Conversion of pressure to depth in the ocean. Deep Sea Research, **23**: 109-111.

Schlesinger, A., Cullen, J., Spence, G., Hyndman, R., Louden, K., and Mosher, D. 2012. Seismic velocities on the Nova Scotian margin to estimate gas hydrate and free gas concentrations. Marine and Petroleum Geology, **35**: 105-115.

Serra, O. 1984. Fundamentals of well-log interpretations. *In* Developments in Petroleum Science 15A I and II: Amsterdam, the Netherlands, Elservier, pp. 423.

Shaw, J., Piper, D.J.W., Fader, G.B.J., King, E.L., Todd, T., Bell, T., Batterson, M.J., and Liverman, D.G.E. 2006. A conceptual model of the deglaciation of Atlantic Canada, Quaternary Science Reviews, **25**: 2059-2081.

Shedd, W., Frye, M., Godfriaux, P., Boswell, R., and Hutchinson, D. R. 2009. Occurrence and variety in expression of the base of gas hydrate stability in the Gulf of Mexico, USA: Fire in the Ice, v. Winter 2009, 11-14.

Sheriff, R.F. 1985. Aspects of Seismic Resolution. *In* Seismic Stratigraphy II - An Integrated Approach. *Edited by* O.R. Berg and D.G. Woolverton. Tulsa, OK U.S.A. AAPG Memoir **39**: pp. 1-10.

Sloan Jr., E. D. 1998. Clathrate hydrates of natural gases. Marcel Dekker, Inc., New York.
Sloan, Jr., E.D. 2003. Fundamental principles and applications of natural gas hydrates. Nature, **426**: 353-363.

Spence, G.D., Haacke, R.R., and Hyndman, R.D. 2010. Seismic indicators of natural gas hydrate and underlying free gas. *In* Geophysical Characterization of Gas Hydrates. *Edited by* M. Riedel, E.C. Willoughby, and S. Chopra. Society of Exploration Geophysicists, Tulsa, OK U.S.A. pp. 39-71.

Stein, R., Littke, R., Stax, R., and Welte, D.H. 1989. 13. Quantity, provenance, and maturity of organic matter at ODP sites 645, 646, and 647: Implications for reconstruction of paleoenvironments in Baffin Bay and Labrador Sea during Tertiary and Quaternary time. Proceedings of the Ocean Drilling Program, Scientific Results, **105**: 185-208.

Stern, L.A., Kirby, S.H., Durham, W.R., Circone, S., and Waite, W.F., 2000. Laboratory synthesis of pure methane hydrate suitable for measurement of physical properties and decomposition behavior. *In* Natural Gas Hydrates in Oceanic and Permafrost Environments. *Edited by* M.D. Max. Kluwer Academic Publishers, Boston, Mass. pp. 323-348.

Stoll, R.D. and Bryan, G.M. 1979. Physical properties of sediments containing gas hydrates. Journal of Geophysical Research, **84** (B4): 1629-1634.

Stoker, M.S., Hoult, R.J., Nielsen, T., Hjelstuen, B.O., Lanberg, J.S., Shannon, P.M., Praeg, D., Mathiesen, A., van Weering, T.C.E., and McDonnell, A. 2005. Sedimentary and oceanographic responses to early Neogene compression on the NW European margin. Marine and Petroleum Geology, **22**(9-10): 1031-1044.

Tankard A.J. and Balkwill, H.R. 1989. Extensional tectonics and stratigraphy of the North Atlantic margins; Introduction; Extensional tectonics and stratigraphy of the North Atlantic margins. AAPG Memoir, **46**: 1-6.

Taner, M.T. and Sheriff, R.E. 1977. Application of Amplitude, Frequency, and Other Attributes to Stratigraphic and Hydrocarbon Determination, American Association of Petroleum Geologists Memoir, **26**: 301-327.

Taner, M.T., Koehler, F., and Sheriff, R.E. 1979. Complex seismic trace analysis, Geophysics, **44**: 1041-1063.

Taylor, M.H., Dillon, W.P., and Percher, I.A., 2000. Trapping and migration of methane associated with the gas hydrate stability zone at the Blake Ridge Diapir: new insights from seismic data. Marine Geology, **164** (1): 79-89.

Thein, J. and von Rad, U. 1987. Silica diagenesis in continental rise and slope sediments off eastern North America (Sites 603 and 605, Leg 93; Sites 612 and 613, Leg 95). *In* Initial Reports of the Deep Sea Drilling Project(DSDP) Leg 95. *Edited by* Poag, C.W.

Tucholke, B.E. and Mountain, G.S. 1979. Seismic Stratigraphy, lithostratigraphy and paleosedimentation patterns in the North American Basin. Deep Drilling Results in the Atlantic Ocean: Continental Margins and Paleoenvironment. American Geophysical Union Maurice Ewing Series, **3**: 58-86.

Tucholke, B.E., Mountain, G.S., 1986. Tertiary paleoceanography of the western North Atlantic Ocean. *In* The Geology of North America, Volume M, The Western North Atlantic Region. *Edited by* P.R. Vogt, B.E. Tucholke. Geological Society of America, Boulder, CO. U.S.A. pp. 631–650.

Tucholke, B.E., Austin, J.A. Jr, & Uchupi, E., 1989. Crustal structure and rift-drift evolution of the Newfoundland Basin. *In* Extensional tectonics and stratigraphy of the North Atlantic Margins). Edited by A.J. Tankard and H.R. Balkwill. American Association of Petrology and Geology, Tulsa, OK U.S.A. pp. 247–263.

Tucholke, B.E. and Whitmarsh, R.B. 2012. The Newfoundland-Iberia conjugate rifted margins. *In* Regional Geology and Tectonics: Phanerozoic Passive Margins, Cratonic Basins and Global Tectonic Maps. *Edited by* D.G. Roberts and A.W. Bally. Elsevier, Amsterdam, **10**: 342-382.

Uddin, M., Wright, J.F., Dallimore, S.R., and Coombe, D. 2012. Gas hydrate production from the Mallik reservoir: numerical history matching and long-term production forecasting. *In* Scientific results from the JOGMEC/NRCan/Aurora Mallik 2007-2008 gas hydrate production research well program, Mackenzie Delta, Northwest Territories, Canada. *Edited by* S.R. Dallimore, K. Yamamoto, J.F. Wright, and Bellefleur: Geological Survey of Canada, Bulletin 601, pp. 261-289.

USGS hydrate map http://woodshole.er.usgs.gov/project-pages/hydrates/primer.html

Vanneste, M., Sultan, N., Garziglia, S., Forsberg, C.F., and L'Heureux, J.-S. 2014. Seafloor instabilities and sediment deformation processes: The need for integrated, multi-disciplinary investigations. Marine Geology, **352**: 183-214.

Vecsei, A. and Hoppie, B.W. 1996. Sequence stratigraphy and diagenesis of the Miocene-Oligocene below the New Jersey continental slope: Implications of physical properties and minerological variations. Proceedings of the Ocean Drilling Program, Scientific Results, **150**: 361-376.

Von de Dick, H. 1989. Environment of petroleum source rock deposition in the Jeanne d'Arc basin off Newfoundland. *In* Extensional tectonics and stratigraphy of the North Atlantic margins. *Edited by* A.J. Tankard and H.R. Balkwill. American Association of Petroleum Geology, Calgary, **46**: pp. 295-303.

Waite, W.F., Stern, L.A., Kirby, S.H., Winters, W.J., and Mason, D.H., 2007. Simultaneous determination of thermal conductivity, thermal diffusivity and specific heat in sI methane hydrate. Geophysical Journal International, **169** (2): 767-774.

Waseda, A. 1998. Organic carbon content, bacterial methanogenesis, and accumulation process of gas hydrates in marine sediments. Geochemical Journal, **32**: 143-157.

Welsink, H.J., Dwyer, J.D., Knight, R.J., 1989. Tectono-stratigraphy of the passive margin off Nova Scotia. *In* Extensional Tectonics and Stratigraphy of the North Atlantic Margin. *Edited by* A.J. Tankard and H.R. Balkwill. American Association of Petroleum Geology, **46**: 215-231.

Westbrook, G.K., Thatcher, K.E., Rohling, E.J., Piotrowski, A.M., Pälike, H., Osborne, A.H., Nisbet, E.G., Minshull, T.A., Lanoisellé, M., James, R.H., Hühnerbach, V., Green, D., Fisher, R.E., Crocker, A.J., Chabert, A., Bolton, C., Beszczynska-Möller, A., Berndt, C., and Aquilina, A. 2009. Escape of methane gas from the seabed along the West Spitsbergen continental margin. Geophysical Research Letters, **36**: L15608, 1-5.

White, R. and Simm, R. 2003. Tutorial: Good practice in well ties. First Break, **21**: 75-83.

Wielens, H. and Jauer, C. 2001. Overpressure, Thermal Maturity, Temperature and Log Responses in Basins of the Grand Banks of Newfoundland. Geological Survey of Canada, Open File 3937.

Williams, L.A. and Crerar, D.A. 1985. Silica Diagenesis, II. General Mechanisms. Journal of Sedimentary Petrology, **55** (3): 312-321.

Williams, H. and Hatcher, R.D., Jr 1982. Suspect terranes and accretionary history of the Appalachian Orogen. Geology, **10**: 530-536.

Williams, H. and Hatcher, R.D., Jr 1983. Appalachian suspect terranes. *In* Contributions to the Tectonics of Mountain Chains. *Edited by* R.D. Hatcher Jr., H. Williams and I. Zietz. Geological Society of America, Memoir **158**: 33-53.

Wood, W.T and Jung, W.-Y. 2008. Modeling the extent of Earth's marine methane hydrate cryosphere. *In* Proceedings of the 6th International Conference on Gas Hydrates. *Edited by* P. Englezos and J. Ripmeester, pp. 1-8.

Yefremova, A.G. and Zhizhchenko, B.P. 1974. Occurrence of crystal hydrates of gas in sediments of modern marine basins. Doklady Akademii Nauk SSSR 214, 1179-1181.

Yilmaz, Ö, and Doherty, S. M. 1987. Seismic Data Processing. Investigations in Geophysics; v. 2. Society of Exploration Geophysicists. Tulsa, OK U.S.A., pp. 526.

Yoneda, J., Masui, A., Konno, Y., Jin, Y., Egawa, K., Kida, M., Ito, T., Nagao, J., and Tenma, N. 2015. Mechanical behavior of hydrate-bearing pressure-core sediments visualized under triaxial compression. Marine and Petroleum Geology, **66** (2): 451-459.

Zoeppritz, K. 1919. On the reflection and propagation of seismic waves at discontinuities. Erdbebenwellen, VIIB, Gottinger Nachrichten I, 66-84.

APPENDIX A Effective Medium Modelling MatLab Script

```
% from Helgerud et al., Elastic-wave velocity in marine sediments with gas
%      hydrates: effective medium modeling, Geophys. Res. Lett., 26, 2021-2024, 1999.

   % id = 1 hydrate in pore fluid or homogeneously distributed gas
   % id = 2 hydrate in sediment frame or gas patchily distributed in pore fluid
   clear xK G xKdry Gdry xKsat Gsat xKhm Ghm Z Pvel Svel;
   clear bulkDensity waterConc waterSat;
   id = 2;

        % depth below SEAFLOOR (m)
        depthMBSF = 25.:25.:700.;
   n = length(depthMBSF);
        % porosity < critical porosity results in mineral grains being load bearing,
otherwise fluid phase bearing.
        %porosity = 0.65 .* exp(-depthMBSF/1268.); % Vancouver Margin
        porosity = 0.65 .* exp(-depthMBSF/800.); % Sackville Spur
   xKdry(1:n) = 0.;
   Gdry(1:n) = 0.;
   xKsat(1:n) = 0.;
   Gsat(1:n) = 0.;
   xKhm(1:n) = 0.;
   Ghm(1:n) = 0.;
   Z(1:n) = 0.;
   waterConc(1:n) = 0.;
   waterSat(1:n) = 0.;
   bulkDensity(1:n) = 0.;
   Pvel(1:n) = 0.;
   Svel(1:n) = 0.;

        % bulk modulii of water,  hydrate and gas
        xKwater = 2.5e9;
```

```
   xKhyd = 7.9e9;
   Ghyd = 3.3e9;
   xKgas = 0.11e9;

         % constant values
         g = 9.8; % m/s^2
         waterDensity = 1032.0;  % kg/m^3
         gasDensity = 230.0;
         hydrateDensity = 900.0;
         critPorosity = 0.38;        % critical porosity generally in range 0.36-0.40 (Nur et
al., 1998)
         xn = 8.75;                % grain contacts at critical porosity generally in range 8-9.5
(Murphy, 1982)

         hydrateConcentration = 0.0; % hydrate content of sediment
         gasConcentration = 0.005; % gas content of sediment

   if gasConcentration > 0.0 % gas in pore fluid
         waterConc = porosity - gasConcentration;
   elseif (hydrateConcentration > 0.0) & (id==1)  % hydrate in pore fluid
         waterConc = porosity - hydrateConcentration;
   else
      waterConc = porosity;   %hydrate in solid
   end
         waterSat = waterConc ./ porosity;

         % bulk modulus of pore fluid for depth in range(0, 1000)

         hydratePoreConc = hydrateConcentration ./ porosity;

   if (hydrateConcentration > 0.) & (id==1)    % bulk modulus of pore fluid (water and
hydrate) for id=1
         xKfluid = 1. ./ ((hydratePoreConc ./ xKhyd) + (1 - hydratePoreConc) ./ xKwater);
```

```
   elseif (gasConcentration > 0.) & (id==1)    % bulk modulus of pore fluid (water and
gas) for id=1
         xKfluid = 1. ./ ((waterSat ./ xKwater) + (1 - waterSat) ./ xKgas);

   else
   xKfluid = xKwater;

   end

  % solid density, bulk and shear modulii of composite sediment (mks units)

  %mineral properties
   %clay
   Dcly = 2580.;
         xKcly = 20.9e9;
   Gcly = 6.85e9;
   %calcite
   Dcal = 2710.;
   xKcal = 76.8e9;
   Gcal = 32.e9;
   %quartz
   Dqtz = 2650.;
   xKqtz = 36.6e9;
   Gqtz = 45.e9;
   %dolomite
   Ddmt = 2870.;
   xKdmt = 80.2e9;
   Gdmt = 49.e9;
   %feldspar
   Dfsp = 2620.;
   xKfsp = 37.5e9;
   Gfsp = 15.e9;
   %other
   Doth = 3580.;
```

```
    xKoth = 106.e9;
    Goth = 65.e9;
    %mineral fractions
    fcly = .19;
    fcal = .12;
    fqtz = .28;
    fdmt = .08;
    ffsp = .3;
    foth = .03;

    %calculate constants of solid phase from constituents usings Hill's (1952) average
formula

    % assume no hydrate (or gas) in solid phase

        xK1 =
(fcly.*xKcly)+(fcal.*xKcal)+(fqtz.*xKqtz)+(fdmt.*xKdmt)+(ffsp.*xKfsp)+(foth.*xKoth);
        xK2 =
1./((fcly./xKcly)+(fcal./xKcal)+(fqtz./xKqtz)+(fdmt./xKdmt)+(ffsp./xKfsp)+(foth./xKoth));
        xK = 0.5 .* (xK1 +xK2);
        G1 = (fcly.*Gcly)+(fcal.*Gcal)+(fqtz.*Gqtz)+(fdmt.*Gdmt)+(ffsp.*Gfsp)+(foth.*Goth);
        G2 =
1./((fcly./Gcly)+(fcal./Gcal)+(fqtz./Gqtz)+(fdmt./Gdmt)+(ffsp./Gfsp)+(foth./Goth));
        G = 0.5 .* (G1 +G2);
        D1 = (fcly.*Dcly)+(fcal.*Dcal)+(fqtz.*Dqtz)+(fdmt.*Ddmt)+(ffsp.*Dfsp)+(foth.*Doth);
        D2 =
1./((fcly./Dcly)+(fcal./Dcal)+(fqtz./Dqtz)+(fdmt./Ddmt)+(ffsp./Dfsp)+(foth./Doth));
        solidDensity = 0.5 .* (D1 +D2);

    if (id==2) & (hydrateConcentration > 0.)    % if id=2 incorporate hydrate into solid
phase (if present)

        % reduce original porosity and calculate solid phase constants including hydrate
        Rporosity = porosity - hydrateConcentration;
```

```
        fcly = fcly .*(1-porosity) ./ (1-Rporosity);
        fcal = fcal .*(1-porosity) ./ (1-Rporosity);
        fqtz = fqtz .*(1-porosity) ./ (1-Rporosity);
        fdmt = fdmt .*(1-porosity) ./ (1-Rporosity);
        ffsp = ffsp .*(1-porosity) ./ (1-Rporosity);
        foth = foth .*(1-porosity) ./ (1-Rporosity);
        fhyd = hydrateConcentration ./ (1-Rporosity);
        % recalculate elastic constants
        xK1 =
(fcly.*xKcly)+(fcal.*xKcal)+(fqtz.*xKqtz)+(fdmt.*xKdmt)+(ffsp.*xKfsp)+(foth.*xKoth)+(fhyd.
*xKhyd);
        xK2 =
1./((fcly./xKcly)+(fcal./xKcal)+(fqtz./xKqtz)+(fdmt./xKdmt)+(ffsp./xKfsp)+(foth./xKoth)+(fhy
d./xKhyd));
        xK = 0.5 .* (xK1 +xK2);
        G1 =
(fcly.*Gcly)+(fcal.*Gcal)+(fqtz.*Gqtz)+(fdmt.*Gdmt)+(ffsp.*Gfsp)+(foth.*Goth)+(fhyd.*Ghy
d);
        G2 =
1./((fcly./Gcly)+(fcal./Gcal)+(fqtz./Gqtz)+(fdmt./Gdmt)+(ffsp./Gfsp)+(foth./Goth)+(fhyd./Gh
yd));
        G = 0.5 .* (G1 +G2);
        D1 =
(fcly.*Dcly)+(fcal.*Dcal)+(fqtz.*Dqtz)+(fdmt.*Ddmt)+(ffsp.*Dfsp)+(foth.*Doth)+(fhyd.*hydr
ateDensity);
        D2 =
1./((fcly./Dcly)+(fcal./Dcal)+(fqtz./Dqtz)+(fdmt./Ddmt)+(ffsp./Dfsp)+(foth./Doth)+(fhyd./hyd
rateDensity));
        solidDensity = 0.5 .* (D1 +D2);
        porosity = Rporosity; % porosity is replaced with reduced porosity
        hydrateConcentration = 0.; % no hydrate in pore water
        waterConc = porosity;   %reset waterConc to reduced porosity

    end
```

```
        % Poisson's ratio
        v = 0.5.*(xK - (2.0./3.0).*G)./(xK + (1.0./3.0).*G);

        % simple relationship of porosity (water) and solid (mineral grains)
    % modified to include the density effect of gas hydrate
    bulkDensity = (waterConc.*waterDensity + gasConcentration.*gasDensity +
hydrateConcentration.*hydrateDensity) ...
                            + (1 - porosity).*solidDensity;

        % effective pressure
        effectPress = (bulkDensity - waterDensity) .* g .* depthMBSF;

    % dry frame shear (Ghm) and bulk Modulii (xKhm)
        Ghm = ((5 - 4.*v) ./ (5.*(2 - v))).*(((3.*(xn.^2).*((1 - critPorosity).^2).*(G.^2)) ./
(2.*(pi.^2).*(1 - v).^2)).*effectPress).^(1.0./3.0);

        xKhm = ((((xn.^2).*((1 - critPorosity).^2).*(G.^2)) ./ (18.*(pi.^2).*(1 -
v).^2)).*effectPress).^(1.0./3.0);

        Z = Ghm./6.0 .* ((9.*xKhm + 8.*Ghm)./(xKhm + 2.*Ghm));

        % Kdry and Gdry

    for i=1:n
      j=length(xK);
      if j==1
        xKK=xK;
        GG=G;
      else
        xKK=xK(i);
        GG=G(i);
      end
          if porosity(i) < critPorosity
```

```
                xKdry(i) = (((porosity(i)./critPorosity)./(xKhm(i) + 4.0./3.0.*Ghm(i))) + ...
                        ((1 - porosity(i)./critPorosity)./(xKK + 4.0./3.0.*Ghm(i)))).^-1 -
4.0./3.0.*Ghm(i);

                Gdry(i) = (((porosity(i) ./ critPorosity)./(Ghm(i) + Z(i)))+((1 -
porosity(i)./critPorosity)./(GG + Z(i)))).^-1 - Z(i);

      else
                xKdry(i) = ((((1 - porosity(i))./(1 - critPorosity))./(xKhm(i) +
4.0./3.0.*Ghm(i)))+ ...
                        (((porosity(i) - critPorosity)./(1 -
critPorosity))./(4.0./3.0.*Ghm(i)))).^-1 - 4.0./3.0.*Ghm(i);

                Gdry(i) = ((((1 - porosity(i))./(1 - critPorosity))./(Ghm(i) + Z(i)))+ ...
                        (((porosity(i) - critPorosity)./(1 - critPorosity))./Z(i))).^-1 - Z(i);

      end
   end

      Gsat = Gdry;

   % Ksat for hydrate same for id=1 or id=2

      if gasConcentration == 0.0

         xKsat = xK.*((porosity .* xKdry - (1 + porosity).*xKfluid.*xKdry./xK + xKfluid) ./
...
                ((1 - porosity).*xKfluid + porosity.*xK - xKfluid.*xKdry./xK));

   % Ksat for gas different for id=1 or id=2

   else

      if id==1    % use previous value of Kfluid
```

```
        xKsat = xK.*((porosity .* xKdry - (1 + porosity).*xKfluid.*xKdry./xK + xKfluid) ./ ...
                ((1 - porosity).*xKfluid + porosity.*xK - xKfluid.*xKdry./xK));

    elseif id==2    % for id=2 assumes gas patches are much larger than average pore
size

        xKsatW = xK.*((porosity .* xKdry - (1 + porosity).*xKwater.*xKdry./xK + xKwater)
./ ...
                ((1 - porosity).*xKwater + porosity.*xK - xKwater.*xKdry./xK));
    xKsatG = xK.*((porosity .* xKdry - (1 + porosity).*xKgas.*xKdry./xK + xKgas) ./ ...
                ((1 - porosity).*xKgas + porosity.*xK - xKgas.*xKdry./xK));

    xKsat = 1. ./ ((waterSat ./ (xKsatW + (4./3.).*Gsat)) + ((1-waterSat) ./ (xKsatG +
(4./3.).*Gsat))) ...
          - (4./3.).*Gsat;

    end
  end

      % p and s wave velocity

      Pvel = ((xKsat + 4.0./3.0.*Gsat) ./ bulkDensity).^0.5;
      Svel = (Gsat ./ bulkDensity).^0.5;
      temp = zeros(3,n);
  temp(1,:) = depthMBSF;
  temp(2,:) = porosity;
  temp(3,:)= Pvel;
```